THE ROLE OF INTERFACIAL REACTIONS IN ALUMINUM/NICKEL REACTIVE MULTILAYER PERFORMANCE

by
Michael D. Grapes

A dissertation submitted to Johns Hopkins University in conformity with the
requirements for the degree of Doctor of Philosophy

Baltimore, Maryland
May 2016

ABSTRACT

Interfacial reactions play an important but often overlooked role in the performance of reactive material systems. These are systems where the reactants must be in physical contact for the reaction to occur. Consequently, the initial stages of the macroscopic reaction are extremely sensitive to the microscopic mechanisms operating at the interface between reactants. In the realm of intermetallic formation reactions, the aluminum/nickel system is one of the most frequently studied reactive materials systems. The literature abounds with data on this reaction, including experimental data spanning a large range of heating rates, overall compositions, and ignition methods, as well as a growing body of molecular dynamics simulations. Despite this substantial body of evidence, literature review reveals a gap in the experimental parameter space at heating rates between those studied by calorimetry and those observed in self-propagating reactions. In this dissertation I explore two approaches aimed at addressing this gap.

Inert-mediated reactive multilayers are reactive multilayers to which inert material is added to suppress the maximum temperature. Taking experimental data, we use the theoretically predicted scaling of flame speed with flame temperature to infer that the rate-limiting process in the Al/Ni self-propagating reaction changes with decreasing temperature. In unmediated reactive multilayers (highest temperatures) the reaction rate appears to be limited by the diffusion of Ni in liquid Al. However, when the reaction temperature is reduced the reaction rate becomes limited first by the interfacial dissolution of Ni atoms and ultimately by the solid-state diffusion of Ni through a layer of intermetallic product.

Nanocalorimetry is a small-scale thermal analysis technique capable of very high heating rates. Here we use it to study the Al/Ni interfacial reaction from 10^3 K/s – 10^5 K/s. Included in this effort is the development of *in situ* nanocalorimetry, which combines nanocalorimetry measurements with time-resolved electron microscopy for structural characterization. Results from these experiments show that while the first phase to form does not change between 10^3 K/s and 10^5 K/s, it is possible to drive the reaction into a regime where the nucleation of the first phase is controlled entirely by a parameter called the critical concentration gradient. This condition represents the minimum amount of mixing that is required before there is a positive driving force for nucleation, and has been predicted to play a role in phase suppression at higher heating rates.

Taken together, these new experimental techniques and results provide valuable insights into the interplay between thermodynamics and kinetics in determining the progression of the Al/Ni interfacial reaction. This insight, in turn, will be valuable in understanding other reactive materials and in predicting reaction performance, particularly ignition.

Readers:

Prof. Timothy P. Weihs (advisor)

Dr. David A. LaVan (National Institute of Standards and Technology)

ACKNOWLEDGEMENTS

Six years as a graduate student and collaborations with NIST and LLNL leave me with an almost overwhelming debt of gratitude to those who have helped me along the way. Thanks go first to my advisor, Professor Tim Weihs. Tim gave me the guidance to find the path and the freedom to explore it on my own (dead ends and all). He is an exemplar of the finest form of leadership, consistently putting the welfare of his students ahead of their work while somehow demanding the best of them. Tim has instilled in me a sense of scientific ethics and the value of relationships that I will carry for the rest of my career. There should be more professors like him.

Second mention goes to Dr. David LaVan, who served as a second advisor to me in my collaboration with the National Institute of Standards and Technology. David's expertise was invaluable in all of the design work I did during my PhD. He taught me how to design a part while simultaneously imagining how it would be machined, and how to make concise and accurate engineering drawings. His obvious enjoyment of hands-on circuit design inspired me to learn more about electronics than I ever expected (or knew I wanted) to.

Thank you also to the other members of my thesis defense committee: Prof. Todd Hufnagel, Prof. Michael Falk, and Prof. James Guest. And thank you to Dr. Ken Livi, who provided me with helpful advice a number of times during my PhD and helped with the cross-sectional microscopy described in Chapter 3.

The Weihs Lab was blessed with a number of excellent post-doctoral fellows during my time here. Dr. Sara Barron set an example of diligence and rigor in experimental science that it took me five years to live up to. Dr. Raman Swaminathan generously involved me in his work with nanocalorimetry when I was a first-year student; without this opportunity much of this work would have gone undone. Dr. Karsten Woll was instrumental in advancing my understanding of theories of nucleation suppression in a concentration gradient. Dr. Shashank Lakshman brought a valuable new perspective to the lab during my last year and encouraged me to apply isoconversional analysis to my nanocalorimetry data. My collaboration with Dr. Thomas Voisin on high strain rate testing in the DTEM was an enlightening diversion that I am glad to have been a part of.

The lab was also populated by a number of graduate students during my time. Dr. Greg Fritz, Dr. Adam Stover, Kyle Overdeep, Alex Kinsey, Longyu Zhao, Kyle Slusarski, Nick Krywopusk, and Elliott Wainwright all put up with me and contributed in their own way to making graduate school a more enjoyable and productive experience. Dr. Greg Fritz generously included me in the original development of his ignition theory, an experience that sparked an interest that has continued to the present. Elliott Wainwright brought fresh energy to the lab that made my last year more fun than I expected. Thanks to Nick Krywopusk for his help with scanning electron microscopy.

I had the pleasure to work closely with two undergraduate students during my first two years as a graduate student. Thanks to Tianwei Zhang, who helped to push the early development of inert-mediated reactive multilayers forward, and to Bernadette Cannon, who had the unenviable job of calibrating dozens of nanocalorimeter sensors for me back when it took a lot longer than it does now.

In my collaboration at the National Institute of Standards and Technology I had the pleasure of working with Drs. Feng Yi, Josh Schumacher, Lawrence Friedman, Brian

Burke, and Jordan Betz. Special thanks to Feng, who taught me the ins and outs of everything nanocalorimetry and was always willing to help, especially when it came to overnighting extra samples across the country when all of mine broke in transit. Dr. Lawrence Friedman performed the finite element analysis presented in Chapter 2, and Dr. Josh Schumacher helped make the FIB cross-section described in Chapter 3.

In my collaboration with Lawrence Livermore National Laboratory I am grateful to have worked with Drs. Thomas LaGrange, Melissa Santala, Bryan Reed, Joe McKeown, and Geoff Campbell. Special thanks to Tom and Melissa, the microscopists who ran the DTEM during our experiments and took time out of their lives to get in those few extra shots. I also had the fortune to be able to spend the summer of 2015 at LLNL working as a summer student. Thanks to Prof. Weihs for allowing me to pursue that opportunity and to Kyle Sullivan for pushing the process forward. Although that work doesn't appear in this document, that job gave me a stronger focus and motivation going into my final year that directly contributed to the quality of my dissertation.

The experimental developments in this work would not have been possible without the efforts of talented machinists both at JHU and at NIST. Thanks to Chris Amigo at NIST, who fabricated the original *in situ* nanocalorimetry holder and patiently modified it when I realized my design was inadequate. Thanks to Mike Franckowiak and Frank Cook in the WSE Machine Shop, who were never too busy to spend time consulting on an idea.

Thanks, finally, to my wife Nichole, who deserves the real credit for the completion of this monumental task. Through all the long days and late nights her support was selfless and unwavering. Without her I would have been less focused, less productive, and less joyful – in short, less of who I am today.

•

The people tell the story, but funding agencies paid the bills. Most of this work was supported by the National Science Foundation through Grant No. DMR-1308966. Some of my early work was also supported by the U.S. Department of Energy Office of Basic Energy Sciences under Grant No. DE-FG02-09ER46648, and by the National Institute of Standards and Technology (NIST) under Grant No. 70NANB9H9146. All of the nanocalorimeter sensors used in this work were fabricated at the NIST Center for Nanoscale Science & Technology. The use of the DTEM and efforts of LLNL Staff Scientists involved in this work were supported by the U.S. Department of Energy under Contract DE-AC52-07NA27344 and FWP SCW0974. Thanks finally to Ken and Adele Rodbell for their generous support in the form of the Donald S. Rodbell Memorial Graduate Fellowship.

TABLE OF CONTENTS

LIST OF TABLES

LIST OF FIGURES

1. Introduction

1.1 Motivation

Solid-state interfacial reactions play an important role in a variety of materials disciplines and as such have been studied extensively for many years. Examples of fields and applications where they are relevant include microelectronics (e.g. reactions at solder interfaces [1], passivation layers for Cu interconnects [2], and formation of functional silicides [3]) and functional coatings (e.g. hydroxyapatite coatings for implants [4] and thermal barrier coatings for turbine blades [5]). Because of their broad applicability, significant efforts have also been made in the scientific community to characterize, understand, and attempt to predict the products of these reactions. A variety of theories have been advanced as to what factors are most important in selecting the first phase to form and the subsequent phase sequence in interfacial reactions, but the foundations of these theories have proven difficult to test experimentally.

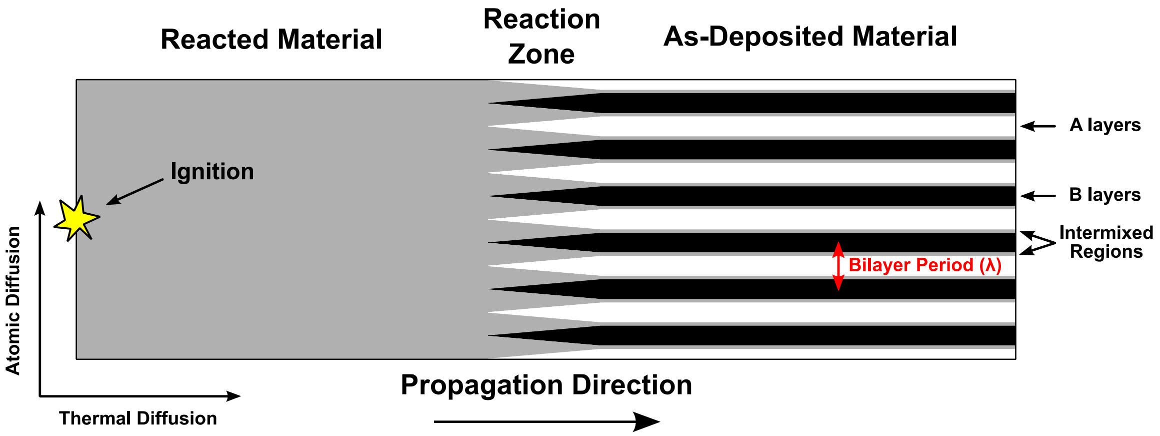

Figure 1.1 Schematic diagram of a self-propagating reaction in a reactive multilayer foil. A and B are two different elemental metals. The bilayer period λ is defined as the sum of the thicknesses of one of each type of layer, and is typically between 10 nm and 200 nm.

Another area in which interfacial reactions are important is the field of "reactive materials". Reactive materials are a subset of the larger field of "energetic materials", encompassing almost everything that is not an organic explosive. Two common examples are intermetallic formation reactions (the topic of this thesis) and thermite reactions. In an intermetallic formation reaction, two metals with a large, negative heat of mixing are combined to form a binary compound with an accompanying heat release,

$$A + B \rightarrow AB + \text{heat} \tag{1.1}$$

Here A and B are elemental metals, one of which is often (although not necessarily) aluminum. This reaction is commonly leveraged in a configuration known as a “reactive multilayer”, depicted schematically in Fig. 1.1. Thermite reactions also involve inorganic reactants, but one of them is a metal oxide and instead of a formation reaction we have a “single-replacement” reduction-oxidation (redox) reaction, i.e.

$$A + BO \rightarrow AO + B + \text{heat} \tag{1.2}$$

Again A and B are metals, one of which starts in the elemental state and the other which starts as an oxide. If AO has a lower free energy than BO, the reaction will occur as written in Eq. (1.2) accompanied heat release. There are a large number of possible intermetallic and thermite reactions depending on the choice of reactants – Fischer and Grubelich compiled a fairly exhaustive summary of them [6].

Often, reactive material performance is discussed on a relatively macroscopic scale that abstracts the actual materials processes that are occurring. However, all reactive materials fundamentally rely on interfacial reactions because they involve distinct reactants that must be physically brought together before the reaction can occur (this is in contrast to organic explosives, which derive their power from the fact that “fuel” and “oxidizer” are incorporated into the same molecule). Whether the interfaces are relatively clean as in vacuum-deposited multilayers (Fig. 1.1), or complex as in a ball-milled thermite mixture, the reaction (or at least its initial stages) is necessarily interfacial in character. Any model that hopes to describe the full complexity of reactive material performance (particularly the early stages such as ignition) will ultimately need to take this into account.

This thesis is devoted to the exploration of the interfacial reaction in one specific intermetallic system, Al/Ni. As will be described in more detail below, the Al/Ni formation reaction is one of the most well-characterized reactive materials systems available. Nevertheless, the development of new experimental techniques has allowed us to explore a previously uncharacterized parameter space in this reaction. This has led to new insights into the role that interfacial reactions play in the performance of these materials.

In the remainder of this introduction I will lay out the background for this work in several parts. I start by presenting some theoretical considerations that are useful in understanding interfacial reaction behavior. Moving to reactive materials, I will give a brief history of self-propagating reactions (at least as they occur in thin films and multilayers) and then provide an overview of the Al/Ni reaction and previous experimental studies. Finally, from the results of previous experiments I will explain the motivation for investigations that make up the remainder of this dissertation.

1.2 Theoretical Concepts Pertaining to Interfacial Reactions

A wide range of experimental phenomena have been observed in investigations of interfacial reactions, as evidenced by the number of different results for Al/Ni alone. While this research effort has abated in recent years, significant effort has been put into the development of new theoretical concepts that could explain phase formation at a reacting interface. Many of these models were originally developed to explain solid-state amorphization, where a metastable amorphous phase nucleates and grows instead of the more stable crystalline phases. However, the concepts are applicable to any type of interfacial reaction. Here, we summarize some of the most significant and frequently-cited concepts in interfacial reactions.[a]

1.2.1 Role of Diffusion

While it is obvious that at some point diffusion between elemental layers must occur if a new compound is to grow, Thompson was the first to observe that diffusion must occur *prior to* formation of the first phase [7]. Previously, it was thought that there should be no barrier to the formation of any amorphous or intermetallic phases at the interface as the thermodynamic driving force for this reaction would be so large [8]. However, Thompson showed that the calculation made to draw this conclusion was in error and that the free energy for formation of an intermediate phase is actually positive (i.e. no driving force) before intermixing occurs. Only after some diffusion is the formation of a new phase thermodynamically favored. Specifically, the composition of the solid solution must reach an equilibrium value given by the common tangent between the free energy curves of the solid solution and the next stable phase.

As a consequence of the dependence of driving force on composition Thompson concluded that not just nucleation rates but also diffusion rates are critical in determining the first phase to form. If A diffuses quickly in β (the B-rich solid solution) and B diffuses slowly in α (the A-rich solid solution) then B-rich phases will be favored. This

---

[a] This section benefited greatly from the excellent review by Kelton and Greer [14] in their chapter "Interfacial and Thin-Film Reactions".

theory explains the preference for Al-rich phases in the Al/Ni system, as diffusion of Ni in Al is faster than diffusion of Al in Ni.

1.2.2 Interfacial Reaction Barriers and Kinetic Instability

Prior to the work of Thompson, Gösele and Tu proposed a theory to explain why in thin film diffusion couples typically only one phase at a time is observed while in bulk diffusion couples all phases are seen simultaneously [9]. Their explanation for this depends on a competitive growth analysis wherein only phases with a positive growth rate can be observed. The growth rate of each phase is expressed in terms of an interfacial reaction component and a diffusive component so that both interface-controlled and diffusion-controlled kinetics can be included. If it is assumed that each phase forms in a contiguous layer, the growth of each phase is dependent upon diffusion fluxes through the other phases to supply the reactants for growth. Gösele and Tu showed that for most phases, the balance of growth rates is such that during initial phase formation only one phase can grow (that with the smallest interfacial reaction barrier) until a critical thickness is reached. If this thickness is reached before either reactant is consumed, a second phase will begin growing and both phases will grow *together*. On the other hand if one reactant is consumed before the critical thickness is reached, the second phase will grow and *consume* the first phase. In this case the second phase is enriched in whichever reactant remains. The first case can be regarded as the "bulk" case (what occurs in bulk diffusion couples) while the second is the "thin film" case, where typically only one product phase at a time is observed.

The relevance of the interfacial reaction rate (what Gösele and Tu termed an "interfacial reaction barrier") lies in the fact that during the initial stages of growth (i.e.

nucleation) the layer is almost certainly operating in an interface-limited regime. If this is the case, then the principal parameter determining which phase forms first should be the interfacial reaction rate – the phase with the smallest interfacial reaction barrier forms first. Unfortunately, this criterion is difficult to test or use for predictions as interfacial reaction barriers for the various phases are generally unknown.

1.2.3 Concentration Gradients

While Thompson motivated the need for interdiffusion from a thermodynamic perspective, his argument was based on phase equilibrium between the reactant and product phases and did not consider the additional impact that concentration gradient might have on the energetic landscape. Generally we expect that it should be more difficult to nucleate a phase with a narrow composition range, such as a line compound, in a concentration gradient than in a region of uniform composition. In particular, if the concentration varies significantly over a length scale similar to the critical nucleus size, any forming nucleus will have to accommodate significant deviations in composition, which will introduce an energetic penalty to the formation of the nucleus. Desré and co-workers developed this concept into a theory that predicts the effects of concentration gradient on the driving force for nucleation [10–13]. In brief, their theory predicts a driving force for nucleation in a concentration gradient that follows

$$\Delta G_{\text{gradient}}(r) = \Delta G_{\text{classical}}(r) + \alpha(\nabla C)^2 r^5 \tag{1.3}$$

where $\Delta G_{\text{classical}}(r)$ is the classical driving force for nucleation (based on the balance of interfacial and volume terms) and $\alpha(\nabla C)^2 r^5$ is the gradient term. The value of α varies with the nucleation mode and the phase forming but is generally positive, so that the gradient term as a whole acts to reduce the driving force for nucleation ($\Delta G < 0$ for a favorable transformation).

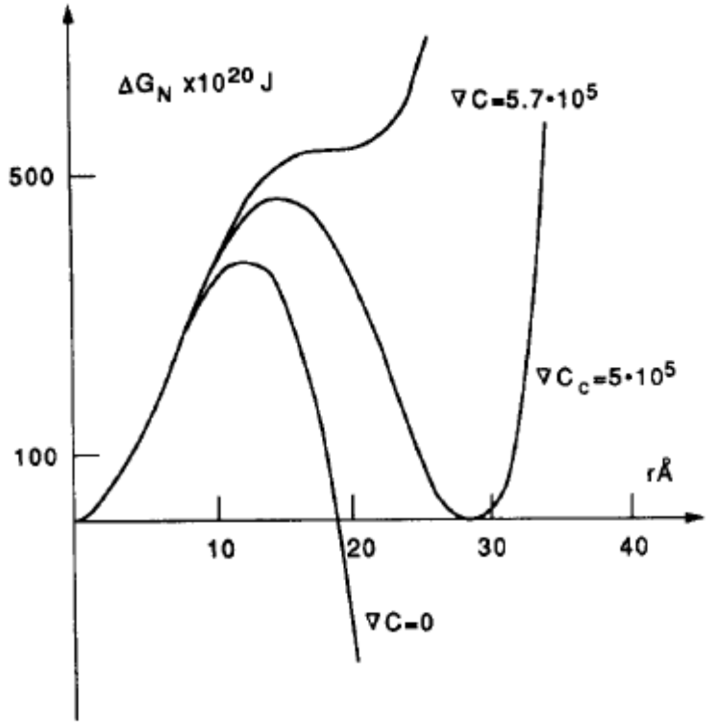

Figure 1.2 Plot illustrating the effect of concentration gradient (∇C) on the driving force for nucleation (ΔG_N) as calculated by Desré. ∇C_c is the "critical concentration gradient". Reproduced from [12].

Desré and co-workers extended their analysis to include the calculation of a so-called "critical concentration gradient" above which the formation of a particular phase is completely suppressed. The critical gradient is calculated as the one at which the driving force as a function of radius is positive everywhere (see Fig. 1.2). However, Kelton and Greer note that this condition technically implies a metastable state [14] and seemed reluctant to recognize it as a unique critical value. Regardless, the form of Eq. (1.3) ensures that at some value of ∇C there will be no free energy benefit to the formation of a nucleus of any size, and thus that nucleation can be suppressed if the concentration gradient is sufficiently large.

1.2.4 Comparisons Between Theories

While the models described above each address a slightly different question, they all point to the need for diffusion and a reduction in concentration gradient before nucleation can occur. In the model of Desré, diffusion is necessary in order to reduce the concentration gradient below the critical value for nucleation. In Thompson's understanding, diffusion was needed to reach a state of chemical equilibrium between the reactant and product phases. While the original work of Gösele and Tu does not focus on diffusion, Kelton and Greer's re-casting of their model highlights the role that diffusion fluxes play in the growth rate [14]. In particular, if diffusion in the reactant phases is included in the analysis it becomes clear that the first product cannot form while there are large diffusion fluxes in the reactants. Thus, it can be argued that even Gösele and Tu's model requires a reduction in the concentration gradient to reduce the driving force for diffusion before the first product phase becomes stable. This commonality is in agreement with the experimental data, which invariably show some chemical mixing prior to phase formation and the appearance of the principle exotherms in calorimetry scans (see, e.g. Fig. 1.8).

The models also differ in important ways. While Thompson required diffusion to occur before a phase could form, he still understood subsequent phase selection to be a question of competitive nucleation between candidate phases, assuming that a metastable phase would never be able to nucleate before a stable phase. The theory of Desré and co-workers is free of such considerations since they argue that a concentration gradient *can* cause a metastable phase to be stable when the normally stable phase is not, if the former has a broad composition range while the latter is a line compound. The work of Gösele and Tu is also devoid of any consideration of nucleation, but in this case the absence is due to the pre-Thompson assumption that the barrier to nucleation in interfacial reactions is inconsequential. However, to its credit the theory of Gösele and Tu is the only one that elegantly explains why products form sequentially in thin film diffusion couples. Considering other limitations and contrasts, Desré presents no explanation of what might happen if the critical gradient for the next phase is reached before the first phase has finished growing. Thompson explained the critical thickness of the amorphous layer in Ni/Zr multilayers in terms of an incubation time for nucleation of the crystalline phase, an idea that is not broadly applicable to other thin film systems.

1.3 History of Self-Propagating Formation Reactions

The origin of the study of self-propagating formation reactions[a] in thin films and multilayers appears to lie in the phenomenon of "explosive crystallization". This refers to a rapid, spontaneous transformation from an amorphous material to a crystalline phase with an accompanying heat release. Remarkably, scientific interest in this phenomenon seems to date back as far as 1855, where it was first observed in electrodeposited Sb films [15,16]. There was renewed interest starting in the late 1970s, when a similar phenomenon was observed in a variety of materials of interest to the semiconductor industry, including (In,Ga)Sb [17], CdTe [18], and Si [19]. Around this time, Schwarz and Johnson [20] hypothesized and then showed that it was possible to design multilayered systems of two polycrystalline materials that spontaneously amorphize (so-

---

[a] I've been careful to qualify this summary as pertaining specifically to formation reactions in thin films. Thermite reactions were discovered later (1893) but experienced much earlier adoption and application. Similarly, self-propagating reactions in mixed powders were discovered as early as 1967 in the USSR [52], and similar reactions in Al/Ni were observed accidentally in ball-milled powders prior to 1990. Discovery and application of this reaction in thin film form evidently had to wait until vacuum deposition technology had advanced sufficiently.

called "solid state amorphization") upon annealing. The requirements for the constituent materials were (a) that they have a large diffusional asymmetry and (b) that they have a large, negative heat of mixing to serve as a chemical driving force. Initial studies showed the feasibility of this approach using Au/La [20] and Ni/Zr [21] multilayers. Shortly thereafter, Floro found that deposited multilayers of Rh/Si were capable of sustaining self-propagating reactions [22], in some cases reacting on the substrate before they could even be removed from the deposition chamber. Floro still classified the phenomenon as "explosive crystallization" because the silicon layers were amorphous, but subsequent research [23–25] increasingly pointed toward the silicide formation reaction itself rather than crystallization as being the primary source of heat in such reactions. Ma *et al.* confirmed this analysis [26], showing that evaporated Al/Ni multilayers were capable of undergoing a "self-propagating explosive reaction" although neither reactant was amorphous. While a wide variety of chemical systems (e.g. Ni/Zr, Ni/Si, Al/Zr, Al/Nb, Al/Pt, Al/Co, Al/Pd, Al/Ru) have since been found to exhibit similar behavior [27], Al/Ni remains the most studied.

1.4 The Al/Ni System

The intermetallic formation reaction between Al and Ni is one of the more energetic on both a per-volume and per-mass basis [6] while both materials are relatively inexpensive. This has made Al/Ni a workhorse reactive material system both in scientific investigations and commercial applications [28–40]. The products of the Al/Ni reaction are also of interest for structural applications, so investigations were for a time driven by the goal of "reaction synthesis" of structural parts by intermetallic reactions [41]. When reacted, Al and Ni can form several intermetallic compounds depending on the overall composition. These are summarized in the Al/Ni binary phase diagram shown in Fig. 1.3.

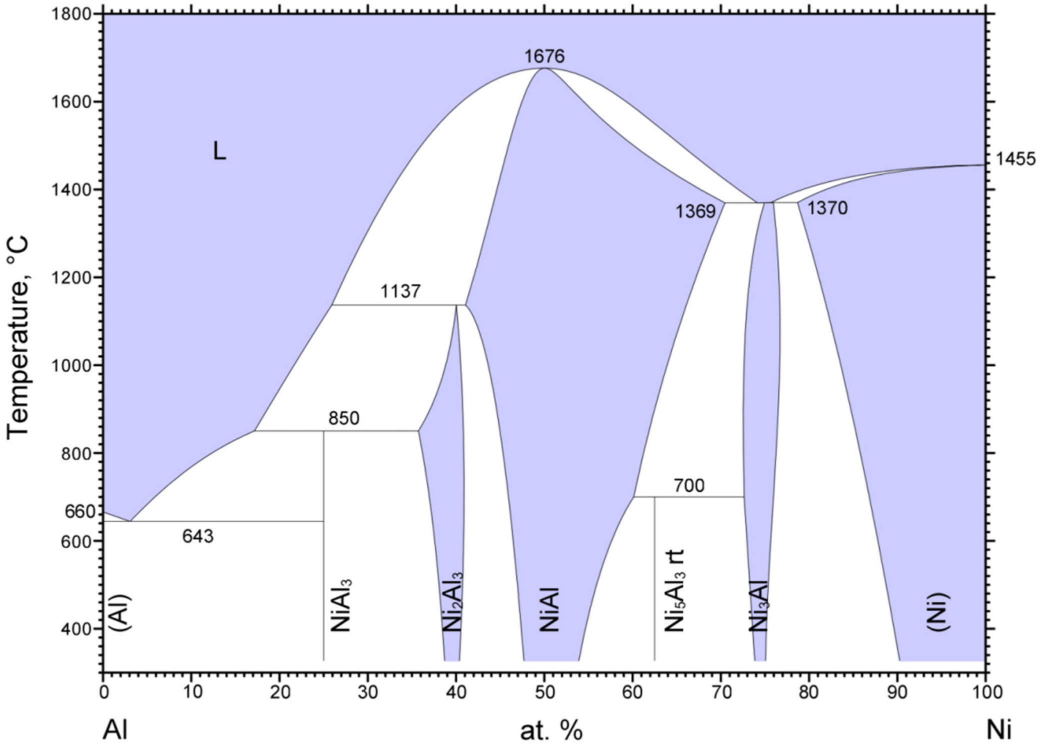

Figure 1.3 Binary phase diagram for aluminum and nickel. Diagram is #100021, © ASM International 2009, adapted from [42].

The equiatomic phase AlNi has a cP2 (CsCl) structure and can accommodate a fairly large range of compositions at high temperatures. Aside from this, the aluminum rich phases are the most relevant for reactive materials. There are two shown, Al_3Ni (a line compound) and Al_3Ni_2. The former has an oP16 (Fe_3C) crystal structure while the latter has an hP5 crystal structure. There is also a metastable Al-rich phase, Al_9Ni_2, which does not appear on the phase diagram but has been observed as a product in some reactions [32,34,35].

The aluminum rich phases are of most interest because only these phases have been observed during interfacial reactions between Al and Ni [43]. Various explanations have been put forward for this depending on whether aluminum or nickel is assumed to be the fast diffuser. The explanation offered by Colgan [43] argues that aluminum is the fast diffuser in the system, and that aluminum-rich phases form because there is a greater supply of aluminum to the reacting interface than nickel. The alternative explanation is that Ni is the fast diffuser, and aluminum-rich phases form and grow into the aluminum layer because compositions favorable to phase formation are reached in the aluminum layer first [32]. The former argument was evidently supported by marker diffusion experiments [43], while the latter is typically argued because the activation energy for diffusion of Ni in Al is much lower than the activation energy for diffusion of Al in Ni [32]. More recent experiments [44] seem to indicate fairly unequivocally that the latter explanation is correct, measuring substantially more diffusion of Ni into Al than vice versa in annealed Al/Ni multilayers.

1.5 Al/Ni Multilayers

Much of this thesis is devoted to the investigation of nanoscale Al/Ni samples designed to isolate the interfacial reaction in detail. Nevertheless, it is instructive to briefly examine the ways that the Al/Ni reaction can be utilized in bulk form. In theory, any method of combining Al and Ni that assures good contact and relatively small diffusion distances can be used to make a reactive material. Several mechanical methods have been successful, including cold-rolling of Al and Ni sheets [45] and ball milling of Al and Ni powders [46]. However, the most controlled and repeatable way to leverage the heat of the intermetallic formation reaction is using physical-vapor-deposited (PVD) reactive multilayers [27]. PVD multilayers can be understood as an idealization of the more randomized microstructures produced by mechanical processing. As such, an understanding of their performance relationships is beneficial for understanding Al/Ni reactive materials in general.

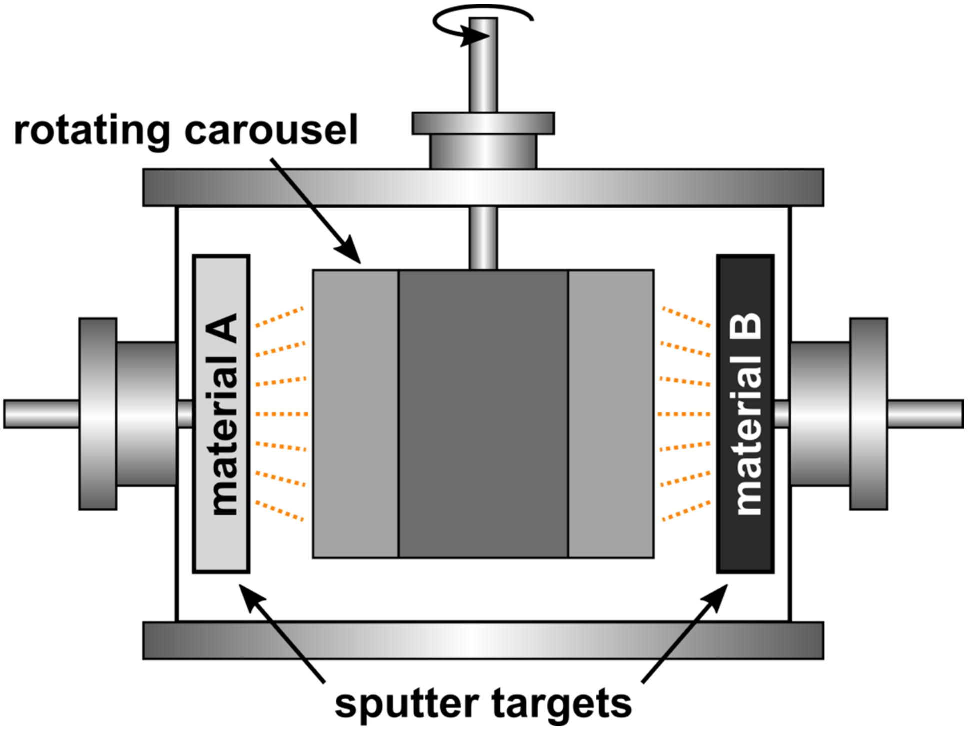

Figure 1.4 A schematic diagram of a system used to fabricate bulk reactive multilayers. "Targets" of the two multilayer components are placed on opposite sides of a vacuum chamber. A plasma is introduced, and heavy ions "sputter" atoms of the target materials off of the target and onto the substrates (center). The substrates are mounted on a rotating carousel, so over time a multilayer structure is built up as depicted in Fig. 1.1.

In a reactive multilayer, the two elemental metal reactants are combined together in a laminar composite with layer thicknesses on the order of 10s to 100s of nm as depicted in Fig. 1.1. When ignited (typically by local heating) the heat generated by the interfacial reaction in the ignition zone is sufficient to heat the adjacent material and initiate a self-propagating reaction where the mixing zone moves across the multilayer with a characteristic velocity. This velocity is strongly linked to the periodicity of the multilayers as defined by the bilayer spacing, λ (see Fig. 1.1). In our lab, reactive multilayers are fabricated by magnetron sputtering onto a rotating carousel as depicted in

Fig. 1.4. By varying the sputtering rate and carousel rotation rate, multilayers with a wide range of bilayer periods can be produced.

The reaction rate and total heat release of Al/Ni reactive multilayers can be tailored by modifying the bilayer period and stoichiometry. One of the most well-known results relates the velocity of the self-propagating reaction to the bilayer spacing as shown in Fig. 1.5(a). Generally, the velocity increases hyperbolically as the bilayer spacing is reduced because the smaller bilayer enables a more rapid reaction. However, at very small bilayer spacing this trend is reversed and the velocity begins to decrease again. As shown in Fig. 1.5(b), this decrease is related to the reduction in the available heat of formation as the bilayer period is reduced. This reduction, in turn, occurs because a small amount of intermixing is always present after deposition and represents heat that is lost in the system. The thickness of this "intermixed width" is fairly constant, so as the bilayer is reduced the intermixed width becomes an increasingly large volume fraction of the total material resulting in an apparent loss of heat.

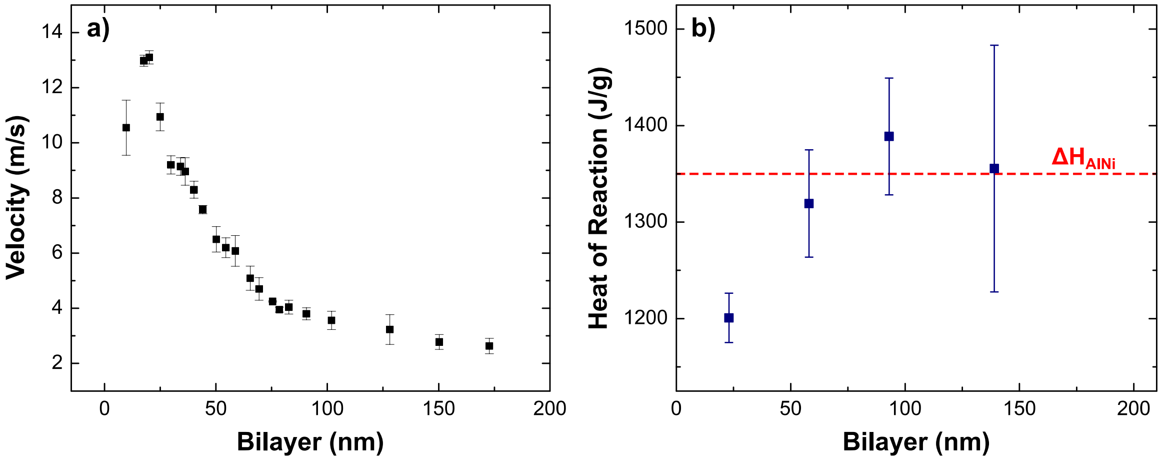

Figure 1.5 Plots of the reaction velocity (a) and heat of reaction (b) for 1Al:1Ni reactive multilayers. As shown in (a), the reaction velocity increases with decreasing bilayer except at very small bilayer periods. This agrees with the measured reduction in available heat of reaction at small bilayers (b). The plotted expected heat of formation, ΔH_{AlNi}, is 1350 J/g taken from [47]. The data in (a) are reproduced from [47]. The data in (b) are reproduced from [48],

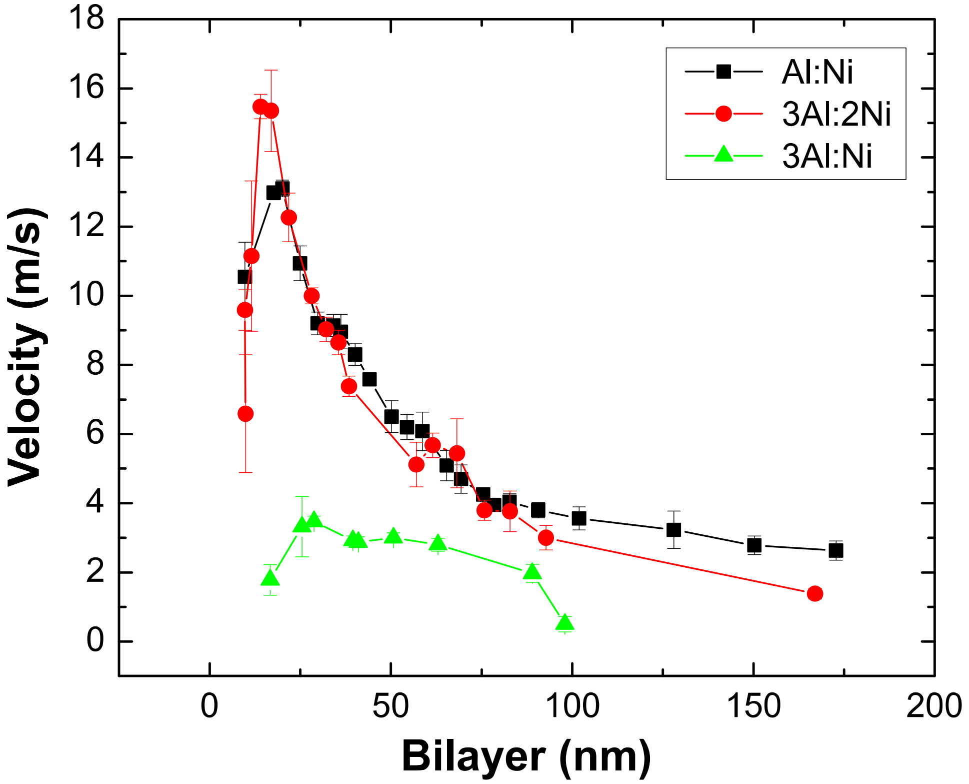

Figure 1.6 Reaction propagation velocity versus bilayer spacing for three different overall compositions in the Al/Ni system. 1Al:1Ni and 3Al:2Ni likely exhibit similar velocities because both compositions should yield reactions with a similar adiabatic temperature. The 3Al:Ni reaction, in contrast, should be significantly colder and thus exhibits generally lower velocities. Data for 1Al:1Ni are reproduced from [47]. Other data are unpublished work of Sara Barron and Rob Knepper.

The effect of stoichiometry (i.e. overall sample composition) is also easily detectable as shown in Fig. 1.6. Here, the origins for variation in velocity with stoichiometry have been less thoroughly examined, but most likely lie in the adiabatic temperature of the reactions. There is a strong link between the propagation velocity in reactive multilayers and the thermally activated process of atomic diffusion [49]. This means that the adiabatic temperature plays a significant role in determining the propagation velocity. The heats of formation for AlNi and Al_3Ni_2 are almost identical [50], so we might expect samples with these compositions to have similar adiabatic temperatures and similar propagation velocities. In contrast, the heat of formation of

Al_3Ni is only about 65 % that of AlNi [50]. Thus the reaction has a significantly lower adiabatic temperature and a correspondingly lower velocity.

1.6 Experimental Studies on Al/Ni

The Al/Ni system has been subject to a number of experimental investigations, both scientific and practical. Here, we restrict our summary to the scientific investigations that specifically considered the fundamental reaction mechanism on an interfacial scale. These can be broadly divided into two categories based on the heating rate at which the reaction was studied. Slow heating investigations characterize interfacial reactions using differential scanning calorimetry at heating rates of < 1 K/s, while rapid heating investigations examine phase formation during self-propagating reactions (heating rates $> 10^6$ K/s).

1.6.1 Slow Heating

In 1989, Ma *et al.* reported a set of results obtained for isothermal annealing of Al/Ni thin film diffusion couples [30]. In all samples, the only phase formed was Al_3Ni. The stated aim was to investigate the effect of interface contamination on the growth rate of Al_3Ni and the degree of Ni penetration into the Al. To this end, interface contamination was deliberately introduced into some samples by venting the vacuum deposition system between layers. In the contaminated samples, the researchers saw significantly slower growth of Al_3Ni and an increase in the amount of "nonuniform" growth – penetration of Ni into Al along Al grain boundaries and subsequent phase formation in these areas. This was offered as an explanation for variations in some previously published results.

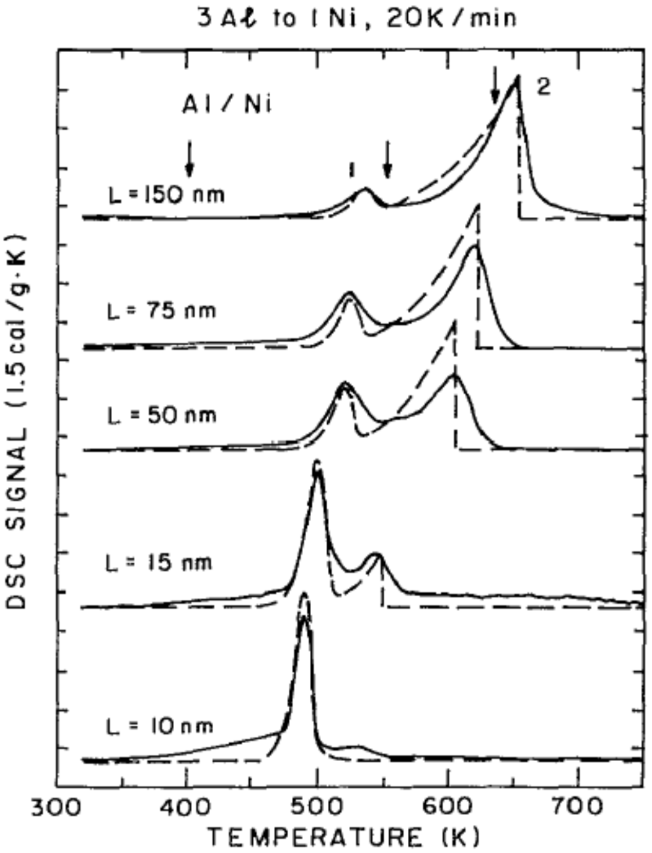

Figure 1.7 DSC scans of evaporated Al/Ni multilayers with overall composition 3Al:1Ni and varying bilayer period. The period *L* in the figure is half of the bilayer period as defined above. Reproduced from [31].

In 1991 Ma *et al.* published the first study utilizing differential scanning calorimetry (DSC) to study the Al/Ni reaction [31]. The foils examined were deposited by e-beam evaporation and had bilayer periods from 10 nm to 150 nm. The resulting DSC scans are shown in Fig. 1.7. Ma and co-workers noted three characteristics: (1) all foils exhibited two exothermic peaks, (2) the first peak was preceded by a broad exothermic signal (visible in Fig. 1.7 and highlighted in Fig. 1.8), and (3) the temperature of the first peak increased with bilayer period. Cross-sectional transmission electron microscopy of samples quenched at the positions indicated by arrows in Fig. 1.7 showed that the first and only phase to form was Al_3Ni. Following Coffey *et al.* [51], the researchers explained the two-peak behavior as due to two-stage growth where the first peak corresponds to 2D interfacial growth of a new phase and the second peak corresponds to 1D growth of this layer through the thickness of the foil. In addition, they saw that the first peak in Fig. 1.7 increased in temperature with increasing bilayer period, and concluded that nucleation of Al_3Ni depended on heterogenous nucleation sites like grain-boundary triple junctions, since the density of these sites scales inversely with the grain size and in sputtered films the grain size is approximately equal to the layer thickness. The resulting model (dashed lines in Fig. 1.7) presents a reasonable fit to the data. No new crystalline phase was identified with the exothermic reaction that precedes the first peak, and it was attributed to the formation of either a Ni-rich solid solution or an amorphous phase.

In 1994 Edelstein *et al.* published a complementary study that reported a much larger variety of behavior [32], observing a different first phase depending on both bilayer period and overall composition. In particular, they saw evidence that in some cases the first phase to form was the metastable Al_9Ni_2 phase rather than Al_3Ni as previously observed. The Al_9Ni_2 phase generally formed in foils with larger bilayer spacings (> 80 nm in their work), while at very small bilayer spacings ($\lambda \approx 10$ nm) they observed either AlNi (for a composition of 3Al:2Ni) or Al_3Ni (for a composition of 3Al:1Ni) as the first phase. Notably, the multilayers studied by Edelstein and co-workers were fabricated by ion beam deposition, an approach that is expected to induce substantially more substrate heating and pre-mixing during deposition than evaporation. Differences in film microstructure owing to different deposition methods were invoked to explain the disagreement with previous results.

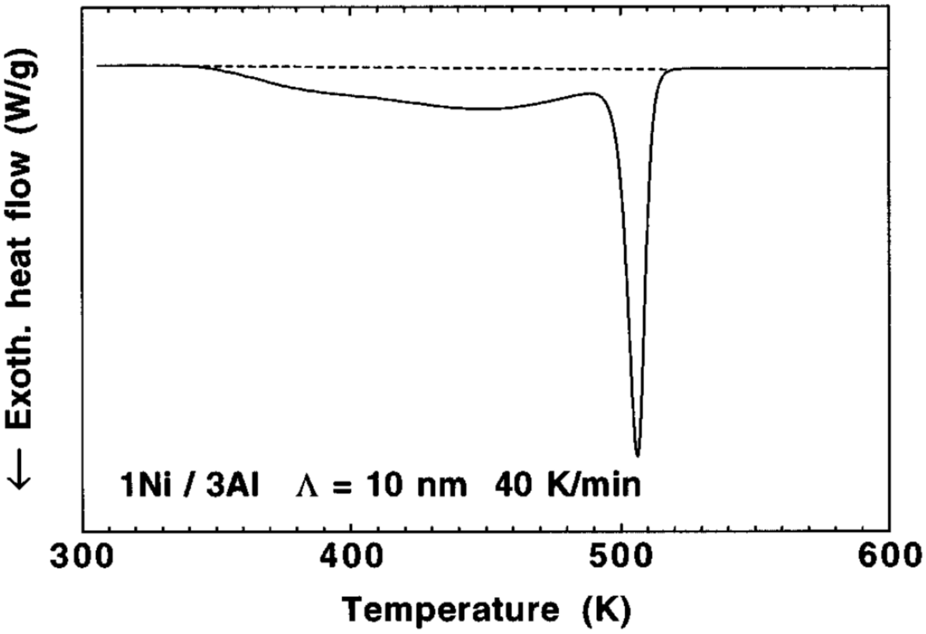

Figure 1.8 DSC scan for a 3Al:1Ni sample with a 10 nm bilayer spacing. The sharp peak corresponds to the formation of Al_3Ni. The broad reaction preceding it has variously been attributed to interdiffusion or formation of B2 AlNi. Reproduced from [33].

Michaelsen *et al.* performed one of the most thorough investigations of the initial stages of the Al/Ni reaction [33], examining both co-deposited and multilayer samples (bilayer periods of 10 nm and 20 nm) over the composition range 48 at% Al - 88 at% Al. Their samples were fabricated by magnetron sputtering, a technique expected to induce more pre-mixing than evaporation but less than ion beam deposition. Similar to Ma *et al.* they observed a gradual exothermic signal prior to the first large peak as shown in Fig. 1.8. However, they attributed this signal to the formation of crystalline AlNi rather than a solid solution or amorphous phase. All samples that were sufficiently aluminum-rich formed Al_3Ni as the first phase regardless of the exact composition. In the case of Al-poor compositions, AlNi was the only phase to form and exhibited an extended range of compositional stability.

The follow-on work of Barmak *et al.* was highly complementary and investigated in more detail the reaction kinetics of a specific film composition (3Al:1Ni) over a larger range of bilayer periods (2.5 nm to 320 nm) [34]. The results obtained were similar to those of Ma *et al.* showing the formation of Al_3Ni in two distinct exothermic peaks. However, this result was somewhat confused by the fact that Al_9Ni_2 was observed coincident with the first peak at larger bilayers. Because of this, it seems possible that the first peak observed was actually Al_9Ni_2 formation, a possibility not adequately addressed in the text. Like Michaelsen *et al.* the first phase was identified as AlNi.

A more recent study by Blobaum *et al.* focused on the formation of the Al_9Ni_2 phase first observed by Edelstein *et al.* [35] As in that work, Al_9Ni_2 was identified as the first phase to form in most foils deposited by sputter deposition (overall composition 3Al:2Ni). More specifically, Al_9Ni_2 was the first phase for foils with bilayer periods from 25 nm to 200 nm, but not for the smallest bilayer period, 12.5 nm. In this foil Al_3Ni was the first phase to form. Based on the observed dependence on bilayer period a model was developed based on critical radii for the formation of Al_3Ni and Al_9Ni_2. Using a combination of experimental and literature values for free energy and interfacial energies, this model predicted that Al_3Ni should form first for very small bilayer periods but Al_9Ni_2 should form first for moderate to large bilayer periods. This analysis matches the work of Edelstein *et al.*, but not that of Ma *et al.* or Michaelsen *et al.* where the Al_9Ni_2 phase was not observed. To-date this discrepancy has not been resolved, but is typically attributed to uncontrolled differences in film composition and microstructure resulting from differing deposition methods and systems.

To summarize the work that has been done at low heating rates, generally a sequence of phases forms that is progressively more Ni-rich until the phase matching the overall composition of the sample is reached. For example, the slow heating reaction sequence for a 1Al:1Ni sample would be

$$\mathrm{Al} + \mathrm{Ni} \rightarrow (\mathrm{Al_9Ni_2} + \mathrm{Ni}) \rightarrow \mathrm{Al_3Ni} + \mathrm{Ni} \rightarrow \mathrm{Al_3Ni_2} + \mathrm{Ni} \rightarrow \mathrm{AlNi} \qquad (1.4)$$

where the step in parentheses is only observed sometimes (typically for large bilayers and samples that have been fabricated by sputtering). The standard interpretation of this is that Ni is the fast diffuser, so the most Al-rich phase forms first and grows to encompass the original Al layer. Additional Ni diffusion into this volume drives the nucleation of the next phase, and the next, until all of the Ni is consumed. This entire reaction can occur in the solid state. Note that the phase formation is sequential – no two phases are expected to coexist except when one is transforming to the next. This is typical for thin films but in contrast to what would be expected for a bulk diffusion couple, where given sufficient time all phases will be present simultaneously.

1.6.2 Rapid Heating

Within the past decade, advances in high-speed structural characterization have enabled investigations of phase formation during the self-propagating reaction in Al/Ni. In contrast to the studies described above, the heating rates in the reaction zone during a self-propagating reaction have been estimated at 10^6 K/s to 10^7 K/s [36]. Thus it is interesting to ask how the first phase to form and overall phase sequence might change in response to such a drastic increase in heating rate. Two techniques have been applied to this problem with similar results.

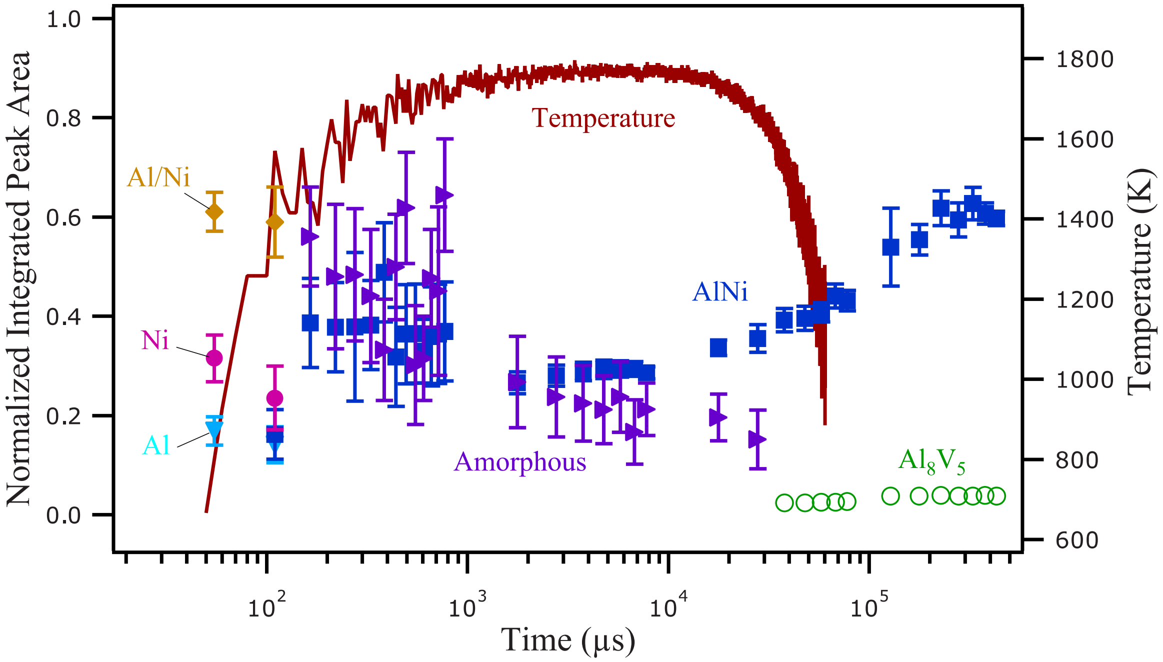

Figure 1.9 Results from *in situ* x-ray microdiffraction experiments on 1Al:1Ni foils. The amorphous phase is attributed to a significant volume fraction of Al-rich liquid. The only intermetallic phase observed is B2 AlNi, as summarized in Eq. (1.5). Reproduced from [37].

In 2008, Trenkle *et al.* reported the first results from a study of self-propagating Al/Ni foils using *in situ* x-ray microdiffraction [36]. More extensive results from these experiments were reported in 2010 [37]. The technique utilized the extremely large x-ray fluxes available from a synchrotron source in conjunction with an extremely fast x-ray detector known as a pixel array detector (integration time of 55 μs). X-ray diffraction patterns were captured from a small spot on the surface of a reacting foil. As the reaction front passed in front of the x-ray spot, information on the phases present before, during, and after the passage of the front was collected. Foils of two different Al/Ni compositions were tested, both with a bilayer period of 100 nm. For foils with an overall chemistry of 1Al:1Ni, the experimental results are depicted in Fig. 1.9 and the phase sequence was found to be:

$$\mathrm{Al} + \mathrm{Ni} \rightarrow \mathrm{Al\ (liquid)} + \mathrm{AlNi} \rightarrow \mathrm{AlNi} \qquad (1.5)$$

For foils with an overall chemistry of 3Al:2Ni, the *in situ* phase sequence was:

$$\mathrm{Al} + \mathrm{Ni} \rightarrow \mathrm{Al}\ (\mathrm{liquid}) + \mathrm{AlNi} \rightarrow \mathrm{Al_3Ni_2} \tag{1.6}$$

The aluminum liquid was identified by a characteristic amorphous halo that appeared as the reaction front passed and decayed in intensity as the foil cooled. The studies noted that it was not possible, with the available temporal resolution, to distinguish whether the AlNi phase that coexists with the liquid for some time, formed during heating or precipitated from the melt.

Fadenberger *et al.* published another study using synchrotron radiation to investigate the 1Al:1Ni reaction in 2010 [38]. This work utilized a detector with a better angular resolution than the pixel array detector used by Trenkle, but inferior temporal resolution (125 μs minimum integration time). Regardless, the results agreed with those presented in Eq. (1.5) insofar as no intermetallic phases were observed other than AlNi. Unlike Trenkle, in this work the authors specifically asserted that solid AlNi forms during the rapid heating, although the experiments evidently lack the temporal resolution to resolve this.

The other method utilized to investigate Al/Ni reactions in the self-propagating is dynamic transmission electron microscopy (DTEM) [39,40]. The dynamic transmission electron microscope is an advanced characterization tool developed at Lawrence Livermore National Laboratory (LLNL) that (at the time) was capable of capturing real space electron images or electron diffraction patterns with 30 ns temporal resolution. Electron transparent Al/Ni multilayers approximately 125 nm thick were fabricated with compositions of 3Al:2Ni, 1Al:1Ni, and 2Al:3Ni and bilayer spacings of 25 nm. After initiating a self-propagating reaction with a laser, the phases present before, during, and after the passage of the reaction front were characterized using electron diffraction. The researchers found that, regardless of the overall film chemistry, the first and only phase to form was equiatomic AlNi.

Taken holistically, the results for self-propagating reactions differ significantly from any of the previous work on similar foils using DSC. Instead of an aluminum rich phase, the first phase to form is equiatomic AlNi. The explanation given by Trenkle *et al.* for this invokes changes in the driving forces for nucleation of the intermediate phases as temperature is increased. The effect of increasing the heating rate is to push equivalent levels of reactant mixing to higher temperatures. As the decomposition temperatures of Al_3Ni and Al_3Ni_2 are approached, the driving forces for the nucleation of these phases will approach zero, with the result that they may be completely suppressed. In contrast, AlNi has the highest decomposition temperature of any Al/Ni intermetallic phase and thus maintains a strong driving force for formation for a much longer time. The result seems to be that the Al-rich intermetallics are suppressed, the aluminum layer melts, and AlNi forms either simultaneously or subsequently as a precipitate from the melt. In the case of Al-rich foils the equilibrium Al_3Ni_2 phase eventually forms, but only after the foil begins to cool and the driving force for Al_3Ni_2 is restored. The DTEM results also support the presence of a liquid phase during the reaction because real space electron images show a banded morphology immediately behind the reaction front, indicative of solid-liquid coexistence.

1.7 Summary

Comparison of Eqs. (1.4) and (1.5) indicates a fairly substantial change in behavior between the slow heating regime, where multiple intermediate phases are observed, and the rapid heating regime, where we see none. How can we account for this drastic change? Clearly it is somehow linked to the effects of heating rate. Consulting the concepts presented in Sec. 1.2, the likely explanation lies somewhere in the fact that some amount of interdiffusion must occur before a new phase can form at the interface. However, we know that this isn't the only factor that influences phase nucleation and growth. Particularly, temperature is also important. For example, for nucleation to occur the temperature must be sufficiently low that there is a driving force to nucleate the new phase but sufficiently high that the transport kinetics are fast enough to support it. The consideration of interdiffusion prior to nucleation sits *on top* of this fact, so in general we can say that the question of what phase nucleates at an interface is controlled by the *combination* of temperature and mixing at any given time.

In an experiment at a constant heating rate, these two parameters are linked. Lower heating rates provide more time at lower temperatures to effect mixing so that the reaction generally traverses a given extent of mixing at a lower temperature than when heating at a higher rate. This is summarized in Fig. 1.10(a), which shows the ranges of mixing and temperature that have been covered by the previous experiments described in Sec. 1.6. The slow heating experiments are on the left, indicating that a given extent of conversion is reached at a much lower temperature than for the rapid heating experiments on the right. Evidently, the criterion for nucleation of the intermediate phases is exceeded by the rapid heating experiments, but crucially we identify a substantial gap between these experiments (about 5 decades in heating rate) that has not been explored by any techniques to-date. This suggests that experiments in this range should be able to shed valuable light on the factors that control whether or not an intermediate phase forms.

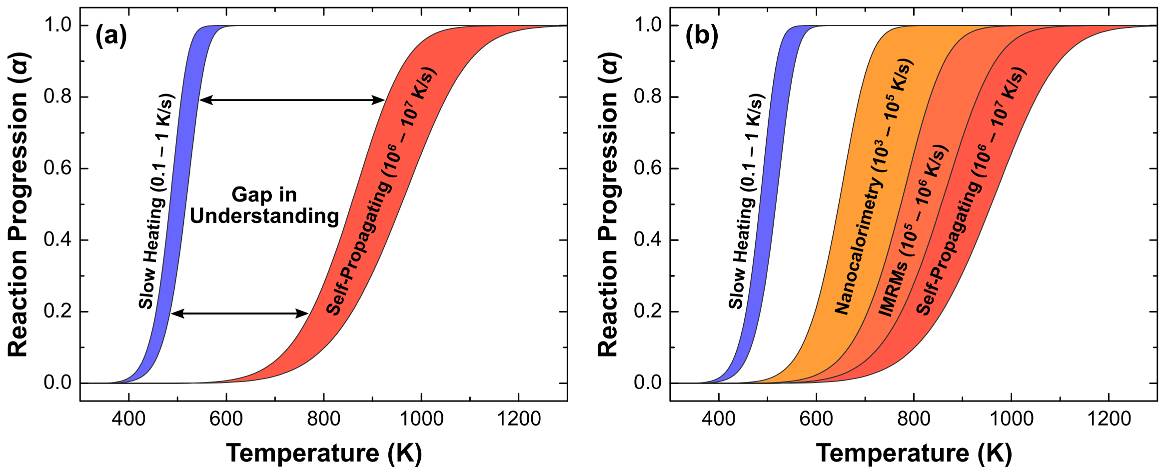

Figure 1.10 Schematic diagram of the experimental parameter space explored in this dissertation. The α versus temperature curves indicate different combinations of mixing and temperature that are explored depending on the heating rate. In (a), a plot of the heating rate range that has been covered by experiments to-date (see Sec. 1.6) shows a large gap in the space that has been explored. In (b), the positioning of the techniques developed in this work (nanocalorimetry and inert-mediated reactive multilayers [IMRMs]) within this space. The $\alpha - T$ curves were simulated assuming an A0.5 kinetic model with $E = 139$ kJ/mol and $A = 3.6 \times 10^{12}$ s^{-1} (see Chapter 5).

In this dissertation, I present experimental results from two techniques that have been developed to address this need. Their position within the schematic parameter space discussed above is shown in Fig. 1.10(b). The first, nanocalorimetry, is an already established technique that we selected specifically for its ability to measure heat output over an exceptionally large range of heating rates, nominally 10^3 – 10^5 K/s. To understand phase formation at these very high heating rates, we developed a new *in situ* nanocalorimetry system that exploits the nanoscale nature of nanocalorimeter samples to enable time-resolved electron diffraction for phase identification. The other technique is actually a new class of reactive material that we have dubbed “inert-mediated reactive multilayers”. These materials take the standard reactive multilayer concept (Fig. 1.1) and incorporate inert material to suppress the heating rate and maximum temperature. This approach constitutes taking the self-propagating reaction and attempting to "slow it down", where nanocalorimetry is taking the slow-heating reaction and trying to "speed it up".

The chapters that follow are arranged roughly chronologically. This jumbles the subjects slightly but places the work from which we were able to derive the most scientific insight toward the end. The early chapters are reserved for a description of the *in situ* nanocalorimetry technique that we developed (Chapter 2) and a report of some of the initial results that we derived using it (Chapter 3). I then transition into a discussion of inert-mediated reactive multilayers (Chapter 4). Finally, in Chapter 5 I present the results of a detailed kinetic study of the Al/Ni interfacial reaction and Al_3Ni formation using nanocalorimetry, which has yielded probably the best evidence to-date of the role of concentration gradient and extent of mixing in determining when the product phase nucleates. Chapter 6 presents some concluding remarks and ideas for how this work could be expanded upon in the future.[a]

References for Chapter 1

[1] G. Zeng, S. Xue, L. Zhang, L. Gao, W. Dai, J. Luo, A review on the interfacial intermetallic compounds between Sn–Ag–Cu based solders and substrates, J. Mater. Sci. Mater. Electron. 21 (2010) 421–440.

[2] R. Rosenberg, D.C. Edelstein, C.-K. Hu, K.P. Rodbell, Copper Metallization for High Performance Silicon Technology, Annu. Rev. Mater. Sci. 30 (2000) 229–262.

[3] F.M. D'Heurle, Nucleation of a new phase from the interaction of two adjacent phases: Some

---

[a] The core chapters described correspond to bodies of work that are (or will become) peer-reviewed journal articles. In all cases, but most notably in Chapter 4, this work necessarily involved explorations and developments that failed to "make the cut" for inclusion into the main body of work. Since it is unlikely that these results will ever see the light of day in a more public format, I have included some of them here for posterity. These topics, where they appear, can be distinguished as Appendices at the end of the chapter to which they most pertain.

silicides, J. Mater. Res. 3 (1988) 167–195.

[4] M. Wei, A.J. Ruys, M.V. Swain, B.K. Milthorpe, C.C. Sorrell, Hydroxyapatite-coated metals: interfacial reactions during sintering., J. Mater. Sci. Mater. Med. 16 (2005) 101–6.

[5] M.J. Pomeroy, Coatings for gas turbine materials and long term stability issues, Mater. Des. 26 (2005) 223–231.

[6] S.H. Fischer, M.C. Grubelich, A survey of combustible metals, thermites, and intermetallics for pyrotechnic applications, in: 32nd Jt. Propuls. Conf. Exhib., American Institute of Aeronautics and Astronautics, Reston, Virigina, 1996.

[7] C.V. Thompson, On the role of diffusion in phase selection during reactions at interfaces, J. Mater. Res. 7 (1991) 367–373.

[8] R.J. Highmore, Nucleation issues in solid state amorphization, Philos. Mag. Part B. 62 (1990) 455–467.

[9] U. Gösele, K.N. Tu, Growth kinetics of planar binary diffusion couples: Thin-film case'' versus bulk cases'', J. Appl. Phys. 53 (1982) 3252–3260.

[10] P.J. Desré, A. Yavari, Suppression of crystal nucleation in amorphous layers with sharp concentration gradients, Phys. Rev. Lett. 64 (1990) 1533–1536.

[11] F. Hodaj, P.J. Desré, Effect of a sharp gradient of concentration on nucleation of intermetallics at interfaces between polycrystalline layers, Acta Mater. 44 (1996) 4485–4490.

[12] P.J. Desré, Effect of sharp concentration gradients on the stability of a two-component amorphous layer obtained by solid state reaction, Acta Metall. Mater. 39 (1991) 2309–2315.

[13] F. Hodaj, A.M. Gusak, P.J. Desré, Effect of sharp concentration gradients on the nucleation of intermetallics in disordered solids: influence of the embryo shape, Philos. Mag. A. 77 (1998) 1471–1479.

[14] K.F. Kelton, A.L. Greer, Nucleation in Condensed Matter: Applications in Materials and Biology, Elsevier, 2010.

[15] G. Gore, On a Peculiar Phenomenon in the Electro-Deposition of Antimony, Philos. Mag. 9 (1855) 73–74.

[16] G. Gore, On the Properties of Electro-Deposited Antimony, Philos. Trans. R. Soc. London. 148 (1858) 185–197.

[17] C.E. Wickersham, G. Bajor, J.E. Greene, Impulse stimulated "explosive" crystallization of sputter deposited amorphous (In,Ga)Sb films, Solid State Commun. 27 (1978) 17–20.

[18] S.V. Krishnaswamy, R. Messier, P. Swab, L.L. Tongson, K. Vedam, Explosive crystallization of rf-sputtered amorphous CdTe films, J. Electron. Mater. 10 (1981) 433–443.

[19] G. Auvert, Explosive crystallization of a-Si films in both the solid and liquid phases, Appl. Phys. Lett. 39 (1981) 724.

[20] R.B. Schwarz, W.L. Johnson, Formation of an Amorphous Alloy by Solid-State Reaction of the Pure Polycrystalline Metals, Phys. Rev. Lett. 51 (1983) 415–418.

[21] B.M. Clemens, W.L. Johnson, R.B. Schwarz, Amorphous zirconium-nickel films formed by solid state reactions, J. Non. Cryst. Solids. 61-62 (1984) 817–822.

[22] J.A. Floro, Propagation of explosive crystallization in thin Rh–Si multilayer films, J. Vac. Sci. Technol. A Vacuum, Surfaces, Film. 4 (1986) 631.

[23] L.A. Clevenger, C.V. Thompson, K.N. Tu, Explosive silicidation in nickel/amorphous-silicon multilayer thin films, J. Appl. Phys. 67 (1990) 2894.

[24] L.A. Clevenger, C.V. Thompson, R.C. Cammarata, K.N. Tu, Reaction kinetics of nickel/silicon multilayer films, Appl. Phys. Lett. 52 (1988) 795.

[25] C.E. Wickersham, Explosive crystallization in zirconium/silicon multilayers, J. Vac. Sci. Technol. A Vacuum, Surfaces, Film. 6 (1988) 1699.

[26] E. Ma, C.V. Thompson, L.A. Clevenger, K.N. Tu, Self-propagating explosive reactions in Al/Ni multilayer thin films, Appl. Phys. Lett. 57 (1990) 1262.

[27] D.P. Adams, Reactive multilayers fabricated by vapor deposition: A critical review, Thin Solid Films. 576 (2015) 98–128.

[28] J. Wang, E. Besnoin, O.M. Knio, T.P. Weihs, Investigating the effect of applied pressure on reactive multilayer foil joining, Acta Mater. 52 (2004) 5265–5274.

[29] J. Wang, E. Besnoin, A. Duckham, S.J. Spey, M.E. Reiss, O.M. Knio, et al., Room-temperature soldering with nanostructured foils, Appl. Phys. Lett. 83 (2003) 3987.

[30] E. Ma, M.-A. Nicolet, M. Nathan, NiAl3 formation in Al/Ni thin-film bilayers with and without contamination, J. Appl. Phys. 65 (1989) 2703.

[31] E. Ma, C.V. Thompson, L.A. Clevenger, Nucleation and growth during reactions in multilayer Al/Ni films: The early stage of Al3Ni formation, J. Appl. Phys. 69 (1991) 2211.

[32] A.S. Edelstein, R.K. Everett, G.Y. Richardson, S.B. Qadri, E.I. Altman, J.C. Foley, et al., Intermetallic phase formation during annealing of Al/Ni multilayers, J. Appl. Phys. 76 (1994) 7850.

[33] C. Michaelsen, G. Lucadamo, K. Barmak, The early stages of solid-state reactions in Ni/Al multilayer films, J. Appl. Phys. 80 (1996) 6689.

[34] K. Barmak, C. Michaelsen, G. Lucadamo, Reactive phase formation in sputter-deposited Ni/Al multilayer thin films, J. Mater. Res. 12 (1997) 133–146.

[35] K.J. Blobaum, D. Van Heerden, A.J. Gavens, T.P. Weihs, Al/Ni formation reactions: characterization of the metastable Al9Ni2 phase and analysis of its formation, Acta Mater. 51 (2003) 3871–3884.

[36] J.C. Trenkle, L.J. Koerner, M.W. Tate, S.M. Gruner, T.P. Weihs, T.C. Hufnagel, Phase transformations during rapid heating of Al/Ni multilayer foils, Appl. Phys. Lett. 93 (2008) 081903.

[37] J.C. Trenkle, L.J. Koerner, M.W. Tate, N. Walker, S.M. Gruner, T.P. Weihs, et al., Time-resolved x-ray microdiffraction studies of phase transformations during rapidly propagating reactions in Al/Ni and Zr/Ni multilayer foils, J. Appl. Phys. 107 (2010) 113511.

[38] K. Fadenberger, I.E. Gunduz, C. Tsotsos, M. Kokonou, S. Gravani, S. Brandstetter, et al., In situ observation of rapid reactions in nanoscale Ni–Al multilayer foils using synchrotron radiation, Appl. Phys. Lett. 97 (2010) 144101.

[39] J.S. Kim, T. Lagrange, B.W. Reed, M.L. Taheri, M.R. Armstrong, W.E. King, et al., Imaging of transient structures using nanosecond in situ TEM., Science (80-.). 321 (2008) 1472–1475.

[40] J.S. Kim, T. LaGrange, B.W. Reed, R. Knepper, T.P. Weihs, N.D. Browning, et al., Direct characterization of phase transformations and morphologies in moving reaction zones in Al/Ni nanolaminates using dynamic transmission electron microscopy, Acta Mater. 59 (2011) 3571–3580.

[41] K. Morsi, Review: reaction synthesis processing of Ni–Al intermetallic materials, Mater. Sci. Eng. A. 299 (2001) 1–15.

[42] I. Ansara, N. Dupin, H.L. Lukas, B. Sundman, Thermodynamic assessment of the Al/Ni system, J. Alloys Compd. 247 (1997) 20–30.

[43] E.G. Colgan, A review of thin-film aluminide formation, Mater. Sci. Reports. 5 (1990) 1–44.

[44] U. Rothhaar, H. Oechsner, M. Scheib, R. Müller, Compositional and structural characterization of temperature-induced solid-state reactions in Al/Ni multilayers, Phys. Rev. B. 61 (2000) 974–979.

[45] A.K. Stover, N.M. Krywopusk, G.M. Fritz, S.C. Barron, J.D. Gibbins, T.P. Weihs, An analysis of

the microstructure and properties of cold-rolled Ni:Al laminate foils, J. Mater. Sci. 48 (2013) 5917–5929.

[46] F. Cardellini, G. Mazzone, M.V. Antisari, Solid state reactions and microstructural evolution of Al-Ni powders during high-energy ball milling, Acta Mater. 44 (1996) 1511–1517.

[47] R. Knepper, M.R. Snyder, G.M. Fritz, K. Fisher, O.M. Knio, T.P. Weihs, Effect of varying bilayer spacing distribution on reaction heat and velocity in reactive Al/Ni multilayers, J. Appl. Phys. 105 (2009) 083504.

[48] P. Swaminathan, M.D. Grapes, K. Woll, S.C. Barron, D.A. LaVan, T.P. Weihs, Studying exothermic reactions in the Ni-Al system at rapid heating rates using a nanocalorimeter, J. Appl. Phys. 113 (2013) 143509.

[49] A.B. Mann, A.J. Gavens, M.E. Reiss, D. Van Heerden, G. Bao, T.P. Weihs, Modeling and characterizing the propagation velocity of exothermic reactions in multilayer foils, J. Appl. Phys. 82 (1997) 1178.

[50] F.R. de Boer, R. Boom, W.C.M. Mattens, A.R. Miedema, A.K. Niessen, Cohesion in Metals, North-Holland, 1988.

[51] K.R. Coffey, L.A. Clevenger, K. Barmak, D.A. Rudman, C.V. Thompson, Experimental evidence for nucleation during thin-film reactions, Appl. Phys. Lett. 55 (1989) 852.

[52] A.G. Merzhanov, Solid Flames: Discoveries, Concepts, and Horizons of Cognition, Combust. Sci. Technol. 98 (1994) 307–336.

2. Overview of In Situ Nanocalorimetry

2.1 Introduction[a]

Since its introduction in 1995 [1], the technique known as "nanocalorimetry" has found increasingly widespread use in materials research, particularly with the development and use of nanomaterials with microstructural scales below 100 nm. As the name suggests, nanocalorimetry enables thermal analysis on very small samples (typically less than 1 μg) and measurements of correspondingly small energy releases or absorptions (sensitivities of ≈ 1 nJ/K are typical). Examples include the melting of thin films and nanoparticles [2–5], the characterization of interfacial reactions between thin films [6,7], and the efficient assessment of combinatorial libraries [8–10].

Traditional nanocalorimeters are based on microfabricated sensors with extraordinary sensitivity achieved by fabricating the active region of the sensor on a very thin silicon nitride membrane to minimize the sensor's heat capacity. This design also typically enables the sensor to achieve increased heating rates over those available in conventional calorimetric techniques such as differential scanning calorimetry (DSC) or differential thermal analysis (DTA). For example, the sensor used in this work is capable of heating as quickly as 10^5 K/s and cooling at rates up to 10^4 K/s. There are a number of benefits to performing experiments at high rates. From an operational perspective, rapid heating minimizes the contribution of heat losses during the heating step so that the nanocalorimeter approximates an adiabatic system [2]. In addition, traditional analysis of nanocalorimetry experiments relies on deviations in the heating rate of the sensor when

---

[a] Sections 2.1 - 2.6 of this chapter are adapted from a peer-reviewed journal article: M.D. Grapes *et al.*, Combining nanocalorimetry and dynamic transmission electron microscopy for in situ characterization of materials processes under rapid heating and cooling, Rev. Sci. Instrum. 85 (2014) 084902.

reactions occur, and these are only measurable when the device is operated quickly. This is the origin of the lower bound on heating rate for nanocalorimetry, which varies based on the magnitude of the reaction in the sample but is typically around 500 K/s. Another benefit to high heating and cooling rates is the short duration of experiments compared to traditional calorimetry (e.g. 20 minutes for a differential scanning calorimetry experiment vs. < 1 s for the same experiment in the nanocalorimeter). Finally, many phase transformations exhibit some rate-dependence when driven at high speeds. The high cooling rates available in the nanocalorimeter have been used to study the glass transition in Ni-Ti-Zr [8] and Au-Cu-Si [10] bulk metallic glasses and polymer [11] samples, and to study recalescence in solidifying aluminum thin films [4]. Recent work has also investigated the heating-rate-dependence of the exothermic formation reaction between Ni and Al [7] using nanocalorimetry.

The best way to characterize dynamic processes experimentally is through *in situ* techniques which allow the state of the system to be observed in real time. High heating and cooling rates present a notable challenge in this regard as they place stringent speed requirements on the characterization tools that can be used. In particular, for traditional nanocalorimetry conventional characterization tools like x-ray diffraction and transmission electron microscopy (TEM) operate on time scales that are impractically slow for *in situ* investigation. There are two solutions to this dilemma: (1) reduce the heating and cooling rates or (2) couple the nanocalorimeter with a technique capable of characterization on much shorter timescales.

The first approach is viable as long as changing the heating rate does not impact the scientific relevance of the investigation. For example, in 2005 Zhang *et al.* showed that *in situ* nanocalorimetry was possible in a conventional TEM, albeit at too low a rate (120 K/s) to measure any properties aside from temperature [5]. The technique known as AC nanocalorimetry has been developed to extend heat capacity measurements to very low heating rates [12–14]. Recently, Vlassak and co-workers have successfully coupled this technique with x-ray synchrotron radiation [15,16] to perform *in situ* characterization at heating rates up to 300 K/s.

For studies in which high heating and cooling rates are important, we describe the design and implementation of a system that couples a nanocalorimeter with high-speed microstructural characterization using the dynamic transmission electron microscope (DTEM). The DTEM is a time-resolved TEM that was developed at Lawrence Livermore National Laboratory. It is capable of sub-μs temporal resolution [17–19] and has been used to study a variety of materials processes at their native timescales including martensitic transformations [20,21], melting and recrystallization [22–28], and exothermic reaction propagation [29,30]. While the nanocalorimetry + DTEM system is theoretically capable of characterizing reactions up to the maximum heating rate of the nanocalorimeter sensor, here we apply the system to study aluminum melting at heating rates of ≈10^4 K/s.

While the new *in situ* nanocalorimetry system combines two well-established techniques, practical implementation required the creation or modification of several critical components. This work outlines the design of these components and the time sensitive interactions between the nanocalorimeter and the DTEM. In Sec. 2.2, we describe the design and interaction of the system's various components. Secs. 2.3 and 2.4 present the first results obtained with the system, studying the melting of an aluminum thin film heated at ≈ 10^4 K/s. Sec. 2.5 describes future applications and improvements that can be made to the system.

2.2 Design of Critical System Components

The integrated nanocalorimeter and DTEM system relies upon a combination of new and existing instrumentation, as illustrated in Fig. 2.2. The sample is deposited on a calibrated nanocalorimeter sensor which is then clamped into a custom-built TEM holder. A 200 kS/s data acquisition system and accompanying software run the nanocalorimetry experiment and interface with the timing electronics of the DTEM to coordinate the capture of an electron image or diffraction pattern at the appropriate time during the experiment. The design of these components is described in more detail in the sub-sections below.

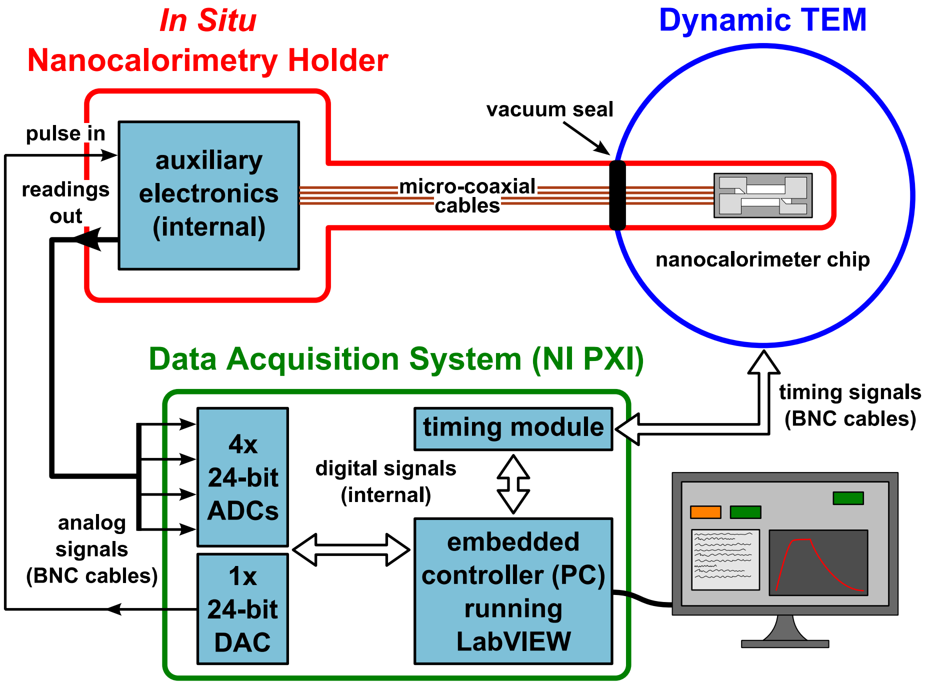

Figure 2.1 Schematic diagram of the combined nanocalorimetry + DTEM system highlighting the interactions and connections between the component systems.

2.2.1 Nanocalorimeter Sensors

The nanocalorimeters used for the *in situ* DTEM system are based on the original design by Allen and coworkers [2], updated for use in TEM studies. Each nanocalorimeter is a small silicon chip measuring roughly 0.55 cm x 1.41 cm. The chips are fabricated on 100-mm-diameter Si wafers and then cleaved apart for individual use. A schematic cross-section and micrograph of a typical sensor are shown in Fig. 2.2. The active region of each sensor consists of a 50 nm thick, 0.5 mm wide Pt heater strip supported by a 150-nm-thick silicon nitride membrane. Two voltage probes make contact with the heater strip with a spacing of 3.7 mm (prior designs have had a spacing of 5.7 mm). The section of the heater between the voltage probes defines the "measurement area" of the nanocalorimeter sensor, where temperature is actively monitored and sample changes are detected. The front side metal layer is fabricated by evaporation and liftoff, and the silicon nitride membrane is created by anisotropic Si etching from the backside using potassium hydroxide. The sample is typically deposited onto the back surface of the silicon nitride directly below the heater, as depicted in Fig. 2.2(a).

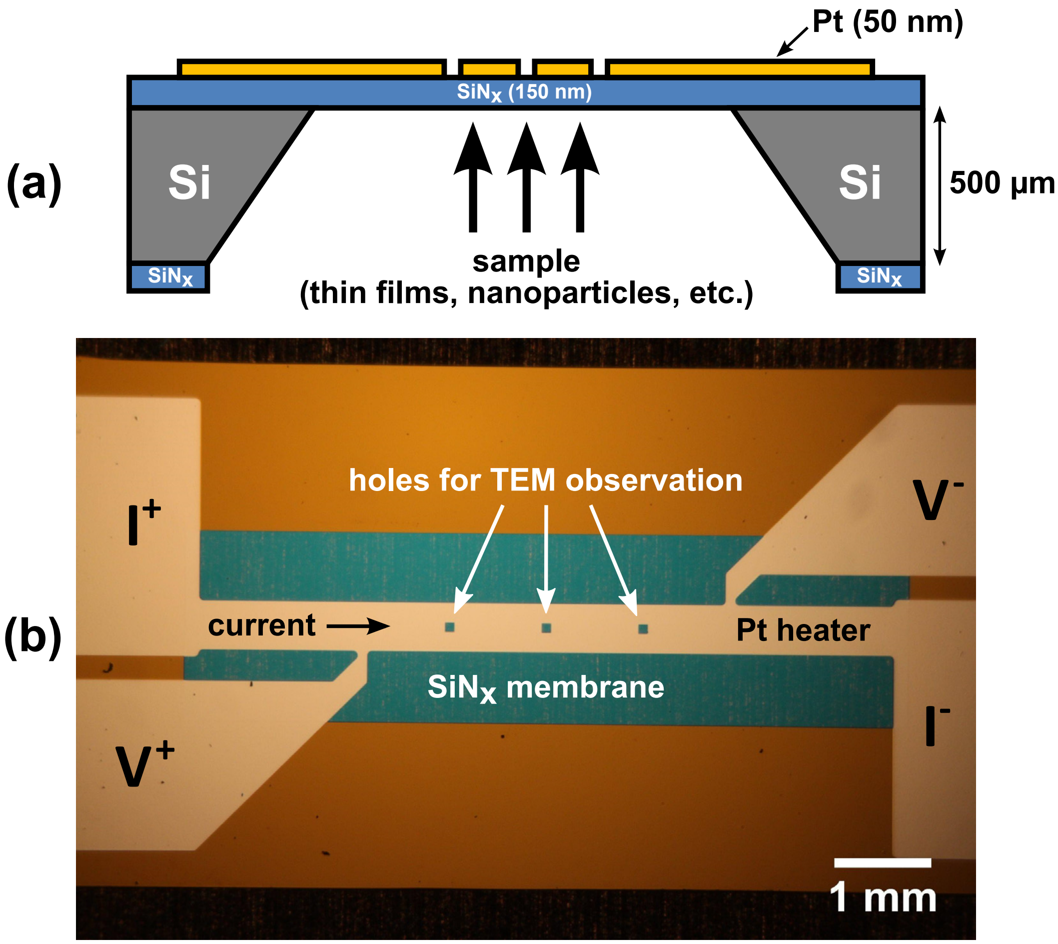

Figure 2.2 The nanocalorimeter sensor used in these experiments: (a) a side-view schematic (not to scale), and (b) a top-view micrograph showing 100 micron square holes for electron imaging.

The heater strip also serves as the temperature sensor in this nanocalorimeter. The sample is heated by flowing current through the heater strip (from I^+ to I^- in Fig. 2.2(b)). The instantaneous current flowing through the strip is determined by measuring the voltage drop across a precision current sensing resistor in series with the heater and calculating the current in the loop, I, from the voltage drop and sense resistance:

$$I = \Delta V_{\text{sense}} / R_{\text{sense}} \tag{2.1}$$

where ΔV_{sense} is the voltage drop across the current sensing resistor and R_{sense} is its resistance. Simultaneously, the voltage drop across the measurement area of the sensor is measured by the voltage probes V^+ and V^-. The resistance of the measurement area, R_{MA}, is calculated by:

$$R_{MA} = \Delta V_{MA}/R \tag{2.2}$$

where $\Delta V_{MA} = V^+ - V^-$ is the voltage drop across the measurement area and I is the current from Eq. (2.1). If the temperature vs. resistance relationship of the platinum strip is known, the temperature in the measurement area, T_{MA}, can be calculated as

$$T_{MA} = T_{\mathrm{calib}}(R_{MA}) = C_0 + C_1 R_{MA} + C_2 R_{MA}^2 + \cdots \tag{2.3}$$

where R_{MA} is the resistance from Eq. (2.2) and T_{calib} is a 2nd – 4th order polynomial fit to resistance vs. temperature calibration data. Each sensor is individually stabilized and calibrated using an optical technique detailed previously [31]. T_{MA} (Eq. (2.3)) is one of two basic outputs in a nanocalorimetry experiment. The other is the power applied to the measurement area, P_{MA}, which is calculated as

$$P_{MA} = I \Delta V_{MA} \tag{2.4}$$

From these two basic outputs, the apparent heat capacity of the measurement area can be calculated from the power and the heating rate (time-derivative of temperature) as

$$C_{p,MA}^{\mathrm{app}} = \frac{P_{MA}}{dT_{MA}/dt} \tag{2.5}$$

This result is “apparent” because it fails to account for the role of heat losses, which reduce the effective power applied to the chip. If heat loss data is available, the heat capacity can be calculated more accurately as

$$C_{p,MA}^{\mathrm{app}} = \frac{P_{MA} + P_{\mathrm{loss}}}{dT_{MA}/dt} \tag{2.6}$$

where P_{loss} is the power of heat loss, a negative function of temperature. For non-zero heat losses, the apparent heat capacity (Eq. (2.5)) is always larger than the true heat capacity (Eq. (2.6)), and the difference scales with temperature in proportion with the heat loss term.

In preparation for these experiments, the nanocalorimeter sensor was modified to improve the temperature uniformity of the measurement area and create electron transparent regions for TEM observation. Temperature uniformity was enhanced by reducing the spacing between the voltage probes to limit the effect of longitudinal temperature gradients (in the current design this spacing is 3.7 mm, while previous sensors used 5.7 mm). To provide regions of electron transparency, three 100 μm x 100 μm square holes were added in the center of the platinum strip (visible in Fig. 2.2b). Platinum scatters electrons quite strongly, so even though the Pt film is only 50 nm thick it would be very difficult to study the specimen through it. In contrast, the silicon nitride is amorphous and relatively electron-transparent so it was left intact to ensure adequate support for the sample.

Temperature uniformity across the measurement area is a common metric by which heater geometries are assessed. While a tighter temperature distribution does not necessarily improve the accuracy of the mean temperature of the sensor, it does enable it to measure sharper endothermic and exothermic peaks. In order to compare the performance of the new design to the conventional nanocalorimeter [2,4] in this regard and to assess the capabilities of future designs, we performed finite element analysis of the temperature distribution within the measurement area for each. The simulations conducted included contributions from Joule heating, radiative and conductive heat losses, and thermal diffusion to obtain the steady-state temperature distribution for a given constant current density. Four designs were tested as enumerated in Table 2.1.

The nanocalorimeter used in earlier work corresponds to Design A while the sensors used in the present investigation employed Design C.

Table 2.1 Specifications for the four heater geometries investigated by finite element modeling. The size of the measurement area is characterized by the length between the voltage probes. The heater width is equal for all designs (0.5 mm), and the total size of the silicon nitride window is constant. Designs C and D employ square holes; the hole size listed is the length of one side of the square.

Design Name	Length of Measurement Area	Hole Size
Design A	5.7 mm	none
Design B	3.7 mm	none
Design C	3.7 mm	100 μm
Design D	3.7 mm	20 μm

The silicon nitride membrane was simulated as having negligible electrical conductivity and negligible black-body emissivity (consistent with observation via thermal imaging and previous work [32]). The Pt conductor was simulated with a temperature-dependent electrical conductivity based on measurements from similar platinum samples. Table 2.2 shows the temperature-dependent emissivity used for platinum along with the other material properties used in the model. In the simulations the outer-edges of the silicon nitride membrane were held at room temperature (295.15 K) to simulate the high thermal conductivity of the Si substrate, and the ends of the Pt conductor were assumed to have a uniform current density. The applied current in the model was increased until the measurement area of the Pt reached an average temperature of 939 K. Simulations were performed taking advantage of the 4-fold geometric symmetry. Quadratic wedge-shaped elements were used throughout. Numerical convergence was verified using mesh-density halving. A mesh seed spacing of 25 μm was used throughout the plane of the membrane and the conductor for the simulation of the original nanocalorimeter design. For the new design simulation, a biased mesh seed spacing was used that tended to 2.5 μm in and around the holes. Two layers of elements were used in the plane for each material. These results were compared to a mesh-halved result using a mesh seed spacing of 5 μm to 50 μm and a single element layer for each material, resulting in approximately one-eighth the number of elements. There were no significant differences in the results between the two mesh resolutions. All physical constants were rescaled using dimensional analysis so that entered material properties were of order unity for better numerical behavior.

Table 2.2 Material properties used for finite element simulation of temperature distribution in nanocalorimeter sensors. See 2.3 for electrical conductivity of Pt.

Material	**Thermal Conductivity ($W\ m^{-1}\ K^{-1}$)**	**Heat Capacity ($J\ kg^{-1}\ K^{-1}$)**	**Density ($g\ cm^{-3}$)**	**Emissivity (dimensionless)**
Pt	71.6	133	21.45	$0.186 + 6.48\times10^{-5}\ T$
SiN_x	3.2	750	3.100	0

The simulation results were quantified by extracting temperatures from a uniform grid of points on the Pt surface. Fig. 2.3 shows contour plots and histograms that compare the temperature distribution within the measurement area for each design. The standard deviations of the distributions are 11.7 K (n = 1859 grid points) for Design A, 3.21 K (n = 1209 grid points) for Design B, 8.24 K (n = 1185 grid points) for Design C, and 3.25 K (n = 1207 grid points) for Design D. Comparing Design A to Design B reveals the improvement in temperature uniformity that can be achieved simply by reducing the length of the measurement area. The effect of adding holes (Designs C and D) is to broaden this distribution due to current concentration around the hole edges, but we see that for sufficiently small holes (Design D) the broadening is minimal. As noted above the sensors used in this work employed Design C. Future work will implement the smaller hole size in Design D to take advantage of that design's improved temperature uniformity.

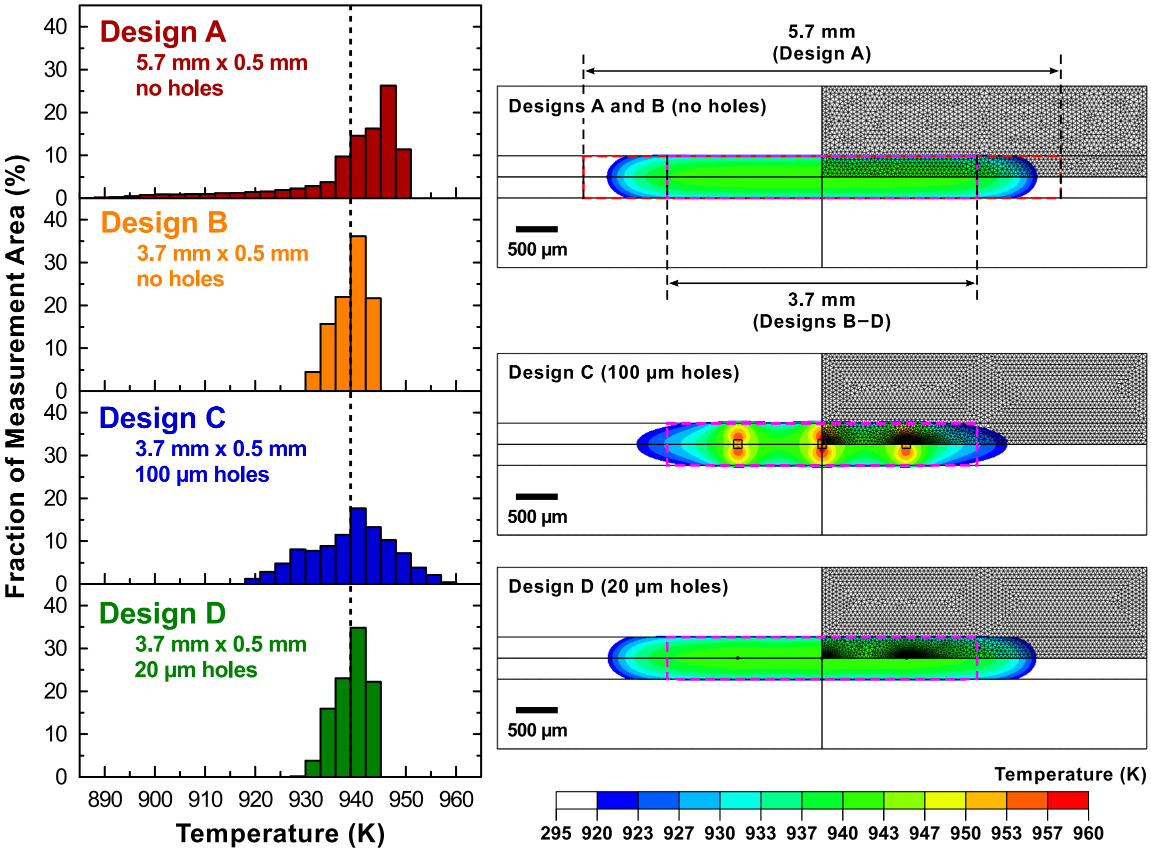

Figure 2.3 Finite element modeling results showing the steady-state temperature distribution of nanocalorimeter sensors under constant current. At left are histograms of temperature values (from a uniformly spaced grid to avoid mesh density bias) comparing the temperature distribution for the four designs. The vertical dashed line indicates the average temperature in all simulations, 939 K. At right are contour plots of the steady state temperature distribution. The dashed boxes indicate the measurement area for each design. In the upper-right quadrant of each plot the mesh geometry is shown. This is the only quadrant that was simulated, with the remaining three inferred from symmetry. The scale of the contour plots is limited to the range from 920 K to 960 K in order to highlight temperature variations around the mean.

2.2.2 Functional Form for Heating Pulses

In order to achieve approximately constant heating rates in a voltage-controlled configuration without feedback, a new equation was developed to calculate the voltage waveform required for approximately constant heating rate. The objective is a constant heating rate, β, defined as the ratio of temperature change to pulse time:

$$\beta = \Delta T / \Delta t \tag{2.7}$$

The temperature in the measurement area of the sensor is governed by the differential equation

$$C_p \dot{T} = \dot{Q}_{\text{ext}} + \dot{Q}_{\text{rxn}} - \dot{Q}_{\text{loss}} \tag{2.8}$$

where C_p is the heat capacity of the measurement area, $\dot{T}$ is the heating rate dT/dt, and the three $\dot{Q}$ terms on the right-hand-side are the externally applied power, the power from any reactions on the chip, and the heat loss power, respectively. Since $\dot{Q}_{\text{rxn}}$ cannot be known *a priori*, it is assumed to be zero. This means that the computed waveform is only designed to deliver a constant heating rate in the absence of reactions on the chip. If the heating rate is constant, we can replace it with the target heating rate, β, and solve for the target applied power:

$$\dot{Q}_{\text{ext}} = C_p \beta + \dot{Q}_{\text{loss}} \tag{2.9}$$

If the heat capacity and heat losses of the chip can be estimated accurately as a function of temperature, this expression gives the applied power required to maintain a constant heating rate. In order to convert it to a voltage waveform we must consider the specifics of the nanocalorimeter heating circuit. The origin of the applied power is resistive heating in the nanocalorimeter strip. This can be computed as

$$\dot{Q}_{\text{ext}} = V_{\text{strip}}(t)^2 / R_{\text{strip}}(t) \tag{2.10}$$

Solving for the voltage and including the result from above, we find

$$V_{\text{strip}}(t) = \sqrt{R_{\text{strip}}(t)\left(C_p \beta + \dot{Q}_{\text{loss}}\right)} \tag{2.11}$$

In order to approximate the resistance of the strip, recall that each chip is calibrated prior to use. This calibration can be used to fit a polynomial that describes the resistance of the strip at any given temperature, $R_{\text{calib}}(T)$. We also know that, if a constant heating rate is achieved, the temperature will follow $T(t) = T_0 + \beta t$, where T_0 is the ambient temperature. This gives us

$$V_{\text{strip}} = \sqrt{J \times R_{\text{calib}}(T_0 + \beta t)\left[C_p\beta + \dot{Q}_{\text{loss}}(T_0 + \beta t)\right]} \tag{2.12}$$

where the one additional modification is the factor J, equal to the ratio of the heater strip's total length to the distance between the voltage probes used to measure the resistance. J is always greater than one and has the effect of increasing the overall voltage applied. Finally, to convert the voltage drop across the strip to the total voltage which must be applied to the circuit we must consider the other loads in the circuit. In the case of the nanocalorimeter system described here, these loads are purely resistive and include the sense resistor (10 Ω – 100 Ω), a ground isolation resistor (≈ 5 Ω), and the resistance of the wires that connect the auxiliary electronics to the chip at the holder tip (≈ 30 Ω). The sum of these resistances is on the same order as the chip resistance (typically 30 Ω – 70 Ω) so the voltage across the strip will be much lower than intended unless we account for the voltage divider effect. Lumping all of the resistances other than the heater strip into an approximate value R_{other}, the voltage across the strip will be related to the total applied voltage $V(t)$ by

$$V_{\text{strip}}(t) = V(t)\frac{R_{\text{strip}}}{R_{\text{strip}} + R_{\text{other}}} \tag{2.13}$$

Solving for the total voltage and substituting from above, we finally arrive at the functional form used for constant heating rate waveforms in these experiments,

$$V(t) = \left(1 + \frac{R_{\mathrm{other}}}{J \times R_{\mathrm{calib}}^{RT}}\right) \sqrt{J \times R_{\mathrm{calib}}(T_0 + \beta t)\left[C_p \beta + \dot{Q}_{\mathrm{loss}}(T_0 + \beta t)\right]} \tag{2.14}$$

Note that here, although the voltage divider term could have been made time-dependent using the same assumptions as above, we found that a constant term based on the room-temperature resistance of the chip gave the best results. As shown in Fig. 3.2(a) and 3.2(b), this waveform accomplishes an approximately constant heating rate. As introduced in Eq. (2.9), the effect of heat loss compensation is to increase the power required to heat the chip at a given rate as the temperature increases. For radiative losses, which scale with T^4, this increase can be quite dramatic as illustrated in Fig. 3.2(c).

2.2.3 In Situ Nanocalorimetry TEM Holder

We designed and fabricated a custom TEM holder for the nanocalorimeter sensor. The basic design requirements for the holder were (a) mechanical compatibility with the goniometer and column of the JEOL 2000FX platform upon which the DTEM is based, (b) a mechanism for stable and repeatable positioning of the nanocalorimeter sensor in the electron beam, (c) the ability to make reliable electrical connections to the pads on the sensor, and (d) vacuum-tight electrical connections to transfer these electrical signals to the external environment. To ensure compatibility with the JEOL 2000FX goniometer the limiting dimensions of the custom holder were adapted from a JEOL EM-BST double-tilting holder. The sensor and the associated electrical connections at the tip had to fit within a 5.1 mm thickness. The bulk of the holder was machined from brass to ensure that it would be non-magnetic – unintended magnetic fields in the TEM can deflect electrons and degrade image quality. Fig. 2.4(a) shows the completed holder.

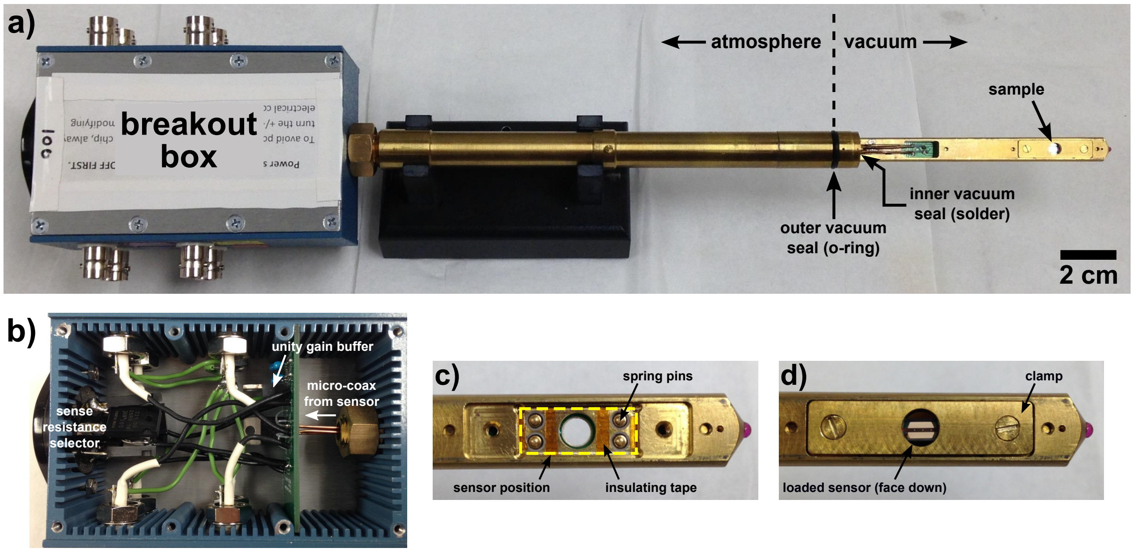

Figure 2.4 Photographs of the custom-built TEM holder developed for *in situ* nanocalorimetry: (a) overview of the entire holder, (b) close-up of breakout box with cover removed to show auxiliary electronics, (c) close-up of sensor mounting region with sensor and clamp removed, showing spring-pin electrical connections for face-down mounting, and (d) close-up of mounting region with sensor (visible through hole) and clamp installed.

Perhaps the most critical component of the holder is the mechanism for mounting the nanocalorimeter sensor and making electrical connections to it. The mount must be stable (not prone to vibration or drift) and reliable (able to maintain its function over many load/unload cycles). In addition, for TEM it is important that the sample be positioned as close as possible to the rotation axis of the holder. This minimizes the z-adjustment required to place the sample at the eucentric height of the TEM, a critical condition for quantitative analysis of diffraction patterns and generally consistent imaging. With all of these requirements in mind we designed the holder to use a face-down mounting approach. The sensor cavity was designed as shown in Fig. 2.4(c) and consists of a 5.84 mm x 14.48 mm rectangular pocket with 1.52 mm circular cutouts in the corners to allow for extra material left over after chip cleavage. It was machined to a depth of 64 μm below the mid-plane of the holder. The remaining thickness is taken up by 64-μm-thick polyimide tape, also visible in Fig. 2.4(c), which is applied to insulate the metal contact pads on the surface of the sensor from incidental contact to the brass holder. Since the sample sits on the silicon nitride membrane (see Fig. 2.2(a)) it is essentially flush with the top surface of the sensor. Thus, the sample is positioned almost exactly at the rotation axis of the holder when the sensor is clamped down. The face-down approach ensures that the sample is in the same position for every measurement regardless of variations in the thickness of the silicon wafer. A clamping block secured by two screws allows the user to apply just enough force to ensure that the sensor is flush with the bottom surface and stable – excessive clamping force can break the silicon chip. A photograph of a loaded, clamped sensor is shown in Fig. 2.4(d).

Since the nanocalorimeter sensor is often replaced, a rapid and reliable way to make electrical connections to it was needed. The space available in the JEOL EM-BST form factor allowed the use of commercially available ultra-low-profile spring pins (#0965, Mill-Max Mfg. Corp.). These pins measure 2.54 mm at rest and 1.93 mm when fully compressed. Four spring pins were soldered to a 0.5 mm thick printed circuit board that was mounted to the underside of the holder tip. The board positions the spring pins directly below the sensor cavity. The spring pins protrude up beyond the bottom of the sensor cavity as shown in Fig. 2.4(c) if no sensor is loaded. When a sensor is clamped in place, the four contact pads (see Fig. 2.2(b)) make contact with the four spring pins and compress them to form a reliable electrical connection.

Electrical connections from the printed circuit board at the holder tip to the auxiliary electronics in the breakout box were made using UT-34 micro-coaxial cable (Micro-Coax, Inc.). These cables have a solid copper outer shield, a PTFE insulating sheath, and a solid copper inner conductor approximately 200 μm in diameter. The solid outer shield greatly simplifies the creation of a vacuum feedthrough for the cables as an air-tight seal can be formed simply by passing them through a small hole and filling the gaps with solder. This also grounds the outer shield to provide noise shielding for the signals carried on the inner conductor. The micro-coaxial cables and vacuum seal are visible at the holder tip in Fig. 2.4(a), and in the breakout box in Fig. 2.4(b).

The final component of the *in situ* nanocalorimetry holder is the auxiliary electronics system housed in the breakout box, shown in Fig. 2.4(b). Besides providing an intermediate interface between the micro-coaxial cables coming from the nanocalorimeter and the BNC cables that transfer signals to the data acquisition system, the auxiliary electronics also house two components which are essential for nanocalorimeter operation: (1) a unity-gain buffer amplifier to supply the necessary current, and (2) selectable current sensing resistors to measure the current flowing through the heater. The buffer amplifier (Burr-Brown BUF634) is necessary because the digital-to-analog converter used to generate the heating waveform is not designed to drive a low impedance circuit like the nanocalorimeter heater, which typically has a resistance ranging from 50 Ω to 140 Ω. The extra power for the amplifier is provided by a +/- 15 VDC power supply (Agilent 3630A). For current measurement, the *in situ* nanocalorimeter holder features a selection of sense resistors (10 Ω, 25 Ω, 50 Ω, 75 Ω, and 100 Ω) for increased measurement flexibility. Higher sense resistance values result in less noise in the current measurement but limit the total power that can be delivered to the sensor.

2.2.4 Data Acquisition System

Because the resolution of the nanocalorimeter output signals (Eqs. (2.3)-(2.5)) is directly related to the resolution with which the raw voltage signals can be measured, the most critical design parameter for the data acquisition system was to include high-precision analog-to-digital converters. Other priorities were ruggedness, portability, and the ability to easily operate the system from software. The data acquisition system uses a 4-slot PXI Express chassis (NI PXIe-1071) with an embedded controller (NI PXIe-8133) and two high-precision dynamic signal analysis cards (NI PXI-4461 and NI PXI-4462). This system is capable of simultaneously generating 2 analog outputs and measuring 6 analog inputs with 24-bit resolution at speeds up to 204.8 kHz, sufficient for nanocalorimeter operation. The PXI platform also provides dedicated timing signals and triggering lines so that signal generation and measurement tasks can be precisely synchronized with each other and external equipment like the DTEM.

The embedded controller runs Windows 7 and LabVIEW and is used to program and perform tasks using the system. A custom LabVIEW virtual instrument (VI) was developed for the nanocalorimetry system to streamline both the execution of experiments and the management of data. The general design strategy was to create a single entry-point for all nanocalorimeter operations and introduce specific functionality into an array of subVIs that are called by the primary VI. A high-level diagram of this organization scheme is shown in Fig. 2.5. Data management is achieved in this approach by assigning each nanocalorimeter sensor a unique identifier and corresponding storage space and asking the user to specify the "working" sensor in the primary VI before running any subVIs. If the working sensor is specified, the locations of all files specific to that sensor are automatically passed to the subVIs when they are called allowing these VIs to read or modify that sensor's properties as necessary and store all new files to the same location.

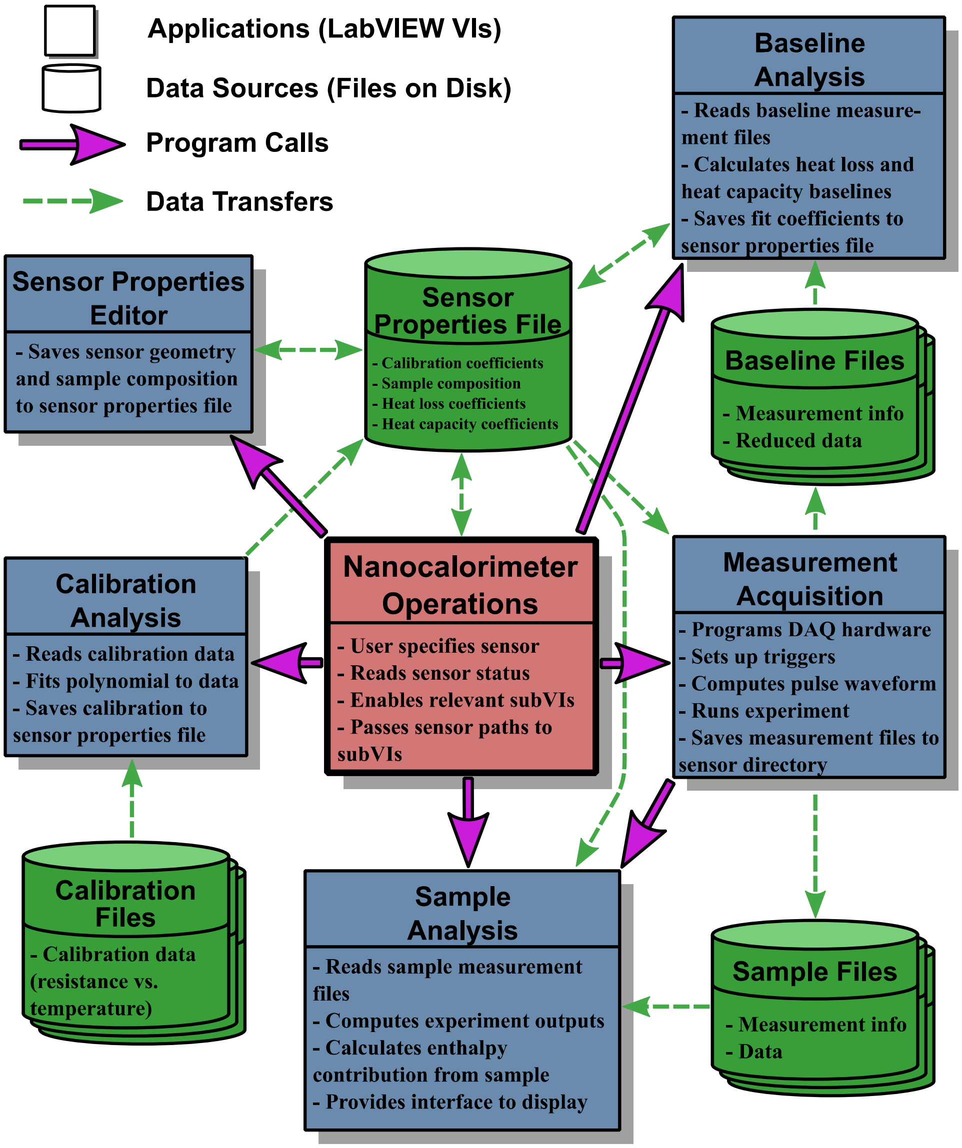

Figure 2.5 High-level diagram depicting the flow of program calls and data within the nanocalorimetry operations software. All calls are initiated from the entry-point program "Nanocalorimeter Operations" and include all information about the working chip needed for the sub-programs to perform their tasks.

The centralized organization scheme also helps to maintain an efficient workflow because the primary VI only allows the user to launch a subVI when it detects that all previous steps in the workflow have been completed. For example, since measurement data cannot be processed unless a sensor has been calibrated, the option to run experiments on that sensor will be disabled until calibration files have been loaded and analyzed. A number of such dependencies exist and can be inferred from the dashed green data transfer arrows in Fig. 2.5. The primary VI includes a display which indicates the state of all dependencies for the working sensor. This allows the user to ascertain the work to be done as soon as the sensor is loaded.

2.2.5 Dynamic Transmission Electron Microscope

The dynamic TEM is a modified JEOL 2000FX transmission electron microscope in which the conventional electron gun has been replaced with a laser-driven Ta photocathode described previously [17]. Electrons are generated by bombarding the photocathode with a high-energy ultraviolet laser. This laser is shaped using an arbitrary-waveform generator and complex optics to obtain a pulse which, when applied to the photocathode, delivers an approximately constant electron flux with beam currents as high as several mA for times ranging from 30 ns to 500 ns. Images are acquired on a single-electron-sensitive CCD detector. During the experiment the detector is set to acquire data for a long time relative to the electron pulse (typically 1 second), so the temporal resolution is wholly determined by the duration of the electron pulse. Depending on the phenomenon to be observed the DTEM can be configured to capture time-resolved electron images or electron diffraction patterns. It is also outfitted with a high-energy “pump” laser which can be used to heat a region of the sample locally and initiate the reaction to be studied. This laser is deactivated when operating in nanocalorimetry + DTEM mode since the nanocalorimeter is used to heat the sample and initiate any reactions.

For *in situ* nanocalorimetry experiments, the most useful results are obtained when the DTEM is operated in electron diffraction mode with a relatively large selected area aperture (≈ 0.55 μm^2) and the maximum pulse time (500 ns). Since the sample is uniformly heated there are few meaningful contrast changes visible when operated in plan-view imaging mode; this approach differs from previous work [33] where a reaction front would traverse the sample and could provide an image showing the unreacted material, the reaction front, and the post-reaction material. On the other hand, operating in diffraction mode allows us to analyze the crystal structure of the sample in the selected area as it evolves or transforms. The maximum pulse length is chosen because it maximizes the number of electrons in the pulse and improves the signal-to-noise ratio of the image/diffraction pattern. While nanocalorimetry experiments are very fast compared to conventional thermal analysis experiments, a few milliseconds is still orders of magnitude longer than the 500 ns maximum pulse time of the DTEM electron source. Since the electron pulse is essentially instantaneous on the timescale of the reaction in the sample, there is no precision lost by using the maximum pulse time.

2.2.6 Timing and Synchronization

Synchronization between the DTEM and nanocalorimetry system is critical if intermediate states during the nanocalorimetry experiment are to be successfully captured. When running, the DTEM photocathode drive laser is continuously pulsed at a 10 Hz repeat rate. Any one of these pulses is capable of generating an electron pulse for imaging. In order to choose just one of the pulses to illuminate the sample, a fast shutter is introduced between the cathode laser optics and the DTEM photocathode. During an experiment, the detector acquires for 1 s and the fast shutter opens briefly during this time to allow a single laser pulse onto the photocathode. In standard DTEM experiments, where the reaction is initiated by a sample pump laser and lasts much less than 100 ms, it is sufficient to control the delay time between the sample pump laser and the cathode laser to select the sample state that is imaged. In contrast, typical nanocalorimeter experiments last 10's to 100's of ms, and an additional complication occurs when the particular state to be imaged is not within the first 100 ms of the experiment. In this case a more elaborate synchronization scheme must be used as described below.

There are two requirements for an image to be acquired at a particular time during a nanocalorimetry experiment. The first is that a cathode laser pulse is available at that time. Since pulses of the cathode laser occur on a fixed "schedule" every 100 ms, the only way to achieve this is to make the cathode laser clock the reference signal for the entire system and trigger the nanocalorimetry experiment to start at an appropriate time relative to this reference. For example, to acquire an image at t = 170 ms relative to the start of the nanocalorimetry experiment the heating pulse would be initiated 70 ms prior to the next "tick" of the cathode laser clock (30 ms *after* the previous pulse). Electron pulses will then be available for imaging at 70 ms, 170 ms, 270 ms, etc. The second requirement is that no pulses other than the one at the time of interest are allowed into the column – otherwise the detector (acquiring for a full second) would overlay multiple images of the sample in different states.

The timing scheme developed to meet these requirements is shown schematically in Fig. 2.6. The 10 Hz reference signal indicating pulses of the cathode laser system is shown at the top in Fig. 2.6(a). Requirement #1 is met by using a delay generator to produce a delayed version of the cathode laser clock (Fig. 2.6(b)) that triggers the start of heating and signal acquisition on the nanocalorimetry system. The delay is adjusted whenever a different time during the experiment is to be studied. Requirement #2 is satisfied by giving the nanocalorimetry system control of the cathode laser fast shutter. A separate output channel is configured to send a "shutter open" signal a short time before the event of interest and a "shutter close" signal a short time later as shown in Fig. 2.6(c). This ensures the exclusion of all imaging pulses other than the one at the time of interest.

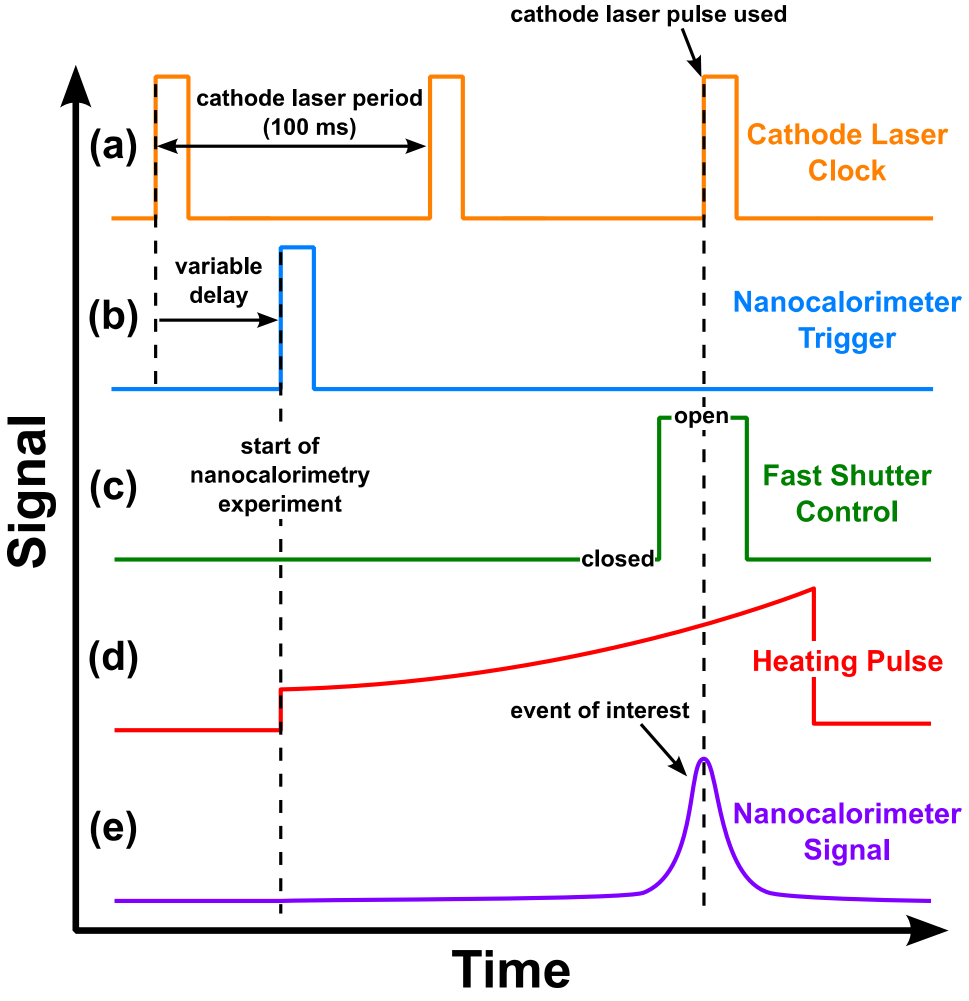

Figure 2.6 Schematic diagram illustrating the synchronization scheme between the nanocalorimetry system and the dynamic TEM. The cathode laser clock serves as the reference signal by which the nanocalorimetry experiment is initiated after some delay. The extra cathode laser pulses are ignored because the fast shutter is only opened briefly at the time of interest.

2.3 In Situ Investigation of Aluminum Melting

Melting experiments are a common metric by which nanocalorimetry systems are assessed. They are convenient because there is a single thermodynamic event (melting), it occurs at a well-defined temperature (the melting temperature), and a range of temperatures can be tested by choosing different elements or compounds with appropriate melting points. Melting experiments can also be conducted using a wide range of heating rates without altering the heat of fusion. This makes them a good standard for assessing nanocalorimeter performance at high heating rates, as opposed to more complex reactions which might proceed differently depending on heating rate. Since the *in situ* nanocalorimetry system is intended to measure reactions up to ≈ 1000 K, we chose to conduct the preliminary tests on aluminum thin films. While aluminum's melting temperature of 933 K is relatively high compared to the melting points of more standard calibration metals (In, Bi, and Sn), it is within the range of the optical calibration technique used [31], is less likely to result in chamber contamination, and allows us to assess performance over a larger fraction of the nanocalorimeter's temperature range.

A sample was deposited by electron-beam evaporation (Denton Infinity 22) consisting of 50 nm of Al (target purity 99.999 %) onto the backside of nanocalorimeter sensors fabricated using Design C (see Table 2.1). A shadow mask was used to limit the deposition to the active area of the device. To prevent oxidation or reaction with the silicon nitride, the Al thin film was capped on both sides by 10 nm of Al_2O_3, also deposited by e-beam evaporation without breaking vacuum. The film thickness during deposition was controlled by a quartz crystal thickness monitor. Each iteration of the heating experiment consisted of two steps: (1) pseudo-constant-rate heating at 10^4 K/s (target) for 80 ms (see Sec. 2.2.2 for a description of this heating program), and (2) free cooling for 200 ms (a small current must be applied to be able to record the resistance and hence temperature, but it is much less than the currents used for heating). Since the experiments were conducted in vacuum the dominant mechanism for heat loss throughout the experiment was thermal radiation (conduction also contributes but its effects are comparably minor within the well-insulated measurement area). As described above, heating was initiated at a pre-defined time prior to the next DTEM imaging pulse so that a DTEM diffraction pattern was acquired during the heating pulse. By performing multiple iterations of the heating experiment and varying the time between initiation and imaging, diffraction patterns were collected at a range of temperatures before, during, and after the melting event. To maximize resolution in the diffraction pattern the electron beam was spread and a ≈ 0.55 μm^2 selected-area aperture was used to select a region in the central TEM window on the sensor (see Fig. 2.2(b)). The same sensor and heating waveform were used for all experiments, and the same region of the sample was characterized throughout. The current sense resistance was 25 Ω for these experiments.

Typical results from the nanocalorimetry system during one heating pulse are shown in Fig. 2.7. The raw data was smoothed by a 1:64 downsampling, so the displayed data has an effective sampling rate of 3.125 kHz. Fig. 2.7(a) shows the evolution of temperature with time. The temperature increases at a roughly constant rate except for an inflection at ≈ 66 ms indicating the melting of aluminum. This event is more pronounced in Fig. 2.7(b), which shows the heating rate (time derivative of temperature) over the same time span. The melting event appears as a downward spike in the heating rate because at that time power is temporarily being used to supply the heat of fusion rather than to heat the sensor. Fig. 2.7(c) shows the applied power as a function of time as calculated by Eq. (2.4). Finally, the signals in Fig. 2.7(b) and 2.7(c) are combined as per Eq. (2.5) to calculate the apparent heat capacity, plotted versus temperature in Fig. 2.7(d). Here the melting event appears as an upward spike. Following the discussion of apparent versus true heat capacity in Sec. 2.2.1, note that the heat capacity values in Fig. 2.7d are inflated relative to the true values for aluminum because heat losses are not accounted for.

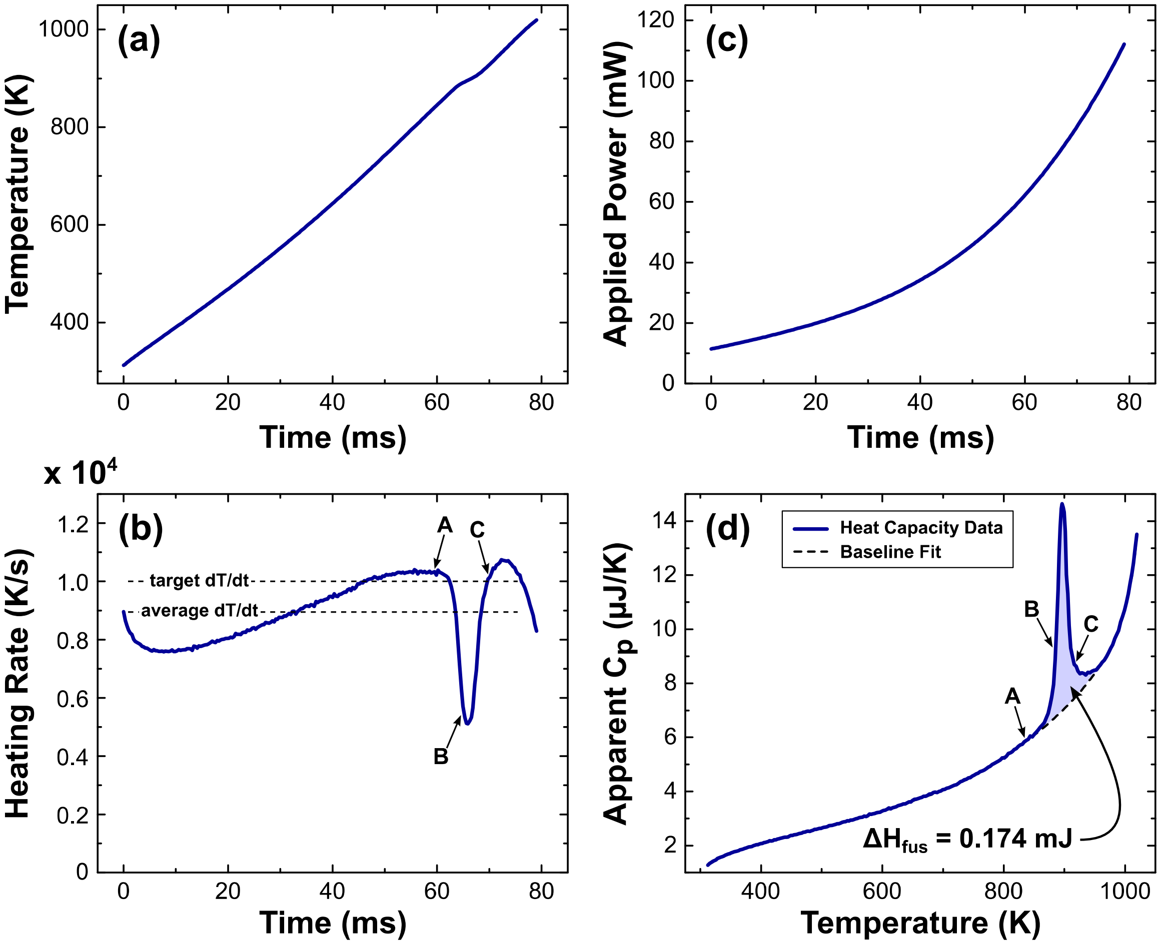

Figure 2.7 Characteristic nanocalorimetry results for the heating segment of the aluminum melting experiment: (a) temperature vs. time, (b) heating rate vs. time, (c) applied power vs. time, and (d) apparent heat capacity (C_p) vs. temperature. The labeled arrows in (b) and (d) indicate the times/temperatures at which DTEM diffraction patterns were captured during the heating scan, and the shaded area in (d) represents the experimental heat of fusion.

Fig. 2.8 shows a sequence of electron diffraction patterns from the experiments. The patterns in the right-hand column were captured during the heating segment of the experiment at the times/temperatures indicated by the arrows in Fig. 2.7(b) and 2.7(d). The patterns in the left-hand column were captured at room temperature between experiments, and are included for comparison because the grain under observation solidified in a different orientation after each experiment. The grain orientation and principal diffraction spots for each of the room temperature diffraction patterns are indicated in Fig. 2.8. The diffuse, radially symmetric intensity present in all diffraction patterns is due to scattering from the amorphous silicon nitride film.

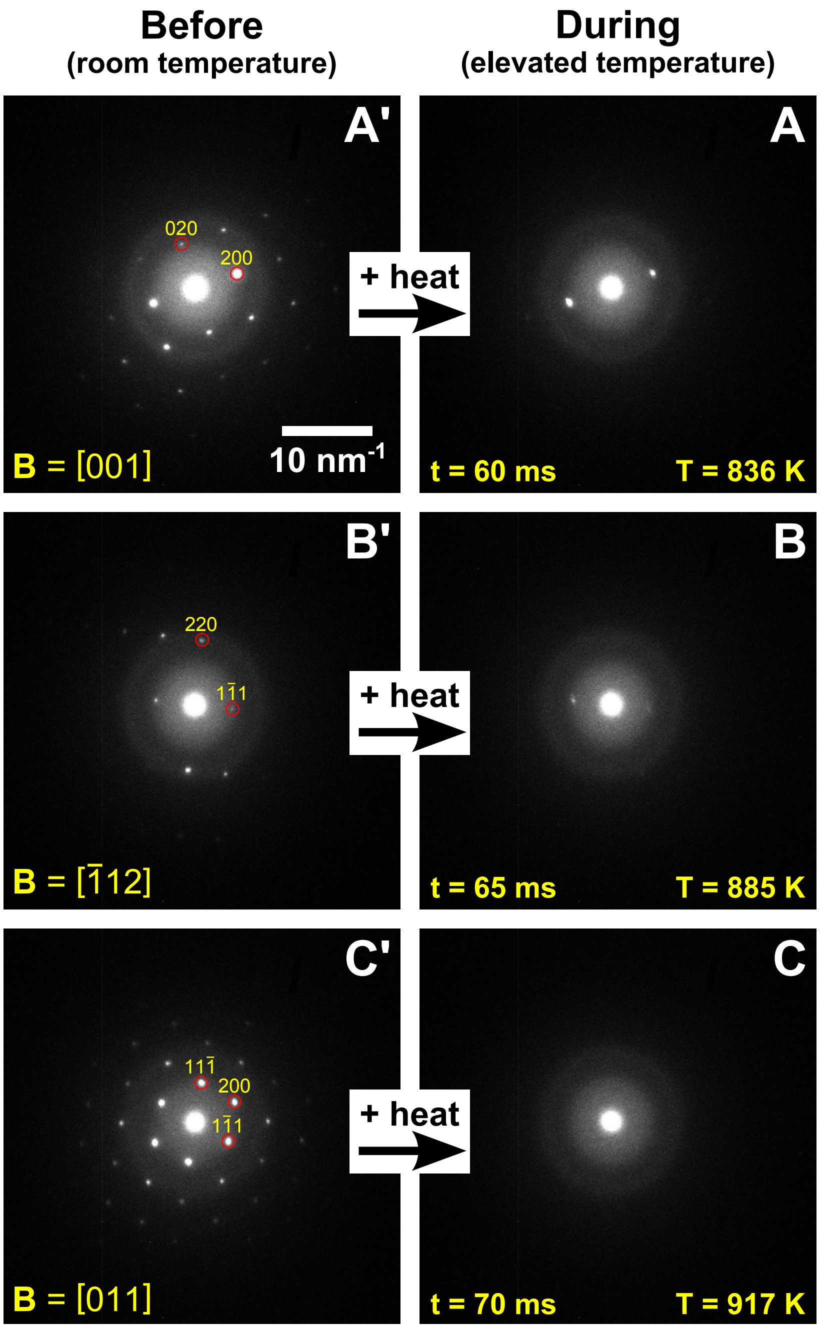

Figure 2.8 Several single-crystal diffraction patterns taken from one grain of the aluminum film during the melting experiments. The patterns on the left were taken at room temperature, while those on the right were taken at different times during the heating segment of the experiment. The time and temperature is given for each pattern on the right, and the crystal orientation and principal diffraction spots are labeled for each pattern on the left. These points are also indicated in the melting curves shown in Fig. 2.7b and 2.7d. All images are displayed with the same brightness and contrast.

2.4 Discussion

The dashed lines on Fig. 2.7(b) show the discrepancy between the target heating rate and the true heating rate. While the heating rate appears roughly constant in Fig. 2.7(a), it actually varies by up to 15 % around the average heating rate of 8945 K/s. This heating rate, in turn, is about 10 % lower than the target heating rate of 10000 K/s. This illustrates the difficulty of achieving a constant heating rate in a system without feedback control, even with the complex heating pulse developed in Eq. (2.14). Fig. 2.7(d) shows how the enthalpy of fusion is estimated from apparent heat capacity data. A baseline curve is fitted to the data everywhere except the spike associated with melting. The integral between these two curves is then the experimental heat of fusion for aluminum, 0.174 mJ. Using the nominal sample dimensions of 50 nm × 4 mm × 0.75 mm (estimated from the dimensions of the shadow mask used for patterning) and the density and molar mass of bulk aluminum (2.70 g/cm^3 and 26.98 g/mol respectively), we calculate the molar heat of fusion to be 11.6 kJ/mol which is about 8.3 % higher than the value reported for melting of bulk Al, 10.71 kJ/mol [34]. This difference is not surprising given the lack of means to directly measure the sample mass along with the other uncertainties in the DTEM nanocalorimetric experiment. The experimental melting point for Al is taken as the peak temperature in Fig. 2.7(d). This value is 896 K, 37 K below the expected value for pure aluminum, 933 K. This error is larger than typically observed for nanocalorimetry [31], suggesting that the sensor used may have been improperly aligned during calibration.

When combined with the nanocalorimetry data in Fig. 2.7, the diffraction patterns in Fig. 2.8 demonstrate the ability of the combined nanocalorimetry + DTEM system to resolve events both thermodynamically and structurally. Pattern A was captured 60 ms into the heating pulse. According to the nanocalorimeter (Fig. 2.7(d)) the pattern was captured prior to melting and DTEM confirms this, showing distinct $\bar{2}00$ and 200 diffraction spots persisting from the room temperature pattern. Note that spots from the (020) axis (visible in the initial pattern A') disappear upon heating. This is likely due to expansion and flexure of the silicon nitride support membrane causing the grain under observation to tilt into an off-axis position where only the (200) spots are excited. Pattern B was captured 65 ms into the heating pulse on the leading edge of the melting peak, and the reduced intensity and broadening of the diffraction peaks indicates that while still present, crystalline order in the sample is beginning to break down. Finally, pattern C was captured at the very end of the melting peak (t = 75 ms). In this case, the DTEM diffraction pattern shows no detectable crystalline diffraction spots indicating that the sample has melted. The only distinguishable feature in this diffraction pattern is from the amorphous silicon nitride, which unfortunately prevents us from detecting an analogous halo due to the presence of molten aluminum.

2.5 Future Work

The aluminum melting experiments presented above effectively demonstrate the ability of the *in situ* nanocalorimetry system to synchronize nanocalorimeter experiments with the DTEM and correlate microstructural and thermodynamic information about the sample. In its present state, this system is already capable of characterizing a wide range of materials phenomena. A forthcoming paper will document initial results in a study examining the effects of heating rate on the intermediate phases formed during the reaction of Ni and Al, and experiments on other reactive materials including thermites and nano-aluminum powder have also been discussed. More generally, we anticipate that the development of the *in situ* nanocalorimetry + DTEM system will impact a variety of materials fields where the interplay between thermodynamic and kinetic control is important, including nucleation and solidification, crystallization in metallic glasses, and phase change materials.

One of the greatest drawbacks to the system in its present state is that it is limited to single-shot electron imaging. While not insurmountable, this restriction means that many identical samples are required to fully characterize an irreversible reaction. Even reversible reactions, which benefit from the ability to repeatedly “pump” and “probe” the sample, take longer to characterize with the single-shot approach. A so-called “movie mode” for the DTEM has been developed where a sequence of 9 or 16 images can be captured during a single experiment. Unfortunately, due to limitations in the current laser optics this mode cannot at present be applied on the longer timescales typical of nanocalorimetry experiments. Extending this capability to the millisecond timescale would dramatically improve the throughput of future *in situ* nanocalorimetry experiments.

Other improvements are possible in the area of sensor design. One of these improvements is detailed in Sec. 2.2.1, where we found that reducing the size of the holes in the Pt heater from 100 μm squares (Design C) to 20 μm squares (Design D) resulted in significantly enhanced temperature uniformity. In addition, we anticipate that reducing the thickness of the silicon nitride support membrane or eliminating it entirely in the imaging region would noticeably improve image quality by eliminating the amorphous background. We are currently developing a process to introduce small holes in the silicon nitride membrane for this purpose.

2.6 Conclusions

By combining nanocalorimetry and dynamic TEM a new high-rate *in situ* characterization tool has been developed which provides thermal and microstructural characterizations across the full range of heating rates available with nanocalorimetry, approximately 10^3 K/s to 10^5 K/s. The system consists of the DTEM, a new TEM-compatible nanocalorimeter sensor, a custom-built *in situ* nanocalorimetry holder, and a data acquisition system with accompanying software. When a synchronization scheme is established it is possible to capture DTEM images or diffraction patterns of intermediate states in the sample at any time/temperature point in a reaction and across the range of heating rates available via nanocalorimetry. This development simplifies the microstructural analysis of reactions which is essential to virtually all nanocalorimeter experiments, and provides the first opportunity to characterize *in situ* those reactions that are dependent on high heating or cooling rates.

2.7 Appendix A: Additional Considerations for Heating Waveforms

For consistency with published results Sec. 2.2.2 is published in the same form as it appeared originally [35]. The form of the heating waveform shown in Eq. (2.14) was used for the investigation reported in this chapter as well as in the chapter on 1:1 Al:Ni samples. However, it was eventually deprecated in favor of a more accurate expression that does not require the somewhat arbitrary assumption that the voltage divider term should not be time-varying. The latter version was used to produce the data obtained on

3:1 Al:Ni samples and is derived here. The first step in doing this is to note that the placement of J in Eq. (2.12) is incorrect. Eq. (2.11) should more accurately be written

$$V_{MA}(t) = \sqrt{R_{MA}(t)\left(C_p^{MA}\beta + \dot{Q}_{\text{loss}}^{MA}\right)} \tag{2.15}$$

where all of the quantities (and the result itself) are ascribed specifically to the measurement area of the sensor. As stated above, we define the factor J as the ratio of the chip's total resistance to the resistance of the measurement area, i.e.

$$R_{\text{chip}}(t) \approx J \times R_{MA}(t) \tag{2.16}$$

However, the appropriate way to convert from $V_{MA}(t)$ to $V_{\text{chip}}(t)$ is *not* to multiply it inside the radical as was originally done in Eq. (2.12). The reason is that, as highlighted by Eq. (2.15), the heat capacity and heat losses are *also* specified only for the measurement area. They should also be scaled by J, resulting in a J^2 inside the radical or multiplication by J *outside* the radical:

$$V_{\text{chip}}(t) = J \times \sqrt{R_{MA}(t)\left(C_p^{MA}\beta + \dot{Q}_{\text{loss}}^{MA}\right)} \tag{2.17}$$

Another way to think about this is that J represents a first voltage divider correction accounting only for the sensor. The relationship between the chip voltage and the measurement area voltage is given by

$$V_{MA}(t) = \frac{R_{MA}(t)}{R_{\text{chip}}(t)} V_{\text{chip}}(t) \tag{2.18}$$

where the ratio of the resistances determines the divider ratio. Substituting Eqs. (2.15) and (2.16) into Eq. (2.18) directly yields the result in Eq. (2.17). This change increases the calculated chip voltage by about 25% over that predicted by Eq. (2.12).

After making this change, we found that a time-varying voltage divider term now yielded better results than the old constant form. To review, this term is

$$V_{\text{chip}}(t) = \frac{R_{\text{chip}}(t)}{R_{\text{chip}}(t)+R_{\text{oth}}} V_{\text{app}}(t) \tag{2.19}$$

Substituting Eq. (2.16) and solving for $V_{\text{app}}(t)$ we obtain the form of heating pulses used for the systematic study on 3:1 Al:Ni presented in this thesis,

$$V_{\text{app}}(t) = \left(1 + \frac{R_{\text{other}}}{J \times R_{MA}(t)}\right) \times J \times \sqrt{R_{MA}(T_0 + \beta t)\left[C_p^{MA}\beta + \dot{Q}_{\text{loss}}^{MA}(T_0 + \beta t)\right]}$$

This form should also be regarded as the most accurate starting point for future developments. Note that while not accounted for here, practical implementation of this waveform also involves gain and offset compensation for the buffer amplifier used in the experiments.

2.8 Appendix B: Two-Stage Background Subtraction for Nanocalorimeter Electron Diffraction

In this chapter only single-crystal diffraction patterns are shown, but all of the *in situ* nanocalorimetry data presented in the remainder of this work are for polycrystalline samples. These samples yield characteristic ring patterns as depicted in Fig. 2.9(a). The typical way these are analyzed is to find the center point of the pattern and then perform a radial integration. The intensity profile resulting from the application of this procedure to Fig. 2.9(a) is shown in Fig. 2.9(b). While the individual peaks in Fig. 2.9(a) are clearly visible in the radially integrated profile, they sit on top of a relatively large background. In general this is undesirable as it makes it difficult to detect the weaker peaks or to compare between patterns. Thus a procedure for background subtraction is needed. For nanocalorimetry samples, we have found that the presence of the silicon nitride membrane generally requires a more complex, two-stage background subtraction. This procedure is described below.

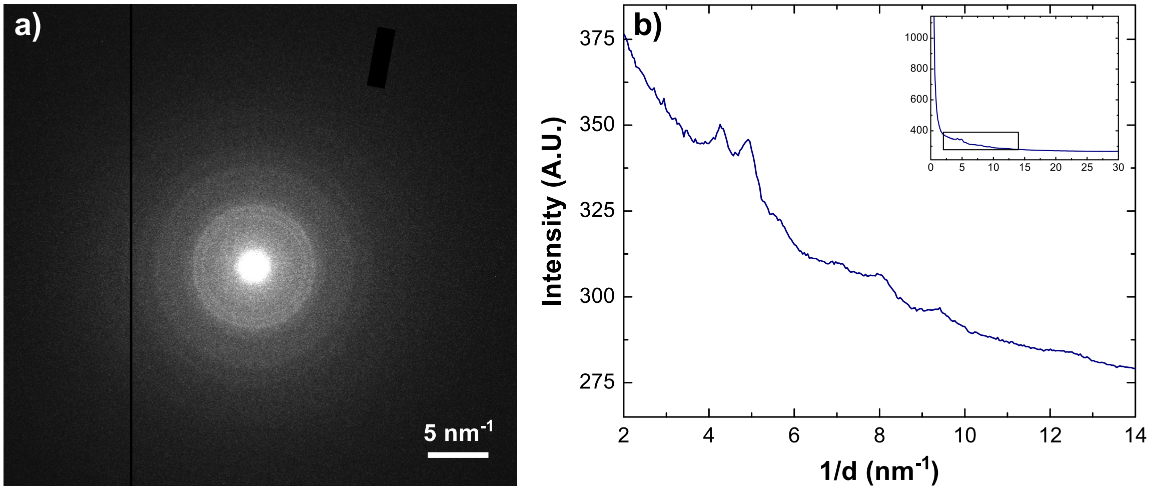

Figure 2.9 Example of a typical polycrystalline electron diffraction pattern (a) and the raw intensity profile obtained by radial integration (b). The sample is unreacted 100 nm Al/Ni imaged in DTEM pulsed mode. The image in (a) has had distortion corrections applied. The black shapes indicate bad areas of the detector that were masked before analysis. The inset in (b) shows the full intensity profile to give a better sense of the level of the signal relative to the overall background.

As evidenced by the inset in Fig. 2.9(b), the primary background is associated with the undiffracted beam and decreases rapidly with increasing 1/d. What may not be apparent is that underneath this signal is also an amorphous halo associated with the silicon nitride membrane. An example of this characteristic intensity is shown in Fig. 2.10.

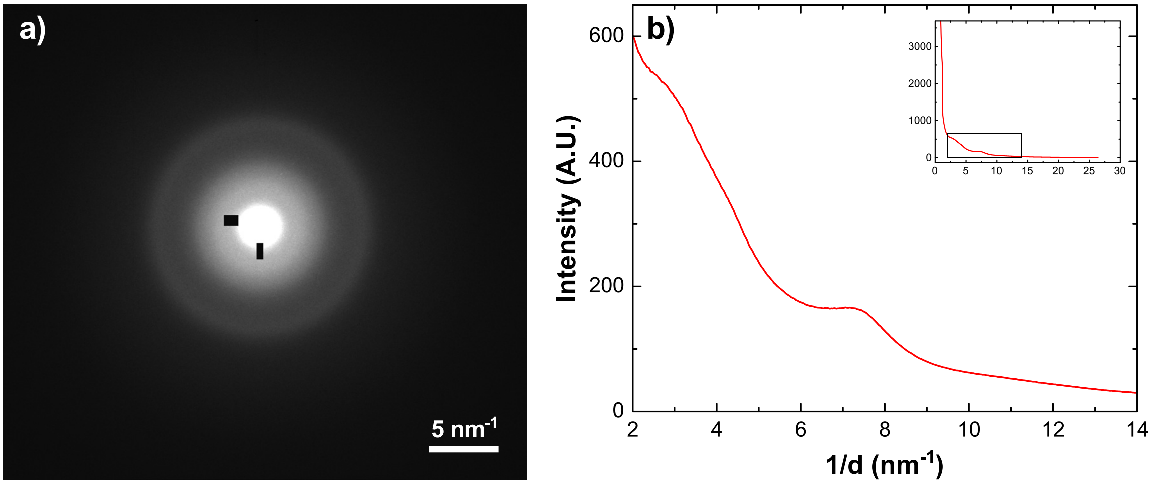

Figure 2.10 Example of the typical SiN_x amorphous diffraction pattern (a) and the raw intensity profile obtained by radial integration (b). This pattern was captured in the DTEM in conventional (thermionic) mode. Additional notes are as in Fig. 2.9.

Because the background intensity profile shown in Fig. 2.10(b) contains variations in intensity, failing to account for these in the background subtraction process will result in a distorted result. To account for them, the first step of background subtraction is to subtract the silicon nitride signal from the signal of interest. Typically a single silicon nitride background image is maintained, but the intensity in individual experiments can vary. This is especially true for DTEM experiments which utilize a laser photocathode. To compensate for this, the silicon nitride background signal is scaled by a factor chosen on a per-pattern basis before the subtraction is performed. For example, to subtract the SiN_x background from the pattern in Fig. 2.9 we used a scaling factor of 0.08. The result is shown, along with two alternate choices of scaling factor, in Fig. 2.11.

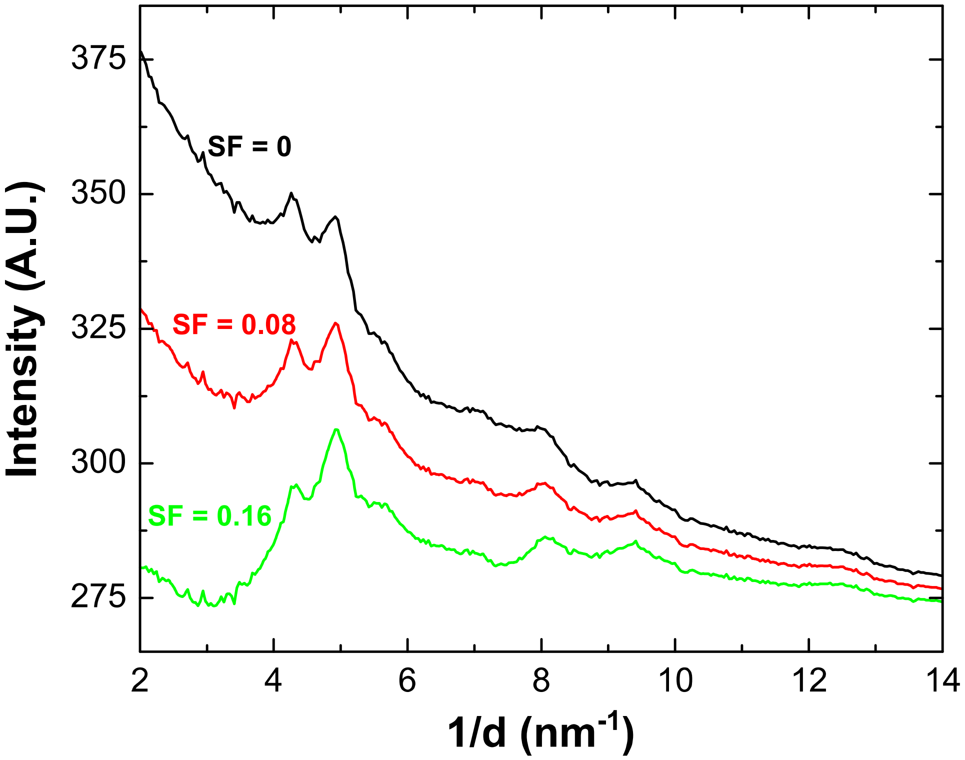

Figure 2.11 Illustration of the effects of scaling factor (SF) on the result of silicon nitride (first-stage) background subtraction. The optimal scaling factor (SF = 0.08) yields a pattern sitting on a smooth featureless background. Scaling factors that are too large (SF = 0.16) or too small (SF = 0) lead to distortions in the pattern around 2 – 4 nm^{-1} and 7-8 nm^{-1} (where the amorphous background is largest) and cannot be fit by a smooth featureless background.

As the SF = 0.16 case in Fig. 2.11 illustrates, we cannot accomplish complete background subtraction using the silicon nitride background alone. Instead, the approach is to find the largest scaling factor that does not distort the data (SF = 0.08 in this case) and then finish the process using a second, featureless baseline. This baseline nominally resembles an exponential decay function, but typically it is manually fitted. The manually fitted background for the example data is shown in Fig. 2.12. Naturally, care must be taken in this step to avoid fabricating features simply by the choice of baseline. However, typically the appropriate choice of baseline is fairly obvious as in Fig. 2.12.

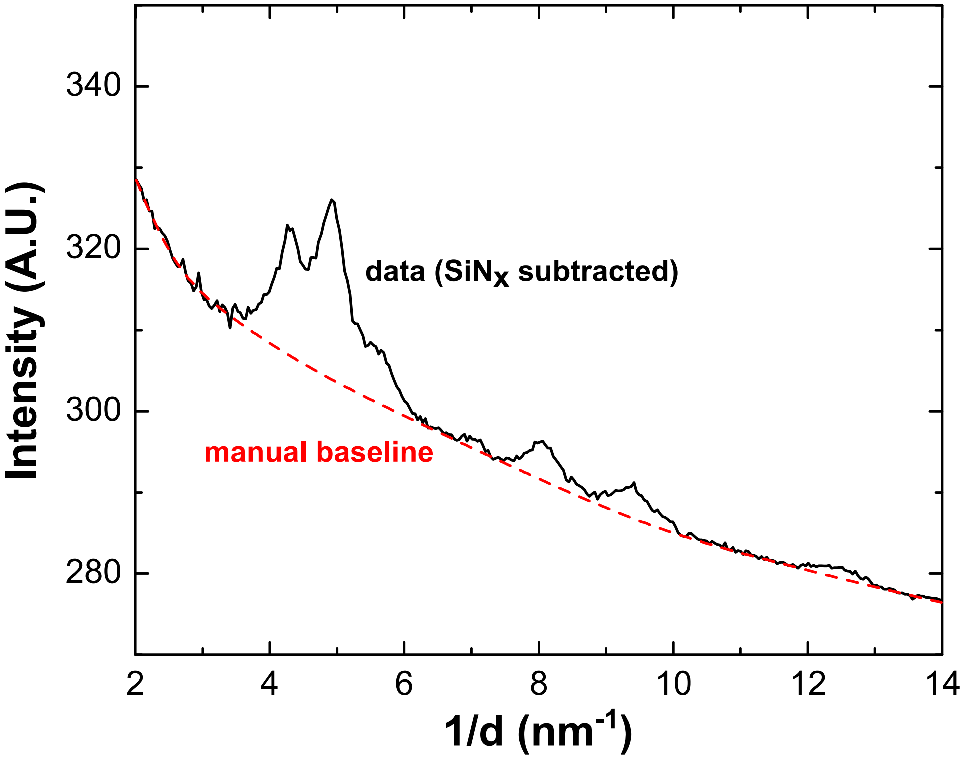

Figure 2.12 Illustration of data after first-stage silicon nitride background subtraction (SF = 0.08) with the second-stage, manual baseline fit. A smoothly decreasing background function with no extra features is an indication that the scaling factor for stage one was chosen correctly.

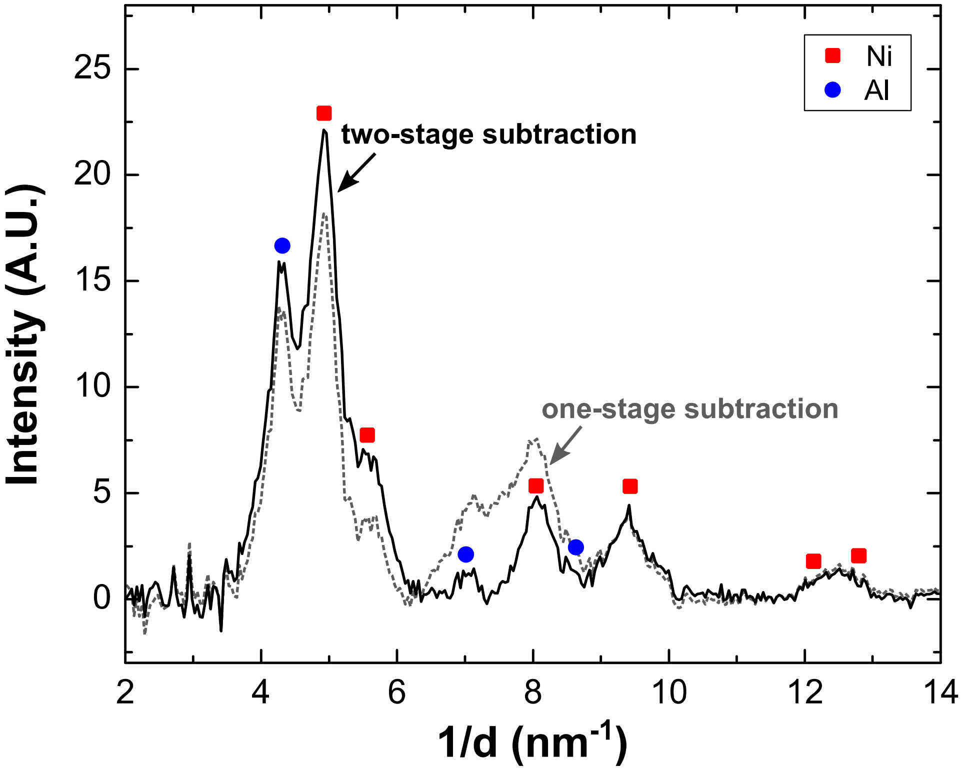

Figure 2.13 The final form of the raw data shown in Fig. 2.9 after two-stage background subtraction. The sample pattern shows elemental Ni and Al, as indexed. Also shown is the result obtained if SF = 0, i.e. without the silicon nitride subtraction. Note the distortion around 7 – 8 nm^{-1}.

The final electron diffraction pattern after both stages of subtraction is shown in Fig. 2.13. It exhibits a flat baseline and low distortion, optimal for comparison to other patterns or phase identification. For comparison, the result of a one-stage subtraction (simply fitting the background and ignoring the silicon nitride contribution) is shown as well. The main distortion in this case is between 7 nm^{-1} and 8 nm^{-1}, the position of the diffuse scattering ring in Fig. 2.10.

References for Chapter 2

[1] S.L. Lai, G. Ramanath, L.H. Allen, P. Infante, Z. Ma, High-speed (10^4 °C/s) scanning microcalorimetry with monolayer sensitivity (J/m2), Appl. Phys. Lett. 67 (1995) 1229.

[2] E.A. Olson, M.Y. Efremov, L.H. Allen, The design and operation of a MEMS differential scanning nanocalorimeter for high-speed heat capacity measurements of ultrathin films, J. Microelectromechanical Syst. 12 (2003) 355–364.

[3] M.Y. Efremov, E.A. Olson, M. Zhang, S.L. Lai, F. Schiettekatte, Z.S. Zhang, et al., Thin-film

differential scanning nanocalorimetry: heat capacity analysis, Thermochim. Acta. 412 (2004) 13–23.

[4] P. Swaminathan, D.A. LaVan, T.P. Weihs, Dynamics of solidification in Al thin films measured using a nanocalorimeter, J. Appl. Phys. 110 (2011) 113519.

[5] M. Zhang, E.A. Olson, R.D. Twesten, J.G. Wen, L.H. Allen, I.M. Robertson, et al., In situ Transmission Electron Microscopy Studies Enabled by Microelectromechanical System Technology, J. Mater. Res. 20 (2005) 1802–1807.

[6] R.K. Kummamuru, L. De La Rama, L. Hu, M.D. Vaudin, M.Y. Efremov, M.L. Green, et al., Measurement of heat capacity and enthalpy of formation of nickel silicide using nanocalorimetry, Appl. Phys. Lett. 95 (2009) 181911.

[7] P. Swaminathan, M.D. Grapes, K. Woll, S.C. Barron, D.A. LaVan, T.P. Weihs, Studying exothermic reactions in the Ni-Al system at rapid heating rates using a nanocalorimeter, J. Appl. Phys. 113 (2013) 143509.

[8] P.J. McCluskey, J.J. Vlassak, Glass transition and crystallization of amorphous Ni–Ti–Zr thin films by combinatorial nano-calorimetry, Scr. Mater. 64 (2011) 264–267.

[9] P.J. McCluskey, C. Zhao, O. Kfir, J.J. Vlassak, Precipitation and thermal fatigue in Ni–Ti–Zr shape memory alloy thin films by combinatorial nanocalorimetry, Acta Mater. 59 (2011) 5116–5124.

[10] J.M. Gregoire, P.J. McCluskey, D. Dale, S. Ding, J. Schroers, J.J. Vlassak, Combining combinatorial nanocalorimetry and X-ray diffraction techniques to study the effects of composition and quench rate on Au–Cu–Si metallic glasses, Scr. Mater. 66 (2012) 178–181.

[11] A.A. Minakov, S.A. Adamovsky, C. Schick, Non-adiabatic thin-film (chip) nanocalorimetry, Thermochim. Acta. 432 (2005) 177–185.

[12] J.-L. Garden, E. Château, J. Chaussy, Highly sensitive ac nanocalorimeter for microliter-scale liquids or biological samples, Appl. Phys. Lett. 84 (2004) 3597.

[13] H. Huth, A.A. Minakov, C. Schick, Differential AC-chip calorimeter for glass transition measurements in ultrathin films, J. Polym. Sci. Part B Polym. Phys. 44 (2006) 2996–3005.

[14] K. Xiao, J.M. Gregoire, P.J. McCluskey, J.J. Vlassak, A scanning AC calorimetry technique for the analysis of nano-scale quantities of materials., Rev. Sci. Instrum. 83 (2012) 114901.

[15] J.M. Gregoire, K. Xiao, P.J. McCluskey, D. Dale, G. Cuddalorepatta, J.J. Vlassak, In-situ X-ray diffraction combined with scanning AC nanocalorimetry applied to a Fe0.84Ni0.16 thin-film sample., Appl. Phys. Lett. 102 (2013) 201902.

[16] K. Xiao, J.M. Gregoire, P.J. McCluskey, D. Dale, J.J. Vlassak, Scanning AC nanocalorimetry combined with in-situ x-ray diffraction, J. Appl. Phys. 113 (2013) 243501.

[17] T. LaGrange, M.R. Armstrong, K. Boyden, C.G. Brown, G.H. Campbell, J.D. Colvin, et al., Single-shot dynamic transmission electron microscopy, Appl. Phys. Lett. 89 (2006) 044105.

[18] T. LaGrange, G.H. Campbell, B.W. Reed, M.L. Taheri, J.B. Pesavento, J.S. Kim, et al., Nanosecond time-resolved investigations using the in situ dynamic transmission electron microscope (DTEM)., Ultramicroscopy. 108 (2008) 1441–1449.

[19] B.W. Reed, T. LaGrange, R.M. Shuttlesworth, D.J. Gibson, G.H. Campbell, N.D. Browning, Solving the accelerator-condenser coupling problem in a nanosecond dynamic transmission electron microscope, Rev. Sci. Instrum. 81 (2010) 053706.

[20] T. LaGrange, G.H. Campbell, P.E.A. Turchi, W.E. King, Rapid phase transformation kinetics on a nanoscale: Studies of the α→β transformation in pure, nanocrystalline Ti using the nanosecond dynamic transmission electron microscope, Acta Mater. 55 (2007) 5211–5224.

[21] T. LaGrange, G.H. Campbell, J.D. Colvin, B.W. Reed, W.E. King, Nanosecond time resolved electron diffraction studies of the α→β in pure Ti thin films using the dynamic transmission

electron microscope (DTEM), J. Mater. Sci. 41 (2006) 4440–4444.

[22] J.T. McKeown, A.K. Kulovits, C. Liu, K. Zweiacker, B.W. Reed, T. LaGrange, et al., In situ transmission electron microscopy of crystal growth-mode transitions during rapid solidification of a hypoeutectic Al–Cu alloy, Acta Mater. 65 (2014) 56–68.

[23] M.K. Santala, B.W. Reed, S. Raoux, T. Topuria, T. LaGrange, G.H. Campbell, Irreversible reactions studied with nanosecond transmission electron microscopy movies: Laser crystallization of phase change materials, Appl. Phys. Lett. 102 (2013) 174105.

[24] M.K. Santala, B.W. Reed, S. Raoux, T. Topuria, T. LaGrange, G.H. Campbell, Nanosecond-scale time-resolved electron imaging during laser crystallization of GeTe, Phys. Status Solidi. 249 (2012) 1907–1913.

[25] M.K. Santala, B.W. Reed, T. Topuria, S. Raoux, S. Meister, Y. Cui, et al., Nanosecond in situ transmission electron microscope studies of the reversible Ge2Sb2Te5 crystalline ⇔ amorphous phase transformation, J. Appl. Phys. 111 (2012) 024309.

[26] A. Kulovits, J.M.K. Wiezorek, T. LaGrange, B.W. Reed, G.H. Campbell, Revealing the transient states of rapid solidification in aluminum thin films using ultrafast in situ transmission electron microscopy, Philos. Mag. Lett. 91 (2011) 287–296.

[27] L. Nikolova, T. LaGrange, B.W. Reed, M.J. Stern, N.D. Browning, G.H. Campbell, et al., Nanocrystallization of amorphous germanium films observed with nanosecond temporal resolution, Appl. Phys. Lett. 97 (2010) 203102.

[28] G.H. Campbell, T. LaGrange, J.S. Kim, B.W. Reed, N.D. Browning, Quantifying transient states in materials with the dynamic transmission electron microscope., J. Electron Microsc. (Tokyo). 59 (Supp.) (2010) S67–74.

[29] J.S. Kim, T. Lagrange, B.W. Reed, M.L. Taheri, M.R. Armstrong, W.E. King, et al., Imaging of transient structures using nanosecond in situ TEM., Science (80-.). 321 (2008) 1472–1475.

[30] J.S. Kim, T. LaGrange, B.W. Reed, R. Knepper, T.P. Weihs, N.D. Browning, et al., Direct characterization of phase transformations and morphologies in moving reaction zones in Al/Ni nanolaminates using dynamic transmission electron microscopy, Acta Mater. 59 (2011) 3571–3580.

[31] P. Swaminathan, B.G. Burke, A.E. Holness, B. Wilthan, L. Hanssen, T.P. Weihs, et al., Optical calibration for nanocalorimeter measurements, Thermochim. Acta. 522 (2011) 60–65.

[32] B.L. Zink, B. Revaz, J.J. Cherry, F. Hellman, Measurement of thermal conductivity of thin films with a Si-N membrane-based microcalorimeter, Rev. Sci. Instrum. 76 (2005) 024901.

[33] T. LaGrange, B.. Reed, M.. Santala, J.. McKeown, A. Kulovits, J.M.K. Wiezorek, et al., Approaches for ultrafast imaging of transient materials processes in the transmission electron microscope., Micron. 43 (2012) 1108–20.

[34] J.A. Dean, N.A. Lange, Lange’s handbook of chemistry, 15th ed., McGraw-Hill, 1999.

[35] M.D. Grapes, T. LaGrange, L.H. Friedman, B.W. Reed, G.H. Campbell, T.P. Weihs, et al., Combining nanocalorimetry and dynamic transmission electron microscopy for in situ characterization of materials processes under rapid heating and cooling, Rev. Sci. Instrum. 85 (2014) 084902.

3. Initial In Situ Nanocalorimetry Results on 1:1 Al:Ni Samples

3.1 Introduction[a]

Thin film and interfacial reactions have been studied extensively for many years. These reactions are of broad interest both in industry (e.g. for microelectronics [1,2], microelectromechanical systems [3,4], and coatings [5]) and in science, where reduced diffusion distances and increased surface area provide an opportunity to study phase formation in a unique environment [6–9]. One of the best characterized thin film reactions is between Al and Ni [10–20]. Al and Ni have a large, negative heat of mixing, making the reaction highly exothermic. Multilayer foils consisting of nanoscale layers of Al and Ni can release this energy very quickly. When a multilayer foil is ignited at one end in a free-standing configuration, the heat released locally is sufficient to ignite the adjacent material and produce a high-velocity reaction front in what is known as a "self-propagating" reaction [11]. Heating rates when reacting in this mode exceed 10^6 K/s. Because of their ability to deliver rapid, local heating, Al/Ni multilayer foils have been exploited as heat sources for rapid room-temperature soldering [12,13].

In order to better understand the reaction in Al/Ni multilayers, many studies have identified the sequence of phases that form as the multilayers are heated [14–17]. Historically, these studies have been accomplished using differential scanning calorimetry. These instruments heat a sample at a controlled rate that is typically less than 1 K/s and measure the heat evolved as a function of temperature. The phase(s)

---

[a] Sections 3.1 - 3.5 are adapted from a peer-reviewed journal article: M.D. Grapes *et al.*, In situ transmission electron microscopy investigation of the interfacial reaction between Ni and Al during rapid heating in a nanocalorimeter, APL Mater. 2 (2014) 116102.

present at different points during the heating cycle are determined by quenching and analyzing the sample with x-ray diffraction. More recently, there has been interest in studying the phase transformations during self-propagation of these reactions, where heating rates are approximately one-million times higher. Since quenching is difficult for reactions progressing at these rates, *in situ* characterization methods are preferred in this regime. To-date such studies have been accomplished using two techniques: synchrotron x-ray microdiffraction [18,19] and time-resolved transmission electron microscopy (TEM) [20].

For multilayers with a 1:1 Al:Ni atomic ratio, slow heating experiments typically have identified two phase transformation sequences depending on the deposition method. For evaporated Al/Ni multilayers [14,21], the phase transformation sequence under slow heating is

$$\mathrm{Al} + \mathrm{Ni} \rightarrow \mathrm{Al_3Ni} + \mathrm{Ni} \rightarrow \mathrm{Al_3Ni_2} + \mathrm{Ni} \rightarrow \mathrm{AlNi} \tag{3.1}$$

For Al/Ni multilayers that are deposited by sputtering or ion-beam deposition the sequence is altered slightly [15,17]:

$$\mathrm{Al} + \mathrm{Ni} \rightarrow \mathrm{Al_9Ni_2} + \mathrm{Ni} \rightarrow \mathrm{Al_3Ni} + \mathrm{Ni} \rightarrow \mathrm{Al_3Ni_2} + \mathrm{Ni} \rightarrow \mathrm{AlNi} \tag{3.2}$$

The distinction between these two sequences is in the first phase to form and is attributed to subtle differences in the initial microstructure of the as-deposited Al/Ni interfaces. These interfaces tend to be more intermixed in sputtered and ion-beam deposited samples, which in turn can impact the nucleation of the Al_9Ni_2 and Al_3Ni phases which have similar free energies of formation [17].

When sputter deposited Al/Ni multilayers are reacted in the rapid, self-propagating mode (heating rates exceeding 10^6 K/s) and characterized using synchrotron x-ray diffraction [18,19] or time-resolved TEM[20], the observed phase transformation sequence becomes

$$\mathrm{Al} + \mathrm{Ni} \rightarrow \text{Al-rich liquid} + \mathrm{Ni} \rightarrow \mathrm{AlNi} \tag{3.3}$$

Note that while at low heating rates we observe a sequence of solid intermetallic phases, at high heating rates all of the intermetallic phases are skipped and instead mixing occurs in a molten Al-rich phase. The shift in phase sequence with heating rate is attributed to a reduction in the amount of atomic intermixing that occurs prior to reaching temperatures where the intermediate intermetallic phases are no longer stable [18]. To-date this characterization has only been performed on sputtered Al/Ni multilayers, but evaporated multilayers are likely to exhibit the same sequence given that the vast majority of mixing occurs through Ni dissolving into molten Al.

3.2 Experiment

To study this phenomenon over a broad range of heating rates this work seeks to demonstrate that one can characterize the AlNi formation reaction at heating rates in the 10^3 K/s to 10^5 K/s range, intermediate between the heating rates in differential scanning calorimetry (DSC) studies and in self-propagating reactions. Given that these heating rates are orders of magnitude larger than what is possible using a standard DSC, we employ a calorimetric technique that is capable of more rapid heating: nanocalorimetry. A nanocalorimeter is a microelectromechanical device whose miniscule heat capacity enables it to achieve very high heating rates [22]. However, as in self-propagating reactions, analyzing the phases formed at these heating rates is difficult using quenching and *ex situ* observations. Thus, an *in situ* approach is preferred so that phases can be detected as they appear. In this work we utilize a newly developed *in situ* nanocalorimetry system [23] that makes use of the dynamic transmission electron microscope [24] (DTEM) to perform structural characterization during the calorimetry experiment. The DTEM is a time-resolved TEM designed, built, and housed at Lawrence Livermore National Laboratory.

The *in situ* nanocalorimetry system is depicted schematically in Fig. 3.1 and consists of the DTEM itself, TEM-compatible nanocalorimeter sensors, an *in situ* nanocalorimetry TEM holder, and a data acquisition system. The DTEM utilizes an ultraviolet-laser-driven photocathode to produce extremely short, high intensity electron pulses [24]. The laser intensity and duration can be manipulated to create electron pulses from 30 ns to 500 ns in length. Nanocalorimeters consist of a platinum strip for heating and temperature measurement suspended on a silicon nitride membrane to minimize heat losses and thermal mass [22]. The temperature-resistance relationship for each sensor is calibrated optically [25] prior to first use, and for TEM investigation the sensor design was modified to include three 100 μm x 100 μm electron-transparent windows in the platinum strip [23]. After a sample is deposited on the sensor it is placed into a custom-built *in situ* nanocalorimetry holder which is compatible with the DTEM goniometer. This holder provides electrical connections between the Pt sensor and a data acquisition system that is synchronized with the DTEM via a custom-built LabVIEW interface. Full details on the design and operation of the *in situ* nanocalorimetry system have been reported elsewhere [23].

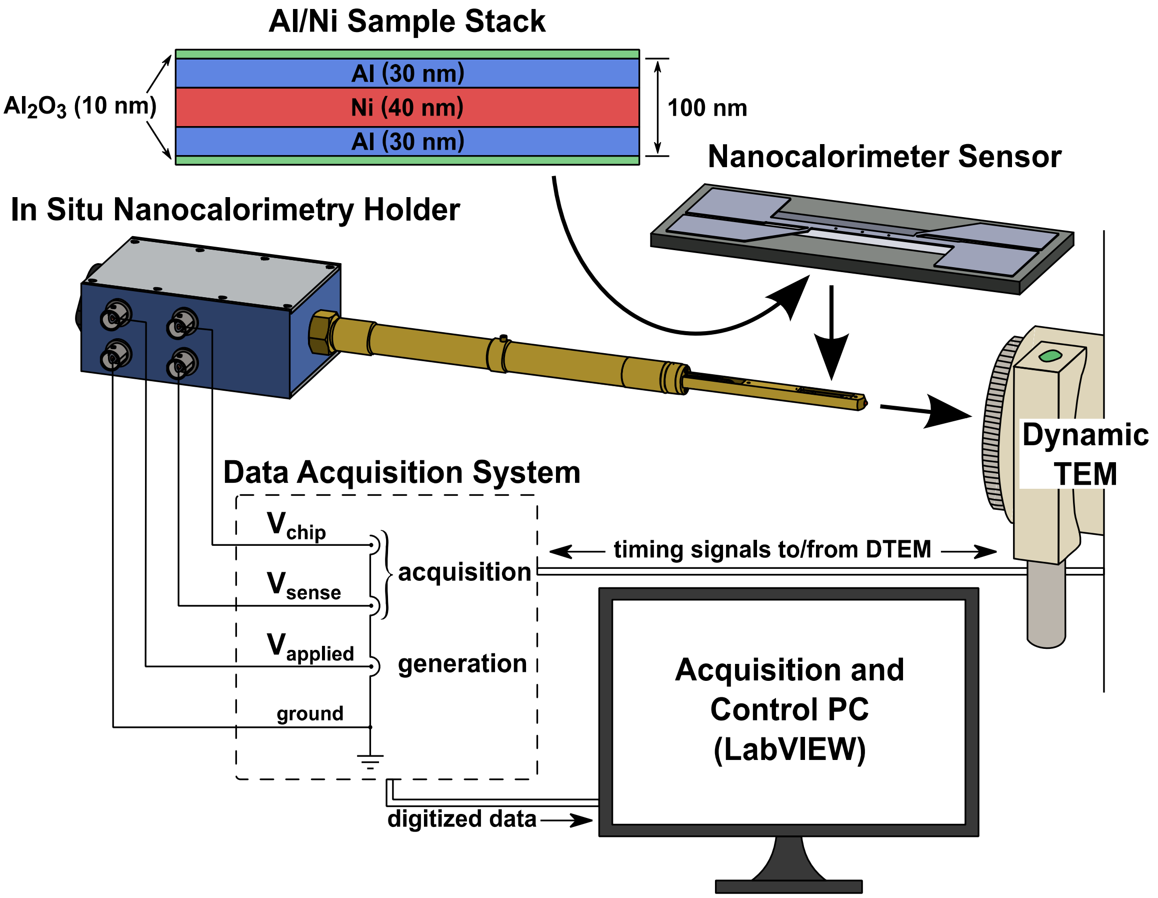

Figure 3.1 Schematic of the experimental system for *in situ* nanocalorimetry showing a nanocalorimeter sensor, the *in situ* nanocalorimetry holder, the dynamic transmission electron microscope (TEM), and the data acquisition system. Also shown is the sample geometry studied in this work, a 100 nm thick Ni/Al bilayer.

The samples tested in this study consisted of 40 nm of Ni (target purity 99.995 %) sandwiched between two 30 nm layers of Al (target purity 99.999 %) for a total bilayer thickness of 100 nm and an overall composition of 50 atomic percent of Al. This sandwich structure is the smallest symmetric repeat unit of a multilayer with a 100 nm bilayer spacing, and matches the structure used in previous nanocalorimetry investigations of the Al/Ni reaction [26]. 10 nm of Al_2O_3 was deposited on both sides of the Al/Ni/Al stack to serve as a passivation layer and diffusion barrier. This sample geometry is illustrated in the upper-left of Fig. 3.1. The sample stack was deposited through a shadow-mask directly onto the underside of the nanocalorimeter sensor by e-beam evaporation. Layer thickness during deposition was measured by a quartz crystal thickness monitor. For the experiments reported here, the DTEM was configured for single-shot mode with an electron-pulse-duration of 500 ns. Selected-area electron diffraction patterns were collected with a ≈ 0.55 μm^2 selected-area aperture positioned in the central electron window of the nanocalorimeter heater strip. Since the Al/Ni formation reaction is irreversible, four nanocalorimeters containing identical samples were reacted and imaged at different times to construct a full picture of the phase formation sequence. The average heating rate during the experiments was 830 K/s.

3.3 Results

Characteristic results from the nanocalorimetry system during the heating segment of one experiment are presented in Fig. 3.2. The plot of temperature vs. time in Fig. 3.2(a) depicts the measurable difference in the temperature evolution of the sample during the first heating (when a reaction is occurring) as compared to the second heating (when the reactants have already been consumed). This difference can be extracted and quantified to give the reaction power, the rate of heat release that is due to a reaction in the sample and not external heating, shown in Fig. 3.2(b). Note the presence of two large exothermic peaks with one small exothermic peak in between them. These peaks are highlighted by fitting each with a Voigt distribution in Fig. 3.2(b). An alternative way to display nanocalorimetry results is to plot dH/dT vs. temperature, shown in Fig. 3.2(c). This curve is the temperature-domain equivalent of Fig. 3.2(b) and can be helpful in understanding how reaction rates change with temperature. The quantity dH/dT is computed by dividing the total reaction power by the heating rate, and the fit peaks and cumulative fit shown in Fig. 3.2(c) were calculated by dividing the peak fits in Fig. 3.2(b) by the heating rate as well.

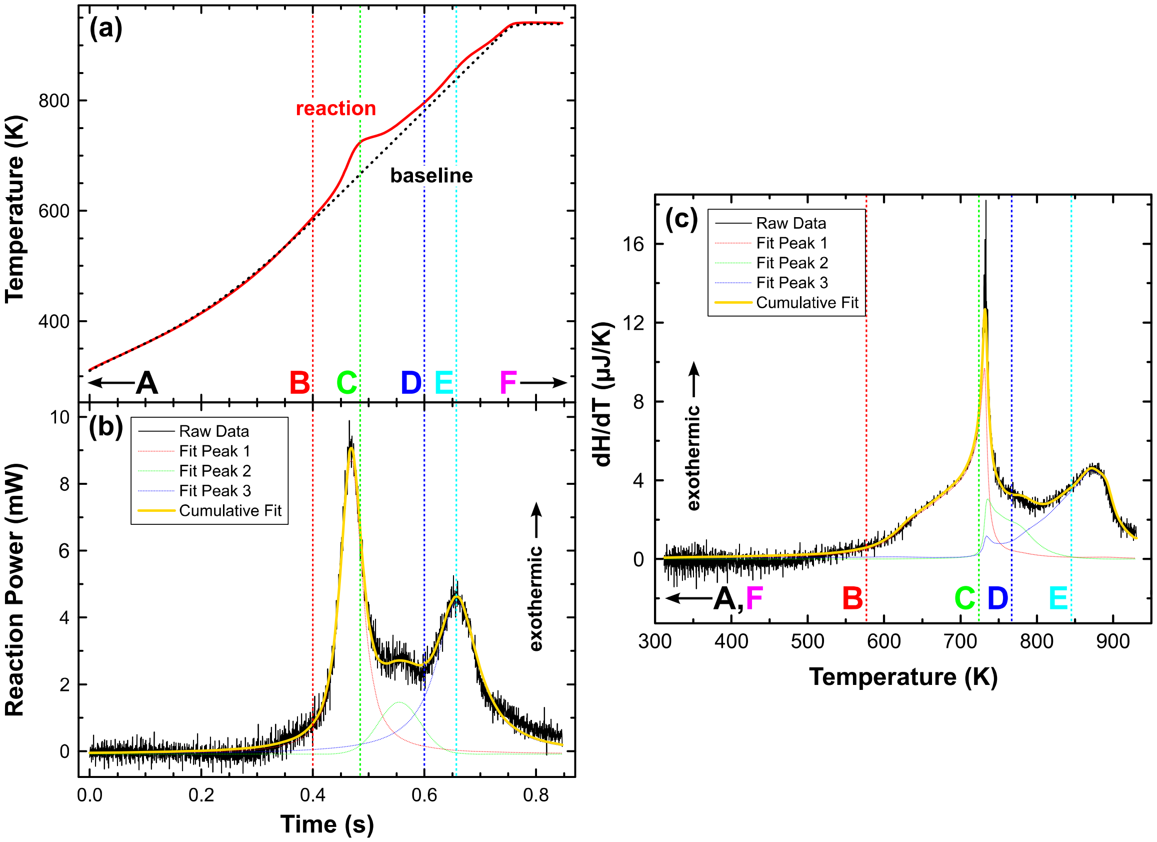

Figure 3.2 Typical nanocalorimetry data for a 100 nm Al/Ni bilayer heated at an average rate of 830 K/s: (a) temperature vs. time for two consecutive scans showing the temperature excursion when a reaction occurs, (b) reaction power vs. time showing heat evolution in three distinct exothermic peaks fitted with Voigt distributions, and (c) dH/dT vs. temperature showing the shape of the three exothermic peaks in the temperature domain. The dashed lines indicate the points at which the diffraction patterns in Fig. 3.3 were taken. The FWHM for the three fitted peaks in (b) are 33 ms, 95 ms, and 86 ms respectively.

Electron diffraction patterns were captured using the DTEM at the times indicated in Fig. 3.2 in order to identify the phase transformations occurring in each of the three exotherms. In addition to the four electron diffraction patterns captured during the heating experiment (B – E), patterns were also taken at room temperature before (A) and after (F) to identify the initial and final phases. Fig. 3.3 presents these results as a sequence of 1D diffraction patterns, obtained by rotational averaging of the original 2D patterns followed by background subtraction. All observable peaks are labeled with the most likely phase or phases. We also label the temperature of the sample when the pattern was captured and the amount of heat that had been released up to that point (as a percentage of the total theoretical heat of formation for AlNi). The sequence is described below.

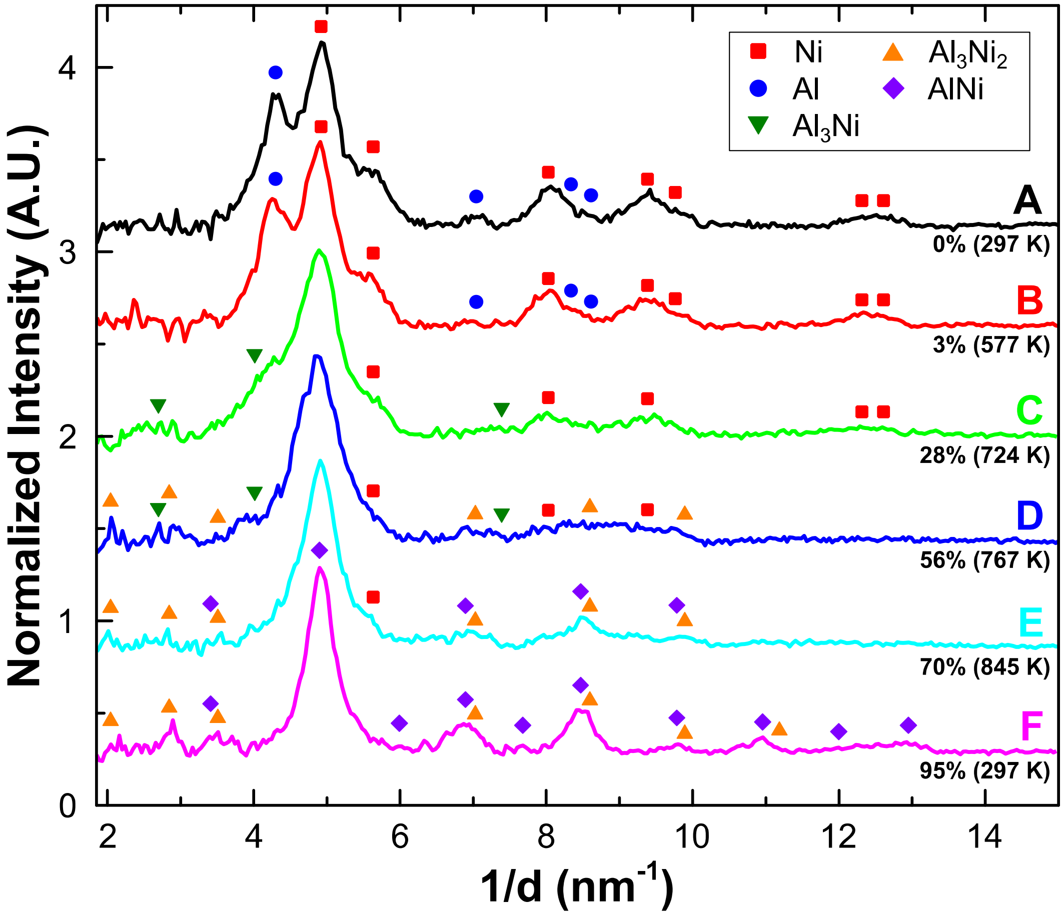

Figure 3.3 Time-resolved electron diffraction patterns captured before, during, and after the reaction of a 100 nm Al/Ni bilayer. The pattern labels correspond to the times in Fig. 3.2. Also labeled for each pattern are the percentage of heat released (as a fraction of the theoretical enthalpy of formation) and the temperature when the pattern was captured. The prominent peak around 4.9 nm^{-1} is unlabeled for patterns C – E because all of the intermetallic phases have one or more peaks in this region and the peak is too broad to distinguish between them.

Pattern A presents the initial state of the sample prior to heating. All of the measured diffraction peaks can be attributed to either fcc Al or fcc Ni. Pattern B is the first pattern captured during the heating experiment. It represents a 280 K temperature increase over Pattern A but still represents a pre-reaction microstructure (3 % reaction completion). As such, it shows essentially no changes from Pattern A other than slight peak broadening and a slight shift to smaller $1/d$ due to thermal expansion. Pattern C was captured more than half-way through the first exotherm as shown in Fig. 3.2(b). Here we see the first clear evidence of a reaction, as the fcc Al peaks have disappeared and have been replaced by peaks from Al_3Ni (*oP*16 structure [27]). Al_3Ni has an exceptionally large number of diffraction peaks (over 450 in the range shown) that are too weak to detect individually in these experiments. However, in certain regions these peaks overlap to give measurable intensities distinct from those of fcc Ni. These regions are labeled in Fig. 3.3 and include a broad peak around 2.72 nm^{-1} (formed by the (011), (101), (020), (111), and (200) reflections) and a shoulder around 4.07 nm^{-1} (formed by the (211), (220), and (002) reflections). Note that in this pattern, and in the two that follow, the prominent peak around 4.9 nm^{-1} cannot be used for phase identification because all of the candidate phases have large peaks in this region. Pattern D represents the state of the sample near the end of the second, small exotherm. Diffraction peaks from Ni and Al_3Ni are still visible, but this pattern shows the first clear evidence for the Al_3Ni_2 phase (*hP*5 structure [27]) in the form of the (001) peak at 2.04 nm^{-1} and the (202)/(022) peak at 7.03 nm^{-1}. There is some evidence for the (100) peak at 2.86 nm^{-1} and the (212)/(122) peak at 8.60 nm^{-1}, but the former is obscured by the nearby Al_3Ni peaks while the latter combines with the shrinking (220) and (311) Ni peaks to form a relatively featureless signal around 8.9 nm^{-1}. In Pattern E, acquired in the middle of the final exotherm, the signal from fcc Ni has almost disappeared except for the shoulder at 5.64 nm^{-1} due to the (200) peak. This makes it easier to see clear peaks due to the Al_3Ni_2 phase. Peaks from AlNi (*cP*2 structure [27]) may also be contributing, but it is very difficult to distinguish between AlNi and Al_3Ni_2 when the peaks are broad unless the AlNi (111) and (210) superlattice peaks at 6.00 nm^{-1} and 7.75 nm^{-1} are visible. This difficulty persists in Pattern F, which shows the final room temperature state of the sample after the heating experiment. There is some evidence for the AlNi superlattice peaks, but the persistence of Al_3Ni_2 peaks at 2.04 nm^{-1} and 2.86 nm^{-1} suggests that the primary phase is still Al_3Ni_2.

3.4 Discussion

The reaction power in Fig. 3.2(b) shows three distinct exotherms. Fitting the exothermic peaks and taking the integral of the cumulative fit curve yields the total heat evolved. Averaged over the four samples reported, the total heat is 1.25 mJ with a standard deviation of 0.042 mJ. The sample mass can be estimated using the intended layer thicknesses, the estimated sample area (3.7 mm x 0.5 mm), and the bulk densities for Al and Ni. We estimate the mass in this way to be 960 ng yielding a normalized average heat of formation of 1302 J g^{-1} $\pm$ 44 J g^{-1}. This is 5.7 % $\mp$ 3.2 % lower than the theoretical value for AlNi [28], 1381 J g^{-1}. Since Al_3Ni_2 peaks are still visible in the final diffraction pattern an incomplete reaction is likely responsible for at least part of this discrepancy. Uncertainty in the estimation of the sample mass may also be a contributing factor. Comparing the positions of the exothermic peaks in Fig. 3.2 to the electron diffraction patterns in Fig. 3.3 we conclude that the first exotherm in the nanocalorimetry data corresponds to the formation of Al_3Ni, the second to an initial stage of Al_3Ni_2 formation, and the third to a second stage of Al_3Ni_2 growth and transformation to AlNi. Thus the overall phase sequence observed in these experiments is the same as that presented in Eq. (3.1) for evaporated Al/Ni layers under slow heating. However, it appears that in these experiments Al_3Ni_2 grows in a two-stage mode, something that has not been reported previously for this phase.

Two facts support the conclusion that Al_3Ni_2 formation occurs across both the second and third exotherms: (1) rather than disappearing, the Al_3Ni_2 diffraction peaks grow stronger between Patterns D and E which span the third exotherm, and (2) the area of the second exothermic peak is too small for complete formation of Al_3Ni_2 to have occurred. Specifically, in these experiments the second exotherm contributes 10 % of the theoretical heat of formation, while literature values for Al_3Ni_2 indicate that the formation of this phase should account for about 38 % of the total heat [29]. Based on this argument Al_3Ni_2 must continue to grow during the third exotherm. The best explanation for a phase forming in multiple exotherms comes from the model proposed by Coffey *et al.*, where the first exothermic peak corresponds to the formation of an interfacial layer of the new phase and the second exothermic peak indicates 1D growth of this layer through the remaining reactants [30]. For a 100 nm bilayer we expect that the second exotherm should be substantially larger than the first exotherm, so this model is a good fit for the data we've obtained. The shape of the third peak in Fig. 3.2(c) is also consistent with this explanation as it displays the gradual rise and rapid fall-off characteristic of diffusion-limited growth [31].

3.5 Future Work and Conclusions

Going forward, one line of investigation will be to extend the present work on the 1:1 Al:Ni composition to higher heating rates where more significant changes in phase formation sequence may occur. However, since characteristic reaction temperatures increase as the heating rate increases [32] there may be a limit on the maximum heating rate that can be studied while still forming the final AlNi phase. In light of this, a second line of investigation will be to study films with the Al-rich compositions of 3:1 and 3:2 Al:Ni (corresponding to the Al_3Ni and Al_3Ni_2 intermetallic phases). By excluding the formation of the highest temperature phase, AlNi, these samples will allow us to study the formation of the Al_3Ni and Al_3Ni_2 intermetallics at heating rates up to the maximum rates possible using nanocalorimetry.

More generally, the *in situ* nanocalorimetry system demonstrated here can be applied to study rapid phase transformations and microstructural changes in a number of fields, for example in the study of bulk metallic glasses. Traditional calorimeters operate at heating and cooling rates that are too low to induce amorphization in these materials, but nanocalorimetry has been shown to be capable of achieving these rates and measuring the enthalpy of the transformation directly [33,34]. This *in situ* nanocalorimetry system would extend that capability by offering the time resolution required to actually observe the amorphization process as it occurs. For studies requiring even more extreme heating and cooling rates, the *in situ* nanocalorimeter could be operated as a dedicated calorimetric sensor in combination with a laser for localized heating. This would extend the potential applications to include simultaneous structural and calorimetric measurements of amorphous melting in Si and Ge [35,36] and of the amorphization and crystallization processes in phase change materials [37].

In conclusion, we have demonstrated that one can study rapid phase transformations in 1:1 Al:Ni bilayers using a new system combining *in situ* nanocalorimetry and dynamic transmission electron microscopy (DTEM). The intermediate phases in the reaction were identified using *in situ* electron diffraction for samples heated at an average heating rate of 830 K/s. Nanocalorimeter data indicates that at this heating rate, the formation reaction occurs in a sequence of three exotherms producing approximately 95 % of the theoretical heat of formation for this stoichiometry. Meanwhile, *in situ* time-resolved electron diffraction confirms that the phase transformation sequence is similar to that observed at much slower heating rates in a DSC, $Al + Ni \rightarrow Al_3Ni + Ni \rightarrow Al_3Ni_2 + Ni \rightarrow AlNi$. The 5 % discrepancy in total heat of formation is likely because the final reaction step did not go to completion, an explanation supported by the persistence of Al_3Ni_2 diffraction peaks in the electron diffraction patterns of as-reacted samples. Future work on the Al/Ni system will aim to analyze the phase transformation sequence for 1:1 Al:Ni bilayers at higher heating rates, and to study bilayers with 3:1 and 3:2 Al:Ni compositions in order to gain a better understanding of the processes by which the Al_3Ni and Al_3Ni_2 intermetallic phases form.

3.6 Appendix A: Slow Heating of 1:1 Al:Ni in a Nanocalorimeter

One of the natural questions that arises in considering the phases formed during high-heating-rate nanocalorimetry tests is what effect does the size of the sample have? It is implicit in the discussion above that the nanocalorimeter samples should behave the same as bulk multilayers when it comes to predicting the limits of behavior, i.e. very slow (DSC) and very fast (self-propagating) heating. If this is not the case then we can’t justify making any comparisons to previous studies on other types of samples. This is difficult to test for the very high heating rate case, but feasible to do at the slow-heating end.

Although the quoted minimum heating rate for nanocalorimetry is typically around 1000 K/s, this is just the limit to obtain reasonable heat flow information. If only the temperature is of interest, the device is capable of arbitrarily slow heating or even isothermal experiments. Heat flow is not of primary importance in this test, since we mainly want to see what phases form and in what sequence. Hence the approach used was to heat at a very low target heating rate (40 K/min), monitor the temperature, and automatically stop the heating when the temperature exceeded a set value. We then transferred the partially reacted sample to a custom holder designed for compatibility with the FEI Tecnai-12 transmission electron microscope at Johns Hopkins University, and performed selected-area electron diffraction to identify the phase(s) present. This process was repeated with multiple chips over a range of temperatures to establish the full phase transformation sequence, and the result is shown in Fig. 3.4.

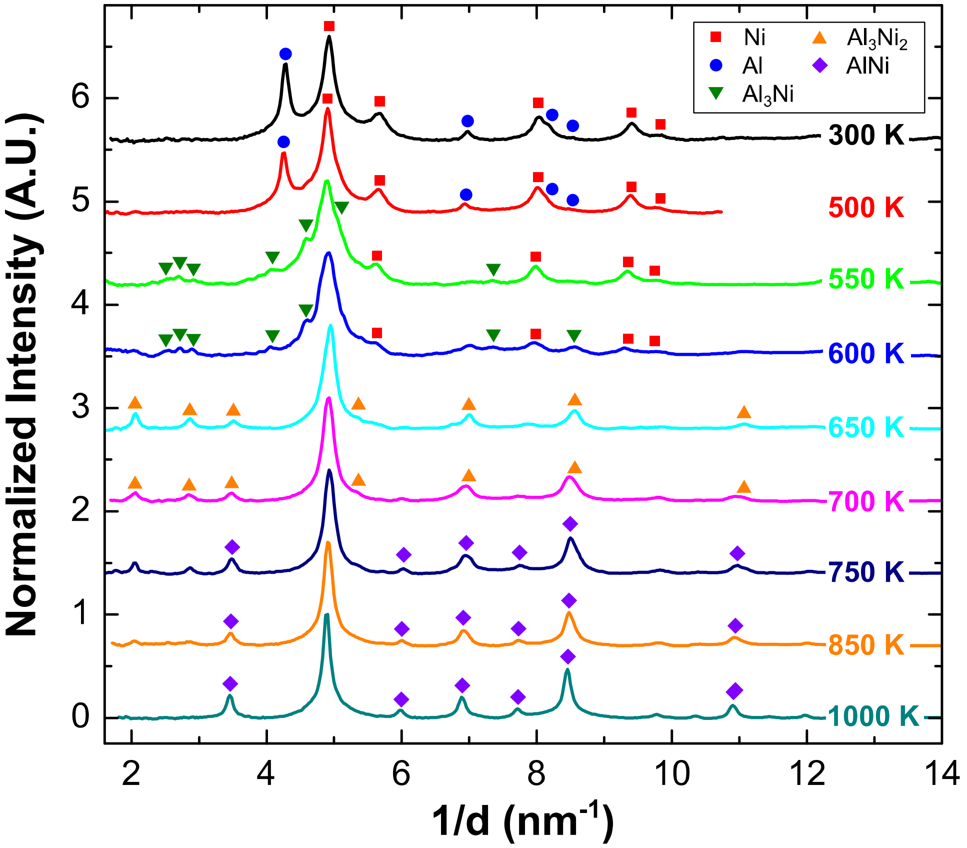

Figure 3.4 Selected-area electron diffraction patterns obtained by heating 1Al:1Ni samples at 40 K/min and quenching at the temperatures shown.

One thing that might be immediately apparent is the marked improvement in diffraction pattern signal-to-noise over what was presented in Fig. 3.3. This highlights some of the challenges inherent in using the Dynamic TEM and will be discussed in more detail in Appendix B. Reading directly from the indexed peaks, we observe the phase transformation sequence that is expected from DSC, i.e. Eq. (3.1). The transformation to B2 AlNi is nearly complete by 850 K and finished by 1000 K. This also matches the range of temperatures at which this phase is expected to be fully formed in slow heating experiments (see, e.g. [17]). Thus we can say with reasonable confidence that sample size does not play a major role in determining the phase sequence, and that as hoped the reaction of a single bilayer on the nanocalorimeter is more or less identical to the reaction that occurs simultaneously at hundreds or thousands of interfaces in a multilayer.

3.7 Appendix B: Investigation of 1:1 Al:Ni at a Higher Heating Rate

The work presented in the main part of this chapter was only one of several heating rates that were tested in the first round of DTEM experiments (August 2012). The original dataset consisted of two different sample thicknesses at two heating rates each: 100 nm Al/Ni at 715 K/s (presented above) and 1800 K/s, and 50 nm Al/Ni at 2500 K/s and 40,000 K/s. The 50 nm data was almost immediately discarded because weak diffraction from the thinner samples made the already challenging analysis of DTEM diffraction patterns virtually impossible. However, both of the 100 nm datasets yielded passable diffraction and (as we'll see) an interesting contrast in calorimeter signal, and were developed in tandem for more than a year (a draft of the paper discussing both experiments side-by-side appears as late as October of 2013). I believe the 1800 K/s experiment was ultimately scrapped because questions arose about whether the results were being distorted by the fact that the samples were in a sense under-heated (more on this below). The quality of diffraction patterns from the 1800 K/s set of experiments was also lower than those from the 715 K/s set which made side-by-side comparison a bit painful. As a consequence, the decision was made to write up the results using only the 715 K/s data (1 out of the 4 original experiments) resulting in the clean but relatively un-insightful study presented above.

Before this, a significant amount of effort was expended in performing various follow-on experiments aimed at explaining the behavior in 1800 K/s samples. Examination of these results (if we accept the original 1800 K/s data as accurate) can shed light on the results already presented and maybe even lead to slightly different conclusions about what was observed at 715 K/s. In the sections below, I begin by presenting the original (unpublished) data from *in situ* nanocalorimetry on 1:1 Al:Ni heated at 1800 K/s. We then explore the idea of quenching nanocalorimeter samples, describe the methods for making cross-sectional samples, examine the results of cross-sectional analytical TEM, and present some possible conclusions.

3.7.1 In Situ Nanocalorimetry

The sample fabrication and experimental methods used to obtain these results are identical to those presented above. Again, DTEM diffraction patterns were captured at four different times during the experiment. Combined with before and after patterns, this yielded a total of six diffraction patterns describing the evolution of structure in the sample. The nanocalorimetry data for a representative sample heated at 1800 K/s is shown in Fig. 3.5. The contrast between the reaction power signal presented here and that shown in Fig. 3.2 should be obvious – at the lower heating rate we could distinguish three exothermic peaks. Here, we see only two. This result is consistent across all samples heated at 1800 K/s. It also worth pointing out the reason why this data was ultimately excluded from the submitted paper – the temperature versus time traces at the top show that the heating program used for these samples "turned off" too early. The baseline temperature trace flattens off while the reaction is still occurring. Contrast this with Fig. 3.2 where heating continues past the end of the reaction. Without this we cannot be certain that we've captured the entire reaction.

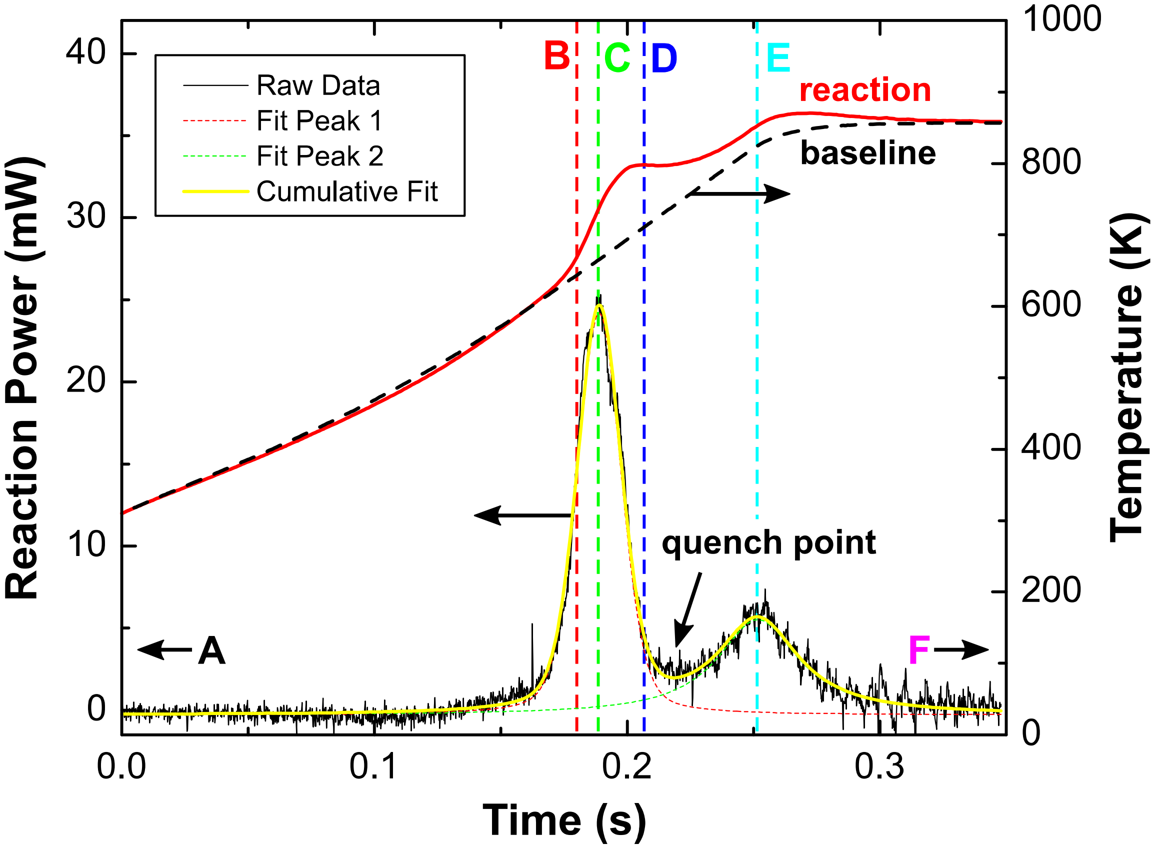

Figure 3.5 Representative nanocalorimetry data for a 100 nm Al/Ni bilayer heated at 1800 K/s. The upper traces are temperature (read on the right-hand axis) and the lower traces are reaction power (read on the left-hand axis). The dashed lines correspond to the diffraction patterns in Fig. 3.6.

If we accept the nanocalorimetry data as accurate, we might ask why at 1800 K/s the reaction occurs in two peaks while at 715 K/s it occurs in three. We start by consulting the DTEM diffraction data as shown in Fig. 3.6. Here, we see nothing that immediately appears different from the data in Fig. 3.3. The signals are very weak (even weaker than what was presented above), but you can argue that we still see all three intermetallic phases. After the first big exotherm (pattern D) we appear to have mainly Al_3Ni + Ni. During the second (pattern E), we can possibly argue for the presence of Al_3Ni_2. However, in the final diffraction pattern (F) we appear to have AlNi or a mixture of AlNi and Al_3Ni_2. Thus, we tentatively conclude that at 1800 K/s the phase transformation sequence is un-altered, but for some reason proceeds in two exothermic peaks rather than three.

The results above are presented with strong reservations. Practically it is almost impossible to index any of patterns C – F without introducing some amount of bias based on the sequence we believe to be occurring. In particular, AlNi and Al_3Ni_2 are extremely difficult to distinguish in low quality diffraction patterns like these. To do so we really need a strong Al_3Ni_2 (100) peak at 2.86 nm^{-1} and/or strong AlNi (111) and (210) (superlattice) peaks at 6.00 nm^{-1} and 7.75 nm^{-1}. Neither of these is the case for our data, and so it is difficult to say more about the final state than that we have AlNi, Al_3Ni_2, or both.[a]

---

[a] This dilemma can to some extent be resolved by capturing diffraction patterns in conventional mode before and after the experiment. The higher quality diffraction patterns provide a reference point for the interpretation of the more challenging pulsed diffraction patterns. Unfortunately, this procedure was not in place when these experiments were performed. However, it was implemented later – for an example see Fig. 5.6.

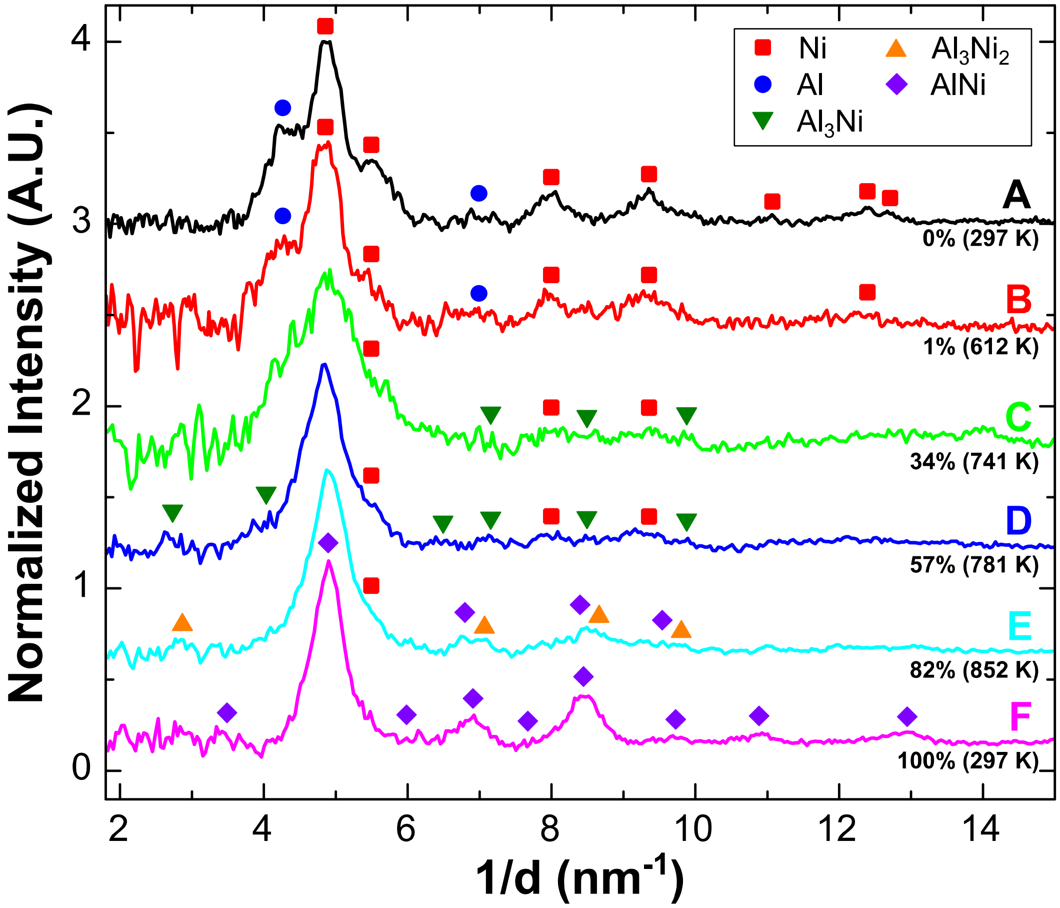

Figure 3.6 Time-resolved electron diffraction patterns captured during the reaction of a 100 nm Al/Ni bilayer at 1800 K/s. The letters correspond to the times indicated in Fig. 3.5. Clearly identifiable peaks are indexed. Also labeled for each pattern are the percentage of heat released (as a fraction of the theoretical enthalpy of formation) and the temperature when the pattern was captured.

3.7.2 Quenching

Although *in situ* nanocalorimetry was conceived primarily to avoid quenching or to study reactions that could not be quenched, quenching is possible at least at moderate heating rates. As always, such data must be reported with the proviso that the sample *may* continue evolving during cooling, although the data below show no evidence of this.

Before we realized just how weak the signals from the DTEM were and optimized our procedure for background subtraction, one of the original ideas considered to explain the DTEM diffraction data was that the rapid heating rate was causing an amorphous phase to form. This would have been supported, for example, by pattern D in Fig. 3.6 or pattern C in Fig. 3.3, which to the untrained eye show Ni and not much else. Quenching was proposed as a way to test for an amorphous phase by applying conventional TEM which gives much clearer diffraction patterns. For the 1800 K/s sample set, the obvious point of interest was between the two exothermic peaks as indicated in Fig. 3.5. To test whether quenching was feasible, we heated a sample to this point, quenched it (by removing all power so that it cooled as quickly as possible), and then heated it a second time to the final temperature. In Fig. 3.7, we show the results of this test. As can be seen, the quench appears successful insofar as the heat from the second exotherm is not released until the sample is reheated past the original quench temperature.

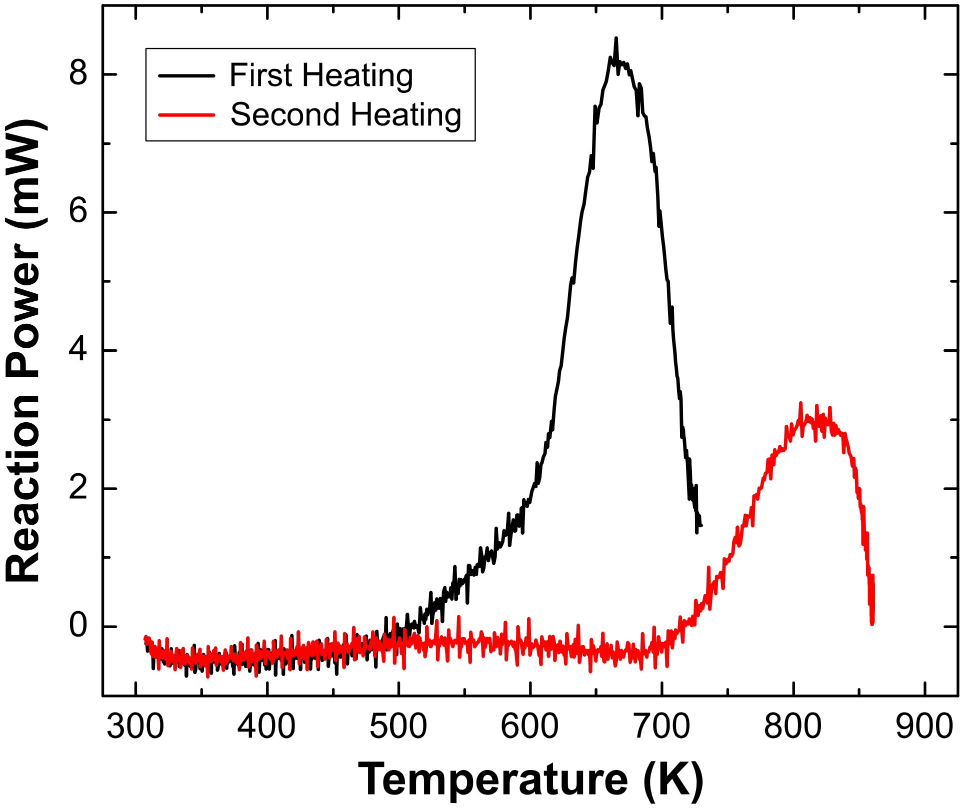

Figure 3.7 Reaction power versus temperature traces testing quenching at 1800 K/s. In the first (black), the reaction was quenched after the first exotherm. In the second (red), the sample is heated past the initial quench point. The release of additional heat in the second exotherm suggests a successful quench.

Having established the feasibility of quenching, samples quenched at this point were examined in the LLNL DTEM in conventional mode, and later in a microscope at JHU (FEI Tecnai-12). It is illustrative to compare the results from both instruments as well as the original DTEM data. This is done in Fig. 3.8. The data show clearly that even in conventional mode the LLNL DTEM produces lower-quality diffraction patterns than a typical conventional TEM. This is likely due to all of the modifications that have been made to that instrument to optimize it for pulsed imaging use [24]. Assessing the lowermost pattern (captured at JHU), we see clearly that the phases present are Al_3Ni and Ni. However, looking at the other two patterns it is easy to see how this signature might be missed, especially if one wasn't looking for it. In any case, these results indicate that the state of the sample after the first large exotherm is predominantly Al_3Ni, the same as we observe under slow heating and at 715 K/s. What's interesting, then, is that at 1800 K/s the transformation to the final phase occurs in one additional exotherm rather than two. At this point we can pose two possible explanations: (1) Al_3Ni_2 is being suppressed, or (2) its formation is occurring concurrent with that of AlNi. To shed more light on this, in the next section we describe the results obtained from a cross-section of a sample that was quenched in this state.

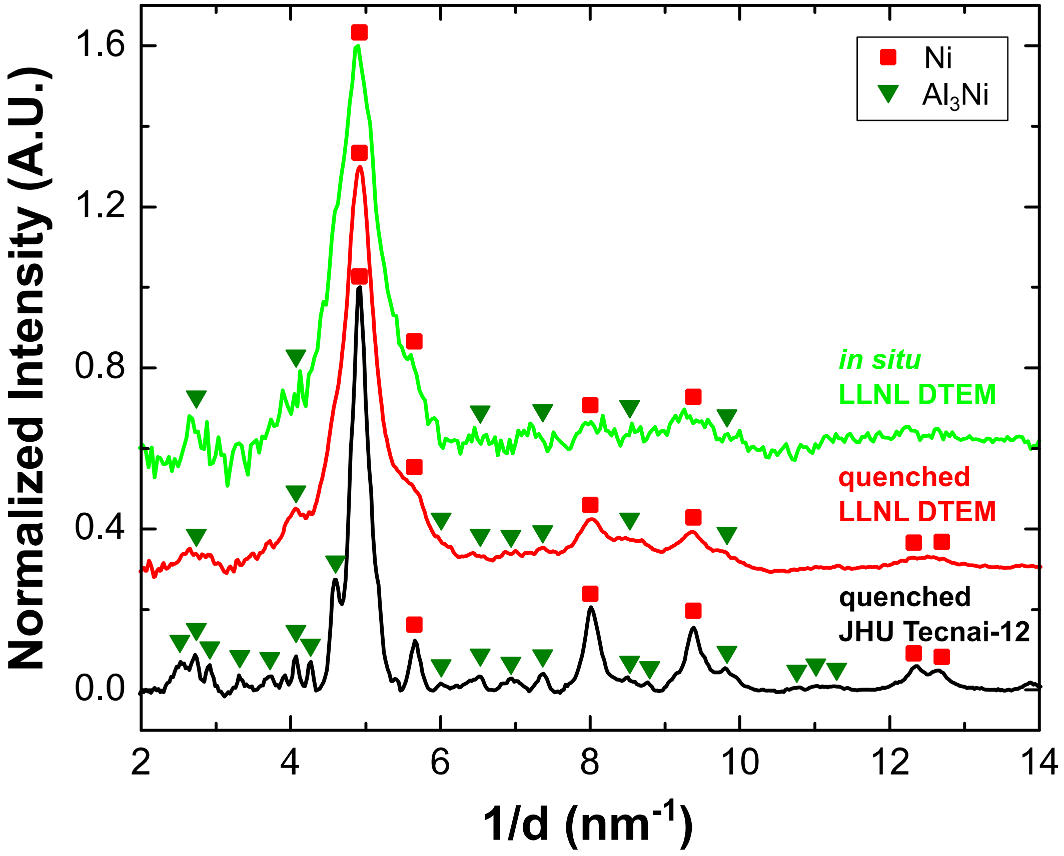

Figure 3.8 Selected-area electron diffraction patterns captured for the same state in the 1800 K/s reaction using three different methods. The *in situ* diffraction pattern is identical to Pattern D in Fig. 3.6. The quenched patterns were obtained using the quenching procedure as outlined. Peaks for Al_3Ni and Ni are labeled. Note the reduction in our ability to resolve the Al_3Ni peaks in particular as we move toward the *in situ* experiment.

3.7.3 Cross-Sectional Study

After quenching into the position between the two exotherms in Fig. 3.5, a cross-section was obtained from a sample by focused-ion-beam (FIB) milling.[a] The sample was on a fragile 150-nm-thick silicon nitride membrane, so some support for the membrane was required before FIB milling could be formed. In addition, the support needed to be electrically conductive to avoid charging during imaging and milling. For the results

---

[a] Our first efforts toward cross-sectional samples actually involved making them by microtome (a technique that uses very sharp knives to make very thin microscope samples, usually of biological specimens). In this procedure the sensor was mounted in epoxy, the silicon support was cut away, and then a microtome was used to cut slices of the Pt + SiN_x + sample. Although significant time was invested, the approach was ultimately scrapped because the samples produced were too damaged to be usable.

shown in Fig. 3.9, we placed several drops of carbon paint (a common tool in electron microscopy) on the backside of the nanocalorimeter sensor to fill the well behind the membrane. After allowing several days to evaporate the solvent, this produced a porous carbon film that was sufficiently structural to support the specimen during milling.

The two primary stages of the milling are shown in Fig. 3.9. First, a coating of Pt is deposited over the entire working area as a protective layer. Then, the area is thinned down to a thickness of ≈ 1 μm by milling at an angle from both sides. The situation after these steps are complete is shown in 3.9(a). After this, a micromanipulator is moved next to the sample and "glued" by depositing more Pt between sample and tip. Then, the ion beam is used to cut away the remaining support on either side and below the sample allowing it to be lifted free. After attaching the sample to a TEM half-grid, additional thinning is performed at progressively lower beam energies to produce a sample that is 50 nm – 100 nm thick as shown in Fig. 3.9(b).

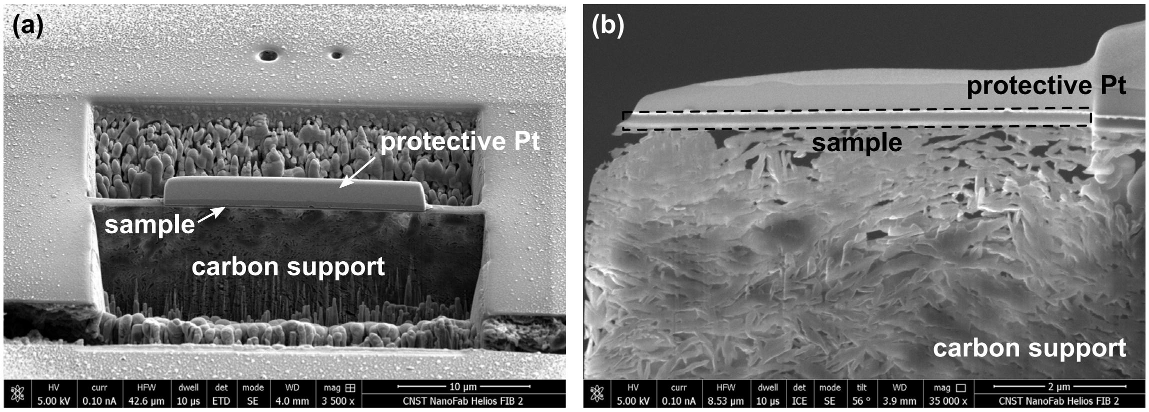

Figure 3.9 These images illustrate the process of producing a FIB cross-sectional TEM specimen from a nanocalorimetry sample. In (a), the region of interest is protected with Pt and then the surrounding area is removed in preparation for removal. After removal, the sample is mounted on a TEM half-grid and thinned to electron transparency as shown in (b). The upper limit of the sample is the Pt heater, visible as a thin bright white line. The lower limit is the start of the carbon support.

This sample was placed in an analytical TEM (Phillips CM-300) for detailed analysis. Among the diagnostics performed were STEM composition mapping using energy-dispersive spectroscopy (EDS), selected-area electron diffraction, general imaging, and high-resolution (phase contrast) imaging. Fig. 3.10 shows the results from compositional mapping. They clearly indicate that we are in an intermediate state since there is some interpenetration of Al and Ni but the individual layering is still distinct. The composition profile suggests that diffusion of Ni into Al is more extensive than vice versa (the maximum composition of Al in the Al layers is lower) and we see schematic evidence for the presence of Al_3Ni in this region since it shows ≈ 75 % Al and ≈ 25% Ni.

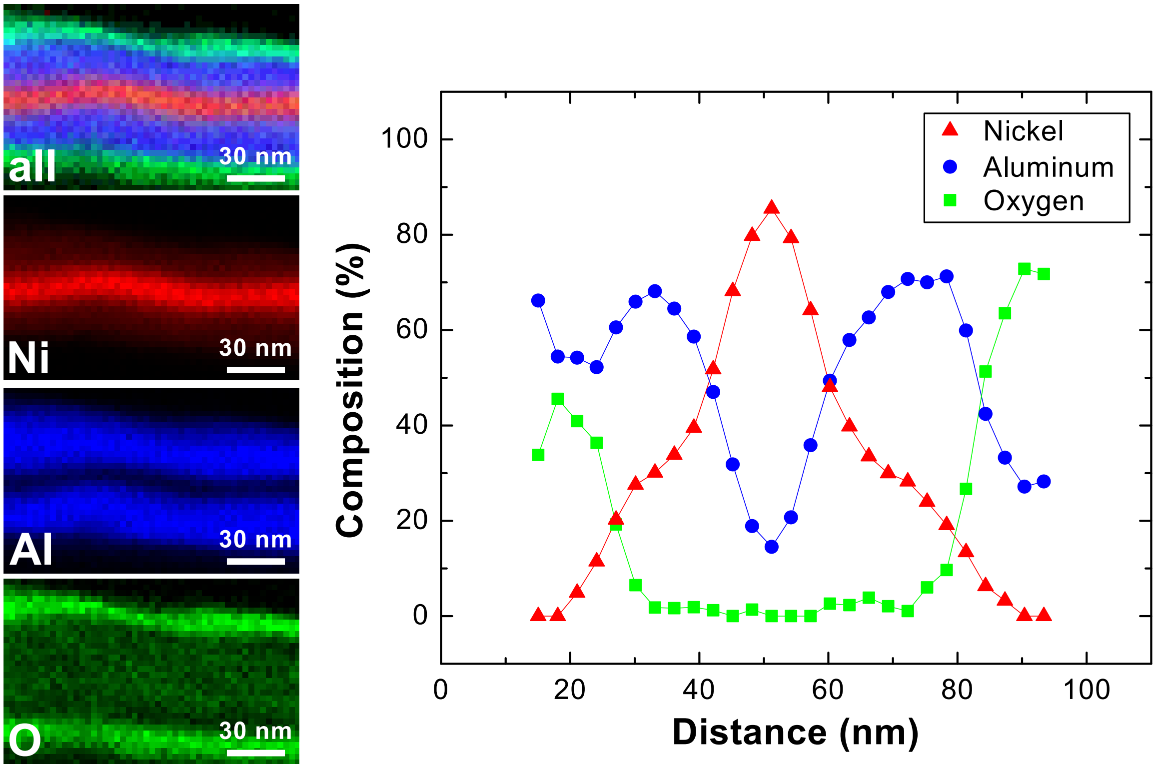

Figure 3.10 Results of EDS compositional mapping of nanocalorimeter cross-section. At left, elemental and composite images of the chemical distribution of the sample. Oxygen at the outside indicates the position of the Al_2O_3 passivation layers. At right, a 1D composition profile from a vertical section through the data at left.

The result of high-resolution TEM (HRTEM) on a region around the central Ni layer is shown in Fig. 3.11. In this image, the periodic contrast visible in some areas is from phase contrast of actual columns of atoms. Fast-Fourier-transform (FFT) analysis of these regions can in some cases enable structural identification (the FFT yields a pattern that can be analyzed in the same way as a single-crystal diffraction pattern). Several such regions are labeled Fig. 3.11. The central region of darker contrast is Ni, and the outer region is Al_3Ni. This matches our diffraction analysis (Fig. 3.8), which said that Ni and Al_3Ni were the main phases present after quenching. However, we also see grains of both AlNi *and* Al_3Ni_2 in the region between pure Ni and Al_3Ni. This indicates that, although they fall below the threshold of detection in the diffraction patterns, both AlNi and Al_3Ni_2 are present in small volumes at the quench point.

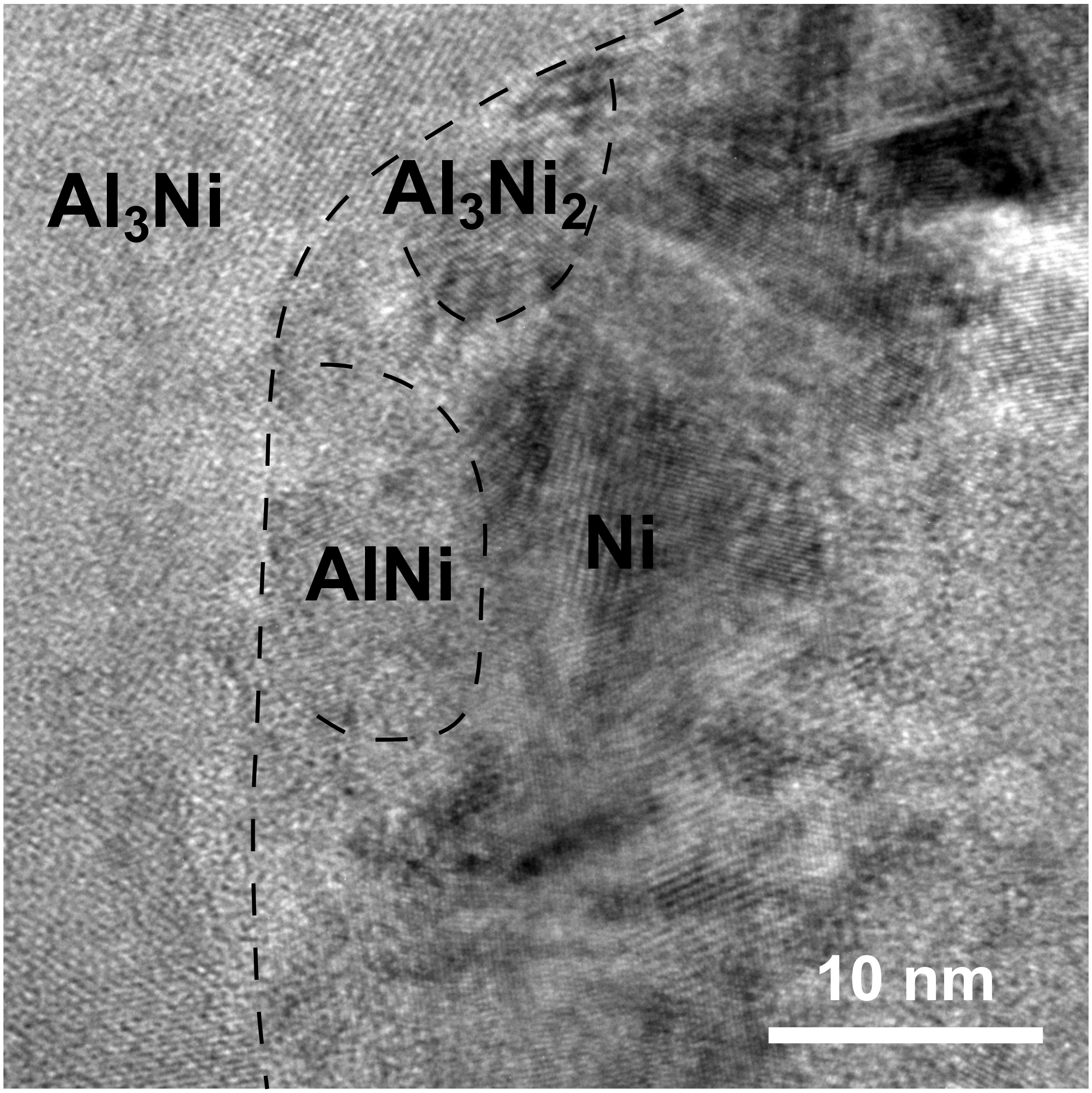

Figure 3.11 High-resolution TEM image of the central region of a quenched cross-sectional sample. FFT analysis of select regions leads to the tentative phase identifications shown.

3.7.4 Discussion

The key difference between samples heated at 715 K/s and samples heated at 1800 K/s is that the former react in three exothermic peaks (Fig. 3.2) while the latter react in two (Fig. 3.5). *In situ* DTEM (Fig. 3.6), quenching (Fig. 3.8), and compositional analysis (Fig. 3.10) all point toward the first peak corresponding to the formation of Al_3Ni. HRTEM of the microstructure after the first exotherm (Fig. 3.11) also supports this, showing large volume fractions of Al_3Ni and Ni. However, it also offers us a clue because in those results we see small grains of both AlNi and Al_3Ni_2. We might not be surprised to see *one* of these since the nucleation of the next phase is likely occurring at the tail end of the previous exotherm. However, it is surprising that we observe them both simultaneously because based on the general "rules" for thin film diffusion couples [7,10] only one phase should nucleate and grow at a time. Here, we are seeing simultaneous nucleation of AlNi and Al_3Ni_2 perhaps because the nucleation of Al_3Ni_2 is delayed by the higher temperatures and steeper concentration gradients associated with the higher heating rate. AlNi is less likely to be affected by these factors because it has a higher melting point and a broader range of stable compositions.

The presence of both phases together suggests that the explanation for the single exotherm in Fig. 3.5 is that both phases nucleate and grow side-by-side. The free energy benefits associated with forming these phases from Al_3Ni + Ni are fairly similar (19 kJ/mol-atom for Al_3Ni_2 and 21 kJ/mol-atom for AlNi [17]) so if they are both able to nucleate it is likely that they grow simultaneously and that transformation to single-phase AlNi occurs only after extensive compositional homogenization can occur at high temperature. If both phases are present that would help to explain the difficulty that we had in identifying the appropriate phases to assign in Patterns E and F in Fig. 3.6.

Turning to the original published results for 715 K/s, this provides an intriguing alternative explanation for the observation in Sec. 3.4 that Al_3Ni_2 forms in both the second and third exotherms and is still present in the final reaction products. If we allow side-by-side growth of both Al_3Ni_2 and AlNi then we do not necessarily need to invoke a two-stage growth model for Al_3Ni_2. Rather, we would argue that the second peak corresponds to the *start* of Al_3Ni_2 growth and the third peak to the *start* of AlNi growth, but that both phases grow simultaneously (i.e. side-by-side) during the third peak. The fact that the heat release in the second peak is too small to correspond to the complete formation of Al_3Ni_2 would then be due to the fact that Al_3Ni_2 does not grow to encompass the entire sample before AlNi nucleates, a logical intermediate stage between DSC experiments (where Al_3Ni_2 growth is completely distinct from AlNi growth) and 1800 K/s (where no distinct Al_3Ni_2 growth peak is observed).

The complete interpretation (from DSC to 1800 K/s) would be as follows: At DSC heating rates, nucleation of Al_3Ni_2 occurs well before AlNi and we observe a distinct exothermic peak corresponding to its growth. At slightly higher heating rates (715 K/s) the nucleation of Al_3Ni_2 is delayed more than that of AlNi for the reasons noted above, so we observe a distinct nucleation event but Al_3Ni_2 does not grow completely before AlNi nucleates. Subsequently they grow simultaneously. Finally, at 1800 K/s the nucleation of Al_3Ni_2 is sufficiently delayed that it is temporally indistinct from that of AlNi, and we get a single growth peak corresponding to both phases.

3.7.5 Conclusion

The conclusions above would require additional experiments to verify and the nanocalorimetry experiments on which they are based raise some questions as to their validity. Nevertheless, if the experimental data are valid they present an intriguing alternative explanation for the original published data, namely that at 715 K/s we are capturing an intermediate state where Al_3Ni_2 nucleation is delayed relative to the slow-heating case, but still sufficiently distinct to yield a separate exotherm. While this is not evidence for phase *suppression*, the effect observed might be a pre-cursor to that. If this analysis is accurate, it is interesting that the effect is observed for the second phase to form (Al_3Ni_2) rather than the first (Al_3Ni). The explanation for this most likely resides in the fact that the driving force for Al_3Ni formation is larger and that there are no other phases (aside from the metastable Al_9Ni_2 that has only been observed in sputtered samples [15–17,38,39]) competing to form in the compositional range at which Al_3Ni is stable.

References for Chapter 3

[1] F.M. D'Heurle, Nucleation of a new phase from the interaction of two adjacent phases: Some silicides, J. Mater. Res. 3 (1988) 167–195.

[2] R. Rosenberg, D.C. Edelstein, C.-K. Hu, K.P. Rodbell, Copper Metallization for High Performance Silicon Technology, Annu. Rev. Mater. Sci. 30 (2000) 229–262.

[3] Y. Fu, H. Du, W. Huang, S. Zhang, M. Hu, TiNi-based thin films in MEMS applications: a review, Sensors Actuators A Phys. 112 (2004) 395–408.

[4] Y. Shacham-Diamand, Y. Sverdlov, Electrochemically deposited thin film alloys for ULSI and MEMS applications, Microelectron. Eng. 50 (2000) 525–531.

[5] M.J. Pomeroy, Coatings for gas turbine materials and long term stability issues, Mater. Des. 26 (2005) 223–231.

[6] K.F. Kelton, A.L. Greer, Nucleation in Condensed Matter: Applications in Materials and Biology, Elsevier, 2010.

[7] U. Gösele, K.N. Tu, Growth kinetics of planar binary diffusion couples: Thin-film case" versus bulk cases", J. Appl. Phys. 53 (1982) 3252–3260.

[8] F. Hodaj, A.M. Gusak, Suppression of intermediate phase nucleation in binary couples with metastable solubility, Acta Mater. 52 (2004) 4305–4315.

[9] R.J. Highmore, Nucleation issues in solid state amorphization, Philos. Mag. Part B. 62 (1990) 455–467.

[10] E.G. Colgan, A review of thin-film aluminide formation, Mater. Sci. Reports. 5 (1990) 1–44.

[11] E. Ma, C.V. Thompson, L.A. Clevenger, K.N. Tu, Self-propagating explosive reactions in Al/Ni multilayer thin films, Appl. Phys. Lett. 57 (1990) 1262.

[12] J. Wang, E. Besnoin, A. Duckham, S.J. Spey, M.E. Reiss, O.M. Knio, et al., Room-temperature soldering with nanostructured foils, Appl. Phys. Lett. 83 (2003) 3987.

[13] X. Qiu, J. Wang, Bonding silicon wafers with reactive multilayer foils, Sensors Actuators A Phys. 141 (2008) 476–481.

[14] E. Ma, C.V. Thompson, L.A. Clevenger, Nucleation and growth during reactions in multilayer Al/Ni films: The early stage of Al3Ni formation, J. Appl. Phys. 69 (1991) 2211.

[15] A.S. Edelstein, R.K. Everett, G.Y. Richardson, S.B. Qadri, E.I. Altman, J.C. Foley, et al., Intermetallic phase formation during annealing of Al/Ni multilayers, J. Appl. Phys. 76 (1994) 7850.

[16] C. Michaelsen, G. Lucadamo, K. Barmak, The early stages of solid-state reactions in Ni/Al multilayer films, J. Appl. Phys. 80 (1996) 6689.

[17] K.J. Blobaum, D. Van Heerden, A.J. Gavens, T.P. Weihs, Al/Ni formation reactions: characterization of the metastable Al9Ni2 phase and analysis of its formation, Acta Mater. 51 (2003) 3871–3884.

[18] J.C. Trenkle, L.J. Koerner, M.W. Tate, N. Walker, S.M. Gruner, T.P. Weihs, et al., Time-resolved x-ray microdiffraction studies of phase transformations during rapidly propagating reactions in Al/Ni and Zr/Ni multilayer foils, J. Appl. Phys. 107 (2010) 113511.

[19] K. Fadenberger, I.E. Gunduz, C. Tsotsos, M. Kokonou, S. Gravani, S. Brandstetter, et al., In situ observation of rapid reactions in nanoscale Ni–Al multilayer foils using synchrotron radiation, Appl. Phys. Lett. 97 (2010) 144101.

[20] J.S. Kim, T. LaGrange, B.W. Reed, R. Knepper, T.P. Weihs, N.D. Browning, et al., Direct characterization of phase transformations and morphologies in moving reaction zones in Al/Ni nanolaminates using dynamic transmission electron microscopy, Acta Mater. 59 (2011) 3571–3580.

[21] T.S. Dyer, Z.A. Munir, The synthesis of nickel aluminides by multilayer self-propagating combustion, Metall. Mater. Trans. B. 26 (1995) 603–610.

[22] E.A. Olson, M.Y. Efremov, L.H. Allen, The design and operation of a MEMS differential scanning nanocalorimeter for high-speed heat capacity measurements of ultrathin films, J. Microelectromechanical Syst. 12 (2003) 355–364.

[23] M.D. Grapes, T. LaGrange, L.H. Friedman, B.W. Reed, G.H. Campbell, T.P. Weihs, et al., Combining nanocalorimetry and dynamic transmission electron microscopy for in situ characterization of materials processes under rapid heating and cooling, Rev. Sci. Instrum. 85 (2014) 084902.

[24] B.W. Reed, T. LaGrange, R.M. Shuttlesworth, D.J. Gibson, G.H. Campbell, N.D. Browning, Solving the accelerator-condenser coupling problem in a nanosecond dynamic transmission electron microscope, Rev. Sci. Instrum. 81 (2010) 053706.

[25] P. Swaminathan, B.G. Burke, A.E. Holness, B. Wilthan, L. Hanssen, T.P. Weihs, et al., Optical calibration for nanocalorimeter measurements, Thermochim. Acta. 522 (2011) 60–65.

[26] P. Swaminathan, M.D. Grapes, K. Woll, S.C. Barron, D.A. LaVan, T.P. Weihs, Studying exothermic reactions in the Ni-Al system at rapid heating rates using a nanocalorimeter, J. Appl.

Phys. 113 (2013) 143509.

[27] P. Villars, L.D. Calvert, Pearson's Handbook of Crystallographic Data for Intermetallic Phases, 2nd ed., ASM International, 1991.

[28] S.H. Fischer, M.C. Grubelich, A survey of combustible metals, thermites, and intermetallics for pyrotechnic applications, in: 32nd Jt. Propuls. Conf. Exhib., American Institute of Aeronautics and Astronautics, Reston, Virigina, 1996.

[29] F.R. de Boer, R. Boom, W.C.M. Mattens, A.R. Miedema, A.K. Niessen, Cohesion in Metals, North-Holland, 1988.

[30] K.R. Coffey, L.A. Clevenger, K. Barmak, D.A. Rudman, C.V. Thompson, Experimental evidence for nucleation during thin-film reactions, Appl. Phys. Lett. 55 (1989) 852.

[31] C. Michaelsen, K. Barmak, T.P. Weihs, Investigating the thermodynamics and kinetics of thin film reactions by differential scanning calorimetry, J. Phys. D. Appl. Phys. 30 (1997) 3167–3186.

[32] H.E. Kissinger, Reaction Kinetics in Differential Thermal Analysis, Anal. Chem. 29 (1957) 1702–1706.

[33] J.M. Gregoire, P.J. McCluskey, D. Dale, S. Ding, J. Schroers, J.J. Vlassak, Combining combinatorial nanocalorimetry and X-ray diffraction techniques to study the effects of composition and quench rate on Au–Cu–Si metallic glasses, Scr. Mater. 66 (2012) 178–181.

[34] P.J. McCluskey, J.J. Vlassak, Glass transition and crystallization of amorphous Ni–Ti–Zr thin films by combinatorial nano-calorimetry, Scr. Mater. 64 (2011) 264–267.

[35] M. Thompson, G. Galvin, J. Mayer, P. Peercy, J. Poate, D. Jacobson, et al., Melting Temperature and Explosive Crystallization of Amorphous Silicon during Pulsed Laser Irradiation, Phys. Rev. Lett. 52 (1984) 2360–2363.

[36] P. Baeri, G. Foti, J. Poate, A. Cullis, Phase Transitions in Amorphous Si Produced by Rapid Heating, Phys. Rev. Lett. 45 (1980) 2036–2039.

[37] M. Wuttig, N. Yamada, Phase-change materials for rewriteable data storage., Nat. Mater. 6 (2007) 824–32.

[38] K. Barmak, C. Michaelsen, G. Lucadamo, Reactive phase formation in sputter-deposited Ni/Al multilayer thin films, J. Mater. Res. 12 (1997) 133–146.

[39] M.H. da Silva Bassani, J.H. Perepezko, A.S. Edelstein, R.K. Everett, Initial phase evolution during interdiffusion reactions, Scr. Mater. 37 (1997) 227–232.

4. Rate-Controlling Processes in Self-Propagating Al/Ni Multilayers

4.1 Introduction

Interfacial reactions can, in principle, occur anywhere two different miscible materials are in contact. They are especially relevant in nanoscale multilayers, since these structures exhibit unusually high ratios of interfacial area to volume. In the particular case that the interfacial reaction is highly exothermic, these are termed "reactive multilayers" [1] and a phenomenon known as a self-propagating reaction can be observed where the heat released by local mixing is sufficient to heat the adjacent material and produce a self-sustaining reaction front that moves through the sample with a characteristic velocity. Practically, reactive multilayers are of interest as heat sources for bonding [2,3], thermal batteries [4], and ignitors [5,6]. Scientifically, self-propagating reactions present a unique opportunity to investigate the processes that control atomic mixing and phase formation at the extremes of concentration gradient and heating rate. Such scientific investigations feed back into practical applications by enabling improved predictions of performance over a range of operating conditions and by identifying ways that performance can be tuned for specific applications.

One of the most-studied reactive multilayer systems is Al/Ni. Al and Ni are readily available, relatively inexpensive, and have a fairly large enthalpy of reaction (1381 J/g [7]). Al/Ni multilayers have been fabricated using a range of physical vapor deposition techniques as well as by mechanical processing, and have been investigated using differential scanning calorimetry (DSC) [8,9], time-resolved x-ray diffraction [10,11], and time-resolved transmission electron microscopy [12], as well is in many theoretical studies [13–18]. The references here are only a small sampling of the available literature - the system is generally very well characterized. Nevertheless, the available data is largely restricted to two regimes of reaction: slow, low temperature reactions as observed in DSC or the early stages of ignition experiments, and rapid, high temperature reactions as characterized using *in situ* techniques. This is because it is possible to heat slowly and prevent ignition, but very difficult to suppress the reaction rate once ignition has occurred. Unfortunately, the available data suggest that the regime between these two extremes may be where the most interesting behavior occurs.

The discrepancies between the phase transformation sequences for slow-heating and rapid-heating experiments have been described in detail previously [11]. In brief, slow-heating experiments such as differential scanning calorimetry reveal a progression of Al-rich phases with increasing Ni concentration

$$\mathrm{Al} + \mathrm{Ni} \rightarrow (\mathrm{Al_9Ni_2} + \mathrm{Ni}) \rightarrow \mathrm{Al_3Ni} + \mathrm{Ni} \rightarrow \mathrm{Al_3Ni_2} + \mathrm{Ni} \rightarrow \mathrm{AlNi} \tag{4.1}$$

where the step listed in parentheses has only been observed in multilayers that were deposited by sputtering or ion-beam deposition [19]. In contrast, rapid-heating experiments show a phase sequence devoid of intermediate intermetallic phases:

$$\mathrm{Al} + \mathrm{Ni} \rightarrow \text{Al-rich liquid} + \mathrm{Ni} \rightarrow \mathrm{AlNi} \tag{4.2}$$

At the heart of this work is an interest in identifying what behavior might occur between these two extremes that can help to explain this change.

Recently, many relevant results pertaining to this question have come from researchers using molecular dynamics (MD) simulations to study the interfacial reaction in Al/Ni laminates. Studies using constant-pressure adiabatic (NPH) simulations [13–15] have observed a mechanism similar to that represented by Eq. (4.2), where the aluminum melts early in the reaction and no intermediate intermetallic phases are observed. Xu *et al.* conducted isothermal (NPT) MD simulations of the Al/Ni interfacial reaction at multiple temperatures ranging from 2000 K (near the adiabatic flame temperature of 1:1 Al/Ni) down to 1300 K, and observed that different mechanisms controlled the mixing rate depending on the simulation temperature [16]. Isothermal simulations at even lower temperatures have explored the mechanisms driving mixing and phase formation in detail [17,18].

These results are interesting but need experimental validation, especially because the potentials used [20–22] have struggled to reproduce Al-rich intermetallic phases that might otherwise be expected. This is challenging because experimentalists lack the level of control over reaction conditions that is so easily achieved in a computer model. The main experimental efforts have used quenching of self-propagating reactions [17,18,23], but ideally one would like to be able to vary the reaction temperature without quenching or altering the reacting chemistry, stoichiometry, or initial intermixing. Such a controlled experiment would allow us to evaluate the effects of temperature independent of any other change in the system. In this work, we introduce a new class of reactive materials intended to satisfy these requirements. Dubbed "inert-mediated reactive multilayers" (IMRMs), these materials incorporate an inert material to suppress the heating rate and maximum temperature without altering the chemistry of the reaction. The adiabatic flame temperature of an IMRM can be tuned continuously over a wide range (in this work we demonstrate temperature reductions as large as ~650 K) simply by varying the ratio of reactive material to inert material in the system. By using flame speed as a macroscopic indicator of the underlying interfacial reaction kinetics, this new class of materials can provide needed experimental support for recent molecular dynamics results.

In the following, we begin by laying out the basic design principles for IMRMs in general and for Al/Ni in particular. We then present the results obtained, assess them in light of the design requirements, and apply an analytical model for flame speed in reactive laminates to give scientific significance to the trends observed. We conclude by using these results to construct a picture of potential reaction mechanisms over the temperature range 1250 – 1950 K, supported by previous experimental and theoretical results.

4.2 Design of Inert-Mediated Reactive Multilayers

A schematic diagram of the IMRM design is shown in Fig. 4.1. It consists of alternating sections of reactive material and inert material with characteristic section thicknesses S_{RM} and S_{IM}. Multilayer sections possess a second level of periodicity characterized by the "bilayer spacing". A bilayer is the characteristic repeat unit of a two-component multilayer and consists of one layer of each material. The bilayer spacing is the sum of these layer thicknesses. In designing the IMRMs for this work, the principle design considerations were (1) what materials to use in each section, (2) how those materials should be arranged within the section, and (3) how thick the sections should be.

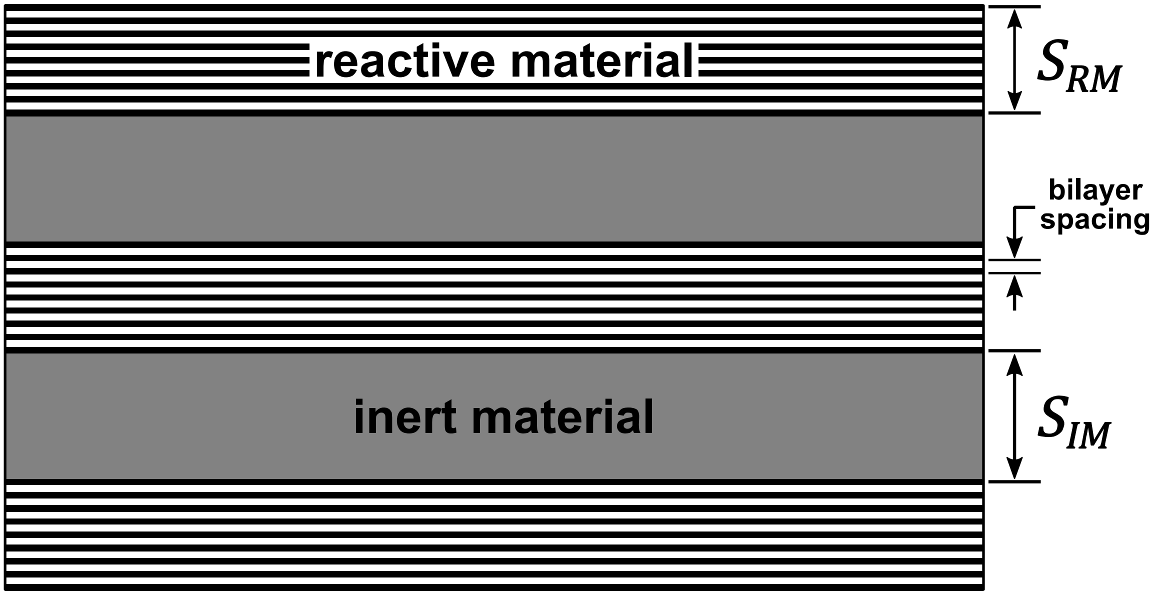

Figure 4.1 A cross-sectional schematic of the generic design for an inert-mediated reactive multilayer (IMRM) showing alternating sections of reactive material (dark/light banded) and inert material (gray), with their corresponding section thicknesses S_{RM} and S_{IM}. The multilayer bilayer spacing is also labeled. Note that the inert material can be a multilayer (as in our work) but it does not have to be and so is depicted ambiguously in the generic design.

4.2.1 Section Composition

The sections below outline the general considerations to be made when selecting materials for the reactive and inert sections, and how those decisions were made for the samples fabricated in this work.

4.2.1.1 Reactive Material

The main requirements for the reactive component of an IMRM are a composition that is of scientific interest and a small bilayer spacing that will yield a high propagation velocity. The latter requirement is motivated by the expectation that quickly propagating sections will be able to accommodate the largest temperature suppression before quenching. The Al/Ni system is extensively well characterized and presents outstanding scientific questions of interest. Consulting a chart of flame speed versus bilayer spacing for 1:1 Al:Ni (e.g., [24]), a bilayer spacing of 23 nm gives a velocity very close to the maximum (~13 m/s). Consequently, the reactive component in this work was Al/Ni reactive multilayers with a 23 nm bilayer and a 1:1 molar ratio (approximately 3Al:2Ni by volume).

4.2.1.2 Inert Material

The ideal inert material undergoes no chemical reactions upon heating that would add or subtract from the energy output of the sample, and does not chemically mix with the material in the reactive sections so as to alter the products formed. It also has high volumetric heat capacity and high thermal conductivity to maximize the temperature reduction per volume and promote thermal uniformity across the sample. These requirements suggest a metallic inert material, which would have the added benefit of being easily incorporated into the physical vapor deposition processes that are typically used for multilayer fabrication. Finally, to conduct the activation energy analysis described in Sec. 5.1 it is helpful if all samples produced have the same net thermal diffusivity in the propagation direction. The easiest way to achieve this is by matching the in-plane thermal conductivity of the inert material to the in-plane thermal conductivity of the chosen reactive material. In general this is impossible to achieve using any single metallic element. Instead, an alloy or multilayer structure of multiple metals should be used where it is possible to tune the ratio of components as needed to adjust the thermal diffusivity.

We selected a multilayer structure of Cu and Ni as the inert material. Cu and Ni form a nearly ideal solution [25] so their enthalpy of mixing is negligible, and since Ni is already a component of the reactive material it presents no contamination concerns. Cu does have the potential to react with Al to form a variety of intermetallic compounds

[26], but this risk is easily minimized by ensuring that Ni layers are always in contact at the interface between reactive and inert sections and minimizing the number of such interfaces. Cu has a very high thermal conductivity (4.0 W $\mathrm{cm^{-1}\ K^{-1}}$) while that of Ni is quite low (0.189 W $\mathrm{cm^{-1}\ K^{-1}}$), so an appropriate mixture of the two can match the thermal diffusivity of a range of reactive material compositions. The in-plane thermal conductivity of 1:1 Al:Ni multilayers is approximately 0.456 $\mathrm{cm^2\ s^{-1}}$, calculated using bulk, room-temperature values for pure Ni and Al. This can be matched using a mixture of 2Cu:3Ni by volume (an atomic ratio of 0.38Cu:0.62Ni). A multilayer was chosen as opposed to an alloy in order to more effectively control stress in the deposited structures. For example, after observing undesirably large residual stresses in IMRM 5 which had 28-nm-bilayer inert multilayers we were able to reduce residual stress significantly by increasing the bilayer spacing in the inert sections for the remaining samples.

4.2.2 Section Thicknesses

The section thicknesses are identified as S_{RM} and S_{IM} in Fig. 4.1. We identified two main concerns in deciding how large they should be:

1. Avoiding chemical contamination of the reactive material by the inert material.
2. Maintaining approximately uniform temperature through the thickness of the sample during reaction.

Chemical contamination is undesirable because it defeats the stated purpose of the IMRM approach: to change nothing about the reaction except the temperature at which it occurs. Contamination is best prevented by selecting inert materials that have relatively low reaction enthalpy with the reactive materials and then arranging the inert and reactive material so as to minimize their opportunity to interact. This is favored by thicker sections that minimize the number of interfaces between the inert and reactive materials in the structure.

Thermal uniformity is important in order to avoid reaction decoupling, a phenomenon observed in previous work that considered "dual-bilayer" Al/Ni multilayers [24]. Dual-bilayer samples are reactive multilayers that feature two different bilayer spacings, one large and one small, arranged in sections with a characteristic thickness. That work found that if the thicknesses of the small bilayer (rapidly reacting) and large bilayer (slowly reacting) sections were small, the reaction in the two sections would couple and propagate with a velocity corresponding to the volume average bilayer spacing of the composite. However, if the section thicknesses became too large the reactions would decouple and each section would propagate at its natural speed. This argues for generally smaller sections.

In order to satisfy both requirements a balance between large and small section thickness is needed. We took the approach of first calculating a reasonable value for the maximum or "critical" section thickness based on thermal uniformity considerations, and then using the largest section thicknesses possible within that limit.

4.2.2.1 Derivation of Critical Section Thickness

The temperature will always vary somewhat between the reactive and the inert sections because only the reactive sections generate heat. The goal here is to derive a concise expression that estimates the temperature variation between reactive and inert layers given reasonable material properties. This expression can then be used to compute a "critical section thickness" based on the maximum allowable temperature variation. To simplify the analysis we assume that the section thicknesses are equal ($S_{\mathrm{RM}} = S_{\mathrm{IM}} = L$)

and that the foil contains an infinite number of sections. This will enable a simple periodic solution. We assume that the heat capacities of inert and reactive material are equal and invariant with temperature, and finally we consider the problem in one dimension only (through the thickness of the IMRM). Fig. 4.2(a) shows the simplified picture of an IMRM based on these assumptions.

Heat flow in an adiabatic reacting system can be described by a thermal balance equation

$$\dot{T} = \alpha \nabla^2 T + \frac{\dot{Q}_{\mathrm{rxn}}}{\rho C_p} \tag{4.3}$$

where T is the temperature in one or more spatial dimensions and time, α is the thermal diffusivity, ∇^2 is the Laplace operator, $\dot{Q}_{\mathrm{rxn}}$ is the rate of heat release from the reaction, and ρC_p is the volumetric heat capacity. Writing Eq. (4.3) explicitly for the one-dimensional case,

$$\dot{T}(z,t) = \alpha_{\perp} \frac{\partial^2 T(z,t)}{\partial z^2} + \frac{\dot{Q}_{\mathrm{rxn}}(z)}{\rho C_p} \tag{4.4}$$

where $\alpha_{\perp}$ is the out-of-plane thermal diffusivity (perpendicular to the layering) and we have explicitly written $\dot{Q}_{\mathrm{rxn}}(z)$ as varying spatially because heat generation in an IMRM is heterogeneous.

The largest spatial variation in temperature will occur when the reaction rate in the reactive sections is at its highest since this represents the largest instantaneous power that must be dissipated into the inert material. We denote this power as a constant $\dot{Q}_{\mathrm{max}}$ and apply it only in the reactive sections to produce the function $\dot{Q}_{\mathrm{rxn}}(z)$ as depicted in Fig. 4.2(b). In a real sample this reaction rate is only achieved for a short time, but by applying it indefinitely we obtain a worst-case estimate of the temperature variation.

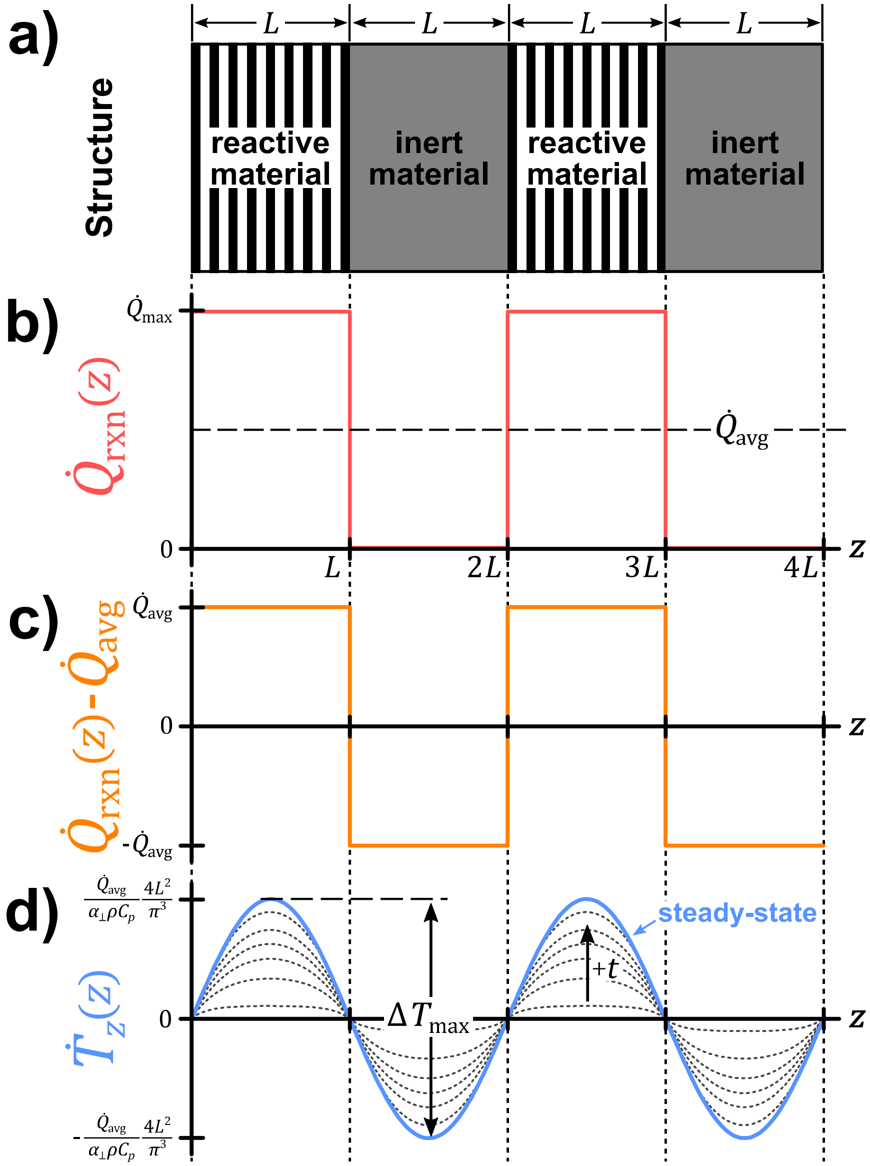

Figure 4.2 An outline of the procedure used to derive the maximum temperature difference ΔT_{max} between inert and reactive sections. To begin, we define a simplified IMRM structure (a) with uniform section thickness $S_{RM} = S_{IM} = L$. To obtain a worst-case estimate we assume that the reactive sections release heat at a constant rate $\dot{Q}_{\text{max}}$ while the inert sections release no heat at all. This makes up the spatially varying rate of heat release $\dot{Q}_{\text{rxn}}(z)$, shown in (b). Averaging the heat input over the entire sample yields the net rate of heat release $\dot{Q}_{\text{avg}} = \dot{Q}_{\text{max}}/2$, also shown in (b). Since we are concerned only in the relative temperature difference, in (c) we subtract $\dot{Q}_{\text{avg}}$ from $\dot{Q}_{\text{rxn}}(z)$ to obtain a spatially varying effective heat input relative to the average. Finally, we use a Fourier series to obtain the steady-state component of the solution to the heat equation (d) whose amplitude yields the maximum temperature difference ΔT_{max}. For details, see Sec. 4.2.2.1.

Since the heat release from reaction does not vary in time we know that after a sufficiently long time the spatially varying component of the solution to Eq. (4.4) will be in steady state. We thus propose a solution to Eq. (4.4) that is the superposition of two contributions, one varying only in time and the other varying only in position:

$$T(z,t) = T_t(t) + T_z(z) \tag{4.5}$$

We are primarily interested in the spatial variation component $T_z(z)$, but it is easiest to first find $T_t(t)$. In order to account for the constant input energy the time-varying component must just be the spatial average of temperature. The reaction is the only energetic contribution, and this comes from just half of the layers, so the reaction power averaged over the entire sample is $\dot{Q}_{\mathrm{avg}} = \dot{Q}_{\mathrm{max}}/2$ and the spatially averaged heating rate is $\dot{T}_{\mathrm{avg}} = \dot{Q}_{\mathrm{avg}}/\rho C_p$. This is easily integrated to obtain the time-varying component of Eq. (4.5):

$$T_t(t) = \frac{\dot{Q}_{\mathrm{avg}}}{\rho C_p} t \tag{4.6}$$

Plugging this into Eq. (4.5) and that result into Eq. (4.4), we find

$$\frac{\partial^2 T_z(z)}{\partial z^2} = -\frac{1}{\alpha_\perp \rho C_p}\left(\dot{Q}_{\mathrm{rxn}}(z) - \dot{Q}_{\mathrm{avg}}\right) \tag{4.7}$$

The effect of subtracting $\dot{Q}_{\mathrm{avg}}$ from $\dot{Q}_{\mathrm{rxn}}(z)$ is to produce a square wave with period $2L$ and amplitude $\dot{T}_{\mathrm{avg}}$ as shown in Fig. 4.2(c). A square wave with period $2L$ and unity amplitude can be represented as a Fourier series of the form

$$f(x) = \frac{4}{\pi}\sum_{n=1,3,5,\ldots}^{\infty} \frac{1}{n}\sin\left(\frac{n\pi x}{L}\right) \tag{4.8}$$

Taking just the largest term in this sum ($n = 1$), we can approximate $\dot{Q}_{\mathrm{rxn}}(z) - \dot{Q}_{\mathrm{avg}}$ as

$$\dot{Q}_{\mathrm{rxn}}(z) - \dot{Q}_{\mathrm{avg}} \approx \dot{Q}_{\mathrm{avg}} \frac{4}{\pi}\sin\left(\frac{\pi z}{L}\right) \tag{4.9}$$

Plugging this into Eq. (4.7) and integrating to solve for the spatial variation term $T_z(z)$, we obtain

$$T_z(z) = \frac{\dot{Q}_{\mathrm{avg}}}{\alpha_{\perp}\rho C_p}\frac{4L^2}{\pi^3}\sin\left(\frac{\pi z}{L}\right) \tag{4.10}$$

This predicts a sinusoidal variation in temperature between sections of reactive and inert material as depicted schematically in Fig. 4.2(d). The peak-to-valley distance is the maximum temperature difference we seek, given by double the amplitude in Eq. (4.10):

$$\Delta T_{\mathrm{max}} = \frac{\dot{Q}_{\mathrm{max}}}{\alpha_{\perp}\rho C_p}\frac{4L^2}{\pi^3} \tag{4.11}$$

We see that increasing the layer thickness or the reaction rate in the reactive sections will increase the maximum temperature difference, while increasing the thermal diffusivity will reduce it. It is useful to replace the maximum reaction rate with the maximum heating rate for a purely reactive sample,

$$\dot{T}^{RM}_{\mathrm{max}} = \frac{\dot{Q}_{\mathrm{max}}}{\rho C_p} \tag{4.12}$$

This value is much easier to obtain than $\dot{Q}_{\mathrm{max}}$ because it can be measured directly in experiments on unmediated reactive multilayers. Finally, given an allowable temperature deviation $\Delta T^{\mathrm{crit}}_{\mathrm{max}}$ we can solve for the critical section thickness

$$L_{\mathrm{crit}} = \sqrt{\frac{\Delta T^{\mathrm{crit}}_{\mathrm{max}}}{\dot{T}^{RM}_{\mathrm{max}}}\frac{\alpha_{\perp}\pi^3}{4}} \tag{4.13}$$

Eq. (4.13) is applied to a specific materials system by substituting appropriate values for the maximum heating rate and thermal diffusivity. For the AlNi/CuNi IMRMs described in this work we performed our calculations using a value of 10^6 K/s for the maximum heating rate of pure Al/Ni and an out-of-plane thermal diffusivity of 0.081 $\mathrm{cm^2\ s^{-1}}$ calculated for 2Cu:3Ni multilayers. Specifying a 1 K difference between sections as the maximum allowable, we obtained a value of $L_{\mathrm{crit}} = 7.9$ μm. This is reasonably large on the scale of thin films so that we only needed a few sections to produce foils that were thick enough to be free-standing.

4.2.2.2 Comparison to Knepper et al.

Knepper *et al.* [24] developed an empirical expression for the critical section thickness in dual-bilayer foils as described in the introduction to this section. The critical section thickness in this context was the largest thickness that each section could be without observing decoupling of the reaction between sections, and the formula they derived was

$$L_{\text{crit}} = A\frac{\alpha_{\parallel}}{\Delta v} \tag{4.14}$$

where A is an empirical constant equal to 1.3 ± 0.3 and Δv is the difference between the propagation velocities of the two sections in isolation. We can apply this formula to IMRMs by taking $\Delta v = v_{RM}$ since the inert layers cannot propagate on their own. For our particular system, we take $\alpha_{\parallel} = 0.67\ \text{cm}^2\ \text{s}^{-1}$ for Al/Ni multilayers (this is the value used in [24] to derive Eq. (4.14)) and $v_{RM} \approx 13\ \text{m s}^{-1}$ for a 23 nm bilayer and obtain $L_{\text{crit}} = 6.7\ \mu\text{m} \pm 1.5\ \mu\text{m}$. This is in reasonable agreement with the result of the theoretical analysis in Sec. 2.2.1.

4.2.3 Final Design

The design details for all samples are given in Table 4.1. We fabricated a total of five IMRM foils ranging from 66% to 90% reactive material, as well as a pure Al/Ni foil ("Control") and a pure Cu/Ni foil ("Inert"). The total sample thickness and number of sections was held constant (18 μm and five, respectively), while the section thicknesses were varied based on the desired volume fraction of reactive material. The maximum section thickness was set at 5.4 μm, well within the limit calculated.

Table 4.1 Design table for the materials fabricated and tested in this work. The "Control" sample is pure Al/Ni multilayers and the "Inert" sample is pure Cu/Ni multilayers. The other five samples are inert-mediated reactive multilayers (IMRMs) that have alternating sections of reactive Al/Ni and inert Cu/Ni. Fig. 4.1 shows a schematic of the IMRM structure. Properties shown are the total thickness (t_{tot}), the volume fraction of reactive material (ϕ_{RM}), the number of each type of section, the section thicknesses S_{RM} and S_{IM}, and the bilayer spacing in each section (λ). All IMRM samples have an odd number of reactive sections and an even number of inert sections so that they are symmetrical with reactive material on the exterior.

Sample ID	t_{tot} **(μm)**	ϕ_{RM}	**Reactive Sections (1:1 Al:Ni)**			**Inert Sections (2:3 Cu:Ni)**		
			#	S_{RM} **(μm)**	λ **(nm)**	**#**	S_{IM} **(μm)**	λ **(nm)**
Control	18	1.00	1	18	23	-		
IMRM 1		0.90	3	5.4		2	0.9	75
IMRM 2		0.82		4.92			1.62	106
IMRM 3		0.75		4.5			2.25	75
IMRM 4		0.70		4.2			2.7	75
IMRM 5		0.66		4.0			3.0	28
Inert	10	0	-			1	10	107

4.3 Experimental

4.3.1 Fabrication

The samples tested were deposited onto polished brass substrates using DC magnetron sputtering from Al (1100 alloy [99 wt % Al, 0.87 wt % (Si, Fe), 0.12 wt % Cu]), Ni/V (93 wt % Ni, 7 wt % V), and Cu (OFHC grade [99.99 wt % Cu]) targets. Vanadium is added to the Ni target to render it nonmagnetic. Multilayers are produced by mounting the substrates on a cooled rotating carousel and passing them over alternating targets. By controlling the sputtering power and rotation rate, a wide range of component ratios and bilayer spacings can be obtained. Sputtering was performed in a vacuum chamber evacuated below 3 x 10^{-6} Torr and then backfilled to 1.3 mTorr with Ar (99.999% pure).

The samples were patterned into strips approximately 1.3 cm wide by taping the substrates prior to deposition. After sputtering, the brass substrates were removed from the vacuum chamber, the tape was removed, and the patterned material was peeled from the substrate to produce free-standing foils. The first layer of the first reactive section and the last layer of the last reactive section were aluminum so that the foils were terminated by aluminum on both sides.

4.3.2 Characterization

Heat flow and total enthalpy of reaction measurements were carried out using a power-compensated differential scanning calorimeter (Perkin-Elmer DSC 8000). The specific enthalpy of reaction was computed by integrating the heat flow data over the temperature range 107 – 490 °C and dividing by the sample mass. At least three DSC measurements were performed on each sample tested. The experimental volume fraction of reactive material, ϕ_{RM}^{exp}, was calculated from enthalpy data by first calculating the mass fraction of reactive material as

$$w_{RM}^{\mathrm{exp}} = \frac{\Delta H_i}{\Delta H_{\mathrm{Control}}} \tag{4.15}$$

where ΔH_i is the total enthalpy of the sample in question and $\Delta H_{\mathrm{Control}}$ is the total enthalpy of the purely reactive "Control" sample, and then converting this mass fraction to a volume fraction using the densities of the inert (ρ_{IM}) and reactive (ρ_{RM}) components:

$$\phi_{RM}^{\mathrm{exp}} = \frac{w_{RM}^{\mathrm{exp}}/\rho_{RM}}{w_{RM}^{\mathrm{exp}}/\rho_{RM} + (1 - w_{RM}^{\mathrm{exp}})/\rho_{IM}} \tag{4.16}$$

This approach was selected (as opposed to measuring the volume fraction directly using cross-sectional microscopy) because (1) it effectively samples a much larger volume of material than can feasibly be done using microscopy, and (2) the result obtained is directly related to the relative heat output which is of most importance for IMRMs. However, we did verify that the results obtained using the two approaches are comparable.

Structural analysis was carried out using x-ray diffraction (Philips X'Pert) in a θ-2θ configuration with Cu-Kα radiation. Cross-sectional images were produced by mounting samples vertically in epoxy, polishing with a succession of abrasive papers and suspensions, and imaging the results in a scanning electron microscope (Tescan MIRA3).

For investigations of propagating reactions, samples were placed between two glass slides with one end protruding outside the glass. The exothermic reaction was initiated by applying an electric spark from a DC power supply (MPJA 14602PS) to the exposed end of the foil. The reaction then propagated into the part of the foil between the glass slides where characterization was conducted.

Temperature measurements were performed using a one-color (single wavelength) pyrometer (Kleiber KG740-LO) covering the temperature range 500 °C – 2500 °C. This instrument works by measuring the intensity of radiation from the sample at a single wavelength and inferring the sample temperature based on an assumed value for the emissivity of the sample. While the emissivity of our samples is not precisely known and may change during reaction, we found the consistency of results from this instrument to be superior to those obtained using a two-color (ratio) pyrometer [11] for these samples. The data from the pyrometer was analyzed assuming an emissivity of $\varepsilon = 0.10$. This is a reasonable value for polished Al (the deposited foils all had Al on the exterior) and matches the value used in previous work with a comparable instrument [27]. The flame temperature was taken as the maximum value of the temperature vs. time curve, and at least ten measurements were averaged for each sample tested.

High-speed videos of reaction propagation under glass were made using a high-speed visible-light camera (NAC Memrecam HX-6) equipped with a 150mm macro lens

(Sigma) and mounted vertically. Frame rates varied between 5000 and 20,000 fps depending on the speed of the reaction studied. The position of the reaction front was extracted from the high-speed videos using the open-source program Tracker (http://physlets.org/tracker/), and the front velocity was obtained from a linear regression of the front position vs. time. At least three videos were analyzed for each sample tested.

The maximum reaction temperature was increased for some samples by raising the initial temperature of the reaction above ambient. For these experiments, two glass slides were placed on a small ceramic heater (Watlow ULTRAMIC) and allowed to equilibrate at the set temperature. To conduct an experiment, the test foil was placed between the glass slides on the hot plate and reacted within 10 – 20 seconds. This procedure was adopted to minimize variations in the initial temperature between experiments. The maximum initial temperature was limited to 100 °C in order to minimize the amount of mixing that could occur prior to reaction initiation.

We found testing under glass slides to be more repeatable because (1) some samples were warped due to residual stresses and needed to be held flat, (2) many samples showed a tendency to curl unpredictably during reaction if unconstrained, and (3) the samples tended to oxidize when hot. For the Control sample studied in this work we compared tests under glass to tests in air and found no significant difference in the propagation velocity (12.5 ± 0.1 m/s under glass and 12.6 ± 0.1 m/s in air). The maximum temperature for foils tested in air was higher, but this is likely due to oxidation that occurs following passage of the reaction front. Fig. 4.3(a) shows a comparison of pyrometry plots under both conditions, and both traces are nominally identical up until the end of rapid heating (presumed completion of the intermetallic reaction). After this point, heating continues for foils tested in air but more slowly than before. The additional heating is most likely due to oxidation as suggested by the surface oxidation that is visible in Fig. 4.3(b). Since this study was specifically concerned with the connection between the propagation velocity and the temperature of the flame front, we focused on samples reacted between glass slides to exclude any effects from oxidation.

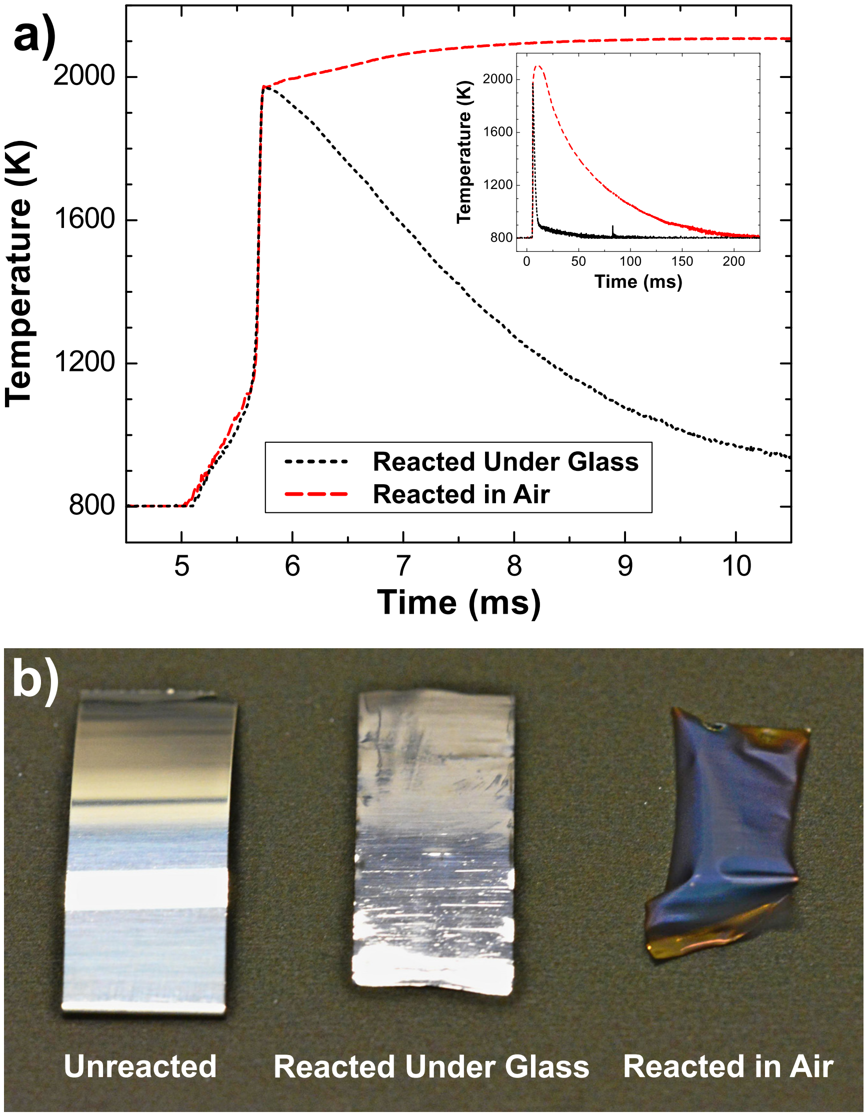

Figure 4.3 Comparison of reactions performed under a glass slide versus in air. In (a) we show temperature versus time traces from one-color pyrometry for the same sample type (Control) reacted under a glass slide and reacted in air. The inset shows the same measurements with an expanded timescale to capture the full duration of the reaction in air. Note that some of the apparent heating observed for the reaction in air may be due to an increase in sample emissivity as oxidation occurs. In (b), a visual comparison of Al/Ni samples before reaction, after reaction under a glass slide, and after reaction in air

suggests that surface oxidation is the origin of the extended reaction in air.

4.4 Experimental Results

Experimental results for the volume fraction of reactive material, the maximum temperature, and the propagation velocity are summarized in Table 4.2. The design values of ϕ_{RM} in Table 4.1 match the measured values of $\phi_{RM}^{\exp}$ in Table 4.2 to within 4% for all samples studied. As anticipated, the flame temperature of the reaction scales with ϕ_{RM}, ranging from 1962 ± 24 K for a fully reactive foil to 1303 ± 33 K for a 66% reactive foil. Propagation velocities scale similarly, ranging from 12.5 ± 0.1 m/s for the fully reactive foil to 0.73 ± 0.04 m/s for a 66% reactive foil.

Table 4.2 Experimental results for the tested foils, showing the experimentally measured volume fraction of reactive material calculated from DSC heats ($\phi_{RM}^{\exp}$), the maximum temperature ($T_{\max}$), and the propagation velocity (v). Some measurements were obtained by preheating samples on a hot plate. These are indicated by a non-zero value of T_{plate} which was the temperature setpoint for those measurements. Samples with no T_{plate} value were reacted at room temperature. Uncertainties are one standard deviation on either side of the mean.

Sample ID	$\phi_{RM}^{\exp}$	T_{plate} (°C)	$T_{\max}$ (K)	v (m/s)
Control	1.00	-	1962 ± 24	12.5 ± 0.1
IMRM 1	0.89 ± 0.003	100	1756 ± 13	13.1 ± 0.03
IMRM 1	0.89 ± 0.003	-	1647 ± 12	9.77 ± 0.1
IMRM 2	0.78 ± 0.004	100	1623 ± 18	9.02 ± 0.2
IMRM 2	0.78 ± 0.004	-	1478 ± 13	5.14 ± 0.02
IMRM 3	0.77 ± 0.004	-	1471 ± 25	4.44 ± 0.06
IMRM 4	0.71 ± 0.003	100	1452 ± 22	6.38 ± 0.1
IMRM 4	0.71 ± 0.003	50	1415 ± 29	4.99 ± 0.1
IMRM 4	0.71 ± 0.003	-	1341 ± 16	4.56 ± 0.2
IMRM 5	0.67 ± 0.003	-	1303 ± 33	0.727 ± 0.04[a]

[a] This sample exhibited unsteady propagation. The reported velocity is the "bulk velocity" down the foil (perpendicular to the direction of band propagation).

Differential scanning calorimetry traces for all samples listed in Table 4.1 are shown in Fig. 4.4. The shapes of the heat flow traces are very sensitive to the chemistry and bilayer spacing of the reactive sections of the sample. Looking at the Control sample, we see a characteristic profile consisting of a sharp first exothermic peak around 220 °C, a very broad middle peak around 260 °C, and a somewhat broad third peak around 350 °C. This profile agrees with those observed previously for sputtered Al/Ni at very small bilayers [24], and is reproduced across all samples implying that the same reactions are occurring in all of them. The sample-to-sample variations in the magnitude and position of the latter two peaks are most likely due to small variations in the bilayer spacing and/or chemistry of the reactive component between depositions. There are more systematic trends in the total area under the curves and the position of the first peak. The total area decreases with decreasing mass fraction reactive as we would expect, while the temperature of the first peak increases. We believe the temperature increase can be attributed to stresses caused by the coefficient of thermal expansion (CTE) mismatch between Al/Ni and Cu/Ni. Al/Ni has a higher CTE than Cu/Ni, so at any temperature above the deposition temperature (~75 °C) the Al/Ni sections will be in compression and the Cu/Ni sections will be in tension. Atomic diffusion tends to be inhibited by compression [28], an effect which would delay intermixing and product growth and shift the exothermic peaks to higher temperatures. The magnitude of the compressive stress should scale inversely with the thickness ratio of reactive to inert material, shifting the peaks to higher temperatures as the volume fraction of reactive material is reduced, thus matching the observed behavior. While interesting, this effect is unlikely to be relevant in the self-propagating regime since most of the reaction occurs above the melting point of Al.

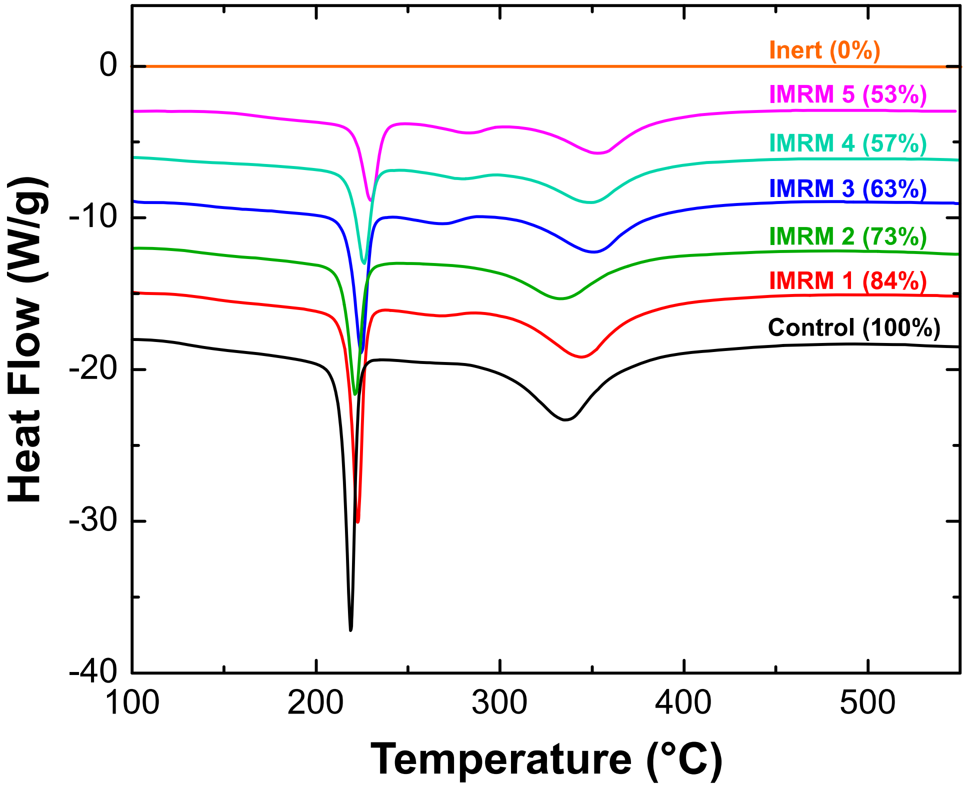

Figure 4.4 Differential scanning calorimetry curves for the samples tested in this work. The curves are labeled with the sample ID and (in parentheses) the *mass fraction* of reactive material in each (area under the curve is proportional to the total energy output per gram of sample).

A cross-sectional scanning electron micrograph of the hottest IMRM sample (IMRM 1) after reaction is shown in Fig. 4.5. Clearly the bulk organization of the sample into inert and reactive sections remains intact through the reaction. While detailed analysis is difficult using SEM, we examined high-magnification images of the inert/reactive interface (inset) and concluded that any interaction between the sections appears to be limited to a distance of ~200 nm. To explore this in more detail, we performed x-ray diffraction (XRD) on the as-reacted samples. The inert material introduces Cu and an excess of Ni into the system, so the presence of Al-Cu or Ni-rich Al-Ni intermetallic phases in the IMRM reaction products would indicate possible chemical contamination of the reactive material. We observed no evidence of these phases in any of the samples tested. A post-reaction XRD scan of IMRM 1 is shown in

Fig. 4.6. One set of peaks in Fig. 4.6 is due to B2 AlNi (the reaction product of 1:1 Al:Ni multilayers) and the other set of peaks comes from an fcc phase with a lattice parameter of approximately 0.356 nm. This is intermediate between that of Cu and Ni, suggesting that these peaks arise from a solid solution of Cu and Ni formed when the Cu/Ni multilayers are heated by the reaction. If unintended products are present, we conclude that they are in such small volume fractions as to be undetectable by XRD.

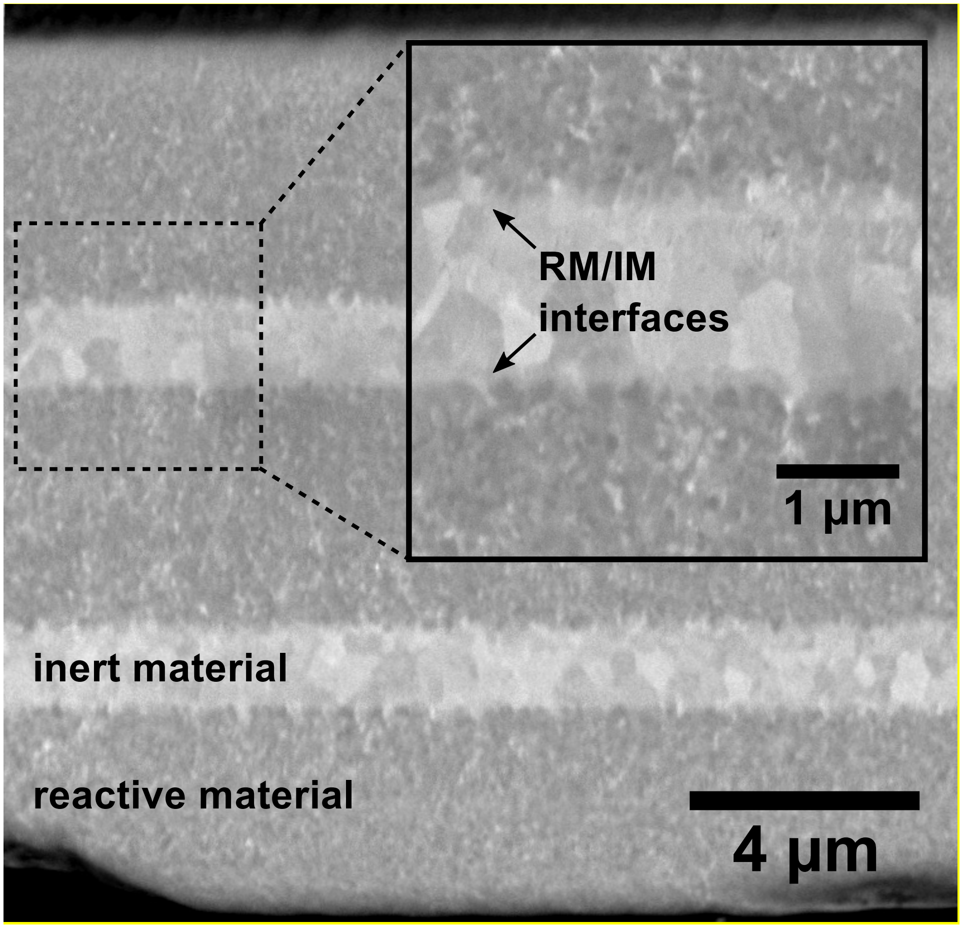

Figure 4.5 Backscattered scanning electron micrograph of sample IMRM 1 after reaction. The boundaries between sections remain intact, with the reactive material appearing dark and the inert material appearing light. The inset shows two inert/reactive interfaces at higher magnification, allowing us to estimate the length scale of interaction between reactive and inert sections at about 200 nm.

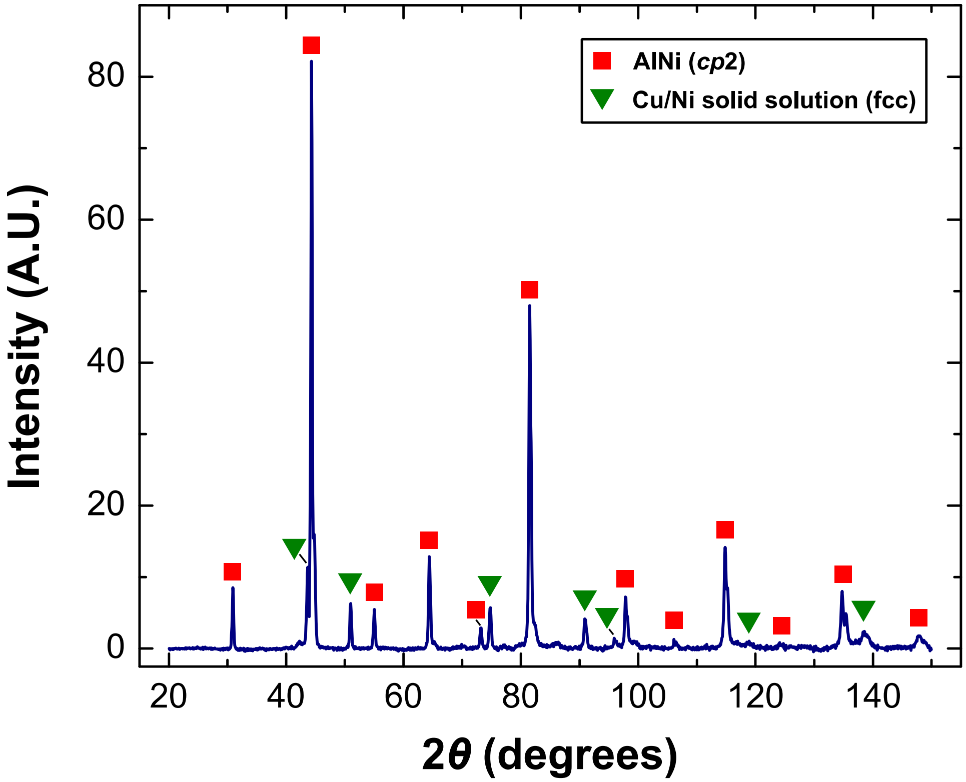

Figure 4.6 X-ray diffraction scan for the hottest IMRM sample (IMRM 1) after reaction in the self-propagating mode. All peaks can be attributed to either AlNi (the product of the reactive layers) or an fcc phase with a lattice parameter of approximately 0.356 nm, likely a Cu/Ni solid solution (the "product" of the inert layers). The splitting of AlNi peaks observed at higher scattering angles is due to the Cu-Kα2 line at 1.544 Å.

The maximum reaction ("flame") temperatures are plotted in Fig. 4.7 versus the experimental volume fraction of reactive material. The data correspond well with predictions, suggesting that the temperatures measured are accurate and lending support to our choice of emissivity for pyrometry analysis. Flame speed is plotted versus flame temperature in Fig. 4.8. Velocities generally increase with temperature. One sample (indicated by an open symbol in Fig. 4.8) exhibited a phenomenon known as unsteady propagation [29] where rather than a smooth flame front aligned perpendicular to the propagation direction we observe a multitude of transverse bands that propagate parallel to the front. This is typical of samples propagating close to the point of extinction.

Following other recent investigations into this phenomenon [29,30], the value reported is the "bulk propagation rate" perpendicular to the direction of band propagation.

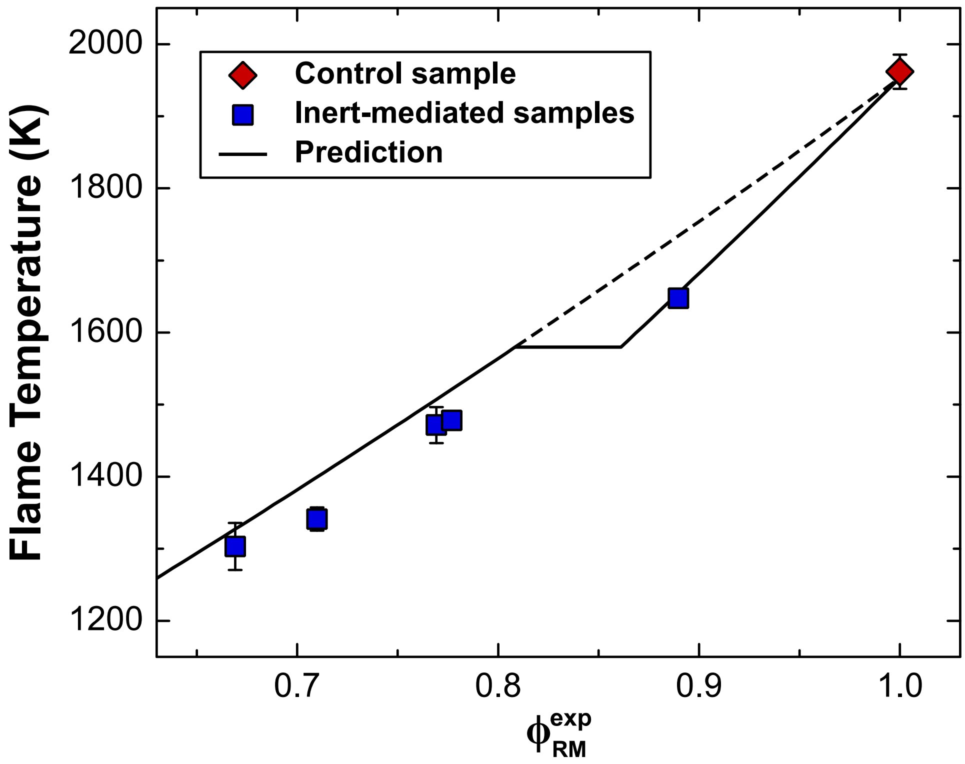

Figure 4.7 Maximum temperature measured by one-color pyrometry plotted versus the volume fraction of reactive material calculated from DSC data. Samples that were preheated prior to reaction (see Table 4.2) are not included. The dashed line is the predicted adiabatic reaction temperature assuming no phase changes, an initial temperature of 293 K, an adiabatic temperature change of 1660 K for a 100% reactive sample, and the bulk, room temperature heat capacities for Al, Ni, and Cu. When we include the estimated effect of melting in the inert sections, a better fit (solid line) is obtained. For this calculation, we assume that the inert sections melt uniformly at 1578 K (the solidus temperature for the composition used).

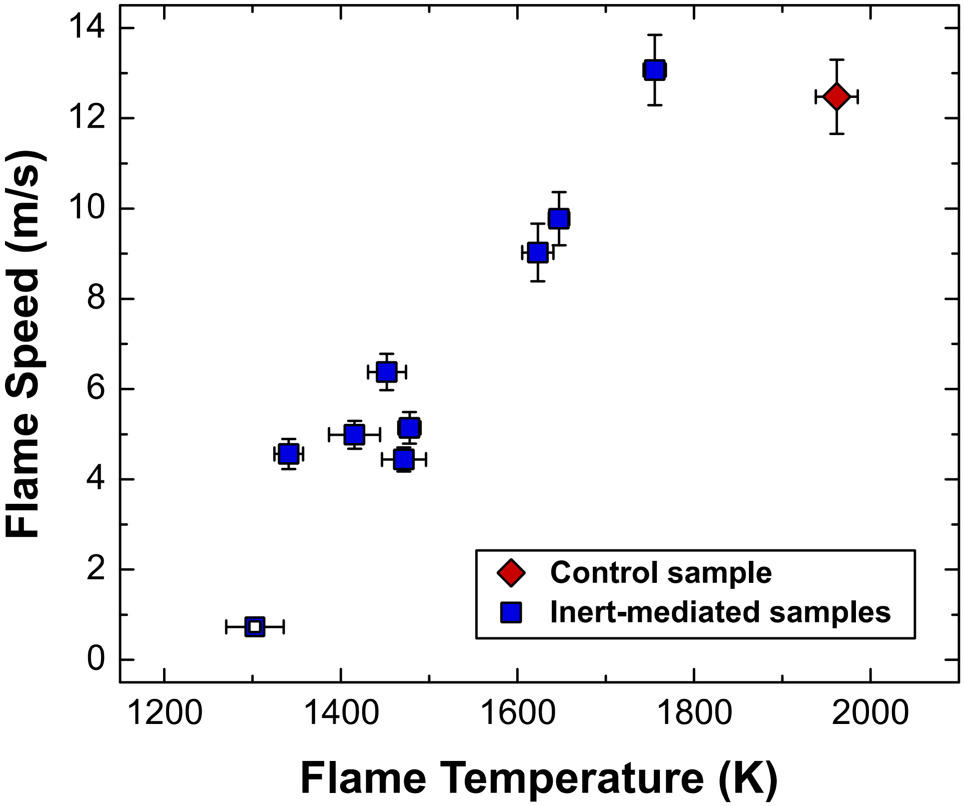

Figure 4.8 Flame speed versus flame temperature for all samples tested in this work. Horizontal error bars are one standard deviation of the experimental temperature measurements. Vertical error bars are obtained from a combination of experimental variation and the estimated variation due to differences in bilayer spacing. Data points without visible error bars have errors smaller than the size of the data point. The open data point indicates that the sample (IMRM 5) exhibited unsteady propagation.

4.5 Analysis

The maximum temperatures and flame speeds for IMRM samples decrease systematically with increasing inert volume fraction, while DSC data indicate that all samples have nominally the same bilayer spacing and chemistry within the reactive sections. X-ray diffraction and cross-sectional microscopy both indicate that the inert material is functioning as intended and is not contaminating the reactive material. This validates our design considerations and confirms that the general concept of inert-mediated reactive multilayers – decoupling the reaction temperature and velocity from the sample chemistry and bilayer spacing – is sound. We now turn to the potential scientific application of these materials. Continuum modeling results [31] suggest that the majority (>90%) of mixing in self-propagating reactions occurs in the upper third of the temperature range traversed. If this is true, we expect that varying the maximum temperature of the reaction should have a significant impact on the mechanism and kinetics of mixing. Since mixing is a critical factor in determining the propagation velocity, we should be able to detect changes in the mixing kinetics by examining how the velocity scales with flame temperature.

To do this, we draw on theories that predict how the velocity should scale with flame temperature assuming a mixing mechanism with simple Arrhenius scaling. By applying these theories to velocity versus temperature data, we can estimate the activation energy for the mixing process as a function of temperature. This has the benefit of requiring far fewer assumptions about materials properties than the traditional approach of fitting a curve to velocity versus bilayer data (e.g., [32]).

4.5.1 Analysis Approach

Several models [32–34] have been developed to describe the propagation velocity of laminar reactive materials. They are derived by solving a boundary value problem for the coupled thermal and atomic diffusion equations. All of the models feature the activation energy for atomic diffusion in a similar role to that occupied by the activation energy for chemical reaction in gas-phase combustion [34], and all predict that velocity should have an inverse dependence on the bilayer spacing. Aldushin and Khaikin [33] presented the earliest model reaching this conclusion, assuming that the rate-controlling mixing process was interdiffusion through a product phase at the interface. Armstrong [34] obtained a similar result by assuming mixing into a homogenous solution. Mann *et* *al.* [32] extended the Armstrong analysis to non-ideal multilayers, enabling predictions of the velocity "fall off" that is observed experimentally at small bilayers in samples with initial intermixing. Any of these models would be sufficient for our analysis. Here we choose to neglect the effects of intermixing and start with Armstrong's result [34] for a quadratic dependence of heat release on concentration:

$$v_f^2 = \frac{6\lambda^2 R T_f^2 A}{\delta^2 E(T_f - T_0)} \exp\left(-\frac{E}{RT_f}\right) \tag{4.17}$$

Here v_f is the flame speed, λ the thermal diffusivity, R the gas constant, T_f the flame temperature, A the Arrhenius prefactor, E the Arrhenius activation energy, δ one-quarter of the bilayer spacing, and T_0 the initial temperature. Of these parameters R is a physical constant, λ and δ are constant by design in IMRMs (see Sec. 2), and A and E are constant for a given mixing mode. Moving non-constant terms to the left-hand side and taking the natural logarithm,

$$\ln \frac{v_f^2(T_f - T_0)}{K^* T_f^2} = \ln \frac{6\lambda^2 R A}{K^* \delta^2 E} - \frac{E}{RT_f} \tag{4.18}$$

Here K^* is a reference value with dimensions of $[T\ t^2\ l^{-2}]$ that we add when taking the natural logarithm to make its argument non-dimensional. From Eq. (4.18) we can obtain the activation energy as

$$\frac{d \ln\left(v_f^2(T_f - T_0)/K^* T_f^2\right)}{d(1/T_f)} = -\frac{E}{R} \tag{4.19}$$

That is, a plot of $\ln\left(v_f^2(T_f - T_0)/K^* T_f^2\right)$ versus $1/T_f$ (all experimentally measured quantities) should have a slope proportional to the activation energy for the mixing process. Some may note the similarity of Eq. (4.19) to the so-called "Zeldovich method" [35,36] which was derived for gaseous flames but has also been applied to condensed-phase reactions. That theory implies a simpler relationship but has in common the factor of v_f^2:

$$\frac{d \ln v_f^2}{d(1/T_f)} = -\frac{E}{R} \qquad (4.20)$$

The reason for the similarity is no doubt the parallel form of the equations for gaseous and condensed-phase flames as observed by Armstrong [34]. Here we use Eq. (4.19) because it was specifically derived for laminar materials.

Before proceeding we note that the analytical models described, and the analysis approach derived from them, are oversimplifications. They assume composition-independent diffusivities, temperature-independent materials properties, and homogeneous mixing from reactants to products. While in-depth investigations invariably find that the actual situation is more complex, there is also substantial data showing that at the very high heating rates observed during self-propagating reactions the assumption of mixing characterized by a single Arrhenius activation energy is reasonably accurate [14–16]. More philosophically, we note that ascribing an "activation energy" to a process is simply an attempt to quantify the extent to which it depends on temperature. Given that temperature is an important parameter in reactive material performance, an Arrhenius activation energy is a valuable tool whether it ultimately refers to diffusion in a solid, diffusion in a liquid, interfacial detachment, or (as is most likely here) some combination of these processes.

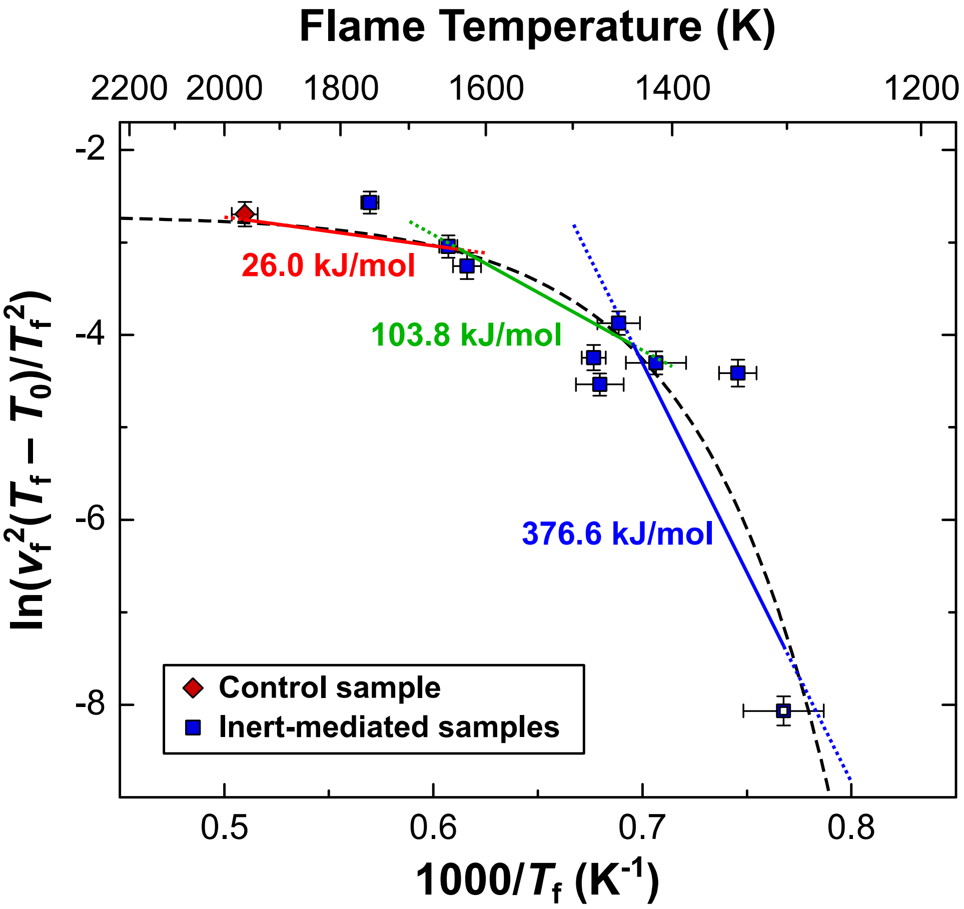

Figure 4.9 Arrhenius plot for the samples tested in this work, analyzed using Eq. (4.19). Horizontal error bars are one standard deviation of the experimental measurements. Vertical error bars are the uncertainty obtained after propagating error from both velocity and temperature measurements. The open data point indicates that the sample (IMRM 5) exhibited unsteady propagation. The dashed curve is a best-fit with the form $y = y_0 + A \exp((x - x_0)/t)$ and coefficients $y_0 = -2.70632$, $A = -0.08677$, $x_0 = 5.14643 \times 10^{-4}$, and $t = 6.42372 \times 10^{-5}$ ($R^2 = 0.764$). To obtain activation energies we approximate this curve using three straight line segments. The temperature ranges for the three segments are approximately 1950 K – 1650 K (red), 1650 K – 1450 K (green), and 1450 K – 1250 K (blue).

4.5.2 Analysis Results

Taking the data obtained from the IMRM samples (Table 4.2) and calculating quantities as prescribed in Eq. (4.19) with $K^* = 1\ \mathrm{K\,s^{-2}\,m^{-2}}$, we obtain the plot shown in Fig. 4.9. While the data show considerable scatter, there is a clear negative slope as predicted (the activation energy is a positive quantity). However, the data are not well approximated by a straight line as we would expect for a single controlling process. Instead, the best fit is a curve as shown, implying perhaps multiple rate-controlling processes operating in different regions of the temperature range. To study this result in more detail we divided the data into three temperature regimes and approximated the best-fit curve using three straight lines as shown in Fig. 4.9. Each line segment gives a different activation energy. Next, we explore these values and propose possible rate-controlling mechanisms to explain them.

4.5.2.1 High Temperature Regime (1650 – 1950 K)

The activation energy obtained from the measured data in the high temperature range is 26.0 kJ/mol. Du *et al.* [37] obtained an identical value in experiments where they measured the diffusivity of Ni in molten Al. This agreement is strong support for the hypothesis that at high temperatures (typical of relatively unmediated Al/Ni reactive multilayers) the rate-limiting process is diffusion of Ni in molten Al. It also suggests that at these temperatures the solid product (AlNi) either does not form until relatively late in the reaction or does not present a barrier to diffusion, since diffusion through AlNi should give rise to a much larger activation energy [38,39]. This result is consistent with *in situ* experiments [11,12] which have established the presence of molten Al in the reaction fronts of Al/Ni multilayers. Molecular dynamics simulations also support this conclusion. Adiabatic (NPH) simulations have found that aluminum melts early in the reaction and mixing occurs primarily into the melt [13–15]. Xu *et al.* [16] used isothermal (NPT) simulations to assess the dominant transport mechanism in Al/Ni multilayers and its thermal sensitivity between 1700 K and 2000 K, and concluded that the rate-controlling process was diffusion of Ni in molten Al with an activation energy of 35.77 kJ/mol.

4.5.2.2 Intermediate Temperature Regime (1450 – 1650 K)

In this temperature regime a linear fit to the data yields an activation energy of 103.8 kJ/mol. This value is too large to be due to diffusion of Ni in liquid Al and too small to be due to solid-state diffusion of Ni through an intermetallic product. More likely processes are the detachment of Ni atoms from the Ni lattice (or an Al-Ni solid solution), or diffusion through said solution. Based on the minimal modeling data available at these temperatures [16] a detachment process (i.e. interface-limited dissolution) seems most likely. Xu *et al.* [16] found that in the temperature range 1300 K – 1600 K dissolution of Ni into molten Al was the rate-limiting process. They analyzed mixing in this regime using the simple dissolution model of Noyes and Whitney [40] and obtained an activation energy of 101 kJ/mol. This result is a good fit to both the activation energy obtained and the temperature range considered here. While the Noyes and Whitney model has been interpreted as applying to both transport-limited [41] and interface-limited [42] kinetics, in the present context the latter interpretation is clearly preferable since the activation energy is higher than that expected for diffusion in the liquid.

4.5.2.3 Low Temperature Regime (1250 – 1450 K)

In the low temperature regime we observe the most aggressive scaling of velocity with temperature, characterized by an activation energy of 376.6 kJ/mol. This is significantly larger than the other two values reported and, if accurate, can only reasonably be attributed to solid-state diffusion. The aluminum layer is still molten in this regime, but a solid intermetallic phase growing at the Ni/molten Al interface could present a significant barrier to diffusion. Given the activation energy obtained and the temperatures considered, the most likely phase is B2 AlNi. Experimental values of activation energy for diffusion of Ni in AlNi at high temperatures vary considerably depending on the precise composition of the AlNi phase but generally fall in the range 200 – 360 kJ/mol [38,39]. The intermetallic phase that forms at these low reaction temperatures could also be the closely related Al_3Ni_2 structure. This phase has never been observed experimentally during a self-propagating reaction due to its relatively low decomposition temperature (1406 K [43]), but it may be stable during self-propagation in the most mediated samples because of the reduced flame temperature. Diffusion data on this phase is unavailable but would likely be comparable to that for AlNi given their structural similarity.

There is substantial modeling support for the formation of solid phases at the Ni/Al interface at moderate temperatures. NPT molecular dynamics simulations at relatively low temperatures (800 – 1000 K) [13,17] clearly show the formation of solid AlNi at the Ni/Al interface. The Al_3Ni_2 phase has not been observed, but this phase is known to be unstable for the family of MD potentials [20–22] used in all simulations described. Xu *et al.* [16] also observed the temporary formation of AlNi intermetallic at the interface in isothermal simulations from 1300 – 1600 K. While they were unable to extract an activation energy for diffusion through this phase, their data clearly showed a substantial decrease in the mixing rate associated with its presence, consistent with our results.

It is worth noting that the activation energy reported for this low-temperature regime is particularly sensitive to a single data point, IMRM 5. Since this sample is also the only one that exhibits unsteady propagation it is reasonable to ask whether any conclusions should be drawn from it at all. There are two perspectives on this. On one hand, as we have noted the analysis approach we are using relies on an already simplified model for uniform flame propagation and unsteady propagation is undeniably an even more complex phenomenon. This argues against inclusion since the assumptions made are unlikely to hold for unsteady propagation. On the other hand, it can be argued that regardless of the specifics of the propagation process (uniform versus unsteady) the bulk propagation rate will still be governed by the balance between atomic and thermal diffusion. In this case its scaling should remain relevant even when the propagation becomes unsteady. At the moment it is impossible to say for sure which of these perspectives is more accurate. The latter view is more consistent with the limited experimental data available [29,30], but additional work would be needed to verify this for the Al/Ni system. Because of this uncertainty we have included the IMRM 5 data point in our analysis but also mark it as a potential outlier. If it were to be ignored, the best interpretation of our results would be to discard the low-temperature regime entirely since the results in the other two temperature ranges are sufficient to describe the rest of the data.

4.6 Discussion

In Fig. 4.10, we present schematic drawings of the processes described in Sec. 5.2 and how they may relate to the microstructure of reactants and products within a single bilayer during the reaction. We conclude our analysis by considering why it might be reasonable to expect such variations in the rate-controlling process as the reaction temperature changes.

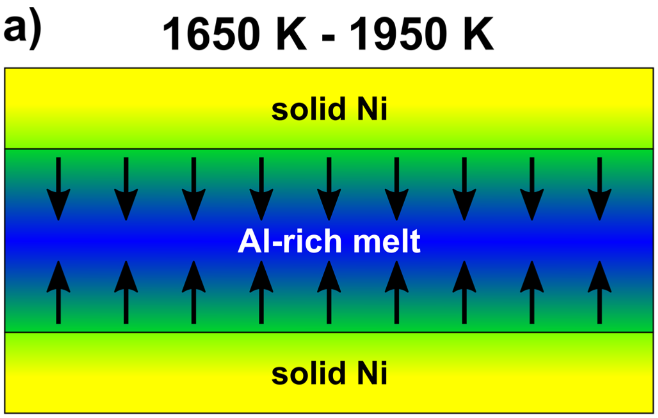

Diffusion of Ni through liquid Al

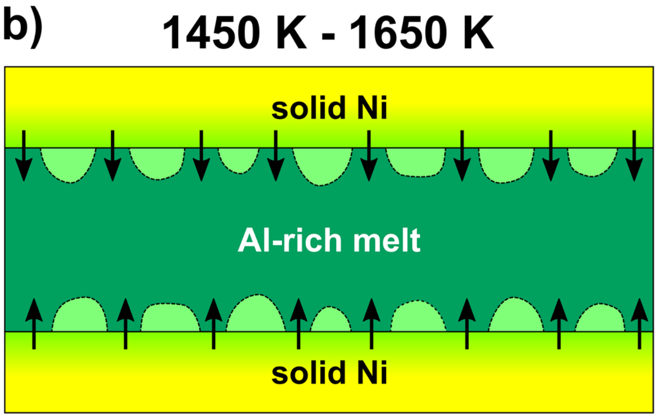

Dissolution of Ni into liquid Al

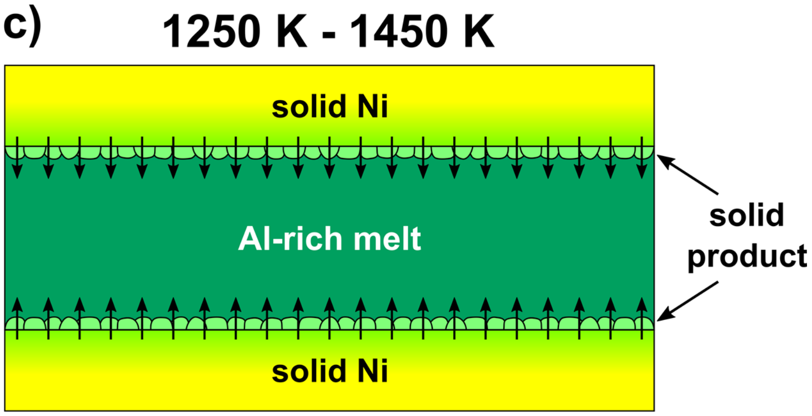

Diffusion of Ni through solid product

Figure 4.10 Proposed dominant mixing mechanisms based on the activation energies obtained in 4.9 and subsequent discussion. At high flame temperatures (a), the rate-limiting process appears to be diffusion of Ni in molten Al characterized by an activation energy of 26.0 kJ/mol. At intermediate flame temperatures (b), we suggest that the rate-limiting process is dissolution of Ni into molten Al characterized by an activation energy of 103.8 kJ/mol. This process occurs at the exposed interfaces between nuclei of solid product. At low flame temperatures (c), the rate-limiting process is characterized by an activation energy of 376.6 kJ/mol. This suggests mixing dominated by diffusion of solid Ni through a continuous layer of solid product at the interface.

As already noted, if diffusion in the liquid is to be rate-controlling at the highest temperatures it seems likely that AlNi is either forming only very late in the reaction or is forming in such a way as to not present a barrier to mixing. There are several reasons why AlNi might not form promptly when the flame temperature is high. First, the melting temperature of AlNi is 1911 K [43] and consequently the driving force for nucleation of AlNi is quite low at the temperatures considered. High flame temperatures also correlate with high heating rates and relatively steep concentration gradients which may further reduce the thermodynamic driving force for nucleating a new phase [44]. The combination of these factors may delay the formation of AlNi until the majority of the mixing has occurred. This is illustrated in Fig. 4.10(a) which depicts mixing dominated by diffusion of Ni into liquid Al with no product phase present.

As flame temperatures decrease, the factors described above that inhibit nucleation become less relevant and it seems more likely that AlNi could nucleate relatively early in the reaction. For this reason Fig. 4.10(b) includes the possibility of solid product grains at the interface even if they are not directly implicated in the mixing process at these temperatures. The suggested location and morphology of these grains is guided by the results of MD simulations and cross-sectional microscopy on quenched reactions [17,18,23] showing hemispherical AlNi grains that have evidently nucleated at the Ni surface and grown into the Al. Such a morphology might be expected because the solid Ni surface presents a low-energy nucleation site and growth into the liquid is preferred because of easier atomic transport.

Whether or not a solid phase is present, our analysis suggests that the dissolution process is still rate-limiting at intermediate temperatures (1450 K – 1650 K). In Sec.

5.2.2, we attributed the measured activation energy specifically to the interface-limited process of detaching Ni atoms from the lattice. While this hypothesis is impossible to prove with the data currently available, it seems reasonable if we note that most of the high temperature regime (1650 K – 1950 K) is above the melting temperature of Ni (1706 K) while the entire intermediate temperature regime is below it. The rate of detachment from the lattice is directly related to the energy required to remove an atom from it [42], a value which will drop significantly as we approach the melting temperature. This observation would explain why at high temperatures we appear to have diffusion-limited mixing while at the intermediate temperatures the detachment process is dominant.

Finally, in the lowest temperature regime analyzed (1250 K – 1450 K) we propose that solid product has most likely formed and constitutes an obstacle to mixing as illustrated in Fig. 4.10(c). Our rationale for depicting the product layer as fine-grained and continuous as opposed to large-grained and discrete as in Fig. 4.10(b) lies in the expected balance between nucleation rate and growth rate. The nucleation rate for a given phase tends to increase as temperature is reduced because the driving force for nucleation scales with undercooling. In contrast, the growth rate tends to decrease as temperature is reduced because the atomic transport required for growth is thermally activated. For this reason one expects a smaller number of larger grains when the temperature is higher and a larger number of smaller grains when the temperature is lower. We suggest that in the low temperature regime the nucleation rate is sufficiently high compared to the growth rate that after a small amount of mixing a large number of product nuclei form at the Ni/Al interface and rapidly impinge on each other, effectively forcing all subsequent mixing to occur via solid-state diffusion through them. Contrast this with the picture of the intermediate temperature regime (Fig. 4.10(b)) which shows larger discrete grains due to the higher temperature, with areas for detachment and dissolution between the grains.

We conclude by briefly comparing our assertions to the results of other recent experimental studies on the Al/Ni reaction, namely those of Rogachev and co-workers obtained by quenching of self-propagating reactions [17,18,23]. These studies have consistently implicated mixing into an Al-rich melt as the rate-controlling process for propagation. This conclusion was first reached based solely on cross-sectional microscopy [23], where the morphology of product AlNi grains in quenched samples (discontinuous at the interface as in Fig. 4.10(b)) suggested that mixing was driven by continuous dissolution of Ni into the melt. Subsequent work comparing quenched microstructures to MD simulations [17,18] reinforced this conclusion. The discussion in [23] notes that the dissolution process might be transport or interface limited. Our results indicate that transport-limited dissolution is most likely at the flame temperature of unmediated Al/Ni, but we also suggest a transition to interface-limited dissolution at intermediate flame temperatures. Thus our results can be seen as consistent with quenching experiments for both intermediate and high flame temperatures.

4.7 Conclusions

In this paper we described a new class of reactive materials termed "inert-mediated reactive multilayers" (IMRMs) that use inert material to decouple the effects of chemistry and maximum temperature in a reactive multilayer. We presented general considerations for the choice of reactive and inert materials and their section thicknesses, and then detailed the results obtained from IMRMs with reactive sections composed of

23-nm-bilayer 1:1 Al:Ni and inert sections composed of 2:3 Cu:Ni. We evaluated these materials under both slow heating and self-propagating conditions. With slow heating (differential scanning calorimetry) we observed predictable scaling of the specific heat output and consistent reaction peaks across all samples. Self-propagating reactions were ignited in all samples – the coldest at a volume fraction of 66% reactive and a maximum temperature 650 K below that for an unmediated foil. X-ray diffraction and cross-sectional electron microscopy on self-propagated samples confirmed that there is little, if any, interaction between the reactive material and the inert material during the self-propagating reactions, even at the highest temperatures. Both the flame temperature and propagation velocity decreased as the volume fraction of reactive material in the samples was reduced. A detailed analysis of the temperature and velocity data yielded experimental values for the activation energies of the processes controlling mixing, which were then used to propose possible reaction mechanisms as a function of temperature. The results are found to be in general agreement with those from recent molecular dynamics and quenching studies.

This work presents several intriguing possibilities for future studies. First, the results for the Al/Ni system could be expanded, either by extending the approach to lower temperatures or performing more tests over a narrower temperature range. This might be done to explore specific mechanisms or the steady-to-unsteady propagation transition in more detail. One could also apply the IMRM concept to other reactive multilayer chemistries (particularly those that we might expect to have significantly different mixing mechanisms, e.g. Ni/Zr) to see how their temperature-dependent activation energies differ. Finally, time-resolved characterization techniques like *in situ* x-ray diffraction could be applied to identify more precisely when product or other intermediate phases form. In summary, we conclude that inert-mediated reactive multilayers provide a flexible experimental approach for those wishing to investigate reactive multilayers in the self-propagating state without employing quenching.

References for Chapter 4

[1] D.P. Adams, Reactive multilayers fabricated by vapor deposition: A critical review, Thin Solid Films. 576 (2015) 98–128.

[2] J. Wang, E. Besnoin, A. Duckham, S.J. Spey, M.E. Reiss, O.M. Knio, et al., Room-temperature soldering with nanostructured foils, Appl. Phys. Lett. 83 (2003) 3987.

[3] J. Braeuer, J. Besser, M. Wiemer, T. Gessner, A novel technique for MEMS packaging: Reactive bonding with integrated material systems, Sensors Actuators A Phys. 188 (2012) 212–219.

[4] M. Ding, F. Krieger, J. Swank, J.C. Poret, C. McMullan, G. Chen, Use of NanoFoil as a New Heat Source in Thermal Batteries, 2009.

[5] C.J. Morris, B. Mary, E. Zakar, S.C. Barron, G.M. Fritz, O.M. Knio, et al., Rapid initiation of reactions in Al/Ni multilayers with nanoscale layering, J. Phys. Chem. Solids. 71 (2010) 84–89.

[6] T.W. Barbee, R.L. Simpson, A.E. Gash, J.H. Satcher, Nano-laminate-based ignitors, 8328967, 2012.

[7] S.H. Fischer, M.C. Grubelich, A survey of combustible metals, thermites, and intermetallics for pyrotechnic applications, in: 32nd Jt. Propuls. Conf. Exhib., American Institute of Aeronautics and Astronautics, Reston, Virigina, 1996.

[8] E. Ma, C.V. Thompson, L.A. Clevenger, Nucleation and growth during reactions in multilayer Al/Ni films: The early stage of Al3Ni formation, J. Appl. Phys. 69 (1991) 2211.

[9] C. Michaelsen, K. Barmak, T.P. Weihs, Investigating the thermodynamics and kinetics of thin film reactions by differential scanning calorimetry, J. Phys. D. Appl. Phys. 30 (1997) 3167–3186.

[10] K. Fadenberger, I.E. Gunduz, C. Tsotsos, M. Kokonou, S. Gravani, S. Brandstetter, et al., In situ observation of rapid reactions in nanoscale Ni–Al multilayer foils using synchrotron radiation, Appl. Phys. Lett. 97 (2010) 144101.

[11] J.C. Trenkle, L.J. Koerner, M.W. Tate, N. Walker, S.M. Gruner, T.P. Weihs, et al., Time-resolved x-ray microdiffraction studies of phase transformations during rapidly propagating reactions in Al/Ni and Zr/Ni multilayer foils, J. Appl. Phys. 107 (2010) 113511.

[12] J.S. Kim, T. LaGrange, B.W. Reed, R. Knepper, T.P. Weihs, N.D. Browning, et al., Direct characterization of phase transformations and morphologies in moving reaction zones in Al/Ni nanolaminates using dynamic transmission electron microscopy, Acta Mater. 59 (2011) 3571–3580.

[13] L. Sandoval, G.H. Campbell, J. Marian, Thermodynamic interpretation of reactive processes in Ni–Al nanolayers from atomistic simulations, Model. Simul. Mater. Sci. Eng. 22 (2014) 025022.

[14] L. Alawieh, T.P. Weihs, O.M. Knio, A generalized reduced model of uniform and self-propagating reactions in reactive nanolaminates, Combust. Flame. 160 (2013) 1857–1869.

[15] M.J. Cherukara, K.G. Vishnu, A. Strachan, Role of nanostructure on reaction and transport in Ni/Al

intermolecular reactive composites, Phys. Rev. B. 86 (2012) 075470.

[16] R.-G. Xu, M.L. Falk, T.P. Weihs, Interdiffusion of Ni-Al multilayers: A continuum and molecular dynamics study, J. Appl. Phys. 114 (2013) 163511.

[17] O. Politano, F. Baras, A.S. Mukasyan, S.G. Vadchenko, A.S. Rogachev, Microstructure development during NiAl intermetallic synthesis in reactive Ni–Al nanolayers: Numerical investigations vs. TEM observations, Surf. Coatings Technol. 215 (2013) 485–492.

[18] A.S. Rogachev, S.G. Vadchenko, F. Baras, O. Politano, S. Rouvimov, N.V. Sachkova, et al., Structure evolution and reaction mechanism in the Ni/Al reactive multilayer nanofoils, Acta Mater. 66 (2014) 86–96.

[19] M.D. Grapes, T. LaGrange, K. Woll, B.W. Reed, G.H. Campbell, D.A. LaVan, et al., In situ transmission electron microscopy investigation of the interfacial reaction between Ni and Al during rapid heating in a nanocalorimeter, APL Mater. 2 (2014) 116102.

[20] Y. Mishin, M. Mehl, D. Papaconstantopoulos, Embedded-atom potential for B2-NiAl, Phys. Rev. B. 65 (2002) 224114.

[21] Y. Mishin, Atomistic modeling of the [gamma] and [gamma]'-phases of the Ni-Al system, Acta Mater. 52 (2004) 1451–1467.

[22] G.P. Purja Pun, Y. Mishin, Development of an interatomic potential for the Ni-Al system, Philos. Mag. 89 (2009) 3245–3267.

[23] A.S. Rogachev, S.G. Vadchenko, A.S. Mukasyan, Self-sustained waves of exothermic dissolution in reactive multilayer nano-foils, Appl. Phys. Lett. 101 (2012) 063119.

[24] R. Knepper, M.R. Snyder, G.M. Fritz, K. Fisher, O.M. Knio, T.P. Weihs, Effect of varying bilayer spacing distribution on reaction heat and velocity in reactive Al/Ni multilayers, J. Appl. Phys. 105 (2009) 083504.

[25] D.J. Chakrabati, D.E. Laughlin, S.W. Chen, Y.A. Chang, Cu-Ni (Copper-Nickel), in: T.B. Massalski (Ed.), Bin. Alloy Phase Diagrams, 2nd ed., 1990: pp. 1442–1446.

[26] J.L. Murray, The aluminium-copper system, Int. Met. Rev. 30 (1985) 211–234.

[27] G.M. Fritz, J.A. Grzyb, O.M. Knio, M.D. Grapes, T.P. Weihs, Characterizing solid-state ignition of runaway chemical reactions in Ni-Al nanoscale multilayers under uniform heating, J. Appl. Phys. 118 (2015) 135101.

[28] A.J. Ardell, S.V. Prikhodko, Coarsening of γ′ in Ni–Al alloys aged under uniaxial compression: II. Diffusion under stress and retardation of coarsening kinetics, Acta Mater. 51 (2003) 5013–5019.

[29] J.P. McDonald, V.C. Hodges, E.D. Jones, D.P. Adams, Direct observation of spinlike reaction fronts in planar energetic multilayer foils, Appl. Phys. Lett. 94 (2009) 034102.

[30] R.V. Reeves, D.P. Adams, Reaction instabilities in Co/Al nanolaminates due to chemical kinetics variation over micron-scales, J. Appl. Phys. 115 (2014) 044911.

[31] L. Alawieh, O.M. Knio, T.P. Weihs, Effect of thermal properties on self-propagating fronts in reactive nanolaminates, J. Appl. Phys. 110 (2011) 013509.

[32] A.B. Mann, A.J. Gavens, M.E. Reiss, D. Van Heerden, G. Bao, T.P. Weihs, Modeling and characterizing the propagation velocity of exothermic reactions in multilayer foils, J. Appl. Phys. 82 (1997) 1178.

[33] A.P. Aldushin, B.I. Khaikin, Combustion of mixtures forming condensed reaction products, Combust. Explos. Shock Waves. 10 (1974) 273–280.

[34] R. Armstrong, Models for Gasless Combustion in Layered Materials and Random Media, Combust. Sci. Technol. 71 (1990) 155–174.

[35] A.A. Ovchinnikov, Y.B. Zeldovich, Role of density fluctuations in bimolecular reaction kinetics,

Chem. Phys. 28 (1978) 215–218.

[36] F. Baras, Determination of transport and kinetic properties in self-propagating high-temperature synthesis, J. Alloys Compd. 455 (2008) 113–120.

[37] Y. Du, Y.A. Chang, B. Huang, W. Gong, Z. Jin, H. Xu, et al., Diffusion coefficients of some solutes in fcc and liquid Al: critical evaluation and correlation, Mater. Sci. Eng. A. 363 (2003) 140–151.

[38] A. Paul, A.A. Kodentsov, F.J.J. van Loo, On diffusion in the [beta]-NiAl phase, J. Alloys Compd. 403 (2005) 147–153.

[39] R. Nakamura, K. Fujita, Y. Iijima, M. Okada, Diffusion mechanisms in B2 NiAl phase studied by experiments on Kirkendall effect and interdiffusion under high pressures, Acta Mater. 51 (2003) 3861–3870.

[40] A.A. Noyes, W.R. Whitney, The Rate of Solution of Solid Substances in Their Own Solutions, J. Am. Chem. Soc. 19 (1897) 930–934.

[41] W. Nernst, Theorie der Reaktionsgeschwindigkeit in heterogenen Systemen, Zeitschrift Für Phys. Chemie. 47 (1904) 52–55.

[42] S. Miyamoto, A theory of the rate of solution of solid into liquid, Trans. Faraday Soc. 29 (1933) 789.

[43] M.F. Singleton, J.L. Murray, P. Nash, Al-Ni (Aluminum-Nickel), in: T.B. Massalski (Ed.), Bin. Alloy Phase Diagrams, 2nd ed., 1990: pp. 181–184.

[44] F. Hodaj, A.M. Gusak, P.J. Desré, Effect of sharp concentration gradients on the nucleation of intermetallics in disordered solids: influence of the embryo shape, Philos. Mag. A. 77 (1998) 1471–1479.

5. A Systematic Study of the Interfacial Reaction in 3:1 Al:Ni Samples

5.1 Introduction

The reactions that can take place when two materials are in contact are of fundamental importance in a variety of fields including microelectronics [1,2], coatings [3], and reactive materials [4]. The relevance of such reactions is only increasing as trends toward miniaturization continue because as features shrink, their surface area to volume ratio increases and they become more sensitive to the effects of interfacial reactions. Since unintended interfacial reactions can often impair the function or reduce the lifespan of a part, continued effort is needed to explore how these reactions can be predicted and controlled. This is a challenge because the energetic landscape and various atomic fluxes at the interface can be extremely complex [5].

A key requirement if these reactions are to be predicted is an understanding of their kinetics. Thermal analysis is one of the best ways to obtain this information. Historically, interfacial reactions were studied calorimetrically using multilayer samples that contained a myriad of interfaces, effectively amplifying the thermal signal from the interfacial reaction to measurable levels [6]. This approach works well, but it is ultimately limited by the assumption that the temperature is uniform and that the reaction at all of the interfaces occurs identically and simultaneously. Since this is never a perfect assumption we must assume that all such experiments suffer from some amount of "blurring" in the thermal signal. This error is difficult to quantify, potentially obscuring the true behavior.

Nanocalorimetry is a chip-based calorimetry technique that utilizes microfabricated sensors with extremely high sensitivity [7]. It has been shown to be capable of measuring thermal signals from a single reacting interface [8,9] and as such can potentially circumvent the limitation outlined above. While nanocalorimetry employs universally higher heating rates than are encountered in conventional calorimetry, it also provides access to a wider range of heating rates. The most robust kinetic analysis results are obtained from multiple-heating-rate datasets that sample a large range of reaction temperatures [10]. Thus nanocalorimetry would seem to offer the potential for both cleaner experiments and the generation of more valuable experimental datasets than is possible using conventional calorimetry. It is somewhat surprising, then, that nanocalorimetry studies of reactions where the heating rate is varied systematically over a wide range are almost entirely absent from the literature at the present time, and that those that have appeared [11] have done little to leverage these unique capabilities.

With this in mind, in this work we present a systematic study of the Al/Ni interfacial reaction spanning two decades in heating rate. Our reasons for selecting this reaction for study are two-fold. First, it seems advisable to validate the testing method on a reaction that has already been studied extensively using conventional calorimetry [12–19]. Second, this interfacial reaction is of particular importance for understanding the performance of Al/Ni reactive multilayers [20]. These are free-standing multilayers of nanolayered Ni and Al that utilize the heat release from the Al/Ni interfacial reaction to achieve extremely high instantaneous temperatures and heating rates. These and related materials [4] are industrially relevant as heat sources for joining [21,22] and have also served as model systems for the study of highly nonequilibrium phase transformations

[23–26]. Advanced *in situ* experiments [23–26] have shown that intermediate phase formation is suppressed when Al/Ni multilayers react in the self-propagating mode (heating rate 10^6 K/s – 10^7 K/s). At least for the period prior to melting this has generally been explained [24] using the theory of Desré and co-workers [27,28] which predicts the suppression of nucleation in steep concentration gradients as are expected for an interface subjected to rapid heating. Thus the second goal of this study was to assess, if possible, the validity of this concentration gradient theory since it has proven to be very difficult to test.

As mentioned, the Al/Ni interfacial reaction has been the subject of extensive study using conventional thermal analysis techniques [12–19]. Generally all of these studies have concluded that product formation is preceded by interdiffusion between Ni and Al, that nucleation occurs heterogeneously at a fixed number of preferential sites, and that the process of product growth is diffusion-controlled. However, their conclusions differ in many important ways including the identity of the first phase (Al_3Ni [12–14], Al_9Ni_2 [15–18], or both [19] have been observed), whether it forms in a single step [16–19] or in two steps [13–15], and whether the product of the interdiffusion step is a metastable solid solution [13,19] or the B2 AlNi intermetallic [15,17]. This diversity of results is not meant to imply that the work was done haphazardly; rather, it illustrates the extreme sensitivity of the interfacial reaction to factors that are not always in the experimenter's control or that vary from study to study such as deposition conditions. As we analyze our data, we will draw on this body of prior work to compare to and inform our results.

In the two following sections, we begin by laying out the experimental tools and data analysis methodologies that were employed in this investigation. The results are reported in Section 4, and then we provide extensive discussion and analysis in Section 5. We conclude by summarizing our findings and commenting on the potential utility of this approach going forward.

5.2 Experimental

Nanocalorimeter sensors were fabricated in bulk on 100-mm-diameter silicon wafers and cleaved apart for individual use. The details of this fabrication process have been reported previously [7]. The active region of the sensor consists of a platinum heater strip on top of a thin silicon nitride membrane as depicted in Fig. 5.1. Guided by recent insights into the interaction between platinum metallization and various adhesion layers at high temperatures [29], the present experiments used sensors fabricated with a 10-nm-thick Ta adhesion layer and 100-nm-thick Pt metallization. The silicon nitride membrane was 100-nm-thick, chosen to provide a balance between mechanical stability and transparency for TEM analysis. Similar to the authors' previous work [30,31] the Pt heater included three 20 µm square holes to facilitate TEM observation. The holes in this work are smaller than those used in previously (100 µm) because the design with 20 µm holes was predicted [30] to exhibit a greater degree of thermal uniformity across the measurement area.

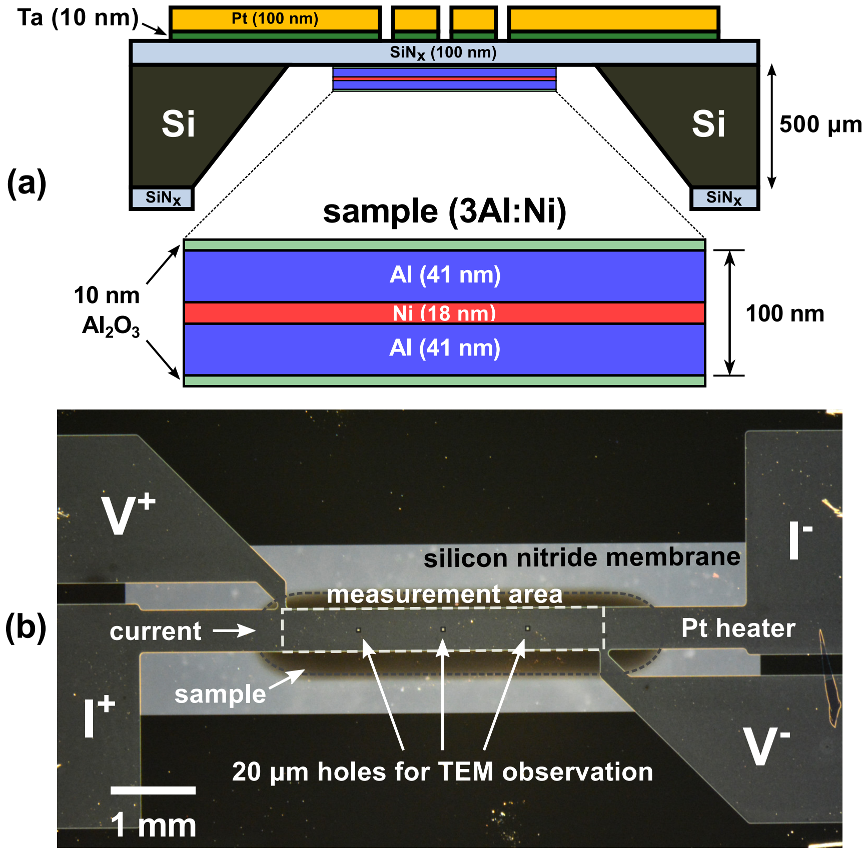

Figure 5.1 Design of the nanocalorimeter sensors and samples used in this work. In (a), a cross-sectional schematic shows the functional part of the device, a patterned platinum thin film on top of a released silicon nitride membrane. The sample has the overall composition 3Al:1Ni (1Al:0.22Ni by volume) and is evaporated onto the underside of the sensor as shown. The trilayer structure shown is equivalent to a bulk multilayer with a 100 nm bilayer period (two reacting interfaces per 100 nm). The 10 nm Al_2O_3 layers are for passivation. In (b), a top-down optical micrograph shows the electrical elements of the system. Current is passed through the heater strip from I^+ to I^- and the voltage drop is measured between V^+ and V^-. The heater strip and voltage "probes" define the measurement area of the sensor as shown (3.7 mm x 0.5 mm). Barely visible in the center of the strip are three 20-µm-square holes in the metallization to enable analysis in a transmission electron microscope. Also visible through the silicon nitride is a deposited 3Al:1Ni sample.

After fabrication, the nanocalorimeter sensors were annealed at 1023 K for 20 min in clean air to coarsen and stabilize the Pt grain structure. Annealing in air (versus high-purity inert gas) actually leads to higher quality films because oxygen reacts preferentially with the Ta adhesion layer to form TaO, which inhibits diffusion of Ta into the Pt [29]. To perform measurements, the temperature of the sensor is inferred by measuring the time-varying resistance of the Pt heater strip. Because the resistance is very sensitive to small variations in the Pt metallization, the sensors must be individually calibrated. This is done in air in a series of heat-and-hold steps as detailed previously [32]. At each step the temperature of the sensor is recorded with a calibrated infrared pyrometer (Pyrometer Optitherm II) and the sensor resistance is measured using a precision source-measure unit (National Instruments PXI-4130). By repeating this over a large number of steps, a calibration of temperature as a function of resistance is obtained. Calibration data was obtained between room temperature ($\approx$ 298 K) and 1000 K.

To investigate the Al/Ni interfacial reaction, we deposited 3:1 Al:Ni samples onto the backside of the sensors as shown in Fig. 5.1a via electron-beam evaporation through a shadow-mask. The 3:1 composition was chosen to match the composition of the first phase expected to form, Al_3Ni. This allowed us to avoid complicating our investigation with multiple reaction products. The evaporation system (Denton Infinity) was pumped to a base pressure of 4×10^{-4} Pa before initiating deposition. The samples tested in this work are depicted schematically in Fig. 5.1a and consisted of 41 nm of Al, 18 nm of Ni, and another 41 nm of Al for a total thickness of 100 nm. They were capped on both sides by 10 nm of Al_2O_3 to prevent oxidation of the metallic Al. The illustrated sample geometry is designed to feature two reacting interfaces, making it equivalent to an Al/Ni multilayer with a bilayer period of 100 nm. Deposition times were controlled by a quartz crystal thickness monitor. The source purities were 99.999% (Al), 99.995% (Ni), and 99.99% (Al_2O_3).

In order to achieve the highest heating rates possible, heat losses were minimized by conducting all experiments in a vacuum of better than 1×10^{-3} Pa. This also provided a consistent environment between *in situ* and *ex situ* tests. A custom-built nanocalorimetry TEM holder described previously [30] was used for all tests as it provided a convenient platform for making electrical connections and maintaining the sample under vacuum. Heating experiments were conducted in a voltage-limited mode based on custom voltage waveforms output by a high-resolution digital-to-analog converter (National Instruments PXI-4461). This waveform was passed through a unity-gain buffer amplifier (Burr-Brown BUF634) to supply the needed current to the chip. A truly constant heating rate cannot be produced without feedback, which is impractical to implement at the high heating rates utilized here. Instead, the voltage waveform was designed to deliver an approximately constant heating rate in the absence of reactions on the sensor. The details of the signals acquired and the subsequent data analysis are provided in Section 3.

Both *in situ* and *ex situ* transmission electron microscopy (TEM) were performed to identify phase transformations in the samples tested. *In situ* electron diffraction was performed in the Dynamic TEM (DTEM) at Lawrence Livermore National Laboratory using an approach described in detail previously [30]. In brief, the DTEM enables time-resolved electron diffraction and imaging with a minimum time resolution of 20 ns. For these experiments, the DTEM was operated in a 9-pulse movie mode with all pulses overlaid to increase the overall signal-to-noise. The pulse duration was 50 ns and the time between pulses was 500 ns so that the resulting electron diffraction patterns span 4.45 μs (0.45 μs of active integration). Time-resolved electron imaging is also available with this instrument but is of minimal utility for the study of interfacial phenomena since the sensors are mounted in plan view. The aforementioned nanocalorimetry TEM holder was built for compatibility with the DTEM and was used for these experiments. *Ex situ* TEM was conducted in an FEI Tecnai 12 using a second custom-built holder specifically designed to hold nanocalorimeter sensors. In both cases, polycrystalline selected-area electron diffraction patterns were analyzed by integrating them radially and then performing a series of background subtractions to correct for scattering from the silicon nitride membrane as described in Sec. 2.8.

5.3 Analysis Methodologies

Reliable analysis methodologies are a necessity if meaningful conclusions are to be drawn from experimental data. In this section we start by outlining the procedure used to extract meaningful thermal analysis data from nanocalorimetry experiments. This approach is different from that typically encountered in conventional calorimetry, and also differs in important ways from some of the nanocalorimetry analysis strategies that have been published previously. We then briefly describe conventional kinetic analysis and the isoconversional approach as it was applied in this work. Finally, we summarize the implementation of the "combined kinetic analysis" which is used to derive a reaction model in one part of this work.

5.3.1 Nanocalorimetry

It seems beneficial to briefly locate the nanocalorimetric technique utilized in this work within the broader context of thermal analysis. We distinguish two main techniques commonly used to measure heat flow: differential scanning calorimetry (DSC) and differential thermal analysis (DTA). Both techniques are "differential" in that they work by comparing the sample under test to a reference. If the reference (usually an empty sample pan) behaves similarly to the sample (aside from the reaction itself), a differential measurement simplifies the process of baseline subtraction because most of the contributions to the signal are identical for sample and reference and thus cancel out. The distinction between DSC and DTA is not always clear since both can function as "calorimeters" (i.e. report heat flow data) and manufacturers are not consistent in their application of these terms. However, here we follow [6] and distinguish DTA as a technique that relies on measurements of the temperature difference between sample and reference in a single furnace. In contrast, DSC utilizes individual sample and reference heaters and relies on measurements of the differential power to the sample required to maintain sample and reference at the same temperature. As such, DSC outputs power "natively" while the DTA-style techniques must infer the power from the differential temperature.

In this work we utilize nanocalorimetry in an *un-referenced* configuration (i.e. non-differential). In the context of the above discussion this approach can best be understood as a differential thermal analysis technique where the sample (via post-reaction baselines) serves as its *own* reference. Like DTA, heat flow in a nanocalorimetry experiment cannot be measured directly and must be inferred instead from temperature measurements. In the case of nanocalorimetry this information is encoded primarily in the heating rate, which follows a baseline determined by the applied power but is allowed to vary based on the power released or absorbed by the sample. Operating in a referenced/differential configuration is of marginal benefit in nanocalorimetry because chip-to-chip variations tend to be too large to obtain reliably good references. Invariably, referenced nanocalorimetry data must still be corrected based on the properties of the sample sensor if the best fidelity is required. As such, we chose to simplify the experiment and do away with the reference entirely, relying instead on the ability of nanocalorimetry to rapidly generate robust baseline data on a per-chip basis.

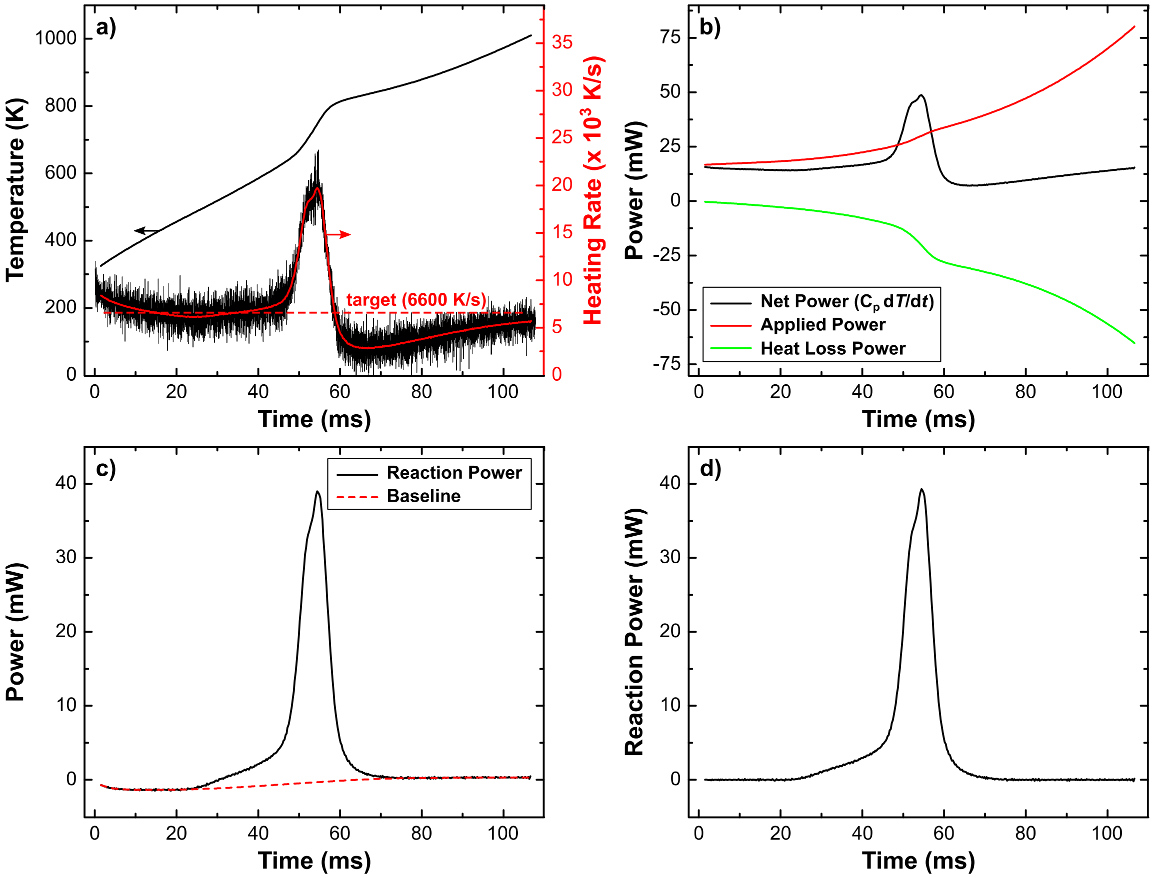

Figure 5.2 Depiction of the steps used to process the nanocalorimetry data in this work, taken from one of the experiments conducted at 6600 K/s. This sensor was processed at a downsampling ratio of 50. In (a) we see the raw temperature output from the sensor (black) and its derivative, the heating rate (red). The increase in heating rate around 50 ms corresponds to a reaction on the sensor. The black noisy signal behind the heating rate is the result that is obtained with a lower downsampling ratio of 4, and is shown to demonstrate that the data smoothing routine we use does not distort or shift the signals in time. After using baseline scans to obtain the heat capacity and heat losses as a function of temperature, their contributions to the overall power applied to the sensor are calculated and plotted along with the applied power in (b). Following Eq. (5.10), the quantities in (b) are combined to obtain the reaction power, plotted in (c). Since the baseline is still not entirely flat (reasons noted in the text), an empirical baseline is fitted (c) and subtracted (d) to obtain the final reaction power used in plotting and subsequent kinetic analysis.

For an un-referenced (single) nanocalorimeter sensor there are only two raw outputs: the voltage drop across the measurement area of the sensor, ΔV_{MA}, and the voltage drop across a current-sensing resistor, ΔV_{sense}. The current-sensing resistor is a high-tolerance, low-TCR power resistor with well-characterized, constant resistance

R_{sense}. From this, the instantaneous current flowing through the circuit as a whole is calculated as

$$I = \Delta V_{\text{sense}} / R_{\text{sense}} \tag{5.1}$$

and the time-varying resistance of the measurement area can subsequently be calculated as

$$R_{MA} = \Delta V_{MA} / I \tag{5.2}$$

A pre-measurement calibration process performed on every chip is used to fit an equation correlating resistance and temperature, $T_{\text{calib}}(R) = C_0 + C_1 T + C_2 R^2 + \cdots$. Applying this calibration to the resistance signal yields the time-varying temperature of the measurement area:

$$T_{MA} = T_{\text{calib}}(R_{MA}) \tag{5.3}$$

An example temperature curve from one of the experiments included in this work is shown in Fig. 5.2a. The raw inputs are sampled at high speed (200 kS/s) so the raw temperature is also obtained at this rate. It can be differentiated to obtain the heating rate, also shown in Fig. 5.2a. Since numerical differentiation is notoriously noisy, the raw voltage data are typically smoothed by a binned-average downsampling before calculations begin. The degree of downsampling is specified as the ratio of the original sampling rate (200 kS/s) to the new sampling rate, and is chosen individually for each sample with the goal of balancing signal clarity and accuracy. The measurement noise is approximately invariant with heating rate so the strongest smoothing is required for the lowest heating rates which have the worst signal-to-noise ratio. For the data reported in this work the downsampling ratios used varied from 200 for the lowest heating rates (1000 K/s) to 4 for the highest (100,000 K/s). The downsampling approach is designed to place the averaged points precisely in the temporal center of their parent bin. As such it avoids distorting or shifting the data temporally, a common issue with smoothing algorithms. This is illustrated in Fig. 5.2a, which shows the heating rate produced with two different downsampling ratios, 4 (an example of a "noisy" signal) and 50 (used in the actual data processing).

The overall thermal balance of the measurement area can be expressed as

$$C_p \dot{T}_{MA} = \dot{Q}_{\text{app}} + \dot{Q}_{\text{loss}} + \dot{Q}_{\text{rxn}} + \cdots \tag{5.4}$$

where $\dot{T}_{MA}$ is the heating rate of the measurement area as discussed above, C_p is its heat capacity (including sample), and the terms on the right hand side are various power contributions, namely the applied power, heat loss power , and reaction power respectively. The ellipsis indicates that we cannot exclude the possibility of other minor contributions to the thermal balance, but we restrict ourselves to these majority contributions here. The term of most interest to the researcher is the power coming from reactions on the sensor, $\dot{Q}_{\text{rxn}}$. Eq. (4.4) holds the promise of a straightforward computation of this term provided we can obtain values (or estimates) of C_p, $\dot{Q}_{\text{app}}$, and $\dot{Q}_{\text{loss}}$. The applied power can be calculated directly from the current and voltage drop:

$$\dot{Q}_{\text{app}} = I \Delta V_{MA} \tag{5.5}$$

The other two terms cannot be derived directly from the experimental scan. However, if we make the assumption that they are functions only of temperature, we can assess this temperature dependence using post-reaction baseline measurements and then estimate their contribution to the original experiment using the experimentally measured temperature profile (Eq. (5.3)). To do this we leverage the fact that the Al/Ni reaction studied in this work is irreversible. This enables us to perform post-reaction baseline measurements of the combined sample and sensor without the complicating factor of additional reactions occurring in the sample.

The heat loss term can be obtained in several ways. Here, we used a continuous slow-heating scan that covers the temperature range of interest in approximately one minute (a heating rate of 10 – 20 K/s on average). Since the heat capacity of the sensor is very small, even at this heating rate (which is high by conventional thermal analysis standards) the sensor is essentially in continuous thermal equilibrium with its surroundings. To understand this, consider Eq. (4.4) in the absence of a reaction:

$$C_p \dot{T}_{MA} = \dot{Q}_{\text{app}} + \dot{Q}_{\text{loss}} \tag{5.6}$$

Solving for $\dot{Q}_{\text{loss}}$,

$$\dot{Q}_{\text{loss}} = C_p \dot{T}_{MA} - \dot{Q}_{\text{app}} \tag{5.7}$$

The thermal equilibrium assumption is that $C_p \dot{T}$ is much smaller than $\dot{Q}_{\text{app}}$ and $\dot{Q}_{\text{loss}}$ and can thus be neglected. The total heat capacity of the sensor and sample is typically 3 μJ/K – 5 μJ/K, while the power and loss terms are on the order of tens of mW (see, e.g. Fig. 5.2b). Taking $C_p = 5\ \mu\text{J/K}$ and $\dot{Q}_{\text{loss}} \approx \dot{Q}_{\text{app}} \approx 10\ \text{mW}$, $C_p \dot{T}_{MA}$ is $< 1\ \%$ of the other quantities for any heating rate below 20 K/s.[a] We can then obtain the heat loss contribution from a single scan as $\dot{Q}_{\text{loss}} = -\dot{Q}_{\text{app}}$. $\dot{Q}_{\text{app}}$ is measured experimentally, so we simply record it and then take its negative for the heat loss curve. This curve is subsequently fitted to a function of the form

$$\dot{Q}_{\text{loss}}(T) = A(T - T_0) + B(T^4 - T_0^4) \tag{5.8}$$

---

[a] As a fraction of the derived signal this approximation is worst at low temperatures where its accuracy is also least important. This analysis also assumes that heat losses are a function only of temperature, i.e. the time constant for heat losses is short relative to even the highest heating rates. This assumption appears to be reasonable since we have observed negligible differences between the heat losses obtained by slow heating and those obtained at higher heating rates using other approaches.

where T_0 is the ambient temperature and A and B are fit coefficients. This equation is formulated to account for generalized conductive (T^1) and radiative (T^4) losses and typically yields very good fits to the data ($R^2 > 0.999$). Once the heat loss fit is obtained we can perform additional baseline scans at higher heating rates to assess the heat capacity term. By rearranging Eq. (5.6) we can compute the heat capacity as

$$C_p = \frac{\dot{Q}_{\text{app}} + \dot{Q}_{\text{loss}}}{\dot{T}_{MA}} \tag{5.9}$$

To perform this calculation we parameterize $\dot{Q}_{\text{app}}$ and $\dot{T}_{MA}$ in terms of temperature and use the heat loss fit as in Eq. (5.8) so that C_p is computed directly as a function of temperature. In theory this could be done from a single baseline scan, but practically the result is made more robust by (1) performing the computation at multiple heating rates and (2) performing a number of duplicate experiments at each heating rate. The evaluation proceeds by first averaging all baseline scans acquired at a given heating rate and computing a single $C_p(T)$ curve for that heating rate, and then averaging these curves. The result is fitted with a 5th-order polynomial so that it can be applied to an arbitrary temperature program.

Finally, then, we can use the derived values for C_p, $\dot{Q}_{\text{app}}$, and $\dot{Q}_{\text{loss}}$ to compute the reaction power directly from Eq. (4.4):

$$\dot{Q}_{\text{rxn}} = C_p(T_{MA})\dot{T}_{MA} - \dot{Q}_{\text{app}} - \dot{Q}_{\text{loss}}(T_{MA}) \tag{5.10}$$

The three terms on the right-hand side of Eq. (5.10) are depicted for a representative experiment in Fig. 5.2b. The resulting $\dot{Q}_{\text{rxn}}$ is shown in Fig. 5.2c. Generally speaking, the result obtained by direct application of Eq. (5.10) has a sufficiently flat baseline to allow immediate interpretation and comparison of results. However, errors in the heat loss and heat capacity calibrations usually prevent the baseline from being completely flat. In particular, since the heat capacity calibration is performed after the reaction is complete it cannot account for the difference in heat capacity between reactants and products. Quantitative analysis requires a completely flat baseline, so a manual fitting is used to correct any remaining offset in the data. For the data reported here the manual baselines took the form of increasing sigmoidal curves as shown in Fig. 5.2c. The final result is shown in Fig. 5.2d.

5.3.2 Kinetic Modeling

If a set of kinetic curves all describe the same net reaction, it is reasonable to reduce them to the extent of conversion, α, which varies from 0 (unreacted) to 1 (fully reacted) over the course of the experiment. For calorimetric data, this parameter is calculated as the ratio of the heat released or absorbed up to time t ($\Delta H_{\text{cum}}(t)$) to the total heat released/absorbed in the reaction (ΔH_{tot}), i.e.

$$\alpha(t) = \frac{\Delta H_{\text{cum}}(t)}{\Delta H_{\text{tot}}} = \frac{\int_0^t \dot{Q}_{\text{rxn}} dt}{\int_0^{t_{\max}} \dot{Q}_{\text{rxn}} dt} \tag{5.11}$$

For differential data these parameters are obtained by numerical integration of the baseline-subtracted differential data. In our work this integration was performed using the trapezoidal rule – more complex integration schemes can yield erroneous results when applied to noisy data. Using the computed total heat of reaction the reaction rate $d\alpha/dt$ can be computed directly from the reaction power as

$$\frac{d\alpha}{dt} = \frac{\dot{Q}_{\text{rxn}}}{\Delta H_{\text{tot}}} \tag{5.12}$$

The theoretical reaction rate for a single-step process is commonly written as

$$\frac{d\alpha}{dt} = f(\alpha)k(T) \tag{5.13}$$

Here $f(\alpha)$ is the "reaction model" which is a function only of conversion and $k(T)$ is a factor that depends only on temperature. If the reaction is assumed to follow Arrhenius kinetics, we can substitute $k(T) = A\exp(-E/RT)$ to obtain

$$\frac{d\alpha}{dt} = f(\alpha)A\exp(-E/RT) \tag{5.14}$$

where A is the pre-exponential factor with units of inverse time and E is the Arrhenius activation energy. The three terms $f(\alpha)$, A, and E are often referred to as a "kinetic triplet" since together they form a complete description of the reaction kinetics (provided the kinetics follow Eq. (5.14)). Although most situations are more complex, the basic goal of most thermal analysis can be understood as the determination of the complete kinetic triplet for the process under investigation.

5.3.3 Isoconversional Analysis

If Eq. (5.14) is accurate, it implies that when α is held constant the reaction rate should depend only on temperature. This idea is the origin of the isoconversional approach. If the temperature at a particular extent of conversion is varied (most commonly by varying the heating rate), the resulting variations in reaction rate will tell us about the reaction's dependence on temperature, i.e. its *activation energy*. If high-quality differential data are available, the requisite analysis can be derived directly from Eq. (5.14) by taking the natural logarithm of both sides:

$$\ln\left(\frac{d\alpha}{dt}\right)_{\alpha,i} = \ln[f(\alpha)A_\alpha] - \frac{E_\alpha}{RT_{\alpha,i}} \tag{5.15}$$

This equation is the differential isoconversional method attributed to Friedman [33]. The α subscripts indicate that we have applied the isoconversional principle, i.e. the equation is valid for a constant extent of conversion. The i subscripts indicate experimental values that we have multiples of, one from each unique heating program/experiment. Using Eq.

(5.15), analysis proceeds by plotting the experimental $\ln(d\alpha/dt)_\alpha$ versus $1/T_\alpha$ data for every heating program and fitting a straight line to the data to obtain E_α and $\ln[f(\alpha)A_\alpha]$. The procedure is repeated over a range of α to build up a continuous curve of "effective activation energy" E_α versus α.

Despite its simplicity, applications of the Friedman method seem to be relatively uncommon in the literature, perhaps because its use of the reaction rate directly makes it more sensitive to experimental noise than the less accurate linear integral methods. The Friedman method is well-suited to nanocalorimetry, however, because it can be applied to any temperature program (the linear integral methods are restricted to constant heating rates). Similar universality has been achieved with advanced integral methods [34], but since the output of the data analysis is a differential quantity (Eq. (5.10)) we opted for the computational simplicity of the Friedman method.

A word of explanation is needed regarding the concept of "effective" or "variable" activation energy. Eqs. (5.13) - (5.15) are written under the assumption that the reaction described occurs in a single-step, i.e. it can be fully described by a single kinetic triplet. In practice and especially in condensed phase reactions this is seldom a very good assumption. To truly simulate these reactions more complex reaction models are needed. However, if we restrict consideration to small regions of α we can argue for approximately single-step behavior within each region. The temperature-scaling in each region is then described by an *effective* activation energy which is some weighted average of the activation energies of all the individual reactions operating in the region. Thus, in general, the result of isoconversional analysis of a complex process is a plot of effective activation energy that varies with α based on the relative contributions of all the underlying processes. Values can be read off this curve to estimate the activation energy of a process in a regime of α where it is expected to dominate, and the nature of the variations in effective activation energy can sometimes be used to infer the particular type of complexity underlying them (see, e.g. [35,36]).

5.3.4 Combined Kinetic Analysis

Application of the isoconversional method yields direct, model-free estimates of E, but the other two components of the kinetic triplet are still needed to fully model a reaction. Of these, the reaction model $f(\alpha)$ is of particular interest because it gives the clearest insight into the nature of the process being studied. A can often be left as a fitting parameter, but the form of $f(\alpha)$ must generally be derived from the data.

A number of approaches for doing this exist as reviewed by the ICTAC Kinetics Committee [10]. Here, we employ the "combined kinetic analysis" as proposed by Pérez-Maqueda and co-workers [37]. This approach allows us to apply the standard linear model-fitting approach to our entire experimental dataset simultaneously, circumventing many of the pitfalls associated with traditional single-curve model fitting. The analysis is based on the typical linearized form

$$\ln \frac{d\alpha/dt}{f(\alpha)} = \ln A - \frac{E}{RT} \tag{5.16}$$

which is obtained by rearranging Eq. (5.14) and then taking the natural logarithm. Standard linear model fitting calls for the substitution of various tabulated reaction models (see, e.g. [38]) for $f(\alpha)$ and the selection of the one that yields the best fit. This is problematic when no clear best fit emerges (either because none of the tabulated models fit or because multiple models yield fits of comparable quality). In combined kinetic analysis, instead of many discrete reaction models we use a single parameterized model

$$f(\alpha) = c\alpha^m(1-\alpha)^n \tag{5.17}$$

This equation is a truncated form of a more complicated parameterized model proposed by Ŝesták and Berggren [39] and is hence referred to as the reduced Ŝesták-Berggren equation. Pérez-Maqueda showed in [37] that Eq. (5.17) is able to accurately mimic the entire body of commonly-used reaction models. As such we can substitute it into Eq. (5.16) to obtain an expression that is valid for any single-step reaction given appropriate choices for m and n:

$$\ln\frac{d\alpha/dt}{\alpha^m(1-\alpha)^n} = \ln cA - \frac{E}{RT} \tag{5.18}$$

To identify the best-fitting reaction model, a nonlinear optimization of m and n is performed (here we used the Broyden Quasi-Newton method) with the objective of maximizing the linear correlation between the left-hand side of Eq. (5.18) and inverse temperature. The slope and intercept of the best fit then give the values of E and $\ln cA$ respectively. If the values of m and n obtained are a good match to one of the tabulated models we can use the corresponding value of c to compute A directly. Even if this is not the case, the derived model can be used to make kinetic predictions and the values of m and n can give us valuable information about the nature of the reaction mechanism. As noted by the original authors, this method yields the most robust results when the optimization is performed on a combined dataset containing multiple kinetic curves obtained under different temperature programs [37]. However, it must be remembered that the analysis is only fully valid for a single-step reaction. Its application should be restricted to those regimes where a single-step approximation seems reasonable.

5.4 Results

Experiments were conducted at 11 nominal heating rates, corresponding to five unique heating rates per decade between 1000 K/s and 100,000 K/s on an approximately logarithmic scale. Two experiments were conducted at each target heating rate. While target heating rates are used throughout the text to reference individual experiments, the actual heating rates that the samples experienced varied continuously during each experiment as is expected for nanocalorimetry (see, e.g. Fig. 5.2a). The correspondence between target and actual heating rate for each set of tests is summarized statistically in Table 5.1.

Table 5.1 Summary of the heating rates at which tests were performed. The target heating rate was used to compute the heating waveform for the experiment. Since the actual heating rate is not constant, summary statistics are provided to give a sense of how large the variations were. Experimental values are an average of values from two runs at the same target.

Target Heating Rate (K/s)	Experimental Heating Rate (K/s)		
	Mean	Minimum	Maximum
1000	953	132	2620
1600	1530	185	4520
2600	2490	412	7800
4100	3870	1020	12,300
6600	6470	2720	20,500
10,000	9920	5080	28,400
17,000	17,300	10,300	45,300
27,000	29,900	14,800	71,100
43,000	54,200	21,900	118,000
69,000	99,200	47,500	199,000
100,000	148,000	48,900	291,000

We struggled to find a way to present the experimental data that would facilitate comparisons without being misleading. The challenge is that the raw output of the nanocalorimetry experiments, Eq. (5.10), is a power. As such, it spans the same two decades of magnitude as the heating rate, and a plot scaled to display the highest powers would give a very poor representation of the lowest. One obvious solution is a logarithmic scale, but this isn't ideal because while it compresses the high power regime it also expands the lowest powers and exaggerates experimental noise. Another solution is to convert the power (a time-domain signal) into the differential heat release per temperature, dH/dT, and then plot it versus temperature. This is the approach used to compare traditional calorimetry data collected at multiple heating rates, but the problem is that nanocalorimetry data are not collected at a constant heating rate, so dH/dT must be calculated based on the instantaneous heating rate as

$$\frac{dH}{dT} = \frac{\dot{Q}_{\mathrm{rxn}}}{\dot{T}} \tag{5.19}$$

While mathematically consistent, doing this divorces dH/dT from most of its traditional meaning, which is as a normalized signal proportional to $\dot{Q}_{\mathrm{rxn}}$. Reaction rates are, after all, fundamentally time-domain signals (see Eq. (5.13)). The interpretation of heat release "per temperature" is only meaningful so long as the time-dependence of temperature itself is not in dispute. As soon as the heating rate is allowed to vary simultaneously, the interpretation of a signal like dH/dT becomes extremely challenging. Finally, perhaps the simplest option is simply to normalize the experimental reaction powers by their maximum values and then plot these curves versus temperature. This gives the truest representation of relative reaction rate as a function of temperature, but obscures the actual heat release in each experiment.

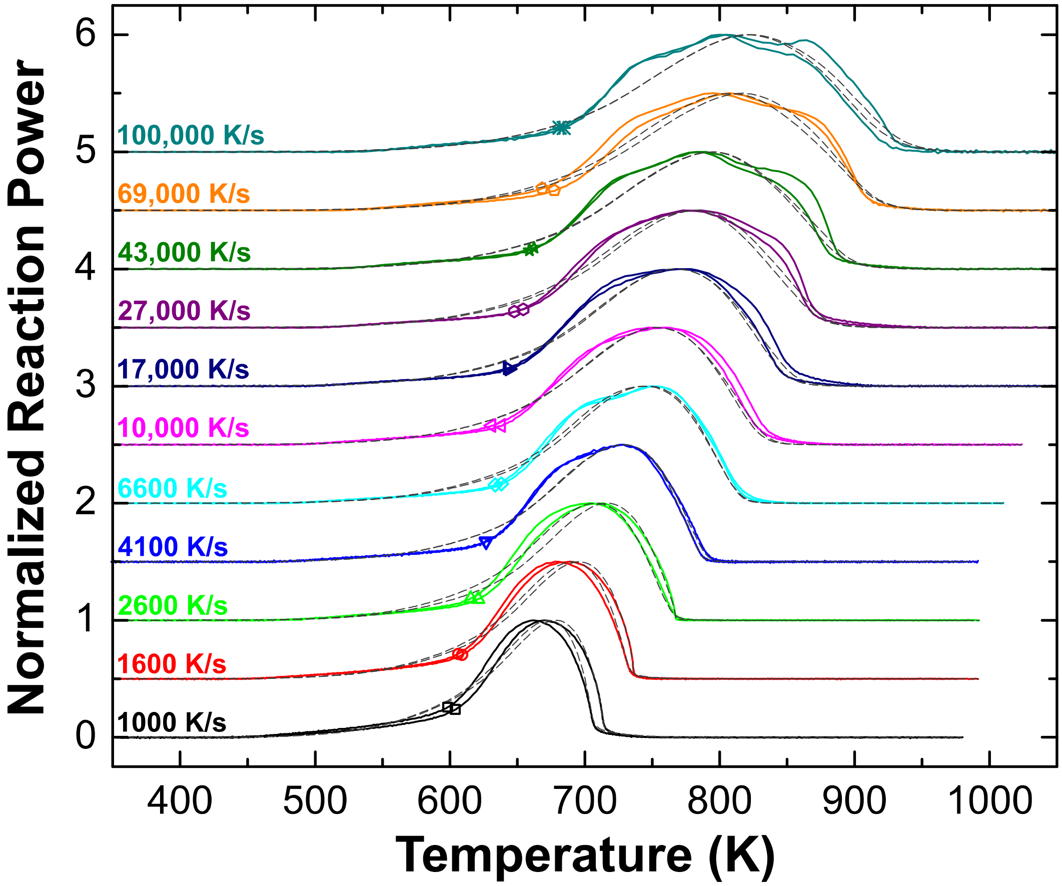

Figure 5.3 Plot of reaction power/reaction rate versus temperature for the 11 heating rates tested. To facilitate comparison, the reaction rates were normalized by dividing by the maximum reaction rate and then offset for clarity. Two scans are presented for each target heating rate to demonstrate repeatability. Where the scans are offset in temperature this most likely reflects a variation in the temperature program. Note that in this format the area under the curves is not directly proportional to heat release. The extra points (shapes) superimposed on the experimental curves indicate the experimentally measured nucleation threshold. The dashed gray curves are simulations of the experiments performed using the kinetic triplet derived for the growth stage of the reaction (Table 5.4).

In summary, then, none of these approaches is without drawbacks. The challenge of presenting signals collected over multiple decades in (variable) heating rate is relatively new but evidently not unique to us, plaguing even results published in high-impact journals [11]. A consensus on how it should be treated has yet to emerge, so here we have compromised by providing two alternative presentations of our data. The first, shown in Fig. 5.3, is a plot of normalized reaction rate versus temperature. The second, shown in Fig. 5.4, is a plot of dH/dT (calculated from Eq. (5.19)) versus temperature. In both presentations, we see one major exothermic feature across all experiments that shifts to higher temperatures as the heating rate increases. In Fig. 5.3 we see that the main exothermic event develops one shoulder (before the peak) around 6600 K/s and a second shoulder (after the peak) around 27,000 K/s. These features are less pronounced in Fig. 5.4. In both depictions we also observe a small but consistent heat release prior to the main reaction peak.

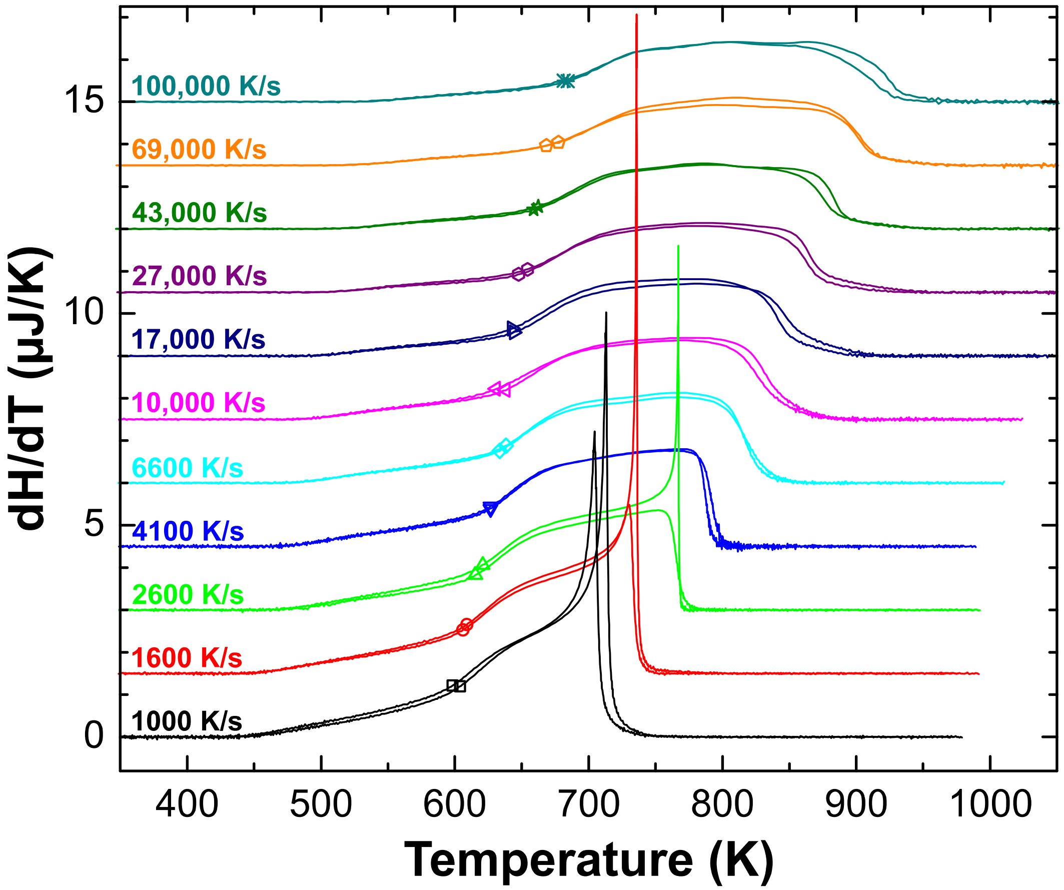

Figure 5.4 Plot of the differential heat release per temperature (dH/dT) versus temperature for the 11 heating rates tested, calculated using Eq. (5.19). This presentation should be familiar to readers who work with conventional calorimetry, but interpretation is challenging because the heating rate in Eq. (5.19) is not constant as typically assumed. For example, the sharp spikes in some of the low heating rate scans are artifacts that appear because the heating rate drops close to zero at the end of the reaction – they do not imply a true acceleration in the kinetics. However, this presentation has the benefit that it does not require arbitrary normalization and the areas under the curves are directly proportional to heat release. The areas under the curves are approximately equal and yield an average heat of reaction of 3.53×10^{-4} J ± 3.0×10^{-5} J. The extra points (shapes) superimposed on the experimental curves indicate the experimentally measured nucleation threshold.

Ex situ transmission electron microscopy (TEM) was used to establish the identity of the initial and final phases. Selected-area electron diffraction (SAED) of a sample prior to reaction showed that the only crystalline phases were fcc Ni and Al. Post-reaction SAED was performed on samples tested at three different heating rates (2600 K/s, 17,000 K/s, and 69,000 K/s) and radially integrated diffraction patterns for these samples are presented in Fig. 5.5. All three samples only show evidence for the Al_3Ni intermetallic phase (oP16).

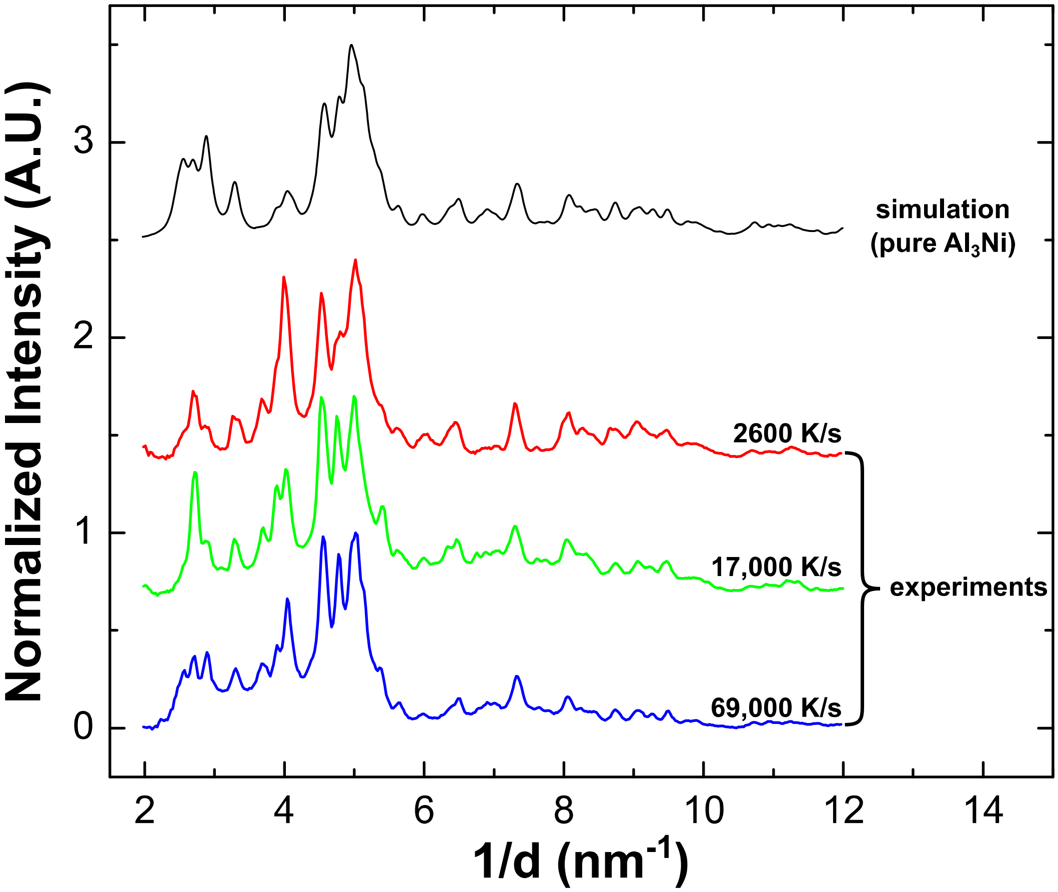

Figure 5.5 Selected-area electron diffraction (SAED) patterns obtained from samples that were reacted at three representative heating rates. It is difficult to index these patterns directly because of the large number of overlapping diffraction peaks. Instead, a simulated diffraction pattern for pure Al_3Ni (oP16) is provided for comparison. While we observe variations in peak intensity, all peaks in the experimental curves are observed in the simulated curve as well leading us to conclude that the final phase is pure Al_3Ni.

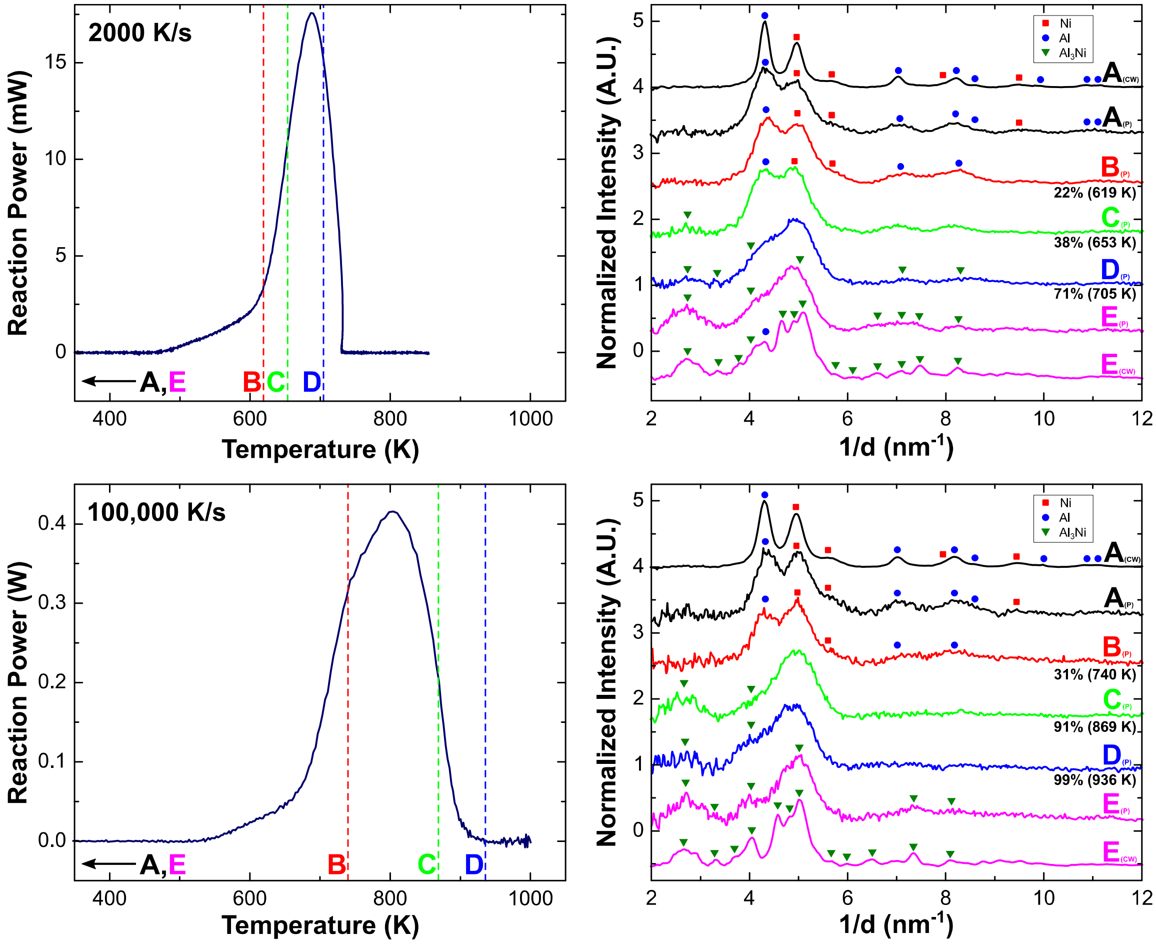

Figure 5.6 *In situ* nanocalorimetry results for two representative heating rates, 2000 K/s (top) and 100,000 K/s (bottom). At left are representative nanocalorimetry curves for these heating rates plotted as reaction power versus temperature. At right are SAED patterns captured using Dynamic TEM at the three points indicated in each plot at left, as well as before and after the experiment. For the before and after patterns (A and E) both a conventional (labeled "CW") and pulsed (labeled "P") pattern were recorded. These patterns were acquired at room temperature. Patterns captured during the heating experiment (B – D) are labeled with the extent of conversion (as a percentage) and the temperature at which they were captured. At both heating rates the diffraction patterns show the consumption of pure Al and Ni and formation of Al_3Ni, with no intermediate products.

In order to assess whether the actual reaction pathways are identical, in situ characterization is needed. Here, we applied a previously developed in situ nanocalorimetry technique to assess the phases present in the sample as a function of time at two extremes of heating rate, 2000 K/s and 100,000 K/s. The time-resolved electron diffraction patterns obtained from these experiments and their relationship to the nanocalorimetric heat release are summarized in Fig. 5.6. These patterns are harder to interpret than those in Fig. 5.5 because each is formed by far fewer electrons, but comparison to the before and after conventional patterns still gives no indication of any phases forming during the reactions other than Al_3Ni. Specifically, we observe the gradual disappearance of the Al (111) peak at 4.30 nm^{-1} and a corresponding increase in intensity around 2.72 nm^{-1}, a signature of Al_3Ni corresponding to the combined intensity of the (011), (101), (020), (111), and (200) reflections.

To obtain an experimental measure of the heat of reaction we integrated the reaction power with respect to time for all samples. The resulting value averaged across all samples (n = 22) is 3.53×10^{-4} J ± 0.30×10^{-4} J. To compare this to literature values it must be adjusted for the mass of sample on the sensor. Using bulk values for the density of Al and Ni, their intended thicknesses, and a measurement area of 0.5 mm x 3.7 mm, we estimate the total sample mass as 7.06×10^{-7} g (2.02×10^{-8} moles of atoms). This gives a heat of reaction of 500 J/g ± 43 J/g (17.5 kJ/(mol-atoms) ± 1.5 kJ/(mol-atoms)). While this value is about half of what has been measured experimentally using more conventional techniques, 38 kJ/(mol-atoms) [40], evaluation of specific quantitative thermodynamic values using nanocalorimetry is notoriously difficult because of the large uncertainty in sample mass. Here, the error may be due to a bad calibration for the thickness monitor during sample deposition or deviations in the density of the deposited films relative to the bulk. We argue that this discrepancy in the measured heat of reaction does not invalidate the analysis that follows since electron diffraction still indicates that we are forming the intended intermetallic phase. The nanocalorimetry results are consistent across all experiments and heating rates so they still permit relative comparisons between experiments.

5.5 Discussion and Analysis

Ex situ electron diffraction results indicate that the final phase for all samples is the expected Al_3Ni intermetallic, and *in situ* electron diffraction shows no evidence of any other intermediate phases at either extreme of heating rate. Thus we conclude that the net reaction recorded in the nanocalorimetry data is the same regardless of heating rate and corresponds to the exothermic mixing of Al and Ni and the formation of the Al_3Ni phase. This confirmation permits us to convert the experimental heat release data to the dimensionless reaction progression, α, and reaction rate, $d\alpha/dt$, using Eqs. (5.11) and (5.12). The resulting reaction progression curves are plotted versus temperature in Fig. 5.7, illustrating the very large range of isoconversional temperatures that are sampled in the present data set (e.g. $\approx$ 200 K at $\alpha = 0.9$). A separate plot of $d\alpha/dt$ is not given because like $\dot{Q}_{\mathrm{rxn}}$, the reaction rate must be normalized for plotting as a set. The two descriptions are indistinguishable when normalized, meaning that a plot of $d\alpha/dt$ is already available as Fig. 5.3.

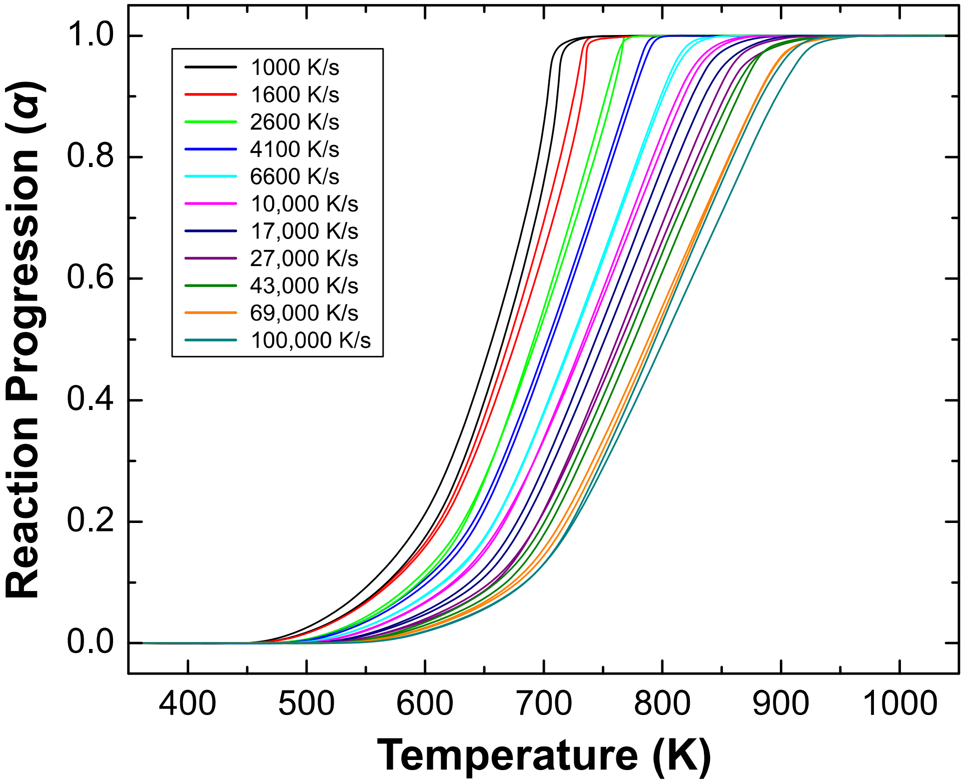

Figure 5.7 Reaction progression (α) versus temperature for the 11 heating rates tested in this work. Both scans are presented for each heating rate to demonstrate repeatability. Where the scans are offset in temperature, this is likely due to variations in the temperature program between the two scans. Isoconversional datasets can be visualized as the intersections of the curves with horizontal (constant α) lines. At large α these datasets span almost 200 K.

Next, we performed isoconversional analysis of the data using the differential method as given in Eq. (5.15). All experiments were resampled onto a uniform grid in α ($0.01 \leq \alpha \leq 0.99$ with $\Delta\alpha = 0.01$) and activation energies were obtained by fitting to isoconversional sets of $\ln d\alpha/dt$ versus $1/T$. Fig. 5.8 depicts a sampling of these isoconversional datasets and their corresponding activation energy fits. The full effective activation energy as a function of conversion is presented in Fig. 5.9. As a quick check we can confirm that all of the values reported in Fig. 5.9 are within the range of activation energies that have been reported in the literature for Al_3Ni formation (96.3 kJ/mol – 183 kJ/mol [19]). However, the effective activation energy as a function of conversion can tell us much more than that – in particular, in Fig. 5.9 we also observe statistically significant variations in the effective activation energy over the course of the reaction. This implies a “complex” (i.e. multi-step) reaction mechanism since a single-step reaction would give rise to a constant activation energy over the entire range of conversion.

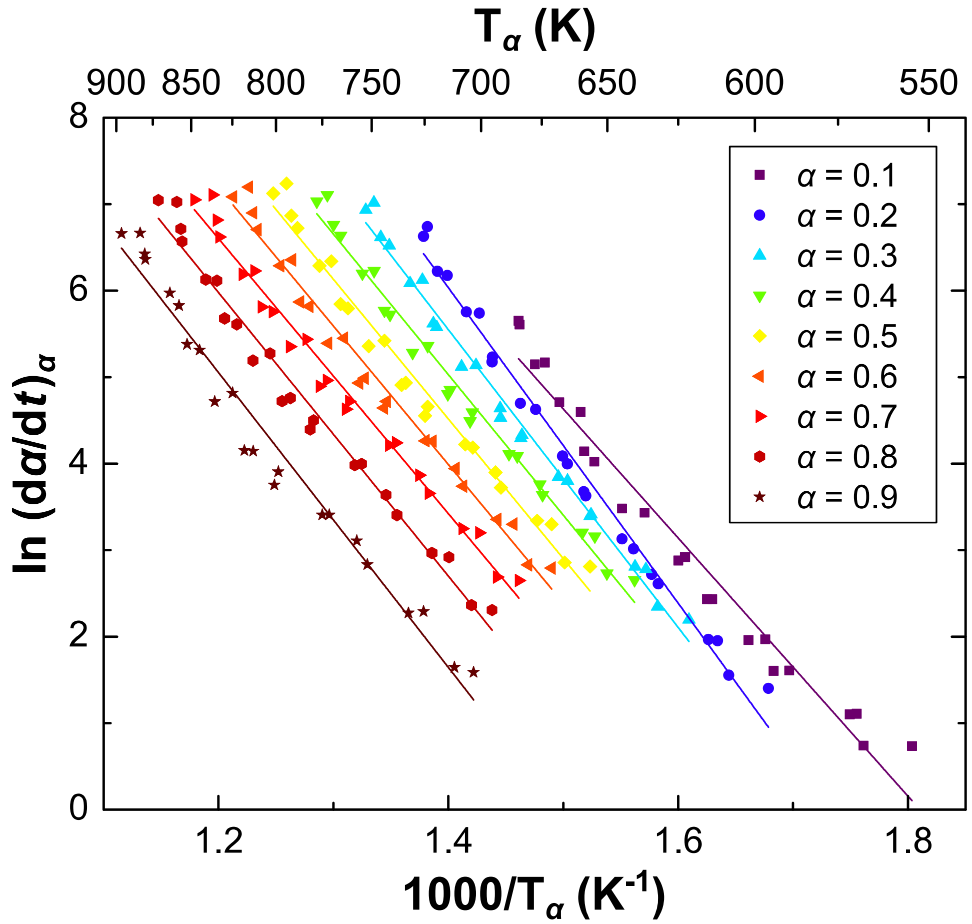

Figure 5.8 Selected isoconversion datasets used in conjunction with Eq. (5.15) to compute the effective activation energy. Each set consists of one data pair from each experiment (n = 22). The data pairs are the reaction rate $(d\alpha/dt)_\alpha$ and sample temperature T_α for that experiment at the specified extent of conversion. Also shown are the lines-of-best-fit for each set. The slopes of these lines yield an estimate of the activation energy for the process at that extent of conversion as reported in Fig. 5.9.

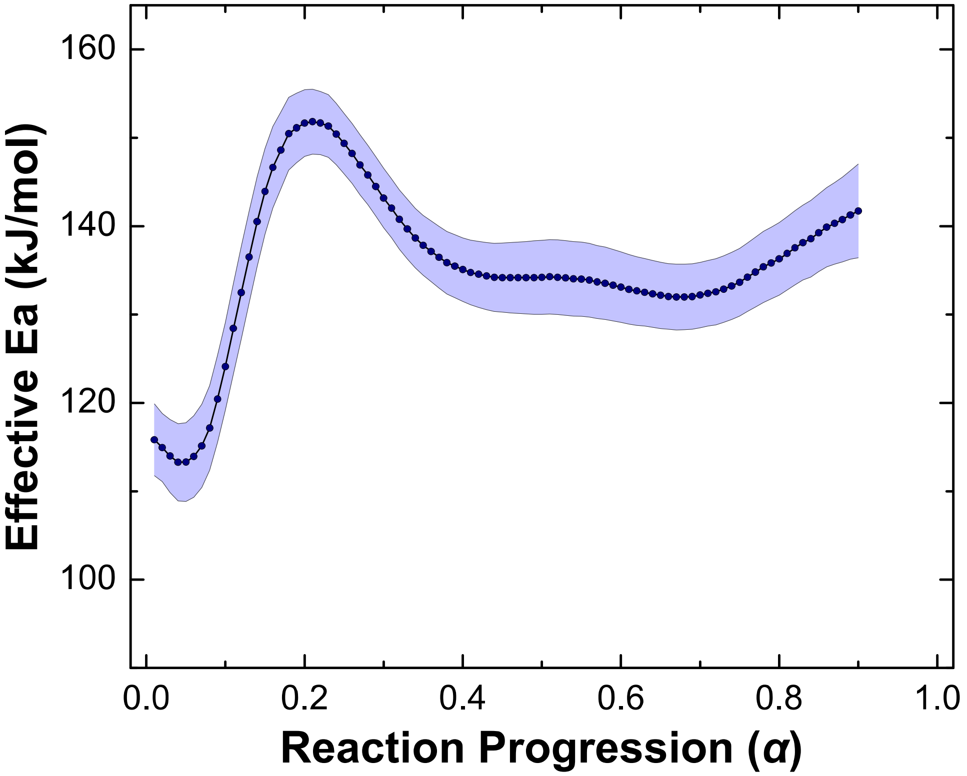

Figure 5.9 Plot of the effective activation energy as a function of reaction progression, obtained from simultaneous isoconversional analysis of all heating experiments performed. Dots indicate actual computed values (spaced 0.01 in α). The confidence band indicates one standard error in the activation energy on either side of the calculated value. The data for $\alpha > 0.9$ yielded unreliable (poorly correlated) regressions, so these results have been omitted. The points shown all arise from fits with $R^2 > 0.965$.

We can obtain some idea of the significance of the features observed in the effective activation energy curve by comparing them to those seen in the experimental reaction profiles (e.g. Fig. 5.3). This is made easier by plotting the normalized reaction rate directly versus conversion as in Fig. 5.10. When we do this we see that the lower activation energy at the beginning of the reaction seems to be correlated with the exothermic shoulder preceding the main exothermic heat release, and that the shoulders/bumps observed at the beginning, middle, and end of the main exothermic peak have corresponding maxima in the effective activation energy as a function of conversion. This suggests that a full description of the reaction kinetics may involve a large number of competitive or cooperative processes working together. While such a prospect is intriguing, a thorough investigation of all of these features is beyond the scope of this work. Instead, we decided to restrict ourselves to a discussion of three fundamental features that were observed universally across all samples, namely:

1) A low-conversion (α) regime with a low reaction rate and activation energy,
2) A relatively abrupt transition from this regime to one of higher reaction rate, and
3) A broad main reaction peak in which the majority (≈ 80 %) of the heat is released.

As will be discussed below, we believe these features correspond to (1) initial intermixing, (2) the onset of nucleation, and (3) growth of the Al_3Ni product phase.

5.5.1 Interdiffusion

The reaction begins with relatively gradual heat release that is visible as a broad shoulder on the front end of the reaction profiles in Fig. 5.3 and an approximately linear region of shallow slope at small α in Fig. 5.10. This regime begins at the start of the reaction ($\alpha = 0.01$) and ends when the sample exhibits a sharp increase in reaction rate. The position of this transition varies across the samples tested but generally occurs between $\alpha = 0.1$ and $\alpha = 0.2$. The details of this variation are more relevant to the discussion of nucleation which is addressed in the next section. For the moment it's sufficient to note that while the transition point varies, all of the samples are in the initial reaction regime until at least $\alpha \approx 0.1$.

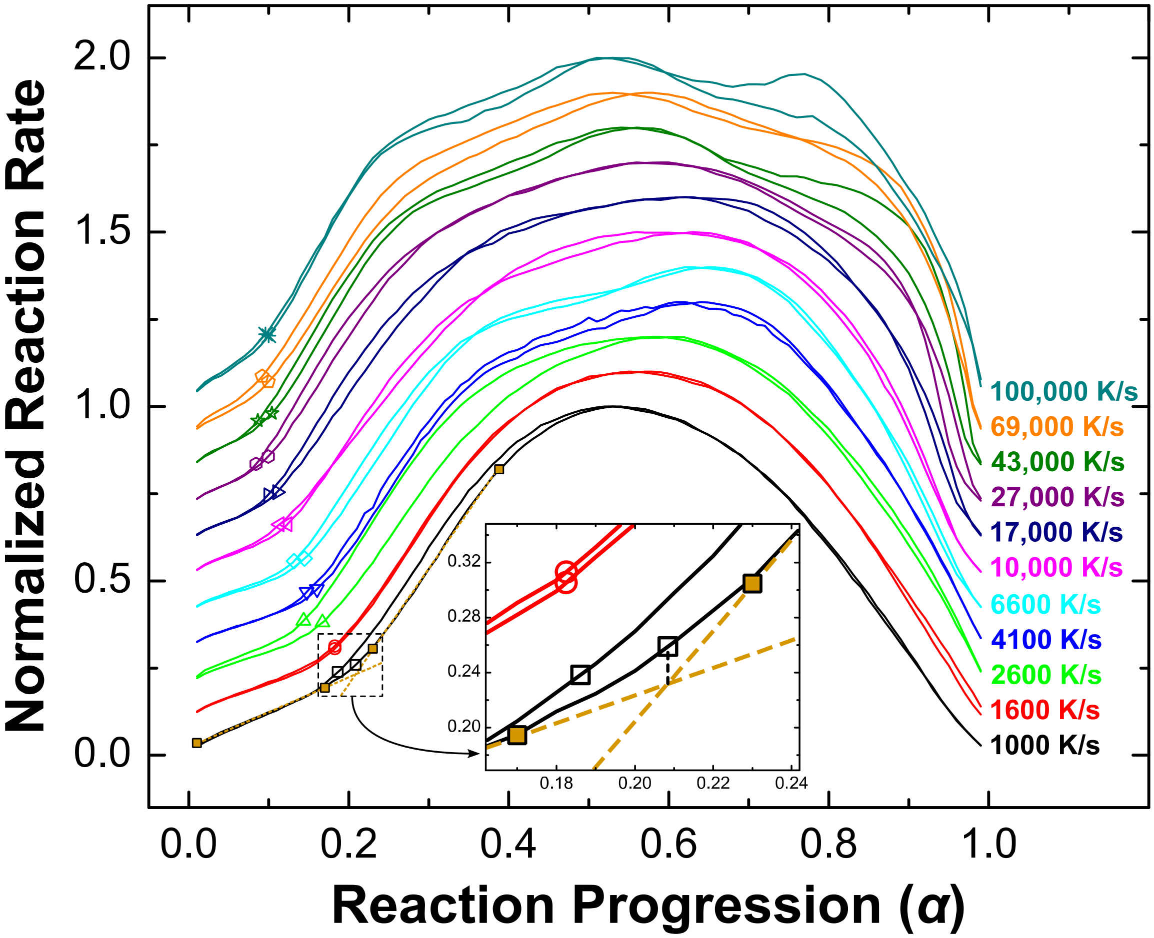

Figure 5.10 Plot of reaction rate $d\alpha/dt$ versus reaction progression for the 11 heating rates tested. To facilitate comparison, the reaction rates are normalized by dividing by the maximum reaction rate. The resulting plots all span the range 0 to 1 but are offset for clarity. In the initial stages of reaction all of the traces exhibit a fairly distinct transition from a shallow to a steeper slope. We identify this transition point as the onset of nucleation and have measured it for each experiment as indicated. The procedure for finding these points is illustrated for the lowermost curve.

The most likely explanation for this observed heat release is the exothermic intermixing of Ni and Al and the formation of a metastable solid solution at the interface. Intermixing is expected to be favorable over immediate product formation because the product phase is thermodynamically unstable until some interdiffusion has occurred [41] and the driving force for product nucleation increases as the concentration gradient is reduced [28]. Similar initial heat release shoulders have been reported in other calorimetric studies of Al/Ni multilayers [13,15,17–19], although those authors have disagreed over whether it is due to intermixing only [13,18,19] or to the formation of a small volume of B2 AlNi [15,17]. Here, it seems most likely that the initial reaction we observe is just interdiffusion since the *in situ* electron diffraction data (Fig. 5.6) show no evidence for product formation until later in the reaction. If this is the case, the solid solution is most likely Al-rich since Ni has been noted to diffuse more easily in Al than vice versa [16]. The Al-Ni phase diagram shows no significant solubility of Ni in Al, but it is quite possible to observe extended metastable solid solubility when the enthalpy of mixing is large and the kinetics of nucleation are slow. This is further supported by more recent work that used x-ray diffraction (XRD) and Auger-electron-spectroscopy (AES) depth profiling to examine compositional variations in annealed Al/Ni multilayers [42]. In that study, after annealing at 393 K for 45 minutes, the authors observed decreased intensity of the Al diffraction peaks and Ni concentrations of more than 20 atomic % in the Al layers without the formation of an intermetallic phase. No measurable Al content was found in the Ni layers.

To estimate the activation energy associated with this process, we restrict ourselves to the range over which all samples exhibit interdiffusion ($0.01 \leq \alpha \leq 0.1$) and consult the effective activation energy plotted in Fig. 5.9. As already noted, the effective activation energy in this regime is noticeably lower than for the rest of the reaction. In particular, the minimum value in this range is 113.3 kJ/mol ± 4.36 kJ/mol at $\alpha = 0.04$. The generally increasing trend of effective activation energy with α in this region, coupled with the observation of transition points that vary with heating rate, strongly suggest a higher activation energy process occurring in parallel. In this case it is appropriate to take the minimum value of the effective activation energy as the best estimate of E_a for the lower activation energy process [35]. The quality of this estimate depends on the degree to which the reaction is operating independently at this extent of conversion and generally over-predicts the true value, but should be reasonable since we don't observe any obvious evidence of parallel reactions at $\alpha = 0.04$.

It would be interesting to compare the activation energy obtained above to previous reports, but it is difficult to find any previous studies that measured an activation energy that was specifically attributed to the interdiffusion process. This is likely because interdiffusion does not give rise to a distinct peak as would be required for traditional Kissinger analysis. Michaelsen *et al.* [17] obtained activation energies for the initial heat release by model fitting to isothermal DSC traces covering this regime, but they attributed this heat release and the associated activation energies to the formation of B2 AlNi. Given the evidence presented above, a careful reading suggests that the initial heat release measured in [17] may actually have been due to interdiffusion. In any case, as the best available comparison these values are presented in Table 5.2 alongside the value obtained here. While the values are clearly different, we see at least qualitative agreement insofar as both results predict a significantly lower activation energy for the initial mixing process than for subsequent nucleation and growth. Notably, the values obtained from [17] were for very small bilayer periods (10 nm and 20 nm) and suggested an increasing trend of activation energy with bilayer period. This might explain some of the discrepancy between their result and ours.

Table 5.2 Activation energies reported in the literature for the interdiffusion and growth stages of the Al_3Ni reaction. This list is not comprehensive, and in particular excludes results that were not obtained for thin films.

Process	Activation Energy (kJ/mol)	Method	Reference
initial intermixing	113.3 ± 4.36	Isoconversional (Friedman)	This work
	74.2 – 81.9[a]	Single-curve model fit	[17]
growth	137.4 ± 3.91	Isoconversional (Friedman)	This work
	139.0 ± 0.374	Multi-curve model fit	This work
	144.5 ± 9.63	Isothermal annealing	[12]
	143.5 ± 9.63[b]	Kissinger	[13]
	158.0	Kissinger	[14]
	165.7	Single-curve model fit	[14]
	158.0 – 168.6[b]	Kissinger	[15]
	183.0 ± 9.63	Kissinger	[19]

[a] This activation energy is for the same reaction feature that we observe in our work (a shoulder preceding the first exotherm), but in the original work it was attributed to the formation of B2 AlNi.

[b] In these studies heat release was observed to occur in two discrete peaks. The activation energies reported here correspond to the second (1D growth) peak.

We can also compare both values to the activation energy reported in the literature for the bulk diffusion of Ni in Al, 144.6 kJ/mol [43]. This is significantly higher than either of the values suggested for the interdiffusion process in Table 5.2, strongly implying that the initial intermixing commonly observed in Al/Ni multilayer samples is assisted by easy diffusion pathways like grain boundaries. The importance of such pathways is also supported by cross-sectional microscopy that has shown preferential growth of intermetallic phases along Al grain boundaries in Al/Ni thin film diffusion [12,13,19]. Diffusion constant correlations [44] predict an activation energy of approximately 54 % of the bulk value for boundary diffusion in fcc metals. Based on the value from [43] we would thus predict an activation energy of ≈ 79 kJ/mol if the process were dominated by boundary diffusion of Ni in Al. This is an excellent match to the values from [17] but lower than the one calculated here.

5.5.2 Nucleation

The initial heat release shoulder that we attribute to intermixing is terminated by a relatively abrupt transition to a more rapidly accelerating reaction rate. We attribute this transition to the nucleation of the intermetallic product. While we do not observe a discrete peak corresponding to this process as has sometimes been reported [13,15], the transition point is sufficiently distinct that it can be used to track the onset of nucleation directly. This is most evident in the plot of normalized reaction rate $d\alpha/dt$ versus the extent of reaction (Fig. 5.10). Examining the initial stages of the reactions ($\alpha < 0.2$), the onset of nucleation is visible as a discontinuous increase in the slope of the curve.

We developed a basic algorithm to extract this transition point from the reaction rate curves in an automated and unbiased way. The algorithm is based on the idea of locating the transition point as the intersection of two straight line fits to the regions of the curve straddling the transition point. To fit the first (left-hand) line, we start with the left-most data point ($\alpha = 0.01$) and add points to the fitting sequentially until the maximum linear correlation is achieved. The second (right-hand) line is fitted by finding the fixed-length fit region that yields the maximum linear correlation in a defined search interval to the right of the first fit. The fit length and search interval for the second fit are defined by the size of the first fit region. Once both lines are fitted, their intersection yields the value of α at the transition, and the other values (i.e. $d\alpha/dt$ and T) can be interpolated from the experimental data. This process is illustrated for the lowermost curve in Fig. 5.10. In this sample the first line was fitted to the region $0.01 \leq \alpha \leq 0.17$

and the second line was fitted to the region $0.23 \leq \alpha \leq 0.39$. Finding the intersection as shown in the inset for Fig. 5.10, we obtain a threshold value of $\alpha = 0.208$.

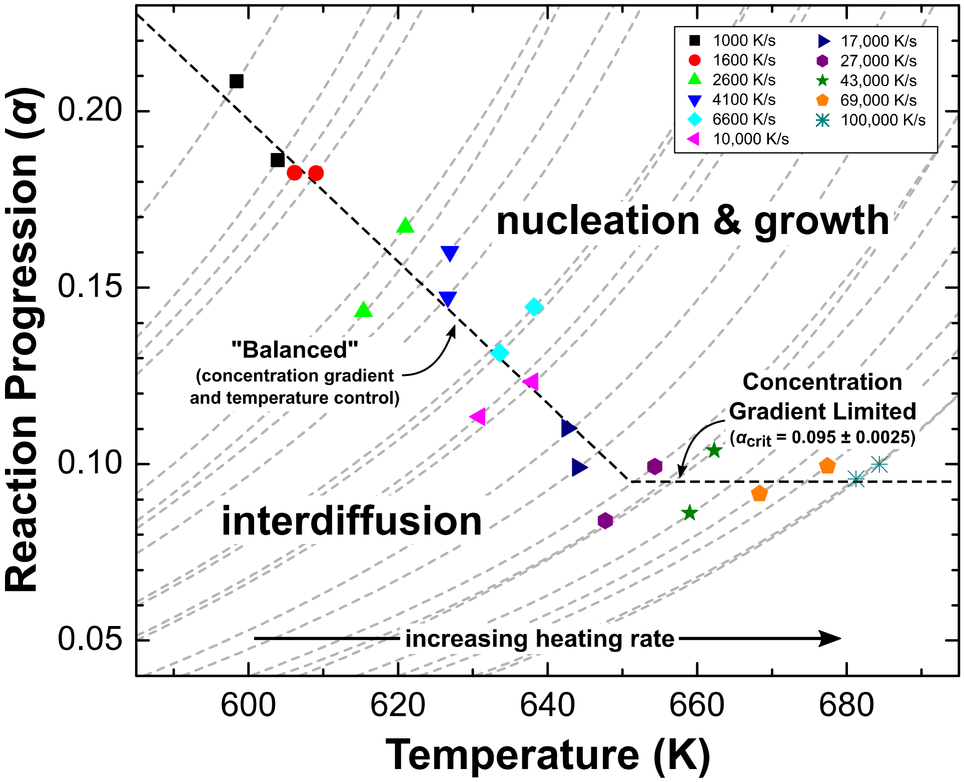

Figure 5.11 Plot of the nucleation threshold in terms of reaction progression and temperature. The plotted points correspond to the experimentally measured nucleation threshold for individual samples, while the light gray dashed lines are the experimental $\alpha - T$ curves as plotted in Fig. 5.7. In the region below and to the left of the points we observe interdiffusion, while above and to the right we observe nucleation and growth of the Al_3Ni intermetallic. For the nucleation threshold, we observe two regimes of scaling between α and T. At low heating rates, they vary cooperatively with α decreasing as T increases. At high heating rates, the extent of conversion at the nucleation threshold is nominally invariant with T. We interpret the variation in the low-heating-rate regime as a balance between thermal and concentration gradient effects. The high-heating-rate zone corresponds to the theoretically predicted "critical concentration gradient" regime, where there is no driving force for nucleation until α_{crit} is exceeded.

The transition points obtained by the application of this algorithm are overlaid on the curves in Fig. 5.10 and appear to track the transition successfully. They are also included in Figs. 5.3 and 5.4. Fig. 5.10 gives the first hint of interesting behavior, showing that the value of α at the transition point initially decreases with increasing heating rate but then becomes fairly constant for the highest heating rates. To examine this phenomenon more closely, in Fig. 5.11 we plot the extent of conversion versus the sample temperature at the onset of nucleation. While the data are noisy, we observe a similar trend where the extent of conversion initially decreases with increasing temperature and then levels off to a fairly constant value at higher temperatures. This behavior is highlighted by the fitted dashed lines.

To understand this behavior, we must consider the roles that the variables plotted (temperature and extent of conversion) might play in product nucleation. The role of temperature in determining the nucleation rate is well-documented [5]. In simplest form it is summarized by classical nucleation theory, which predicts a nucleation rate that is proportional to the product of two temperature dependent terms, one related to the probability of overcoming the energy barrier for nucleation and the other related to the transport rate of atoms to the incipient nucleus. We expect the first rate contribution to increase with decreasing temperature because the driving force for nucleation becomes larger the more the system is undercooled below the transformation temperature. In contrast, the contribution related to transport is expected to *decrease* with decreasing temperature since transport is a thermally activated process. Close to the transition temperature (in this case the peritectic decomposition temperature for Al_3Ni) the nucleation barrier term tends to dominate the nucleation rate, but when the undercooling becomes large the exponentially decaying transport rate can become the dominant factor. Thus, we predict schematically that the nucleation rate exhibits both a transport-limited regime (increasing with increasing temperature) and a driving-force-limited regime (decreasing with increasing temperature), with transport control dominating well below the transformation temperature and driving-force control dominating close to the transformation temperature.

The role of α in determining the nucleation rate is less commonly considered because it does not factor into nucleation in homogeneous systems. However, in interfacial reactions we expect some interdiffusion to be required before nucleation can occur since the reactants are initially separated. Indeed, Thompson [41] showed theoretically that some amount of interdiffusion is required before the nucleation of a product phase is thermodynamically favorable. This manifests as some dependence of the nucleation rate on α. The concept was given a more rigorous mathematical underpinning by Desré and co-workers [27,28], who quantified the energetic penalty to the driving force for nucleation associated with nucleating within a concentration gradient. On a basic level this penalty arises because the forming nucleus is forced to accommodate some amount of compositional variation. Generally, Hodaj and Desré predicted that the driving force for nucleation should increase as the concentration gradient is reduced. In terms of the reaction progression this suggests that for interfacial reactions nucleation is easier when α is larger as α is approximately inversely proportional to the concentration gradient. The model also predicts that at some concentration gradient dubbed the "critical" concentration gradient, the driving force becomes identically zero making it impossible to nucleate the phase until the concentration gradient is reduced. In terms of reaction progression this would manifest as a critical extent of conversion, α_{crit}, required for mixing.

Turning again to the data plotted in Fig. 5.11, we see that it spans the temperature range from ≈ 600 K to 690 K. This is an undercooling of ≈ 400 K to 500 K relative to the peritectic decomposition temperature for Al_3Ni, 1127 K. This large undercooling, coupled with the observation of extended metastable solid solutions in this and previous work, strongly suggests that nucleation in the present experiments occurs in the heavily undercooled regime where transport, rather than thermodynamic driving force, is the rate limiting process. Thus we can interpret the first, linearly decreasing portion of Fig. 5.11 as a regime where the nucleation threshold is determined by the balance of concentration gradient and temperature contributions. The trend is decreasing because in this region the strong temperature scaling of the nucleation rate is enough to counteract the concentration gradient penalty. In other words, the increasing heating rate pushes mixing to higher temperatures and allows the system to overcome progressively steeper concentration gradients. The extent of conversion at the nucleation point drops accordingly. If this scaling continued indefinitely it would predict that in the limit of very high heating rate we could nucleate at $\alpha \approx 0$, nullifying the concentration gradient penalty entirely. Instead, we observe a fairly abrupt transition to a regime where the extent of conversion is nominally invariant with nucleation temperature. While at first surprising, this transition is actually entirely consistent with the theoretically predicted critical concentration gradient. In this understanding, the constant extent of conversion observed at high temperatures (labeled α_{crit} in Fig. 5.11) corresponds to the critical concentration gradient for the formation of Al_3Ni. Regardless of additional temperature enhancement (i.e. increases in the heating rate) we fail to observe nucleation prior to α_{crit} because there is no driving force for nucleation until this amount of mixing is complete.

This conclusion, if accurate, is significant because despite its frequent citation the Desré theory of nucleation in a concentration gradient has received scant direct experimental support. The concept has been invoked to explain the suppression of phase formation in self-propagating Al/Ni multilayer reactions [23,24], but this explanation is almost impossible to verify precisely in such an overdriven system. Here, nanocalorimetry appears to provide the optimal balance of heating rate and measurement fidelity needed to observe this transition directly. The result indicates that while the basics of the concentration gradient theory are accurate, the limiting case of the *critical* concentration gradient is probably only realized in systems that are being driven fairly far from equilibrium. Nucleation effects that have been attributed to the critical concentration gradient in slower experiments [18] are probably better interpreted using a balance between concentration gradient and temperature contributions.

The lack of significant heat release associated with initial nucleation and growth warrants additional comment, particularly as it compares to those studies that have observed kinetically distinct nucleation-and-growth peaks [13,15] that contribute up to 50 % of the total heat release for a 100 nm bilayer period. We suggest that this discrepancy may be due to a significant reduction in the density of nucleation sites in our samples relative to those previous works. Interface contamination (particularly oxidation) has been shown to inhibit the growth of Al_3Ni [12] and alter the position of DSC peaks [13]. Given that these reductions in growth rate have never been attributed to a change in the activation energy for the process, it seems likely that the effect of interface contamination is to alter the availability of nucleation sites at the interface than to change the mechanism of growth [13]. Our samples were deposited in a vacuum system with a base vacuum of 4×10^{-4} Pa, compared with 1.3×10^{-5} Pa in [13] and 1×10^{-5} Pa in [15]. In addition, compared with the relatively continuous deposition onto a rotating substrate used in [15], the e-beam evaporation system used here necessitated a 5 – 10 minute delay between layer depositions to allow for source heating and stabilization, during which time additional oxidation could occur. Thus it seems reasonable that the observed discrepancy can be explained by a reduction in nucleation site density due to increased incorporation of oxygen at the Al/Ni interfaces.

5.5.3 Growth

Based on the discussion in the previous two sections, we propose that after initial mixing and product nucleation the remaining heat release observed in our samples comes from the exothermic growth of Al_3Ni until all of the reactants are consumed. In the absence of a distinct exothermic signal from nucleation, we assign this process to the entire range of conversion from the termination of intermixing until reactant consumption, i.e. $0.2 \leq \alpha \leq 1.0$. Consulting Fig. 5.9, the effective activation energy exhibits a local maximum at $\alpha = 0.21$ but then decreases before remaining approximately constant over a majority of the range (between approximately 35 % and 85 % completion). From here it increases marginally up until the data ends at $\alpha = 0.9$. While the features at the extremes of the range clearly argue for some degree of complexity in the growth process, the broad plateau suggests that as a first approximation we can consider the entire range as being governed by a single activation energy and hence a single reaction mechanism.[a]

The average effective activation energy taken over the range $0.2 \leq \alpha \leq 0.9$ is 137.4 kJ/mol ± 3.91 kJ/mol. In keeping with the large body of previous work on Al/Ni interfacial reactions [12–19], we anticipate that this activation energy is for some type of diffusion-limited growth process. This has typically been analyzed as simple 1-D diffusion [12–14,18] although some studies [15,17] have found a better fit to varying

---

[a] Note that while this is usually the case a single effective activation energy does not strictly guarantee a single reaction mechanism since the activation energy analysis is unable to detect parallel processes with the same activation energy (see, e.g. [36]).

orders of JMAEK (Johnson-Mehl-Avrami-Erofeev-Kolmogorov) model. The activation energies obtained in these studies are reported in Table 5.2.

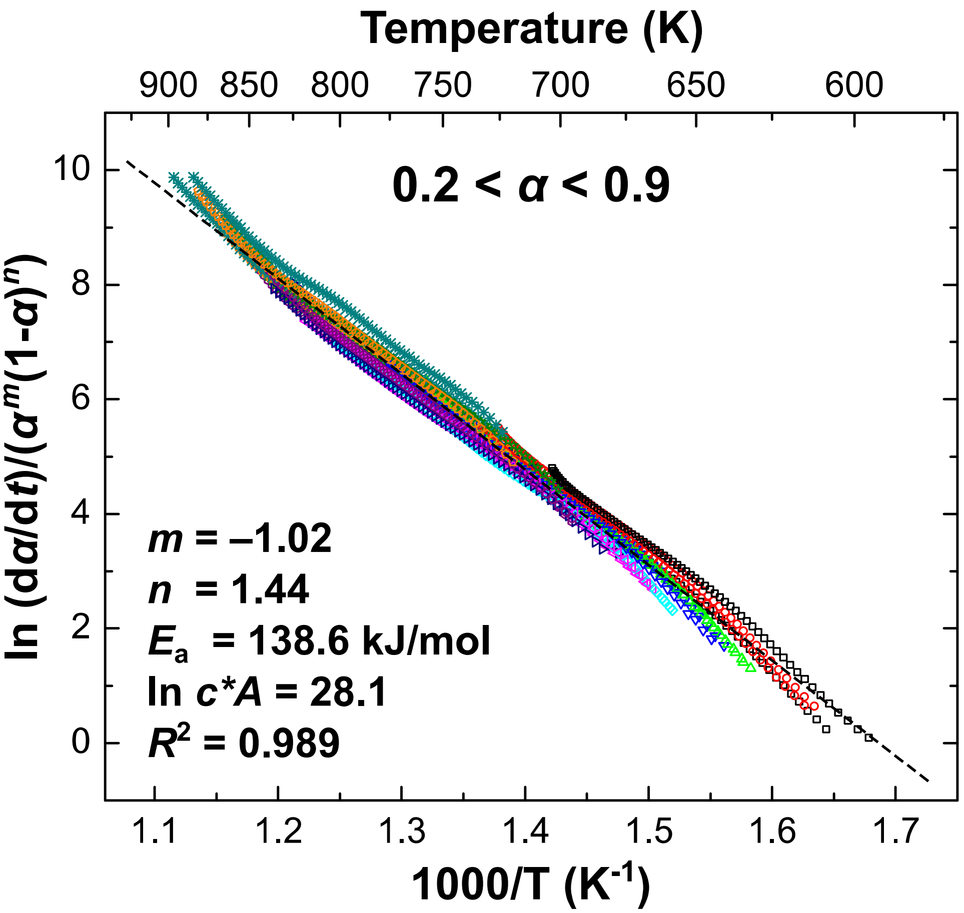

Figure 5.12 Plot of the combined kinetic analysis best fit for the conversion range $0.2 \leq \alpha \leq 0.9$. The fitting dataset includes all experiments, so the total number of fitted points is 71 × 22 = 1562. To produce this plot, the values of m and n have been optimized to yield the maximum linearity of $\ln(d\alpha/dt)/(\alpha^m(1-\alpha)^n)$ versus inverse temperature (see Eq. (5.18)). The colored sets of points show the experimental data after this processing, with a linear correlation of -0.994 ($R^2 = 0.989$). After optimizing for linearity, a linear regression (black dashed line) is used to obtain values for the activation energy and intercept as shown.

To further characterize the rate-controlling process in this regime we applied the "combined kinetic analysis" as described in Sec. 5.3.4. Taking the subset of each experiment from $0.2 \leq \alpha \leq 0.9$ (the high activation energy regime), we performed the optimization as described and obtained the best fit as shown in Fig. 5.12. The slope of the best fit line yields an activation energy of 138.6 kJ/mol ± 0.372 kJ/mol, in good agreement with the average value obtained for this region from isoconversional analysis. More significantly, we obtain values of –1.02 and 1.44 for m and n, respectively. In general, these values can be thought of as affecting mainly either the beginning (m) or end (n) of the reaction. The finding of $m \approx -1$ implies $f(\alpha) \propto 1/\alpha$ in the early stages of the reaction, i.e. a reaction rate that decreases hyperbolically with α. This type of scaling is a hallmark of the diffusion models, arising because of the broadening of the concentration gradient and corresponding reduction in the driving force for diffusion as mixing occurs. Knowing this, we compared the values of m and n obtained in Fig. 5.12 to those expected for commonly used diffusion models as listed in Table 5.3. As expected, any of the models could be a match based only on the value of m. However, none of the models provided a good match for the value of n.

Table 5.3 Commonly employed diffusion models and their equivalent expression in terms of the reduced Sestak-Berggren equation (Eq. (5.17)). Note that the parameter values reported differ slightly from those in [37], most likely due to a different choice of fit range and point density. Also included is the JMAEK model with $n = 0.5$, corresponding to 1-D diffusion-limited growth from a fixed number of randomly distributed nuclei.

model [code]	$f(\alpha)$	$c\alpha^m(1-\alpha)^n$		
		c	m	n
1-D diffusion [D1]	$1/(2\alpha)$	0.5	-1	0
2-D diffusion [D2]	$-1/\ln(1-\alpha)$	0.988	-1.002	0.441
3-D diffusion (Jander) [D3]	$3(1-\alpha)^{2/3}/[2(1-(1-\alpha)^{1/3})]$	4.476	-1.001	0.966
3-D diffusion (Ginstling-Brounshtein) [D4]	$3/[2((1-\alpha)^{-1/3}-1)]$	4.464	-1.002	0.623
Avrami-Erofeev [A0.5]	$0.5(1-\alpha)[-\ln(1-\alpha)]^{-1}$	0.4980	-1.001	1.471

The value of n mainly affects the scaling of the reaction rate at later times, i.e. the character of the reaction shutoff. This idea is illustrated in Fig. 5.13 for the models listed in Table 5.3. For the D1 model where $n = 0$, no extra decay is predicted prior to shutoff (the reaction simply stops abruptly when the reactants are consumed). The multi-dimensional diffusion models (D2-D4) all feature $n > 0$ because the geometry of the system tends to inhibit diffusion as the reaction approaches completion, but the largest value expected for any of these models is $n = 0.966$ while our analysis yielded $n = 1.44$. This implies that the reactions we observe in our samples shut off earlier than can be predicted by even the most aggressive 3-D diffusion model (D3).

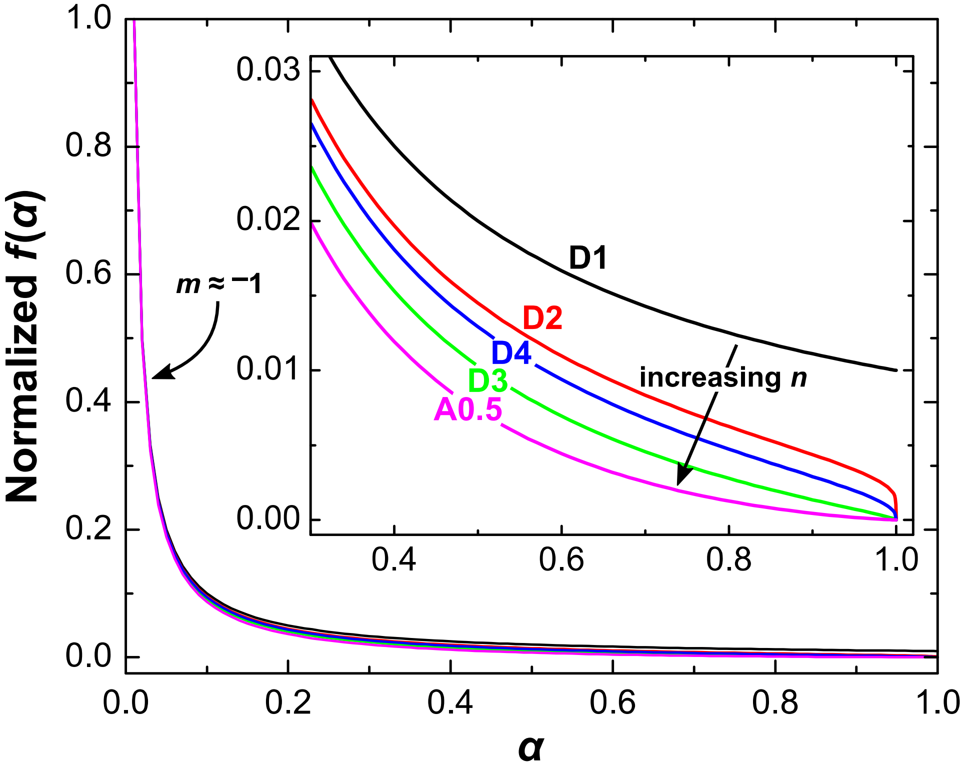

Figure 5.13 Plot of the reaction models listed in Table 5.3, normalized by the value of each model at $\alpha = 0.01$. All of the models listed exhibit $1/\alpha$ behavior at small α ($m \approx -1$) and so are indistinguishable in this limit. In the inset, the large α behavior is magnified to show how the models differ in shutoff behavior. In terms of the reduced Sestak-Berggren approximation, this corresponds to variations in the value of the exponent n, where larger values predict an earlier decay in the reaction rate.

In their work on the early stages of Al/Ni interfacial reactions, Michaelsen *et al.* [17] encountered a similar problem where predictions based on a 1-D diffusion model were inadequate to explain the rapid decay of reaction rate observed in their experiments. To solve this problem, they turned instead to a JMAEK model with $n_{\text{JMAEK}} = 0.5$, typically prescribed for 1-D diffusion-limited growth from a fixed number of nucleation sites. Unlike the most common JMAEK models (e.g. A2 and A3) which predict sigmoidal growth profiles, JMAEK models with $n_{\mathrm{JMAEK}} < 1$ actually predict decelerating kinetics similar to those observed for the diffusion models. When we included the JMAEK model with $n_{\mathrm{JMAEK}} = 0.5$ in our considerations (denoted A0.5 in Table 5.3 and Fig. 5.13) it stood out immediately as the best fit. When transformed to reduced Sestak-Berggren form, it yields $m \approx -1$ just like the diffusion models but $n = 1.47$, larger than for any of the diffusion models and a very good match to the value obtained in our combined kinetic analysis, $n = 1.44$.

Formally, $n_{\mathrm{JMAEK}} = 0.5$ is expected for diffusion-limited growth in a single dimension from a fixed number of randomly distributed nuclei. In a system like ours this implies plate-like nuclei, i.e. nuclei that are very thin relative to their lateral dimensions. In the work of Michaelsen *et al.* [17] the authors suggested grain boundaries as one possible origin of such nuclei. However, in that context they were considering the initial intermixing that presumably encompasses only a small fraction of the overall sample, so that nucleation at grain boundaries and lateral growth might reasonably accomplish the observed heat release. It is harder to imagine how this model can apply to the majority of the growth as we observe here. However, no model that we explored provided a better fit to the observed kinetics in the growth regime than the JMAEK model with $n_{\mathrm{JMAEK}} = 0.5$. For this reason we present it here as “the” reaction model for Al_3Ni growth in our samples, with the understanding that additional work is needed to explain its microscopic origins and in particular how the growth mode in our samples compares to what has been reported previously. Since the A0.5 model matched the fitted parameters so well, we reran the analysis as a regular model fit and obtained the full kinetic triplet as reported in Table 5.4. The fit plot for this case (not shown) is virtually identical to that already presented in Fig. 5.12, and the activation energies obtained by the two approaches exhibit negligible differences. Compared to the activation energies that have been reported previously for Al_3Ni growth (Table 5.2) our values are similar to those that have been reported for evaporated samples [12,13] but slightly lower than those that have been obtained for sputtered samples [14,15,19]. This implies a slight difference in diffusion mechanism between films obtained by different techniques.

Table 5.4 Full kinetic triplet ($E_a, A, f(\alpha)$) obtained for the growth of Al_3Ni ($0.2 \leq \alpha \leq 0.9$) by linear fitting of the experimental data to a JMAEK model with exponent $n_{\mathrm{JMAEK}} = 0.5$. The fit plot is essentially identical to that presented in Fig. 5.12 and yields $R^2 = 0.989$.

Activation Energy E_a **(kJ/mol)**	**Pre-Exponential Factor** A **(× 10^{12} s^{-1})**	**Reaction Model** $f(\alpha)$
139.0 ± 0.374	3.604 ± 0.221	$0.5(1-\alpha)[-\ln(1-\alpha)]^{-1}$

Interestingly, re-examination of growth curves that have been reported previously [13–15] shows that they too exhibit an earlier deceleration than would be expected for pure 1-D diffusion. This is especially apparent when they are compared directly to the predictions from a 1-D diffusion model [13]. This discrepancy has garnered little attention previously, perhaps because in multilayer samples there are other factors such as thermal non-uniformity or variations in the bilayer period that can be invoked to explain peak broadening. However, the fact that we see this effect even in nanocalorimetry experiments where bilayer variations and temperature gradients are unlikely suggests that a more nuanced understanding of the growth mechanism for Al_3Ni may be needed.

5.5.4 Predictive Modeling

The best test of the quality of experimental kinetic parameters is to feed them back into a model and compare the model's predictions to the experimental results [10]. Unfortunately, the results obtained for the initial mixing and product nucleation stages are not in the form of conventional kinetic parameters, which makes them difficult to incorporate into simulations. On the other hand, for the growth stage we were able to derive a reaction mechanism in the form of a standard kinetic triplet (Table 5.4). Thus, while we are continuing to work toward a unified model that incorporates all of the phenomena described, we can for the moment present a model that at least covers the growth stage. Since this stage represents ≈ 80 % of the total heat release, it should be the most significant component needed to successfully simulate reaction curves.

The simulations performed utilized the kinetic triplet as reported in Table 5.4 and, for comparison to experiments, the same arbitrary temperature programs measured experimentally. Reaction profiles were simulated by integrating the reaction rate equation (Eq. (5.14)) numerically using a simple first-order forward (Euler) integration scheme. The results are overlaid on the normalized reaction rate curves in Fig. 5.3 and demonstrate reasonable agreement. In particular, the simulations reproduce the position of both the peak reaction rate and the reaction shutoff fairly accurately, including cases where the measured curves split due to variations in the temperature program. The fits are generally best for the lowest heating rates where the peaks exhibit no shoulders; the current model includes no mechanism to explain the shoulders so the fits are necessarily worse in measurements that contain them. Finally, the model tends to over-predict the reaction rate at early temperatures and, being single-step, does not reproduce the discontinuous change in reaction rate at the nucleation point that has been observed experimentally. It is interesting to note that in a number of the experiments, the extra heat release predicted prior to the nucleation point appears to be approximately equal and opposite to the heat release that is under-predicted in the first shoulder. This suggests that there may be a link between the pre-nucleation regime (where mixing seems to be inhibited) and the “extra” heat that is released upon nucleation. Despite these shortcomings, it is worth noting that even with just a single kinetic triplet we have been able to schematically reproduce experimental reaction curves that span more than two decades in heating rate. This speaks to both the apparent universality of behavior (at least schematically) across all samples studied and to the robustness of analysis afforded by analyzing the reaction over a wide range of heating rates.

5.6 Conclusions

We have studied in detail the interfacial reaction between Ni and Al to form the intermetallic phase Al_3Ni. The application of high-heating-rate nanocalorimetry in a systematic way has yielded fresh insights into this already well-characterized system. By combining nanocalorimetry data with evidence from *in situ* and *ex situ* electron diffraction, we identified regimes of conversion corresponding to interdiffusion, nucleation, and growth respectively. For the interdiffusion regime, we observe a lower effective activation energy than is observed for subsequent growth or that would be expected for bulk diffusion of Ni in Al. This strongly suggests that the interdiffusion process is dominated by boundary diffusion. In the growth regime we observe several shoulders in the kinetic curves that have yet to be explained. However, the overall heat release appears to follow a JMAEK model with $n = 0.5$, suggesting 1D-diffusion controlled growth from a fixed number of randomly distributed nuclei. This is generally consistent with the consensus viewpoint that nucleation in Al/Ni interfacial reactions occurs heterogeneously at defects like grain boundary triple junctions. Finally, perhaps the most exciting result of this study is what appears to be the direct observation of the complete inhibition of nucleation by a steep concentration gradient. This provides much-needed experimental context for a theory that has been invoked to explain phase suppression in a wide range of systems, particularly self-propagating reactive multilayers.

Future work on the system studied here is needed to incorporate the three regimes characterized into a coherent reaction model that reproduces interdiffusion, nucleation, and growth. Investigation of the shoulders that were left un-treated would also be interesting, although it would likely require an investment in additional characterization. More broadly, the success of this study suggests that the combination of isoconversional analysis and nanocalorimetry is a powerful tool for kinetic analysis that can potentially yield new insights into even well-characterized systems. As automated data extraction becomes more advanced, the need for large, feature-rich datasets will continue to increase. In the realm of kinetic analysis, nanocalorimetry should be a strong contender to deliver these datasets given its now proven ability to generate them with both speed and precision.

References for Chapter 5

[1] F.M. D'Heurle, Nucleation of a new phase from the interaction of two adjacent phases: Some silicides, J. Mater. Res. 3 (1988) 167–195.

[2] R. Rosenberg, D.C. Edelstein, C.-K. Hu, K.P. Rodbell, Copper Metallization for High Performance Silicon Technology, Annu. Rev. Mater. Sci. 30 (2000) 229–262.

[3] M.J. Pomeroy, Coatings for gas turbine materials and long term stability issues, Mater. Des. 26 (2005) 223–231.

[4] D.P. Adams, Reactive multilayers fabricated by vapor deposition: A critical review, Thin Solid Films. 576 (2015) 98–128.

[5] K.F. Kelton, A.L. Greer, Nucleation in Condensed Matter: Applications in Materials and Biology, Elsevier, 2010.

[6] C. Michaelsen, K. Barmak, T.P. Weihs, Investigating the thermodynamics and kinetics of thin film reactions by differential scanning calorimetry, J. Phys. D. Appl. Phys. 30 (1997) 3167–3186.

[7] E.A. Olson, M.Y. Efremov, L.H. Allen, The design and operation of a MEMS differential scanning nanocalorimeter for high-speed heat capacity measurements of ultrathin films, J. Microelectromechanical Syst. 12 (2003) 355–364.

[8] R.K. Kummamuru, L. De La Rama, L. Hu, M.D. Vaudin, M.Y. Efremov, M.L. Green, et al., Measurement of heat capacity and enthalpy of formation of nickel silicide using nanocalorimetry, Appl. Phys. Lett. 95 (2009) 181911.

[9] P. Swaminathan, M.D. Grapes, K. Woll, S.C. Barron, D.A. LaVan, T.P. Weihs, Studying exothermic reactions in the Ni-Al system at rapid heating rates using a nanocalorimeter, J. Appl. Phys. 113 (2013) 143509.

[10] S. Vyazovkin, A.K. Burnham, J.M. Criado, L.A. Pérez-Maqueda, C. Popescu, N. Sbirrazzuoli, ICTAC Kinetics Committee recommendations for performing kinetic computations on thermal analysis data, Thermochim. Acta. 520 (2011) 1–19.

[11] J. Orava, A.L. Greer, B. Gholipour, D.W. Hewak, C.E. Smith, Characterization of supercooled liquid Ge2Sb2Te5 and its crystallization by ultrafast-heating calorimetry., Nat. Mater. 11 (2012) 279–83.

[12] E. Ma, M.-A. Nicolet, M. Nathan, NiAl3 formation in Al/Ni thin-film bilayers with and without contamination, J. Appl. Phys. 65 (1989) 2703.

[13] E. Ma, C.V. Thompson, L.A. Clevenger, Nucleation and growth during reactions in multilayer Al/Ni films: The early stage of Al3Ni formation, J. Appl. Phys. 69 (1991) 2211.

[14] C. Michaelsen, K. Barmak, Calorimetric determination of NiAl3-growth kinetics in sputter-deposited Ni/Al diffusion couples, J. Alloys Compd. 257 (1997) 211–214.

[15] K. Barmak, C. Michaelsen, G. Lucadamo, Reactive phase formation in sputter-deposited Ni/Al multilayer thin films, J. Mater. Res. 12 (1997) 133–146.

[16] A.S. Edelstein, R.K. Everett, G.Y. Richardson, S.B. Qadri, E.I. Altman, J.C. Foley, et al., Intermetallic phase formation during annealing of Al/Ni multilayers, J. Appl. Phys. 76 (1994) 7850.

[17] C. Michaelsen, G. Lucadamo, K. Barmak, The early stages of solid-state reactions in Ni/Al multilayer films, J. Appl. Phys. 80 (1996) 6689.

[18] M.H. da Silva Bassani, J.H. Perepezko, A.S. Edelstein, R.K. Everett, Initial phase evolution during interdiffusion reactions, Scr. Mater. 37 (1997) 227–232.

[19] K.J. Blobaum, D. Van Heerden, A.J. Gavens, T.P. Weihs, Al/Ni formation reactions: characterization of the metastable Al9Ni2 phase and analysis of its formation, Acta Mater. 51 (2003) 3871–3884.

[20] E. Ma, C.V. Thompson, L.A. Clevenger, K.N. Tu, Self-propagating explosive reactions in Al/Ni multilayer thin films, Appl. Phys. Lett. 57 (1990) 1262.

[21] J. Wang, E. Besnoin, A. Duckham, S.J. Spey, M.E. Reiss, O.M. Knio, et al., Room-temperature soldering with nanostructured foils, Appl. Phys. Lett. 83 (2003) 3987.

[22] J. Braeuer, J. Besser, M. Wiemer, T. Gessner, A novel technique for MEMS packaging: Reactive bonding with integrated material systems, Sensors Actuators A Phys. 188 (2012) 212–219.

[23] J.C. Trenkle, L.J. Koerner, M.W. Tate, S.M. Gruner, T.P. Weihs, T.C. Hufnagel, Phase transformations during rapid heating of Al/Ni multilayer foils, Appl. Phys. Lett. 93 (2008) 081903.

[24] J.C. Trenkle, L.J. Koerner, M.W. Tate, N. Walker, S.M. Gruner, T.P. Weihs, et al., Time-resolved x-ray microdiffraction studies of phase transformations during rapidly propagating reactions in Al/Ni and Zr/Ni multilayer foils, J. Appl. Phys. 107 (2010) 113511.

[25] J.S. Kim, T. Lagrange, B.W. Reed, M.L. Taheri, M.R. Armstrong, W.E. King, et al., Imaging of transient structures using nanosecond in situ TEM., Science (80-.). 321 (2008) 1472–1475.

[26] J.S. Kim, T. LaGrange, B.W. Reed, R. Knepper, T.P. Weihs, N.D. Browning, et al., Direct characterization of phase transformations and morphologies in moving reaction zones in Al/Ni nanolaminates using dynamic transmission electron microscopy, Acta Mater. 59 (2011) 3571–3580.

[27] P.J. Desré, Effect of sharp concentration gradients on the stability of a two-component amorphous layer obtained by solid state reaction, Acta Metall. Mater. 39 (1991) 2309–2315.

[28] F. Hodaj, P.J. Desré, Effect of a sharp gradient of concentration on nucleation of intermetallics at interfaces between polycrystalline layers, Acta Mater. 44 (1996) 4485–4490.

[29] F. Yi, W. Osborn, J. Betz, D.A. LaVan, Interactions of Adhesion Materials and Annealing Environment on Resistance and Stability of MEMS Platinum Heaters and Temperature Sensors, J. Microelectromechanical Syst. 24 (2015) 1185–1192.

[30] M.D. Grapes, T. LaGrange, L.H. Friedman, B.W. Reed, G.H. Campbell, T.P. Weihs, et al., Combining nanocalorimetry and dynamic transmission electron microscopy for in situ characterization of materials processes under rapid heating and cooling, Rev. Sci. Instrum. 85 (2014) 084902.

[31] M.D. Grapes, T. LaGrange, K. Woll, B.W. Reed, G.H. Campbell, D.A. LaVan, et al., In situ transmission electron microscopy investigation of the interfacial reaction between Ni and Al during rapid heating in a nanocalorimeter, APL Mater. 2 (2014) 116102.

[32] P. Swaminathan, B.G. Burke, A.E. Holness, B. Wilthan, L. Hanssen, T.P. Weihs, et al., Optical calibration for nanocalorimeter measurements, Thermochim. Acta. 522 (2011) 60–65.

[33] H.L. Friedman, Kinetics of thermal degradation of char-forming plastics from thermogravimetry. Application to a phenolic plastic, J. Polym. Sci. Part C Polym. Symp. 6 (1964) 183–195.

[34] S. Vyazovkin, Modification of the integral isoconversional method to account for variation in the activation energy, J. Comput. Chem. 22 (2001) 178–183.

[35] S. Vyazovkin, V.I. Goryachko, A.I. Lesnikovich, An approach to the solution of the inverse kinetic problem in the case of complex processes. Part 3. Parallel independent reactions, Thermochim. Acta. 197 (1992) 41–51.

[36] S. Vyazovkin, Conversion dependence of activation energy for model DSC curves of consecutive reactions, Thermochim. Acta. 236 (1994) 1–13.

[37] L.A. Pérez-Maqueda, J.M. Criado, P.E. Sanchez-Jiménez, Combined kinetic analysis of solid-state reactions: a powerful tool for the simultaneous determination of kinetic parameters and the kinetic model without previous assumptions on the reaction mechanism., J. Phys. Chem. A. 110 (2006) 12456–62.

[38] A. Khawam, D.R. Flanagan, Solid-state kinetic models: basics and mathematical fundamentals., J. Phys. Chem. B. 110 (2006) 17315–28.

[39] J. Šesták, G. Berggren, Study of the kinetics of the mechanism of solid-state reactions at increasing temperatures, Thermochim. Acta. 3 (1971) 1–12.

[40] F.R. de Boer, R. Boom, W.C.M. Mattens, A.R. Miedema, A.K. Niessen, Cohesion in Metals, North-Holland, 1988.

[41] C.V. Thompson, On the role of diffusion in phase selection during reactions at interfaces, J. Mater. Res. 7 (1991) 367–373.

[42] U. Rothhaar, H. Oechsner, M. Scheib, R. Müller, Compositional and structural characterization of temperature-induced solid-state reactions in Al/Ni multilayers, Phys. Rev. B. 61 (2000) 974–979.

[43] Y. Du, Y.A. Chang, B. Huang, W. Gong, Z. Jin, H. Xu, et al., Diffusion coefficients of some solutes in fcc and liquid Al: critical evaluation and correlation, Mater. Sci. Eng. A. 363 (2003) 140–151.

[44] A.M. Brown, M.F. Ashby, Correlations for diffusion constants, Acta Metall. 28 (1980) 1085–1101.

6. Conclusions and Future Work

6.1 Conclusions

In Chapter 2, I described the development of an *in situ* nanocalorimetry system that allows us to measure heat evolution and phase formation simultaneously at very high heating rates. This capability was demonstrated for the melting of an aluminum thin film, and utilized throughout the rest of the work to inform analysis. For example, in Chapter 3 this capability allowed us to identify the phases present in each exothermic peak observed in a nanocalorimetry experiment, and propose a possible explanation for the apparent disappearance of one of these peaks when the heating rate was increased. In Chapter 5, this capability helped us to confirm that the first and only phase formed in our samples was Al_3Ni, and that its formation most likely occurred *after* the initial heat release that we have attributed to interdiffusion. While to-date this system has only been used for the investigation of the Al/Ni reaction, its applicability is not limited to this case and I hope that in the future it will find utility in other investigations.

In Chapter 3, we examined *in situ* nanocalorimetry results for the 1Al:1Ni reaction. This composition is expected to exhibit the largest number of intermediate phases. In experiments at "low" heating rates (about 715 K/s) we found that the phase transformation sequence was unaltered from what is observed in conventional calorimetry (< 1 K/s), but that the formation of Al_3Ni_2 was spread across two exothermic peaks in contrast to what is typically observed. In the main text of that chapter, we proposed that this feature may be due to two-stage growth of this phase, where the first exotherm corresponds to growth of a planar layer at the interface and the second exotherm denotes 1D growth of this phase. While we cannot exclude this explanation, the results from a slightly higher heating rate (1800 K/s) suggest that this feature could also be a consequence of the delayed formation of Al_3Ni_2 (or early formation of AlNi) in response to the shift of mixing to higher temperatures by the increased heating rate.

In Chapter 4, we presented the design of a new class of reactive material called inert-mediated reactive multilayers. Intended primarily for scientific explorations, these materials combine a traditional reactive multilayer (Al/Ni in our case) with inert material that reduces the heating rate and suppresses the maximum temperature of the reaction. Using velocity-temperature relationships, we were able to use these materials to identify changes in the apparent rate-controlling process for the self-propagating reaction and attribute these changes to changes in the structure and/or identity of phases that form at the interface between Al and Ni due to the lower concentration gradients and temperatures.

Finally, in Chapter 5 we conducted a detailed kinetic analysis of the Al/Ni interfacial reaction using 3Al:1Ni samples. These samples are optimal for investigating the interfacial reaction because they are not expected to exhibit any intermediate phases. Thus, we were able to identify distinct features in the kinetic curves corresponding to initial intermixing, product nucleation, and product growth. For the intermixing stage, isoconversional analysis yielded an estimate of the activation energy for interdiffusion that suggests the dominant mixing mechanism is diffusion of Ni along Al grain boundaries. For product growth, we were able to derive a kinetic triplet for the growth process that assumes a JMAEK model with $n = 0.5$ and an activation energy of 139 kJ/mol. This is in good agreement with previously published results. Finally, for the nucleation process we identified an intriguing interplay between the extent of conversion and the temperature at which the product nucleated that seems to point directly to the concept of critical concentration gradient.

Taken holistically, this body of work represents a significant advance in the understanding of (1) how variations in concentration gradient and temperature affect the progression of the Al/Ni interfacial reaction and (2) how that interfacial reaction affects the macroscopic performance of Al/Ni reactive materials. While all of the results were for Al/Ni, the techniques and concepts developed are likely to be applicable to a range of intermetallic formation reactions.

6.2 Future Work

A number of prospects for future development are presented by the results that have been obtained in the preceding chapters. Several of these are highlighted below.

6.2.1 Detailed Development of Phase Suppression Criteria

If the interpretation presented in Chapter 5 is accurate, we can understand the observed variation of nucleation threshold with reaction progression (α) and temperature (T) shown in Fig. 5.11 as a direct measurement of a portion of a “phase formation” boundary in $\alpha - T$ space. This presents the intriguing question of whether this boundary could be expanded to cover a wider range of temperatures and even predict phase suppression. The goal would be to do this rigorously, informed by the available theoretical models. However, for the purposes of illustration a schematic diagram of what this boundary might look like is presented in Fig. 6.1.

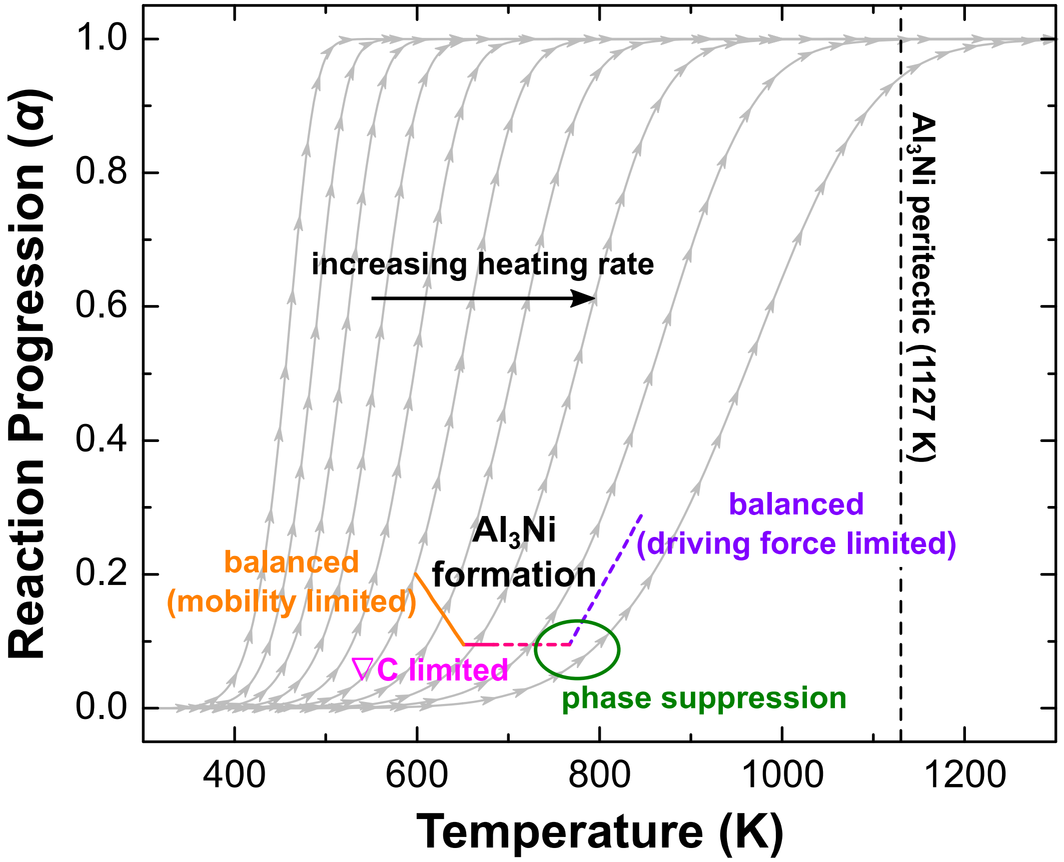

Figure 6.1 Schematic of a proposed phase formation boundary for Al$_3$Ni. Solid portions indicate the result from the experiments in this work (Chapter 5). Dashed lines are hypothetical variations at higher temperatures. At low temperature, the transition boundary is negatively sloped because the nucleation rate is mobility limited and is thus enhanced with increased temperature. At moderate temperatures, the transition boundary is horizontal indicating pure concentration-gradient-limited behavior. Finally, at high temperatures the boundary is positively sloped because the nucleation rate becomes driving force limited and decreases with increasing temperature. If a sample is heated so quickly that it passes around the "corner" of the phase formation boundary, Al$_3$Ni is suppressed. While the drawing is schematic, note that this can likely occur well below the equilibrium stability temperature of the phase (in this case 1127 K).

The solid lines in Fig. 6.1 are taken directly from the experimental result in Chapter 5 (Fig. 5.11). The dashed lines represent hypothetical extensions of this boundary to higher temperatures. As shown, we might expect the concentration-gradient-limited (horizontal) boundary to persist for some time while both atomic mobility and thermodynamic driving force remain high. However, as temperature continues to increase the undercooling is being reduced so that at some point we expect a transition to a second balanced regime where now increasing temperature reduces the driving force and requires an *increase* in mixing (reduction in concentration gradient) before nucleation occurs. This is in direct contrast to the low-temperature balanced regime, where increasing temperature *enhances* the nucleation rate because we are limited by atomic mobility. The overlaid gray sigmoidal curves show the combinations of mixing and temperature sampled at different constant heating rates. The process of phase suppression is illustrated by the right-most curve, which heats past the "corner" of the phase formation boundary and thus never achieves a condition where it is optimal to nucleate that phase. This idea has been put forward before in the general sense that if a sample does not achieve "enough" mixing before getting to "some temperature", nucleation will not occur. Diagrams like the one shown in Fig. 6.1 informed by a combination of experiment and theory would make such criteria much more rigorous.

6.2.2 In Situ Investigation of Phase Formation in IMRMs

One of the hypotheses that came out of the work on inert-mediated reactive multilayers (Chapter 4) was that at higher levels of mediation, intermetallic product (either Al_3Ni_2 or AlNi) was forming earlier in the reaction and/or in larger volume fractions than it does at higher temperatures. This would be consistent with the idea that at low temperatures the rate-limiting process is diffusion through a solid intermetallic at the Al/Ni interface. One way to test this hypothesis would be to perform *in situ* x-ray microdiffraction at a synchrotron and compare the phases observed as a function of time for different inert-mediated samples. In their original synchrotron studies [1,2], Trenkle *et al.* noted that it was very difficult to resolve the exact point at which AlNi formed. However, if a phase other than AlNi is present in the reacting front it would be easily detectable and a significant result demonstrating the effectiveness of the IMRM approach.

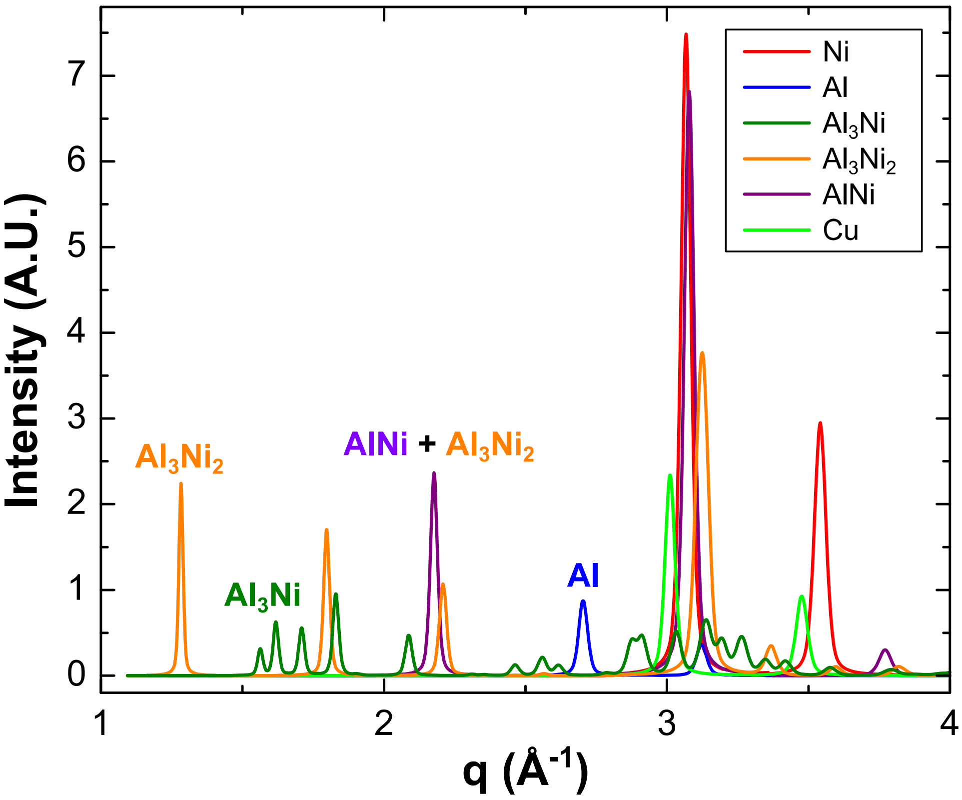

Figure 6.2 Simulated diffraction peaks for possible phases in an IMRM synchrotron experiment. The strongest peaks for Ni, Cu, AlNi, and Al_3Ni_2 all overlap and thus are unlikely to be useful. However, there are peaks that can be uniquely attributed to a phase at small scattering angles as shown. These areas are labeled for the respective phases. AlNi does not have such a region, so the (100) reflection around 2.2 Å^{-1} must be combined with information from the unique Al_3Ni_2 peak at 1.28 Å^{-1} to identify which phase is present. The simulation assumes a radiation wavelength of 1.5 Å and peak widths approximately equal to those reported in [1,2].

One of the biggest challenges in conducting a synchrotron experiment with IMRMs would be that the inert material (Cu and Ni in our design) does not react and thus contributes persistent diffraction peaks that might interfere with the observation of the phases of interest. To assess the magnitude of this challenge, simulated diffraction patterns for the various phases that might be present in a reacting IMRM are shown in Fig. 6.2. The peak widths for these simulations are approximately equal to those reported by Trenkle *et al.* [1,2]. Indeed, we see that the principal peaks for Ni, Cu, AlNi, and

Al_3Ni_2 ((111), (111), (110), and (110) respectively) all fall around 3.1 $Å^{-1}$ and thus are unlikely to be useful. However, most of the Al-rich intermetallic phases have unique peaks at low scattering angles. Assuming these peaks can be detected with sufficient intensity, they would enable the unique identification of one or more intermetallic phases.

6.2.3 High-Throughput Kinetic Analysis Using Nanocalorimetry

As described in detail in Chapter 5, the only reliable way to arrive at a meaningful kinetic model for a reaction is to perform kinetic analysis on a series of reaction curves acquired using different temperature programs [3]. Such datasets can be quite time-consuming to generate using conventional calorimetry since this often involves re-calibration of the thermal analysis instrument at each desired heating rate. In addition, at the heating rates used the time required for a single experiment can range from tens of minutes to hours. If duplicate measurements are to be performed the time investment is even greater. This limits the utility of such analyses in iterative development and often restricts them to analysis of only the “most important” problems, even when the information derived could be useful in other contexts.

Nanocalorimetry presents an intriguing alternative because of the extremely high heating rates available. For example, the cumulative time required to perform all of the measurements (including baseline scans) reported in Chapter 5 was less than 20 minutes. This is a robust, 11-heating-rate dataset (with duplicates) acquired in less time than it would take for a single measurement using conventional calorimetry. Of course, in our case this time was more than compensated by all of the pre-experiment preparation required (e.g. sensor fabrication, annealing, and calibration). However, given a demand these tasks could be automated and optimized (similar to the microelectronics industry) to deliver calibrated nanocalorimeter sensors at a competitive price point.

In this case, we could imagine an array of nanocalorimeter sensors on a single wafer that are all calibrated and individually addressable. The sample of interest would be deposited onto the entire wafer of sensors simultaneously, and then an automated system would run a specified set of heating rate experiments on the samples. This parallel approach would avoid the time-consuming process of loading individual sensors and pumping down a vacuum system, and one could conceivably deposit samples and generate a large, robust dataset for kinetic analysis of the reaction in a single afternoon. This would open up rigorous multi-heating-rate kinetic analysis to a much wider variety of application areas than it is currently used in.

6.2.4 Generalized Ignition Modeling Informed by Nanocalorimetry

Looking at the "phase formation map" in Fig. 6.1, it looks very similar to a construction known as the "reaction map" that I have developed in the context of ignition modeling.[a] An example is shown in Fig. 6.3. Here, as in Fig. 6.1, the x and y axes correspond to temperature and extent of reaction respectively. However, where the phase formation map considers constant heating rate trajectories (i.e. ignores heat generation and heat loss), the reaction map looks at non-constant heating rate trajectories that include heat generation and heat loss *without* any external heating. It is useful for ignition because it clearly delineates the combinations of α and T that enable the sample to react to completion and those that do not. The map shown in Fig. 6.3 was derived for a diffusion-limited reaction modeled using a specific approximation for 1-D diffusion

---

[a] Note that while the reaction map is my own construction, it was inspired by the original efforts of Dr. Greg Fritz as summarized in [6].

limited growth [4], but the lessons learned in the process of analyzing the data presented in Chapter 5 suggest that a more generalized model for ignition could likely be obtained by using the reduced Sestak-Berggren equation to represent an arbitrary reaction model.

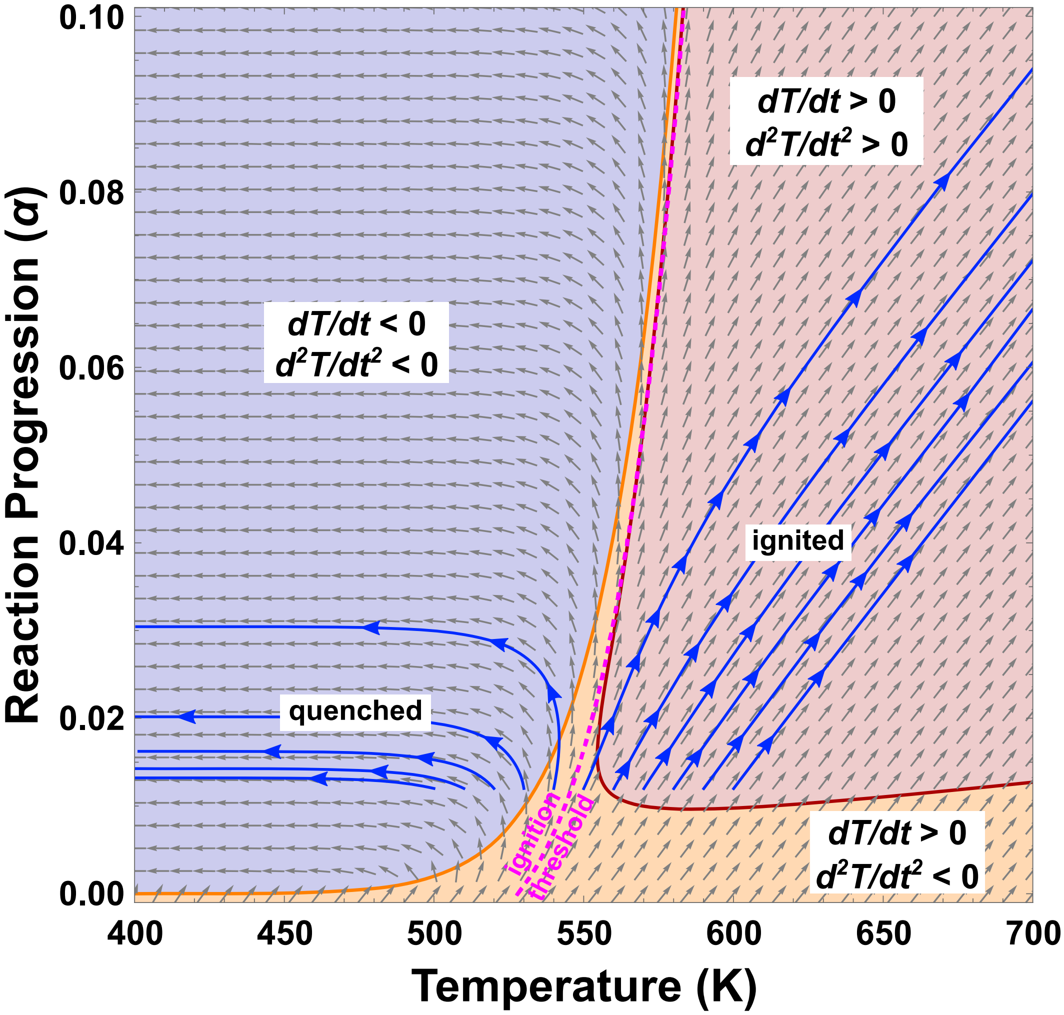

Figure 6.3 An example of a reaction map for a diffusion limited reaction. The dashed magenta line represents the derived ignition threshold as a function of α and T. Blue curves are simulated reaction trajectories based on different starting points. The orange and red curves correspond to the critical points of the first and second derivative respectively. Calculation was performed assuming $D_0 = 2.18 \times 10^{-6}\ \mathrm{m^2\ s^{-1}}$ and $E = 137\ \mathrm{kJ/mol}$.

In Chapter 5, we showed that detailed kinetic models can be derived relatively quickly from multiple-heating-rate datasets generated by nanocalorimetry. If the reaction map and the ignition threshold can be generalized to an arbitrary reaction model, the information obtained from nanocalorimetry could then be inserted directly into the ignition model to make predictions about the ignition threshold of a material under a variety of conditions. This could conceivably yield much more detailed insight into ignition than can be obtained from conventional ignition experiments, and is more likely to be valid than an equivalent conventional calorimetry study because the heating rates in nanocalorimetry are much closer to those that are observed in typical ignition processes [5]. In keeping with the theme of this dissertation, this would be a valuable link between microscopic interfacial reactions (measured by nanocalorimetry) and an important macroscopic property, ignition.

References for Chapter 6

[1] J.C. Trenkle, L.J. Koerner, M.W. Tate, S.M. Gruner, T.P. Weihs, T.C. Hufnagel, Phase transformations during rapid heating of Al/Ni multilayer foils, Appl. Phys. Lett. 93 (2008) 081903.

[2] J.C. Trenkle, L.J. Koerner, M.W. Tate, N. Walker, S.M. Gruner, T.P. Weihs, et al., Time-resolved x-ray microdiffraction studies of phase transformations during rapidly propagating reactions in Al/Ni and Zr/Ni multilayer foils, J. Appl. Phys. 107 (2010) 113511.

[3] S. Vyazovkin, A.K. Burnham, J.M. Criado, L.A. Pérez-Maqueda, C. Popescu, N. Sbirrazzuoli, ICTAC Kinetics Committee recommendations for performing kinetic computations on thermal analysis data, Thermochim. Acta. 520 (2011) 1–19.

[4] R.J. Highmore, J.E. Evetts, A.L. Greer, R.E. Somekh, Differential scanning calorimetry study of solid-state amorphization in multilayer thin-film Ni/Zr, Appl. Phys. Lett. 50 (1987) 566–568.

[5] G.M. Fritz, J.A. Grzyb, O.M. Knio, M.D. Grapes, T.P. Weihs, Characterizing solid-state ignition of runaway chemical reactions in Ni-Al nanoscale multilayers under uniform heating, J. Appl. Phys. 118 (2015) 135101.

[6] G.M. Fritz, S.J. Spey, M.D. Grapes, T.P. Weihs, Thresholds for igniting exothermic reactions in Al/Ni multilayers using pulses of electrical, mechanical, and thermal energy, J. Appl. Phys. 113 (2013) 014901.

CURRICULUM VITAE

Michael D. Grapes was born in 1988 in Columbia, MD. He attended the University of Maryland, College Park from 2006 to 2010, graduating with a B.S. in Materials Science and Engineering and a minor in Nanoscience and Technology. From 2010 to 2016 he was a graduate research assistant in the Department of Materials Science at Johns Hopkins University advised by Professor Timothy P. Weihs. After earning his Ph.D. in May 2016, Michael took a post-doctoral position in the Materials Science Division at Lawrence Livermore National Laboratory.